Aspects of Preheating
and Higgs Cosmology

Francisco Torrentí Salom

Madrid, July 2018

Memoria de tesis doctoral presentada ante el Departamento de Física Teórica de la Universidad Autónoma de Madrid, para la obtención del título de Doctor.

Tesis doctoral dirigida por:

Prof. Juan García-Bellido Capdevila (IFT UAM/CSIC)

Dr. Daniel G. Figueroa (EPFL)

Instituto de Física Teórica
UAM-CSIC

UAM UNIVERSIDAD AUTONOMA DE MADRID

Declaration

The research results presented in this dissertation are based on the original work done in collaboration with other researchers during the course of my PhD, from February 2014 to July 2018. These results have appeared/will appear in the following scientific publications:

- [1] *Decay of the standard model Higgs field after inflation*.
  By Daniel G. Figueroa, Juan Garcia-Bellido, Francisco Torrentí.
  Phys. Rev. D 92 (2015) no.8, 083511 [arXiv:1504.04600]

- [2] GW *production from the decay of the standard model Higgs field after inflation*.
  By Daniel G. Figueroa, Juan Garcia-Bellido, Francisco Torrentí.
  Phys. Rev. D 93 (2016) no.10, 103521 [arXiv:1602.03085]

- [3] *Parametric resonance in the early Universe – a fitting analysis*.
  By Daniel G. Figueroa, Francisco Torrentí.
  JCAP 1702 (2017) no.02, 001 [arXiv:1609.05197].

- [4] *Adiabatic regularization with a Yukawa interaction*.
  By Adrian del Rio, Antonio Ferreiro, Jose Navarro-Salas, Francisco Torrentí.
  Phys. Rev. D 95 (2017) no.10, 105003 [arXiv:1703.00908].

- [5] *Gravitational wave production from preheating – parameter dependence*.
  By Daniel G. Figueroa, Francisco Torrentí.
  JCAP 1710 (2017) no.10, 057 [arXiv:1707.04533]

- [6] *Higgs-curvature coupling and post-inflationary vacuum instability*.
  By Daniel G. Figueroa, Arttu Rajantie, Francisco Torrentí.
  Phys. Rev. D 98 (2017) no.02, 023532 [arXiv:1709.00398].

- [7] *Decay of the standard model Higgs into the SU(2)×U(1) gauge fields after inflation*
  By Daniel G. Figueroa, Juan Garcia-Bellido, Francisco Torrentí.
  To be published.

Results presented in the thesis chapters correspond to the following publications:

* ⋆ Chapter 2 corresponds to Ref. [3].
* ⋆ Chapter 3 corresponds to Ref. [5].
* ⋆ Chapter 4 corresponds to Ref. [1].
* ⋆ Chapter 5 corresponds to Ref. [2].
* ⋆ Chapter 6 corresponds to Ref. [7].
* ⋆ Chapter 7 corresponds to Ref. [6].
* ⋆ Appendix A corresponds to unpublished contents.
* ⋆ Appendix B corresponds to Ref. [4]

Acknowledgements

I would like to express my gratitude to my two PhD advisors, Juan Garcia-Bellido and Daniel G. Figueroa, for their continuous support during the development of this thesis. I am very grateful to Dani for his inmense generosity, patience and motivation during the last four years. We have shared many hours working together, and in all our discussions, I have always learned many things. I am also very grateful to Juan for having offered me the opportunity to pursue a PhD with him. He has always supported me in all my pursuits, as well as provided me with constant motivation during all my PhD study.

I would like to thank all people from the IFT for their support, especially people working in administration and IT. I am especially grateful to my office mates (Federico, Sebastian and Eduardo) for wonderful times together. I am also very grateful to all my collaborators: Stefan Antusch, Antonio Ferreiro, Jose Navarro-Salas, Arttu Rajantie, Adrian del Rio, Mikhail Shaposhnikov, and Wessel Valkenburg. I have had many insightful discussions with them, which have deeply impacted the contents of this thesis. It is also important to emphasize that a great part of this thesis has been carried out in other scientific institutions: CERN, EPFL, UNIGE, Imperial College, and IFIC. I am very grateful to all these institutions for their kind hospitality.

Last but not least, I would like to thank Mariangeles, my parents Julia and Paco, and my brother Felipe, who have provided me with unfailing support and continuous encouragement throughout my many years of study.

Contents

Contents

Contents

Introduction

According to the inflationary paradigm, the Universe experimented an early stage of acceler-ated expansion. Inflation can explain why our Universe is flat and homogeneous at large scales. More importantly, it provides a natural mechanism for structure formation: the accelerated expansion generates an almost scale-invariant spectrum of scalar fluctuations, which eventually become seeds for matter accretion, and allow the formation of galaxies and clusters. Infla-tion also produces tensor perturbations (gravitational waves), which remain for the moment undetected. The inflationary paradigm is one of the cornerstones of modern cosmology.

The particle physics realization of inflation is, however, unknown. In the simplest scenarios, inflation is sustained by the slow-roll motion of a scalar field called the *inflaton*. The existence of such field is hypothetical, and an explanation of its origin usually requires physics beyond the Standard Model (SM). Many extensions of the SM provide different inflaton candidates, which can sustain the accelerated expansion, and are compatible with results from Cosmic Microwave Background experiments.

In this thesis we focus on the period following *immediately after inflation*. The inflationary epoch dilutes any matter that might have previously existed. As a result, the energetic budget of the Universe when inflation ends is dominated by the inflaton, which is typically in the form of a condensate. This is very different to the Universe in which we live. Hence, inflation must be followed by a process of *reheating*: an energy transfer from the inflationary sector to Standard Model species. Reheating constitutes, this way, the link between inflation and the onset of the hot Big Bang theory.

A full understanding of reheating is complicated, because details depend a lot on the as-sumed particle physics model at high energies. It usually proceeds through a series of different stages, the first one of them being *preheating*: an explosive, out-of-equilibrium production of particles due to non-perturbative effects. An example of preheating mechanism is *parametric resonance*, which occurs when the inflationary potential is monomial after inflation. In this case, the inflaton oscillates around the minimum of its potential, and in each oscillation, particles coupled to it are excited due to adiabaticity violation. This stage is normally followed by a process of *perturbative reheating*, in which the inflaton decays perturbatively. Finally, all particle species thermalize at a certain temperature.

This general picture is similar in many reheating scenarios, but details are still unknown. For example, the form of the inflationary potential or the inflaton couplings to other species can only be specified within the context of a particle-physics model. Fortunately, the second decade of the 21st century has witnessed two important breakthroughs, which might help us understand better the physics of the early Universe: the discovery of the Higgs boson, and the first direct detection of gravitational waves.

The Standard Model Higgs was detected for the first time in 2012, in the Large Hadron Collider at CERN. The Higgs was the last missing particle of the Standard Model, and it could be, so far, the only fundamental scalar field ever discovered in nature. Scalar fields might play an essential role in cosmology, such as in inflation. Consequently, this has prompted the development of *Higgs Cosmology*: the research on the implications of the Higgs field in the physics of the early Universe.

Afterwards, the LIGO collaboration detected in 2015, for the first time, the gravitational wave signal from the collision of two Black Holes, which has been followed by additional detections from other colliding astrophysical binaries. Gravitational waves (GW) are ripples of spacetime which propagate at the speed of light. The Universe is expected to be permeated by various GW backgrounds of cosmological origin, and non-equilibrium phenomena after inflation constitute a powerful source. Each process generates a particular GW spectrum, with its own distinct features. If these backgrounds were detected, we could probe particle physics scenarios inaccessible otherwise.

In this thesis we study various aspects of the out-of-equilibrium dynamics of the Universe after inflation. With an extensive use of analytical and numerical techniques, we reexamine the process of preheating after inflation, as well as study some of their implications for *Higgs Cosmology* and primordial production of gravitational waves. The aim of this thesis is threefold:

- First, we want to improve our knowledge of preheating in the early universe. Previous analysis in the literature have usually been focused on specific high-energy physics models, and specific couplings between the inflationary sector and the preheated particles. In this thesis we carry out a systematic parametrization of parametric resonance in the case of quartic and quadratic potentials, for a wide range of particle couplings. We will capture the full non-linear dynamics of the process with classical lattice simulations, from the initial resonant excitation until the later non-linear regime. We will also study parametric resonance when the oscillating field is energetically subdominant.

- Second, we want to understand better the role that the Standard Model might have played in the early Universe, and in particular, after inflation. We will work in scenarios where the Higgs is not the inflaton. The Higgs typically forms a condensate when inflation ends, which decays afterwards into the SM gauge bosons and fermions. Our aim is to study this process in detail, by fully parametrizing the postinflationary dynamics of the

Higgs field and its decay products. For this, we will use lattice techniques extensively, modelling the Higgs-gauge interactions with different degrees of complexity. We will also study the effects of a non-minimal Higgs-curvature coupling in the Higgs postinflationary dynamics, and its implications for vacuum stability after inflation.

- Third, we want to connect preheating to our currently most promising observable: gravitational waves. During preheating, various peaks form in the GW spectrum, with a frequency and amplitude dictated by the coupling constants in the involved theory. We want to provide parametrizations for the gravitational wave spectra generated during preheating in certain models. This could be useful to interpret results from future gravitational wave observatories. As we shall see, the decay of the Higgs field after inflation also produces a GW background, which we also study.

This thesis is structured in one introductory chapter, six chapters based on results (divided in two parts), and one concluding chapter. In Chapter 1 we review the theoretical framework in which the thesis is based. Part I of our research results (chapters 2 and 3) is focused on preheating. In Chapter 2 we provide a fitting analysis of parametric resonance through all its different stages, based on lattice simulations in 3+1 dimensions. In Chapter 3 we expand the previous lattice simulations to study GW production during preheating, and compute the amplitude and frequency of the GW backgrounds today. Part II (chapters 4 to 7) is focused on the non-perturbative, out-of-equilibrium dynamics of the Standard Model after inflation. In Chapter 4 we study the post-inflationary decay of the Higgs condensate into gauge bosons after inflation, using lattice simulations of global and Abelian-Higgs models. We characterize in detail the evolution of the Higgs and its decay products, and provide a master formula for the Higgs decay time as a function of all unknowns. In Chapter 5 we study the gravitational waves produced during the Higgs decay with lattice simulations, and provide a full parametrization of the GW spectra. In Chapter 6 we extend the previous work to include explicitly the SU(2)×U(1) gauge structure of the SM in the lattice, and quantify the effect of the non-Abelian interactions in the Higgs post-inflationary dynamics. In Chapter 7 we study the post-inflationary dynamics of the Standard Model Higgs, when it is coupled to the scalar curvature. We also study the implications of such term for vacuum stability after inflation. Finally, in Chapter 8 we will summarize the main findings of our thesis, as well as present future research avenues. The thesis is also complemented with two appendices of technical nature. In Appendix A we provide a complete lattice formulation of scalar and gauge theories in an expanding universe. Finally, in Appendix B we consider the case of non-perturbative excitation of fermionic species.

Introducción

De acuerdo con el paradigma inflacionario, el Universo experimentó una etapa temprana de expansión acelerada. Inflación podría explicar por qué nuestro universo es plano y homogéneo a grandes escalas. Aún más importante, proporciona un mecanismo natural de formación de estructura: la expansión acelerada genera un espectro de fluctuaciones escalares casi-invariante de escala, que con el tiempo acumulan materia, y permiten la formación de galaxias y cúmulos. Inflación también produce perturbaciones tensoriales (ondas gravitacionales), que de momento no han sido detectadas. El paradigma inflacionario es, sin duda, una de las piedras angulares de la cosmología moderna.

Sin embargo, desconocemos cuál es el mecanismo concreto que genera inflación a altas energías. En los escenarios más simples, la inflación es sostenida por un campo escalar llamado *inflatón*. La existencia de dicho campo es hipotética, y para explicar su origen, se require normalmente física más allá del Modelo Estándar (ME). Muchas extensiones del ME proponen distintos candidatos para el inflatón, que podrían mantener la expansión acelerada durante el tiempo necesario, y que son compatibles con los resultados experimentales del Fondo Cósmico de Microondas.

En esta tesis nos centrarnos en lo que ocurre *inmediatamente después de inflación*. La época inflacionaria diluye cualquier materia que pudiera haber existido previamente. Por lo tanto, al terminar inflación, la energía del Universo está dominada por el inflatón, que normalmente forma un condensado. Por lo tanto, a continuación debe haber un proceso de *recalentamiento*: una transferencia de energía del sector inflacionario a las distintas especies del Modelo Estándar. El recalentamiento constituye, de esta manera, la conexión entre la inflación y el Big Bang caliente.

Es difícil alcanzar un entendimiento completo del proceso de recalentamiento, porque los detalles dependen en gran medida del modelo de física de partículas a altas energías. Por lo general, se pueden distinguir varias fases. La primera de ellas es el *precalentamiento*: una producción explosiva de partículas fuera de equilibrio, debida a efectos no perturbativos. Un ejemplo de mecanismo de precalentamiento es *resonancia paramétrica*, que tiene lugar cuando el potencial inflacionario después de inflación es monomial. En este caso, el inflatón oscila alrededor del mínimo de su potencial, y en cada oscilación, las partículas a las que está acoplado

se excitan debido a efectos de resonancia. Esta etapa va normalmente seguida por un proceso de *recalentamiento perturbativo*. Finalmente, todas las partículas termalizan a cierta temperatura.

Esta descripción es similar en muchos escenarios de recalentamiento, pero los detalles del proceso son desconocidos. Por ejemplo, la forma del potencial inflacionario, o los acoplamientos de inflatón a otras especies, sólo pueden hallarse en el contexto de un modelo de física de partículas. Afortunadamente, la segunda década del siglo XXI ha sido testigo de dos avances importantes, que podrían ayudarnos a comprender mejor la física del Universo primitivo: el descubrimiento del bosón de Higgs y la primera detección directa de ondas gravitacionales.

El Higgs del Modelo Estándar fue detectado por primera vez en 2012, en el Gran Colisionador de Hadrones del CERN. El Higgs, una partícula escalar, ha sido la última partícula del Modelo Estándar en ser descubierta. Creemos que los campos escalares podrían haber desempeñado un papel importante en cosmología, como en inflación. En consecuencia, ésto ha impulsado el desarrollo de *Higgs Cosmology*: la investigación sobre las implicaciones del campo de Higgs en la física del Universo primitivo.

Posteriormente, la colaboración LIGO detectó en 2015, por primera vez, una señal de ondas gravitacionales (OG) proveniente de la colisión de dos agujeros negros, que ha sido seguida por otras detecciones posteriores. Las OG son ondas del espacio-tiempo que se propagan a la velocidad de la luz. Creemos que el Universo está impregnado de diversos fondos de OG de origen cosmológico, y los procesos fuera del equilibrio después de inflación son, precisamente, una fuente poderosa de éstos. Cada proceso genera un espectro de ondas gravitacionales específico, con unas características particulares que se pueden parametrizar. Si se detectaran estos fondos, podríamos explorar rangos de energía inaccesibles actualmente.

En esta tesis estudiamos varios procesos fuera del equilibrio después de inflación. Usando técnicas analíticas y numéricas, reexaminaremos el proceso de precalentamiento después de inflación, y estudiaremos algunas de sus implicaciones en *Higgs Cosmology* y producción primordial de ondas gravitacionales. Los objetivos de la tesis son tres:

- En primer lugar, como hemos dicho, queremos mejorar nuestro conocimiento del precalentamiento en el universo primordial. La mayor parte de análisis previos se han centrado, generalmente, en modelos concretos y acoplamientos específicos entre el sector inflacionario y las partículas precalentadas. En esta tesis llevamos a cabo una parametrización sistemática del proceso de resonancia paramétrica, en el caso de potenciales cuártico y cuadrático, para una amplio rango de acoplamientos. Capturaremos completamente la dinámica no lineal del proceso con simulaciones lattice, desde el regimen linear inicial hasta el régimen estacionario final. También estudiaremos resonancia paramétrica cuando los campos oscilantes son energéticamente subdominantes.

- En segundo lugar, queremos comprender mejor el papel que el Modelo Estándar podría haber desempeñado en el Universo primitivo y, en particular, después de inflación. Nos centraremos en escenarios donde el Higgs no es el inflatón. Cuándo termina inflación, el Higgs forma normalmente un condensado, y a continuación se desintegra en bosones gauge y fermiones. Nuestro objetivo es estudiar este proceso en detalle, parametrizando por completo la dinámica postinflacionaria del Higgs y sus productos de desintegración. Para ésto, usaremos técnicas lattice, modelando las interacciones Higgs-gauge de distintas maneras. También estudiaremos los efectos de un acoplamiento Higgs-curvatura en la dinámica postinflacionaria del Higgs, así cómo sus implicaciones para la estabilidad del vacío.

- En tercer lugar, queremos conectar el precalentamiento con nuestro observable más prometedor: las ondas gravitacionales. Durante el precalentamiento, se forman varios picos en el espectro de ondas gravitacionales, con una frecuencia y amplitud dictadas por las constantes de acoplamiento. Queremos proporcionar parametrizaciones para el fondo de ondas gravitacionales generado durante el precalentamiento en ciertos modelos. Esto podría ser útil para interpretar resultados de futuros detectores de ondas gravitacionales. Como veremos, la desintegración del campo de Higgs después de inflación también produce un fondo de ondas gravitacionales, que también estudiaremos.

Esta tesis se estructura en un capítulo introductorio, seis capítulos de resultados (divididos en dos partes) y un capítulo final. En el Capítulo 1 revisamos el marco teórico en el que se basa la tesis. La Parte I de los resultados de nuestra investigación (capítulos 2 y 3) se centra en el precalentamiento. En el Capítulo 2 proporcionamos un análisis del proceso de resonancia paramétrica a través de todas sus diferentes etapas (crecimiento lineal inicial, evolución no lineal y relajación hacia el equilibrio), basada en simulaciones lattice en 3+1 dimensiones. En el Capítulo 3 extendemos las simulaciones lattice anteriores para estudiar la producción de ondas gravitacionales durante el precalentamiento, y calculamos su amplitud y frecuencia en la actualidad. La Parte II (capítulos 4 a 7) se centra en la dinámica no perturbativa y fuera de equilibrio del Modelo Estándar después de inflación. En el Capítulo 4 estudiamos la desintegración postinflacionaria del condensado de Higgs en bosones gauge después de inflación, utilizando simulaciones lattice. Caracterizaremos en detalle la evolución del Higgs y sus productos de desintegración, y obtenemos una fórmula maestra para el tiempo de desintegración de Higgs en función de todas la circunstancias y parámetros. En el Capítulo 5 estudiamos las ondas gravitacionales producidas durante la desintegración de Higgs con simulaciones lattice, y proporcionamos una parametrización completa de los espectros de ondas gravitacionales. En el Capítulo 6, ampliamos el trabajo anterior para incluir explícitamente la estructura gauge SU(2)×U(1) del Modelo Estándar en la lattice, y cuantificamos el efecto de los términos de interacción no abelianos. En el Capítulo 7 estudiamos la dinámica post-inflacionaria del Modelo Estándar, en presencia de un acoplamiento no mínimo del Higgs a

la curvatura. También estudiamos las implicaciones de dicho término para la estabilidad del vacío después de inflación. Finalmente, en el Capítulo 8 resumimos los principales hallazgos de nuestra investigación, así como presentamos posibles extensiones de nuestro trabajo. La tesis también incluye dos apéndices de naturaleza técnica. En el Apéndice A proporcionamos una formulación lattice completa de teorías escalares y gauge en un Universo en expansión. Finalmente, en el Apéndice B estudiamos el caso de excitación no perturbativa de fermiones.

Chapter 1.

Theoretical framework

1.1. Matter and spacetime

In this chapter we review some key aspects of cosmology and particle physics, which are necessary for the development of this thesis. In particular, we review the Friedmann equations, as well as basic aspects of background inflationary cosmology.

In the theory of General Relativity, matter and energy determine the local geometry of spacetime. This relation is dictated by the Einstein field equations,

$$R_{\mu\nu} - \frac{1}{2}Rg_{\mu\nu} + \Lambda g_{\mu\nu} = 8\pi G T_{\mu\nu} \, , \tag{1.1}$$

where $g_{\mu\nu}$ is the spacetime metric, $R_{\mu\nu}$ is the Ricci curvature tensor, R is the Ricci scalar, G and Λ are the gravitational and cosmological constants respectively, and $T_{\mu\nu}$ is the stress-energy tensor. Note that the gravitational constant is usually written in terms of the full Planck mass, $M_P \equiv G^{-1}$, or the reduced Planck mass, $m_P \equiv (8\pi G)^{-1}$.

According to the Cosmological Principle, the Universe at large scales is homogeneous and isotropic. This is in agreement with observations of the Cosmic Microwave Background (CMB) and Large Scale Structure (LSS). The only 4-dimensional spacetime metric $g_{\mu\nu}$ compatible with these two properties is the Friedmann-Lemaitre-Robertson-Walker (FLRW) metric, which can be written in polar coordinates $[x^\mu = (t, r, \theta, \phi)]$ as

$$ds^2 \equiv g_{\mu\nu}dx^\mu dx^\nu = -dt^2 + a^2(t)\left[\frac{dr^2}{1 - kr^2} + r^2(d\theta^2 + \sin^2\theta d\phi^2)\right] \, . \tag{1.2}$$

Here, $a(t)$ is the scale factor describing the time-evolution of the spatial slices, and $k = -1, +0, +1$ is the spatial curvature. In the $k = 0$ case, the FLRW metric can be written in cartesian coordinates simply as $ds^2 = -dt^2 + a^2(t)(dx^2 + dy^2 + dz^2)$. On the other hand, compatibility with the cosmological principle requires the following perfect-fluid form for the

stress-energy tensor,

$$T^{\mu\nu} = (\rho + p)u^\mu u^\nu + pg^{\mu\nu} , \tag{1.3}$$

where ρ is the energy density of the fluid, p is the pressure, and u^μ is the 4-velocity (with $u_\mu u^\mu = -1$). By substituting Eqs. (1.2)-(1.3) into (1.1), we find the first and second Friedmann equations,

$$\left(\frac{\dot{a}}{a}\right)^2 = \frac{8\pi G}{3}\rho + \frac{\Lambda}{3} - \frac{k}{a^2} , \tag{1.4}$$

$$\frac{\ddot{a}}{a} = -\frac{4\pi G}{3}(\rho + 3p) + \frac{\Lambda}{3} , \tag{1.5}$$

where $\dot{} = d/dt$. We also define the Hubble parameter as $H(t) \equiv \dot{a}/a$. By combining appropriately the two Friedmann equations, the following energy-conservation constraint is found,

$$\dot{\rho} + 3\frac{\dot{a}}{a}(p + \rho) = 0 . \tag{1.6}$$

The Friedmann equations describe how the scale factor of the Universe evolves with time as a function of the energy density and pressure. The content of the Universe can successfully be modelled, for most of its history, as a sum of different perfect fluids with constant equation of state $w \equiv p/\rho$. In particular, during different expansion epochs, the energy density of our Universe has been dominated by either radiation (RD, $w = 1/3$) or matter (MD, $w = 0$). The cosmological constant term can also be interpreted as coming from a fluid with $w = -1$. In each of these regimes, the time-evolution of the scale factor is different,

$$
\begin{aligned}
\text{MD}: \quad w &= 0 &&\Rightarrow && a(t) \propto t^{1/2} , \\
\text{RD}: \quad w &= 1/3 &&\Rightarrow && a(t) \propto t^{2/3} , \\
\Lambda\text{D}: \quad w &= -1 &&\Rightarrow && a(t) \propto e^{Ht} .
\end{aligned} \tag{1.7}
$$

Note also that, for a generic constant equation of state w with $w > -1$, we have $a(t) \propto t^{\frac{2}{3(1+w)}}$. It is useful to define the following density parameters for radiation, matter, cosmological constant, and curvature,

$$\Omega_R \equiv \frac{8\pi G}{3H^2}\rho_R , \quad \Omega_M \equiv \frac{8\pi G}{3H^2}\rho_M , \quad \Omega_\Lambda \equiv \frac{\Lambda}{3H^2} , \quad \Omega_K \equiv -\frac{k}{H^2 a^2} . \tag{1.8}$$

With these definitions, the first Friedmann equation (1.4) can be rewritten as

$$H^2(a) = H_0^2 \left(\Omega_R^{(0)} \left(\frac{a_0}{a}\right)^4 + \Omega_M^{(0)} \left(\frac{a_0}{a}\right)^3 + \Omega_K^{(0)} \left(\frac{a_0}{a}\right)^2 + \Omega_\Lambda^{(0)} \right) , \tag{1.9}$$

where the (0) superindex indicates the values of the density parameters today, and H_0 is the current Hubble parameter, which according to the measurements of the Planck experiment [8], it is constrained as $H_0 = (67.8 \pm 0.9) \text{km s}^{-1} \text{Mpc}^{-1}$. Observations of the Cosmic Microwave Background indicate that we live in a flat Universe with $|\Omega_K^{(0)}| < 0.005$, formed by a combination of a cosmological constant with $\Omega_\Lambda^{(0)} \approx 0.7$, and matter with $\Omega_M^{(0)} \approx 0.3$, as well as a small fraction of radiation $\Omega_R^{(0)} \sim 10^{-4}$ [9]. However, due to the different dilution rates in (1.9), these ratios changed in the past: there was a period of radiation-domination in the very early Universe, followed by a later stage of matter-domination. It is also convenient to define a new parameter as $\Omega \equiv \Omega_R + \Omega_M + \Omega_\Lambda$. With this, Eq. (1.9) simply becomes

$$\Omega - 1 = \Omega_k \, . \tag{1.10}$$

From here, we work out that $\Omega > 1$ implies an open Universe $(k < 0)$, $\Omega < 1$ implies a closed Universe $(k > 0)$, and $\Omega = 1$ implies a flat Universe $(k = 0)$.

The Einstein field equations (1.1) can be obtained from the minimization of the Einstein-Hilbert action with respect the metric $g_{\mu\nu}$. This action is written as the sum of two contributions, $S \equiv S_g + S_m$ where S_g is the gravitational part, and S_m is the matter part. They are defined as

$$S_g = \frac{1}{16\pi G} \int d^4x \sqrt{-g}(R - 2\Lambda) \, , \qquad S_m \equiv \int d^4x \sqrt{-g} \mathcal{L}_m \, , \tag{1.11}$$

where g is the determinant of the metric, and $\mathcal{L}_m$ is the matter Lagrangian. From the condition $\delta S / \delta g_{\mu\nu} = 0$ we recover the Einstein equations (1.1), with the stress-energy tensor defined as

$$T^{\mu\nu} \equiv \frac{2}{\sqrt{-g}} \frac{\delta(\sqrt{-g}\mathcal{L}_m)}{\delta g_{\mu\nu}} \, . \tag{1.12}$$

In this thesis, we will describe the content of the Universe as a sum of different interacting matter fields. We will typically consider different combinations of real scalar fields (which we denote generically as χ), complex scalar fields (φ), Abelian gauge fields (A_μ), and non-Abelian gauge fields (B_μ^a). The typical Lagrangians we will consider are of the form [10]

$$-\mathcal{L}_m = \frac{1}{2}\partial_\mu\chi\partial^\mu\chi + \frac{1}{2}(D_\mu\varphi)^\dagger(D^\mu\varphi) + \frac{1}{4}F_{\mu\nu}F^{\mu\nu} + \frac{1}{4}G_{\mu\nu}^a G_a^{\mu\nu} + V(|\varphi|, \chi) \, , \tag{1.13}$$

where $F_{\mu\nu}$ and $G_{\mu\nu}^a$ are the Abelian and non-Abelian field strengths respectively, and D_μ is the gauge covariant derivative. They are defined in terms of components as

$$\begin{aligned} F_{\mu\nu} &\equiv \partial_\mu A_\nu - \partial_\nu A_\mu \, , \tag{1.14} \\ G_{\mu\nu}^a &\equiv G_{\mu\nu}^a T_a \, , \quad G_{\mu\nu}^a \equiv \partial_\mu B_\nu^a - \partial_\nu B_\mu^a + \frac{g_2}{2} f^{abc} B_\mu^b B_\nu^c \, , \\ (D_\mu)_{ij} &\equiv \delta_{ij} \left(\partial_\mu - i(g_1/2)A_\mu \right) - i(g_2/2) B_\mu^a (\sigma_a)_{ij} \, . \tag{1.15} \end{aligned}$$

Here, g_1 and g_2 are the Abelian and non-Abelian gauge couplings respectively, and $T_a \equiv \sigma_a/2$ are the generators of the SU(2) group, where σ_a ($a = 1, 2, 3$) are the Pauli matrices obeying $[\sigma_a, \sigma_b] = i f_{abc} \sigma_c$ with $f_{abc} = 2\epsilon_{abc}$. This Lagrangian is invariant under local transformations of the SU(2) $\times$ U(1) group. The Lagrangian includes a potential $V = V(\chi, |\varphi|)$, containing all the interactions and self-interactions of the different real and complex scalar fields. The equations of motion are simply obtained from the minimization of Eq. (1.13) with respect the different field variables. These are

$$\ddot{\chi} - \frac{1}{a^2}\partial_i\partial_i\chi + 3\frac{\dot{a}}{a}\dot{\chi} = -\frac{\partial V}{\partial \chi}, \tag{1.16}$$

$$\ddot{\varphi} - \frac{1}{a^2}D_iD_i\varphi + 3\frac{\dot{a}}{a}\dot{\varphi} = -\frac{\partial V}{\partial \varphi^\dagger}, \tag{1.17}$$

$$\partial_0 F_{0\nu} - \frac{1}{a^2}\partial_i F_{i\nu} + (1-\alpha)\frac{\dot{a}}{a}F_{0\nu} = \frac{g_1}{2}\mathfrak{Im}[\varphi^\dagger(D_\nu\varphi)], \tag{1.18}$$

$$(\mathcal{D}_0)_{ab}(G_{0\nu})^b - \frac{1}{a^2}(\mathcal{D}_i)_{ab}(G_{i\nu})^b + \frac{\dot{a}}{a}(G_{0\nu})^b = \frac{g_2}{2}\mathfrak{Im}[\varphi^\dagger\sigma_a(D_\nu\varphi)]. \tag{1.19}$$

In practice, we will typically solve self-consistently these equations in cubic lattices of different sizes. In particular, in Appendix A we present an equivalent action to the one of Eq. (1.13), written in this case in a discrete spacetime. The action is written in Eq. (A.55), and its minimization yields the discrete equations of motion (A.68)-(A.71), which are the ones we solve in the lattice. Note also that we have not included fermion spieces in action (1.13): we will briefly consider them in Appendix B.

1.2. Inflation

The theoretical framework reviewed in the previous section constitutes an important part of the hot Big Bang theory, which successfully describes the evolution of the Universe from the first fraction of a second till today. Its validity is sustained on three observational evidences. The first one is the expansion of space, as confirmed by the redshift of distant galaxies. The second is the existence of the cosmic microwave background (CMB), which is a relic radiation coming from the recombination epoch, when electrons and protons formed the first bound hydrogen atoms. The third one is the observed abundance of primordial elements, which agrees with the predictions of Big Bang nucleosynthesis (BBN). According to this theory, the scale factor has evolved, during nearly the whole cosmic history, as a power law $a(t) \propto t^n$, where $n = \frac{1}{2}, \frac{2}{3}$ for the RD and MD stages respectively.

However, the hot Big Bang theory possesses several shortcomings or *problems* of theoretical nature, related with the initial conditions of the Universe. The most important one is the *horizon problem*, which is associated to the observed homogeneity and isotropy of the Universe.

For example, cosmological observations have confirmed that the CMB is very homogeneous, with very small anisotropies of the order $\Delta T/T_0 \approx 10^{-5}$, with $T_0 \approx 2.726$K the average temperature [11]. Another example is the distribution of galaxies in the Universe, which is also homogeneous at large scales.

Homogeneity could be explained if all the regions of our visible universe were causally connected in the past. This can be characterized in terms of the Hubble comoving radius, defined as $\mathcal{H}^{-1} \equiv (aH)^{-1}$: causal connection requires the Hubble comoving radius to be a decreasing function with time. However, this is not possible for the power-law expansions considered above: for a scale factor evolving as $a \sim t^n$, we find that $\mathcal{H} \sim (1/n)t^{n-1}$, which grows with time for both $n = \frac{1}{2}, \frac{2}{3}$. This seems to be in contradiction with the observed uniformity of the CMB.

Another important shortcoming of the hot Big Bang theory is the *flatness problem*. From cosmological observations, we know that our Universe is approximately flat at present time, i.e. $|\Omega_k| \ll 1$. However, when the scale factor is a power-law function with time, the solution $|\Omega_k| = 0$ is a point of unstable equilibrium in the Friedmann equations, Eq. (1.9). Compatibility with observations requires then the extreme fine-tuning $\Omega_k \approx 10^{-16}$ at the time of BBN, and even a smaller value at earlier times [9].

Inflation was introduced originally by Alan Guth in the 1980s to overcome the shortcomings of the hot Big Bang theory, and it was immediately extended by others [12, 13, 14, 15]. As noted by Guth, all shortcomings could be solved if the Universe went through a stage of accelerated expansion in the past, defined as $\ddot{a} > 0$. The key point is that, unlike in a power-law expansion, in this case the Hubble comoving radius *decreases* with time,

$$\frac{d^2 a}{dt^2} > 0 \quad \Longleftrightarrow \quad \frac{d}{dt}\mathcal{H}^{-1} < 0 \,. \tag{1.20}$$

We can compute a simple estimate of the required number e-folds of inflation to solve the horizon problem. For this, let us denote the scale factor and Hubble rates at the onset of inflation with the subindex 'i'. Similarly, let us also indicate the same quantities evaluated at the end of inflation with the subindex 'f', and evaluated today with the subindex '0'. We require then that $(a_0 H_0)^{-1} < (a_i H_i)^{-1}$. Let us assume for simplicity, that the Universe expands exponentially during inflation, so that $a = a_i e^{H_i t}$ and $H_i = H_f$. Let us also assume that the Universe expands as RD after inflation. In this case, we find

$$\frac{(a_0 H_0)^{-1}}{(a_i H_i)^{-1}} = \frac{(a_0 H_0)^{-1}}{(a_f H_f)^{-1}}\frac{(a_f H_f)^{-1}}{(a_i H_i)^{-1}} = \frac{a_0}{a_f}\frac{a_i}{a_f} = \frac{T_f}{T_0}\frac{a_i}{a_f} \simeq 10^{29}\left(\frac{a_i}{a_f}\right), \tag{1.21}$$

where in second equality we have used that $H_0/H_f \propto (a_0/a_f)^{-2}$ and $H_i = H_f$, in the third equality we have used $a \propto T^{-1}$, and in the last equality we have used $T_f \sim 10^{16}$GeV for

definiteness. Then, we require

$$\frac{a_f}{a_i} > 10^{29} \quad \implies \quad \mathcal{N} \equiv \log\left(\frac{a_f}{a_i}\right) \approx 67 , \tag{1.22}$$

where $\mathcal{N}$ is the number of e-folds of inflation. Hence, an early phase of accelerated expansion that lasts $\sim$70 e-folds could explain the homogeneity of the Universe. One can also prove that during an accelerated expansion $\ddot{a} > 0$, the solution $|\Omega_k| \ll 1$ becomes, instead an attractor solutions of the Friedmann equations. This could also explain the observed flatness of the Universe.

Compelling evidence supports the idea of an inflationary phase in the early Universe [16]. However, the specific particle physics realization of inflation is uncertain. In many scenarios, inflation can be sustained by the slow-roll motion of a scalar field ϕ, denoted as inflaton, as long as the form of its potential $V(\phi)$ obeys certain conditions, as we shall explain below. The action of such field is written as

$$S = -\int \sqrt{-g} d^4 x \left(\frac{1}{2}\partial_\mu \phi \partial^\mu \phi + V(\phi)\right) . \tag{1.23}$$

The inflaton stress-energy tensor is, from Eq. (1.12),

$$T_{\mu\nu} = \partial_\mu \phi \partial_\nu \phi - \left(\frac{1}{2}\partial_\alpha \phi \partial^\alpha \phi\right) g_{\mu\nu} . \tag{1.24}$$

The inflaton EOM is obtained by minimizing action (1.23) with respect ϕ, while the time-evolution of the scale factor is obtained from the Friedmann equation (1.4). These are

$$\ddot{\phi} - \nabla^2 \phi + 3H\dot{\phi} = -\frac{dV(\phi)}{d\phi} , \tag{1.25}$$

$$H^2(t) = \frac{8\pi G}{3}\left(\frac{1}{2}\dot{\phi}^2 + \frac{1}{2}(\nabla\phi)^2 + V(\phi)\right) . \tag{1.26}$$

On the other hand, the energy density ρ_ϕ and pressure p_ϕ of the inflaton are, from Eq. (1.12),

$$\rho_\phi \equiv T_{00} = \frac{1}{2}\dot{\phi}^2 + \frac{1}{2}(\nabla\phi)^2 + V(\phi) , \tag{1.27}$$

$$p_\phi \equiv \frac{1}{3}\sum_i T_i^i = \frac{1}{2}\dot{\phi}^2 - \frac{1}{6}(\nabla\phi)^2 - V(\phi) . \tag{1.28}$$

As commented, in order to explain the initial conditions of the hot Big Bang theory, we need to achieve an accelerated expansion of the Universe, defined as $\ddot{a} > 0$. By inspecting the Friedmann Eq. (1.5), we see that this is achieved if

$$\rho_\phi + 3p_\phi < 0 \quad \Longleftrightarrow \quad \omega_\phi \equiv \frac{p_\phi}{\rho_\phi} < -\frac{1}{3} , \tag{1.29}$$

where ω_ϕ is the effective equation of state of the inflaton. From the expressions of ρ_ϕ and p_ϕ, we observe that if the inflaton satisfies the conditions $\dot{\phi}^2 \ll |\nabla\phi|^2, |V(\phi)|$, then $p_\phi \approx -\rho_\phi$ and $w_\phi \approx -1$, and an accelerated expansion is achieved. As we want to explain the homogeneity and isotropy of the Universe, we will assume a homogeneous inflaton $\phi \equiv \phi(t)$. Hence, the first condition for successful inflation is simply written as

$$\dot{\phi}^2 \ll |V(\phi)| \, . \tag{1.30}$$

Before moving on, let us derive a useful relation between the time-derivatives of the inflaton and the Hubble parameter. If we differentiate Eq. (1.26) with respect time, we get

$$2H\dot{H} = \frac{8\pi G}{3}\dot{\phi}\left(\ddot{\phi} + \frac{dV}{d\phi}\right) \, , \tag{1.31}$$

and substituting Eq. (1.25) into the right hand side of this expression, we obtain

$$\dot{H} = -4\pi G\dot{\phi}^2 \, . \tag{1.32}$$

We have seen in Eq. (1.22) that inflation must last during at least $\mathcal{N} \sim 70$ e-folds, in order to solve the horizon problem of the hot Big Bang theory. The inflaton must obey then the condition (1.30) during all that time, and for this to happen, it must not accelerate much during inflation. From the inflaton EOM (1.25), this second condition can be written as ($' \equiv d/d\phi$)

$$|\ddot{\phi}| \ll 3H|\dot{\phi}|, V'(\phi) \, . \tag{1.33}$$

Conditions (1.30) and (1.33) are written in terms of the slow-roll parameters ϵ and η as

$$\epsilon \equiv \frac{3\dot{\phi}^2}{2V(\phi)} \ll 1 \, , \quad \eta \equiv -\frac{\ddot{\phi}}{H\dot{\phi}} \ll 1 \, . \tag{1.34}$$

If these conditions are obeyed, we say that the scalar field is in a *slow-roll regime*. In this regime, the field and Friedmann equations, Eqs. (1.25) and (1.26), are written as

$$H^2 \simeq \frac{8\pi G}{3}V(\phi) \, , \tag{1.35}$$

$$\dot{\phi} \simeq -\frac{V'(\phi)}{3H} \, , \tag{1.36}$$

By substituting Eq. (1.35) into (1.36), we can find an expression for the inflaton EOM of the form $\dot{\phi} = \dot{\phi}(\phi)$,

$$\dot{\phi} \simeq -\frac{V'(\phi)}{\sqrt{24\pi G V(\phi)}} \, , \tag{1.37}$$

where we have removed the explicit dependence on H. Finally, the solution for the scale factor in this regime corresponds to a quasi-de Sitter spacetime,

$$a(t) \simeq a_i e^{\int_{t_i}^{t} H(\phi) dt'} . \tag{1.38}$$

Slow-roll conditions (1.30) and (1.33) are guaranteed if the potential function obeys the following relations,

$$\epsilon_V \equiv \frac{m_p^2}{2} \left(\frac{V'(\phi)}{V(\phi)} \right)^2 \ll 1 , \qquad \eta_V \equiv m_p^2 \left(\frac{V''(\phi)}{V(\phi)} \right) \ll 1 , \tag{1.39}$$

where ϵ_V and η_V are two new slow-roll parameters, defined in this case in terms of the potential. We can prove that in the slow-roll regime, the new parameters are related with the old ones with the identities $\epsilon_V \simeq \epsilon$ and $\eta \simeq \eta_V - \epsilon_V$. The first expression can be easily proven by substituting Eq. (1.36) into the definition of ϵ, given in Eq. (1.34). To prove the second expression, let us first differentiate Eq. (1.36) with respect time

$$\ddot{\phi} \simeq -\frac{V''(\phi)}{3H} \dot{\phi} + \frac{V'(\phi)\dot{H}}{3H^2} = -\frac{V''(\phi)}{3H} \dot{\phi} - 4\pi G \frac{V'(\phi)\dot{\phi}^2}{3H^2} , \tag{1.40}$$

where in the second equality, we have used (1.32). We have then, for η,

$$\eta \equiv -\frac{\ddot{\phi}}{H\dot{\phi}} \simeq \frac{V'(\phi)}{3H^2} + 4\pi G \frac{V'(\phi)\dot{\phi}}{9H^3} \equiv \frac{1}{8\pi G} \left(\frac{V''(\phi)}{V(\phi)} - \frac{1}{2} \frac{V'(\phi)^2}{V(\phi)^2} \right) = \eta_V - \epsilon_V , \tag{1.41}$$

where in the second equality we have used Eq. (1.40), and in the third equality, we have used Eqs. (1.35) and (1.36).

Note that the scale factor can be equivalently expressed in terms of the number of e-folds $\mathcal{N}(t)$ as $a(t) \equiv a_i e^{\mathcal{N}(t)}$. By differentiating this expression with respect time, we find

$$H(t) \equiv \frac{\dot{a}}{a} = \frac{d\mathcal{N}}{dt} . \tag{1.42}$$

We can then write the number of e-folds as a function of $\epsilon_V(\phi)$ as

$$\mathcal{N}(t) \equiv \int_{t_i}^{t} dt' H(t') = \int_{\phi(t_i)}^{\phi(t)} \frac{H}{\dot{\phi}} d\phi \simeq \sqrt{8\pi G} \int_{\phi(t_i)}^{\phi(t)} \frac{d\phi}{\sqrt{2\epsilon_V(\phi)}} , \tag{1.43}$$

where in the third equality, we have used that $\epsilon_V \simeq \epsilon \simeq 4\pi G \dot{\phi}^2 / H^2$. As obtained in Eq. (1.22), we need at least $\mathcal{N} \approx 70$ e-folds to solve the initial condition shortcomings of the hot Big Bang theory.

Many particle-physics models exist, that provide a potential function $V(\phi)$ such that conditions (1.39) are fulfilled. For an extensive review on inflationary models, see e.g. Ref. [17].

A paradigmatic example are models of chaotic inflation, in which the potential has a monomial shape of the type

$$V(\phi) = \frac{1}{n} \lambda M^{4-n} \phi^n \, , \qquad (1.44)$$

with λ a dimensionless parameter, M a mass scale, and $n \geq 1$. In particular, for $n = 2, 4$,

$$V(\phi) = \begin{cases} \frac{1}{4} \lambda \phi^4, & \lambda \approx 9 \times 10^{-14} \\ \frac{1}{2} m^2 \phi^2, & m \approx 6 \times 10^{-6} m_p \end{cases} \, , \qquad (1.45)$$

where the strengths of the λ and m parameters are fixed observationally by the measured amplitude of the observed CMB anisotropies. For these kind of potentials, the slow-roll parameters are, from Eq. (1.39),

$$\epsilon_V(\phi) = \frac{n^2}{2} \left(\frac{m_p}{\phi} \right)^2 \, , \qquad \eta_V(\phi) = n(n-1) \left(\frac{m_p}{\phi} \right)^2 \, . \qquad (1.46)$$

Hence, in these models, inflation is sustained for field values greater than the Planck mass, $\phi \gg m_p$, for which the slow-roll parameters are $\epsilon_V, \eta_V \ll 1$.

Inflaton ends when the slow-roll parameters become approximately of order unity, $\epsilon(t_f) \approx 1$. In the case of the chaotic models of Eq. (1.45), this happens when $\phi \sim m_p$. As inflation dilutes all matter previously present, the inflaton dominates the energetic budget of the Universe at this time. Hence, inflation must be followed by a process of reheating, in which the energy of the inflationary sector must be transferred to Standard Model species, which will eventually thermalize and provide the initial conditions for the hot Big Bang era. The first part of reheating usually consists in a out-of-equilibrium, non-perturbative production of particles called preheating. In the next Chapter, we will analyze preheating for the chaotic inflationary models presented in Eq. (1.45).

Part I.

Fitting analysis of preheating

Chapter 2.

Parametric resonance in the early universe: a fitting analysis

Particle production via parametric resonance in the early Universe, is a non-perturbative, non-linear and out-of-equilibrium phenomenon. Although it is a well studied topic, whenever a new scenario exhibits parametric resonance, a full re-analysis is normally required. To avoid this tedious task, many works present often only a simplified linear treatment of the problem. In order to surpass this circumstance in the future, we provide a fitting analysis of parametric resonance through all its relevant stages: initial linear growth, non-linear evolution, and relaxation towards equilibrium. Using lattice simulations in an expanding grid in 3+1 dimensions, we parametrize the dynamics' outcome scanning over the relevant ingredients: role of the oscillatory field, particle coupling strength, initial conditions, and background expansion rate. We emphasize the inaccuracy of the linear calculation of the decay time of the oscillatory field, and propose a more appropriate definition of this scale based on the subsequent non-linear dynamics. We provide simple fits to the relevant time scales and particle energy fractions at each stage. Our fits can be applied to post-inflationary preheating scenarios, where the oscillatory field is the inflaton, or to spectator-field scenarios, where the oscillatory field can be e.g. a curvaton.

Results presented in this Chapter have been published in Ref. [3].

2.1. Introduction

In this chapter we consider inflaton potentials with simple monomial shapes. This gives rise to a relevant particle creation phenomena in the early universe: parametric resonance. This is the case of chaotic inflation models, like the ones of Eq. (1.45), where the inflaton rolls down a monomial potential during the whole inflationary period. Although these scenarios are under tension with cosmological data [16], the simple addition of a small non-minimal gravitational

18

coupling could reconcile them with the observations [18]. Some scenarios which fit perfectly well the observational data, e.g. Higgs-Inflation [19, 20] and Starobinsky inflation [13], also exhibit a monomial potential with a single minimum, but only during the stages following inflation.

In all the scenarios we consider, soon after the end of inflation, the inflaton is in the form of a homogeneous condensate, and starts oscillating around the minimum of its potential. Each time the inflaton crosses zero, all particle species coupled to the inflaton are created in energetic bursts. In the case of bosonic species, the production of particles is resonant, and the energy transferred grows exponentially within few oscillations of the inflaton [21, 22, 23, 24, 25, 26, 27, 28]. In the case of fermionic species, there is also a significant transfer of energy [29, 30, 31, 32, 33, 34], but Pauli blocking prevents resonance from developing. The production of particles in this way, either of fermions or bosons, represents the archetypical example of what is meant by an initial 'preheating' stage of reheating. For recent reviews on parametric resonance and preheating mechanisms in general, see [35, 36].

Inflationary preheating is, however, not the only case where parametric resonance takes place in the early Universe. If a light spectator field is present during inflation, this field forms a homogeneous condensate during the inflationary period, and oscillates around the minimum of its potential afterwards. This is the case e.g. of the curvaton scenario [37, 38, 39, 40]. The curvaton may decay after inflation via parametric resonance, transferring abruptly all its energy to the particle species coupled to it [41, 42, 43, 44]. Another example of a spectator field, naturally decaying through parametric resonance after inflation, is the SM Higgs field. In this chapter, we will consider the case of a curvaton with quadratic potential, while the post-inflationary decay of the SM Higgs will be studied in more detail in Chapters 4 and 6.

In this thesis, we will often refer to the oscillatory field as the *mother* field, and to the created species as the *daughter* fields. Particle production of daughter fields via parametric resonance, corresponds to a non-perturbative effect, which cannot be captured by perturbative coupling expansions, not even if the couplings involved are small [25]. During the initial stage of parametric resonance, the system is linear, and analytical methods can be applied. As the particle production is exponential for bosonic species, the daughter field(s) eventually 'backreact' onto the mother field, making the system non-linear. In order to fully capture the non-linearities of the system, we need to study this phenomenon in the lattice. The approach of classical field theory real-time lattice simulations can be considered valid as long as the occupation number of the different species is much larger than one, and hence their quantum nature can be ignored [45, 46]. Lattice simulations have been successfully carried out for different preheating scenarios during the last years (see e.g. [35, 36] and references therein), but each time a new scenario exhibits parametric resonance, a new analysis is often required. Moreover, lattice simulations are computationally expensive and time consuming, and not everybody has the expertise on the appropriate numerical packages [47, 48, 49, 50, 51].

Consequently, many studies often resort to over-simplified analytical analysis, which capture only the initial linear stage.

In this chapter, we present a systematic study of parametric resonance, fitting the dynamics through all the relevant stages, from the initial linear growth till the relaxation towards equilibrium, passing through an intermediate non-linear stage. We have used massively parallelized lattice simulations to characterize the dynamics of parametric resonance through all its stages. We have parametrized the dynamics by scanning over the relevant circumstances and parameters: role of the oscillating field, particle coupling, initial conditions, and background rate of expansion. We have obtained in this way, for the first time, simple fits to the most significant quantities, like the characteristic time scales and energy fractions of the different particle species. Our fitted formulas can be applied to the study of parametric resonance in scenarios where the mother field dominates the energy budget of the universe (i.e. preheating), or in scenarios where the mother field represents only a sub-dominant component (e.g. inflationary spectator fields).

This chapter is structured as follows. In Section 2.2 we describe in more detail the scenarios in which parametric resonance takes place and introduce some notation. We present in Section 2.3 and 2.4 the results from lattice simulations for preheating with quartic and quadratic potentials respectively. I also show, for each case, analytical estimations for the time decay of the mother field. In Section 2.5 we present the analogous lattice study for scenarios where the mother field represents only a sub-dominant energy component of the Universe. Finally, in Section 2.6 we summarize our results and conclude.

2.2. Parametric resonance: general description

In this section we describe the general features of parametric resonance, as well as introduce some notation, which will be useful for the rest of the thesis. Let us denote the oscillating mother field as ϕ, and the daughter field as X. In this thesis, we will consider scenarios where the potential $V_{\text{inf}}(\phi)$ of the mother field is monomial. In particular, we consider

$$V(\phi, \chi) = V_{\text{inf}}(\phi) + \frac{1}{2} g^2 \phi^2 X^2 \,, \qquad V_{\text{inf}}(\phi) = \frac{1}{n} \lambda M^{4-n} \phi^n \,, \tag{2.1}$$

where λ is a dimensionless coefficient, M is some mass scale, g^2 is a dimensionless coupling constant, and $n = 2, 4, 6 \ldots$. Here, we have assumed that the mother and the daughter fields are coupled with a quadratic interaction term $g^2 \phi^2 X^2$. This interaction has been often assumed in the context of preheating, and has two important advantages. First, it does not lead to a tree level decay of the mother field into the daughter species, so all the transfer of energy from ϕ into X will be due only to the non-perturbative effects characteristic of parametric resonance.

And second, this choice is particularly convenient when the theory is simulated in the lattice, since any other form of interaction would require the introduction of a new mass scale.

We will study the particular cases of quartic potential ($n = 4$) and quadratic potential ($n = 2$) in Sections 2.3 and 2.4 respectively. For each case, we will first study their properties in the initial linear regime, and then present results from lattice simulations, which fully capture all the non-linearities of the system. However, we will treat first the case of arbitrary power-law potentials, so that we can explain the general features of parametric resonance and introduce notation.

By substituting Eq. (2.1) into (1.16), we find the following equations of motion (EOM),

$$\ddot{\phi} - \frac{1}{a^2}\nabla^2\phi + 3H\dot{\phi} + g^2 X^2 \phi + \frac{dV_{\text{inf}}(\phi)}{d\phi} \;=\; 0 \,, \tag{2.2}$$

$$\ddot{X} - \frac{1}{a^2}\nabla^2 X + 3H\dot{X} + g^2\phi^2 X \;=\; 0 \,, \tag{2.3}$$

where $\dot{} = d/dt$ with t cosmic time, and $H \equiv \dot{a}/a$ is the Hubble rate. Let us assume for the moment that ϕ corresponds to an inflaton, and that Eqs. (2.2) and (2.3) describe parametric resonance during preheating after inflation. Inflation homogeneizes the Universe, as well as dilutes the number density of other matter that could have previously existed. Hence, we can safely consider ϕ as homogeneous initially, and we can forget about the gradient term $a^{-2}\nabla^2\phi$ in the EOM. Backreaction effects are also initially negligible, so we can ignore the interaction term $g^2 X^2 \phi$. The solution for ϕ under the previous circumstances admits an oscillatory solution as [52]

$$\phi(t) \approx \Phi(t)F(t) \,, \quad \Phi(t) \equiv \phi_{\text{i}}\left(\frac{t}{t_{\text{i}}}\right)^{-2/n} \,, \tag{2.4}$$

with $\Phi(t)$ a decreasing amplitude from some initial time t_{i}, and $F(t)$ an oscillatory function. The time t_i corresponds to the onset of the oscillatory regime, defined as the time when the effective mass of the inflaton becomes larger than the Hubble rate. From Eq. (2.3), it is characterized by the relation

$$H(t_i) = \frac{1}{\phi(t_i)}\frac{dV_{\text{inf}}}{d\phi}(t_i) \,. \tag{2.5}$$

The details of $\Phi(t)$ and $F(t)$ depend, of course, on the specific choice of potential. In fact, $F(t)$ is not periodic (except for $n = 2$), but the frequency of oscillations changes only relatively slowly in time as

$$\Omega_{\text{osc}} \equiv \sqrt{\frac{d^2 V_{\text{inf}}}{d\phi^2}} \equiv \omega_*\left(\frac{t}{t_{\text{i}}}\right)^{1-2/n} \,, \quad \omega_* \equiv \sqrt{\lambda}M^{2-n/2}\phi_{\text{i}}^{(n/2-1)} \,. \tag{2.6}$$

We can therefore use the initial field amplitude ϕ_i and angular frequency ω_*, to define natural field and space-time variables as

$$\vec{x} \to \vec{y} \equiv \omega_* \vec{x}, \qquad t \to z \equiv \omega_* \tau, \qquad \tau \equiv \int \frac{dt}{a(t)}, \tag{2.7}$$

$$\phi \to \varphi \equiv a(t) \frac{\phi}{\phi_\mathrm{i}}, \qquad X \to X_c \equiv a(t) X,$$

which, with the exception of X_c, are all dimensionless. The EOM of the X_c field can be written, from Eq. (2.3), as

$$\frac{d^2 X_c}{dz^2} + \left(q\varphi^2 - \nabla_y^2 \right) X_c = \frac{1}{a} \frac{d^2 a}{dz^2} X_c, \tag{2.8}$$

where q is the so-called *resonance parameter*, defined as

$$q \equiv \frac{g^2 \phi_\mathrm{i}^2}{\omega_*^2}. \tag{2.9}$$

Note that for certain potentials, the definition for the resonance parameter conventionally includes a numerical factor of $\sim \mathcal{O}(1)$ multiplying the dimensionless ratio in Eq. (2.9). This is the case, for example, of the quadratic potential $V_\mathrm{inf}(\phi) = m^2 \phi^2 / 2$, which we consider in detail in Section 2.4. In this case, the resonance parameter is usually defined as $q \equiv g^2 \phi_\mathrm{i}^2 / 4m^2$, introducing the extra factor $1/4$ to match the definition in the *Mathieu* equation, see Eq. (2.44). For the quartic potential $V(\phi) = \lambda \phi^4 / 4$, studied in Section 2.3, Eq. (2.9) gives $q = g^2 / \lambda$, matching exactly the resonance parameter definition in the *Lamé* equation, see Eq. (2.17). Of course, this is purely conventional, and what really matters is just the dimensionless ratio $\propto g^2 (\phi_\mathrm{i} / \omega_*)^2$ captured in Eq. (2.9).

In most of the relevant situations in the early Universe where parametric resonance takes place, the field X_c is considered to be a quantum field, initially in vacuum. The scalar field X_c can be promoted into a quantum operator by means of the standard quantization procedure

$$X_c(\mathbf{x}, t) \equiv a(t) X(\mathbf{x}, t) = \int \frac{d\mathbf{k}}{(2\pi)^3} e^{-i\mathbf{k}\cdot\mathbf{x}} \left[\hat{a}_\mathbf{k} X_\mathbf{k}^{(c)}(t) + \hat{a}_{-\mathbf{k}}^\dagger X_\mathbf{k}^{(c)*}(t) \right], \tag{2.10}$$

where the creation/annihilation operator satisfies the canonical commutation relations

$$[\hat{a}_\mathbf{k}, \hat{a}_{\mathbf{k}'}^\dagger] = (2\pi)^3 \delta^{(3)}(\mathbf{k} - \mathbf{k}'), \tag{2.11}$$

with other commutators vanishing. The (initial) vacuum state is defined as usual as $\hat{a}_\mathbf{k}|0\rangle = 0$. From Eq. (2.8) we obtain the EOM for the latter as

$$\frac{d^2}{dz^2} X_\mathbf{k}^{(c)} + \left(\kappa^2 + q\varphi^2 \right) X_\mathbf{k}^{(c)} \simeq 0, \qquad \kappa \equiv \frac{k}{\omega_*}, \tag{2.12}$$

where we have discarded a term $\propto \frac{1}{a}\frac{d^2a}{dz^2}$ in this equation, as it is negligible at sub-horizon scales $\kappa^2 \gg \frac{1}{a}\left(\frac{da}{dz}\right)^2 \sim \frac{1}{a}\frac{d^2a}{dz^2}$. Given the oscillatory nature of φ, Eq. (2.12) can exhibit unstable solutions of the type $X_{\mathbf{k}}^{(c)} \sim e^{\mu_q(\kappa)z}$, with $\mu_q(\kappa)$ some complex exponent. For certain values of $\{q, \kappa\}$, $\mathfrak{Re}[\mu_\kappa] > 0$, causing an exponential growth of the given field mode amplitude. It is precisely this unstable behavior, occurring only within finite-momenta *resonance bands* with $\mathfrak{Re}[\mu_\kappa] > 0$, that we call parametric resonance.

In this chapter we consider two circumstances in which parametric resonance can be realized: *i)* when the mother field dominates the energy budget of the Universe, and *ii)* when the mother field is only a sub-dominant energy component of the Universe.

i) Inflaton Preheating. In this case we identify the mother field with the field responsible for inflation, the inflaton. In particular, we will consider chaotic inflation models with quartic and quadratic potentials. Short after inflation ends, the Hubble rate just becomes smaller than the inflaton mass. As the inflaton has a very large vacuum expectation value (VEV), the inflaton amplitude starts then oscillating around the minimum of its potential. This induces a strong creation of all particles coupled to it, if the coupling strength is sufficiently large. The creation of these particles represents possibly the most important particle creation stage in the history of the Universe: as the inflaton and its decay products are the dominant energy component of the Universe, this stage represent the creation of (most of) the matter in the universe. This adds an extra difficulty, as the time-evolution of the scale factor must be obtained by solving self-consistently the field EOM together with the Friedmann equations.

ii) Inflationary Spectator Fields. In this second type of scenarios, we consider the mother field to be just a spectator field during inflation, hence representing a very subdominant component of the energy budget. However, this does not prevent the amplitude of these fields to be rather large at the end of inflation (though not as large, in principle, as in single field chaotic inflation scenarios). When inflation ends and the Hubble rate becomes smaller than the effective mass of the spectator field, the amplitude of the field starts oscillating around the minimum of its potential. The expansion rate of the universe after inflation is determined by the inflationary sector, which we will not model explicitly. The most obvious case of a spectator-field is a curvaton, which is normally described with a quadratic potential[1] of the type $V(\phi) = \frac{1}{2}m^2\phi^2$ in the context of a RD background [37, 38, 39]. We will restrict our numerical analysis to this case (Section 2.5), taking m as a free parameter varied over a certain range.

Before moving on, let us remember that another relevant case of a spectator-field (with quartic $\propto \phi^4$ potential) is the Standard Model (SM) Higgs in the weak coupling limit [54, 55, 56],

---

[1]Other polynomial potentials have been considered, but the realization of the curvaton mechanism seems much more contrived in those cases [53].

which also undergoes a regime of parametric resonance after inflation. We will extensively study the properties of the Higgs decay in Part II of this thesis.

2.3. Preheating with quartic potential

2.3.1. Analysis in the linear regime

Let us consider the case of a massless self-interacting inflaton with potential

$$V_{\text{inf}}(\phi) = \frac{1}{4}\lambda\phi^4 \, , \tag{2.13}$$

coupled to another scalar field X through the interaction term $g^2\phi^2 X^2$. In the case of chaotic inflation, we have $\lambda \approx 10^{-13}$, while the strength of the coupling g^2 is in principle arbitrary. However, in order not to spoil inflation, radiative corrections in the effective inflaton potential must be under control. This sets the constraint $g \lesssim 10^{-3}$ [17].

When $\phi \gg m_p$, the inflationary potential is in a slow-roll regime: the inflaton slowly rolls down its potential, and its potential energy drives the inflationary expansion. However, when $\phi \sim m_p$, the inflaton starts oscillating around the minimum of its potential, and preheating starts. In the previous section, we defined the time t_i as the onset of the oscillatory regime, when the condition (2.5) is obeyed. In our case, this translates to the condition $H(t_{\text{i}}) = \sqrt{\lambda}\phi(t_{\text{i}})$. Imposing the slow-roll condition to the field ϕ at very early times, and solving numerically Eqs. (1.25) and (1.26) in a self-consistent way, we find that at time $t = t_i$, the amplitude and time-derivative of the inflaton are

$$\phi(t_{\text{i}}) \equiv \phi_{\text{i}} \simeq 3.05 m_p \, , \quad \dot{\phi}(t_{\text{i}}) \simeq -3.54\sqrt{\lambda}m_p^2 \, . \tag{2.14}$$

It is convenient to write the system in terms of dimensionless variables, in a similar fashion as in Eq. (2.7). From Eq. (2.6), the natural oscillation frequency is $\omega_* \equiv \sqrt{\lambda}\phi_i$. Hence, let us define the following new set of natural field and spacetime variables,

$$\varphi \equiv \frac{a}{\phi_{\text{i}}}\phi \, , \quad \chi \equiv \frac{a}{\phi_{\text{i}}}X \, , \quad z \equiv \sqrt{\lambda}\phi_{\text{i}}\int_{t_i}^{t}\frac{dt'}{a(t')} \, , \quad \vec{y} \equiv \sqrt{\lambda}\phi_{\text{i}}\vec{x} \, . \tag{2.15}$$

In these variables, the equation for the inflaton and daughter fields, Eqs. (2.2) and (2.3), are written as

$$\varphi'' - \frac{a''}{a}\varphi - \nabla_y^2\varphi + \left(\varphi^2 + q\chi^2\right)\varphi = 0 \, , \quad \chi'' - \frac{a''}{a}\chi - \nabla_y^2\chi + q\varphi^2\chi = 0 \, , \tag{2.16}$$

where $' \equiv d/dz$, ∇_y is the laplacian in terms of spacetime dimensionless variables, and q is the resonance parameter, defined as

$$q \equiv \frac{g^2}{\lambda} \ . \tag{2.17}$$

As explained in the previous section, we can take the inflaton as homogeneous at initial times, as well as ignore the interaction term in the mother field equation. The EOM of the homogeneous part of φ reduces in this case to

$$\varphi'' + \varphi^3 = \frac{a''}{a}\varphi \ . \tag{2.18}$$

In the quartic model, the energy density of the inflaton scales (after averaging over oscillations) as in a RD background with $\rho_\phi \propto 1/a^4$ [52], so the scale factor behaves as $a \propto \sqrt{t} \propto z$. In this case, the term on the *rhs* of Eq. (2.18) simply vanishes, $a''/a = 0$. The solution of Eq. (2.18), with initial conditions $\varphi(0) = 1$ and $\varphi'(0) = 0$, is the Elliptic function

$$\varphi(z) = \text{cn}(z; 1/2) \ . \tag{2.19}$$

On the other hand, the equation for the Fourier modes of the field χ becomes

$$\chi_k'' + \left(\kappa^2 + q\varphi(z)^2\right)\chi_k = 0 \ , \quad \kappa \equiv \frac{k}{\sqrt{\lambda}\varphi_i} \ , \tag{2.20}$$

where we have conveniently defined a dimensionless momentum κ. Given the behavior of $\varphi(z)$ in Eq. (2.19), Eq. (2.20) corresponds to the Lamé equation. This equation has a well-known structure of resonance bands, whose properties have been studied in detail, for example, in Ref. [26]. The solution of Eq. (2.20) admits solutions of the type $\chi_k \propto e^{\mu_k z}$, with μ_k a parameter known as the Floquet index. In some regions of the (κ,q) parameter space, the Floquet index is positive $\mathfrak{Re}[\mu_k] > 0$, and the amplitude of the daughter field modes grows exponentially. The instability $\chi_k \propto e^{\mu_k z}$ of the resonant modes is naturally interpreted as a strong particle creation of the χ field, because the occupation number grows as $n_k \sim |\chi_k|^2 \propto e^{2\mu_k z}$.

We show in the left panel of Fig. 2.1 the dependence of μ_k on κ and q, which is usually called the stability/instability chart of the Lamé equation. In the white regions of the parameter space, $\mathfrak{Re}[\mu_k] = 0$, so there is no field excitation. On the contrary, in the coloured regions, $\mathfrak{Re}[\mu_k] > 0$. The darker the colour, the greater the Floquet index, with a maximum value given by $\mu_k \leq \mu_{k,\text{max}} \equiv 0.2377...$ [26].

From the violation of the adiabaticity condition for $q \gg 1$, i.e. $\omega_k' > \omega_k^2$, we can determine an estimation of the maximum (comoving) momentum possibly excited in broad resonance. For resonance parameters $q \in \frac{1}{2}[n(n+1), (n+1)(n+2)]$ with $n = 1, 3, 5, ...$ (i.e. $q \in [1, 3]$, [6,
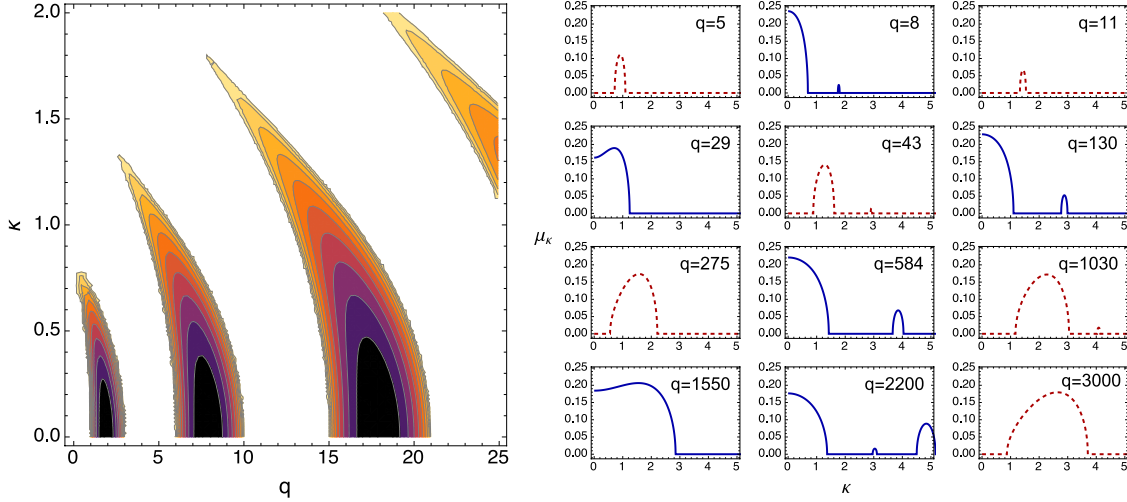
Figure 2.1.: Left: We show the stability/instability chart of the Lamé equation (2.20). Coloured bands indicate the regions of the (q,κ) parameter space in which the real part of the Floquet index is a positive number $\mathfrak{Re}[\mu_\kappa] > 0$ and hence the solution of the Lamé equation is exponential. The darker the colour, the greater the index, up to a maximum of $\mu_\kappa \approx 0.237$ for black areas. White areas are the regions in which $\mathfrak{Re}[\mu_\kappa] = 0$. Right: Some examples of the Floquet index derived numerically from the Lamé equation for resonance parameters ranging between $q = 5$ and $q = 3000$. In each panel, we plot the corresponding Floquet index μ_κ as a function of the momentum κ. We have divided the different q's in two groups: those inside one of the resonance bands $q \in [1,3], [6,10], [15,21], ...$ (blue solid lines), which excite modes down to $\kappa = 0$, and those which are in between resonance bands (red dashed lines), which only excite modes down to some minimum momentum $\kappa_{\min} > 0$.

10], ...), the excited modes form an infrared band that go from $k = 0$ up to

$$k \lesssim k_L \sim \left(\frac{q}{2\pi^2}\right)^{1/4} \sqrt{\lambda}\phi_{\mathrm{i}} \, . \tag{2.21}$$

On the other hand, for $q \in (3,6), (10,15), ...$, there is still a resonance of the type $\chi_k \propto e^{\mu_k z}$, but within a shorter range of momenta $k_{\min} \leq k \lesssim k_L$ (with $k_{\min} > 0$), and also with a smaller Floquet index μ_k. Hence, for this second set of resonance parameters, the resonance is weaker. These properites are clearly observed in the stability/instability chart plotted in the left panel of Fig. 2.1. We also show the resonance bands for different values of q in the right panel of Fig. 2.1.

Remember that in this explanation, we have ignored the non-linear interaction terms $\propto \chi^2\varphi$ and $\propto \varphi^2\chi$ in the field EOM (2.16). This is only valid at initial times, when the energy from the daughter field, despite growing exponentially, is still subdominant with respect the inflaton. When this is no longer true, the daughter field backreacts onto the mother field through the non-linear terms, inducing the decay of the inflaton condensate amplitude. This regime can be captured with classical lattice simulations, like the ones we will present in Section 2.3.2.

Before moving to the analysis of our lattice results, we would like to present an analytical estimate of the time scale of the mother field decay. Using a linear approximation, we can estimate the moment z_{eff} at which an efficient transfer of energy has taken place from ϕ into the χ field. This time is characterized by the condition $\rho_\chi(z_{\text{eff}}) = \rho_\phi(z_{\text{eff}})$, where ρ_ϕ and ρ_χ are the energy densities of the mother and daughter fields respectively. This will just be a crude estimate of the time scale of the mother field decay, since by then backreaction and rescattering effects will have become important, invalidating the linear approach. However, the nonlinear effects due to backreaction of the decay products simply tend to shut off the resonance, so the calculation in the linear regime should provide, in principle, a reasonable estimate.

For simplicity, let us consider the resonance parameter to be within one of the resonant bands, $q \in [1,3], [6,10], [15,21], \ldots$. The growth of the fluctuations in the initial stages of resonance is described by the linear Eq. (2.20). The energy density of the created particles due to the resonance, is given by

$$\rho_\chi = \frac{1}{2\pi^2 a^3} \int dk k^2 n_k \Omega_k \,, \quad \Omega_k^2 \equiv \frac{k^2}{a^2} + g^2 \overline{\phi^2} \,, \tag{2.22}$$

where we have introduced an oscillation-averaged effective mass for the χ field,

$$m_\chi^2 = g^2 \overline{\phi^2} = g^2 \frac{\phi_i^2}{a^2} \overline{\varphi^2} \,, \qquad \overline{\varphi^2} \equiv \frac{1}{Z_T} \int_z^{z+Z_T} dz' \varphi^2(z') \simeq 0.46 \,, \tag{2.23}$$

with $Z_T \simeq 7.416$ the oscillation period of the inflaton solution, Eq. (2.19). From Eqs. (2.21) and (2.23), we conclude that

$$\frac{m_\chi^2}{(k_L/a)^2} \sim \mathcal{O}(1) q^{1/2} > 1 \,. \tag{2.24}$$

In other words, in broad resonance $q \gg 1$, the decay products are always non-relativistic. Correspondingly we can approximate the effective mode frequency as $\Omega_k \simeq m_\chi \sim g\frac{\phi_i}{a}\varphi_{\text{rms}}$, where $\varphi_{\text{rms}} \equiv \sqrt{\overline{\varphi^2}} \simeq \frac{2}{3}$. If q is within a resonant band, then all modes with momenta $0 \le k \lesssim k_L$ are excited with some Floquet index varying within $[0, \mu_{k,\max}(q)]$. This corresponds to the cases with blue solid lines in the right panel of Fig. 2.1. We can therefore model the occupation number of the excited modes simply as a step function $n_k = e^{2\overline{\mu}z}\Theta(1 - k/k_L)$, with $\overline{\mu} \simeq 0.2$ a mean Floquet index. It follows that

$$\rho_\chi(z) \simeq \frac{\varphi_{\text{rms}}}{6\pi^2 a^4} e^{2\overline{\mu}z} g\phi_i k_L^3 \simeq \frac{q^{5/4}}{2^{3/4} \cdot 3^2 \cdot \pi^{7/2}} \frac{e^{2\overline{\mu}z}}{a^4} H_i^4 \,, \tag{2.25}$$

where we have used $H_i \equiv H(t_i) = \sqrt{\lambda}\phi_i$ in the second equality. This is how the energy density of the daughter fields will grow, at least as long as their backreaction into the mother field remains negligible. On the other hand, the energy of the oscillating field, since the onset of the

oscillations, decays as

$$\rho_\varphi(z) = \frac{1}{2a^2}\dot{\phi}^2 + \frac{\lambda}{4}\phi^4 = \frac{\lambda\phi_i^4}{4a^4}\left[\overline{2\left(\varphi' - \varphi\frac{a'}{a}\right)^2 + \overline{\varphi^4}}\right] \simeq \frac{3\lambda\phi_i^4}{4a^4} = \frac{H_i^4}{4\lambda a^4}, \quad (2.26)$$

where in the second equality we have transformed to the natural variables of Eq. (2.15), and in the third equality we have done an oscillation average. We can now find z_{eff} by simply equating Eqs. (2.25) and (2.26),

$$q^{1/4}e^{2\overline{\mu}z_{\text{eff}}} = \frac{2^{-1/4} \cdot 3^2 \cdot \pi^{7/2}}{g^2}. \quad (2.27)$$

By isolating z_{eff}, we then find

$$z_{\text{eff}} \simeq +\frac{1}{2\overline{\mu}}\left[6 - \ln\lambda - \frac{5}{4}\ln q\right]. \quad (2.28)$$

For instance, for chaotic inflation with quartic potential, $\lambda \simeq 10^{-13}$, and hence $\ln\lambda \simeq -30$. Moreover, looking at Fig. 2.1 we see that the mean Floquet index of the resonant modes when q is within a resonant band is approximately $\overline{\mu} \simeq 0.2$. Hence, we find in this case

$$z_{\text{eff}} \sim 2.5\left(36 - 2.9\log_{10}q\right) \quad \Rightarrow \quad 83 \gtrsim z_{\text{eff}} \gtrsim 18, \text{ for } q \in [10, 10^{10}]. \quad (2.29)$$

It is clear that the larger the q, the shorter it takes for the mother field to transfer energy efficiently into the daughter fields. This is expected, as the stronger the interaction is, the faster the decay should be. However, the dependence is only logarithmic, so the time scale does not change appreciably, and is always some value of the order $z_{\text{eff}} \sim \mathcal{O}(10)$ according to the above calculation.

2.3.2. Lattice simulations of preheating with quartic potential

In this section, we present results from lattice simulations of preheating with quartic potential. Before, in order to gain some insight on the field dynamics, we only used the homogeneous part of the equation for φ, as well as the Fourier transformed equation of χ. Now, we will be rather solving the (lattice version) of the full Eqs. (2.16) in real space. Simulations have been carried out with a modified version of *Latticeeasy*, which is a software for lattice simulations of preheating with scalar fields [47].

We have simulated resonance parameters in the range $0.4 \lesssim q \lesssim 10^4$. We have taken $\lambda = 9 \cdot 10^{-14}$ for the inflaton self-coupling, so this corresponds to couplings in the range $6 \cdot 10^{-7} \lesssim g \lesssim 3 \cdot 10^{-5}$. We are not capable of simulating appropriately resonance parameters outside of this range: the lower limit is due to the natural limitations of the lattice to simulate
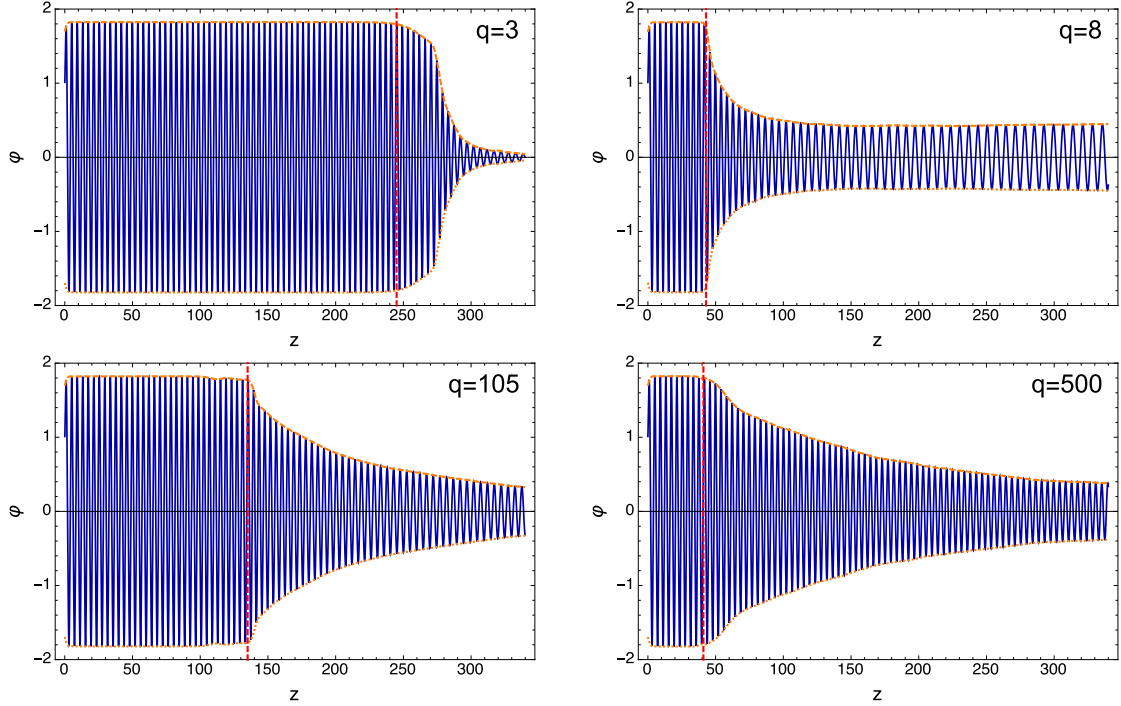
Figure 2.2.: We show the initial oscillations of the volume-averaged conformal amplitude of the inflaton field φ. We show the cases $q = 3$, $q = 8$, $q = 105$, and $q = 500$ for the preheating scenario with quartic potential. We use notation of Eq. (2.15). The dashed vertical red line indicates the time z_{br}, when backreaction of the daughter fields become relevant, triggering the decay of the inflaton amplitude and energy density (see also Fig. 2.4).

fields with narrow resonance bands, while the upper limit emerges due to lack of UV coverage. Fortunately, as we shall see, the results for the q's simulated are well described by simple power-law fits, allowing in principle to extrapolate the outcome to larger q.

Let us move now into the results from the lattice simulations. In Fig. 2.2 we plot the conformal amplitude of the inflaton field for the resonance parameters $q = 3, 8, 105$ and 500. It is clearly appreciated that during a certain number of oscillations, the conformal amplitude of the inflaton φ remains just constant, like if it was not coupled to the daughter field(s). However, there is a time (which differs for the different q's) when the amplitude of the conformal inflaton starts decreasing significantly. This is the initial moment when the inflaton starts decaying due to the backreaction from the daughter fields. We shall refer to that time as z_{br} (the *br* subindex meaning *backreaction*). During the time $0 \leq z \lesssim z_{br}$, the daugther fields have been experiencing parametric resonance, so their energy density has been growing exponentially from initially small quantum fluctuations. As the energy flows from the mother field into the daughter fields, at $z \simeq z_{br}$ the amount of energy transferred onto the χ bosons is not anymore a negligible fraction of energy stored in the mother field. Therefore, from then onwards, the (conformal) inflaton amplitude starts to decrease noticeable, see Fig. 2.2. The time z_{br} corresponds, in other
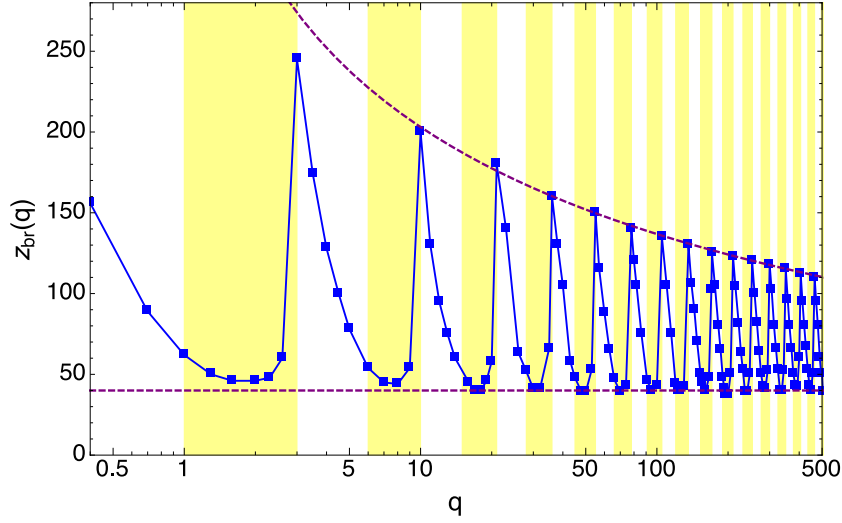
Figure 2.3.: We depict z_{br} as a function of q for the range $0.4 < q < 500$. Each point corresponds to the value obtained directly from a lattice simulation, and we have joined the different points with straight lines. Yellow vertical bands indicate the position of the resonance bands of the Lamé equation $q \in (1,3), (6,10) \dots$. The dashed, purple, lower line indicate the estimate $z_{\mathrm{br}}(q) \approx 40$ [Eq. (2.30)] for q values within resonance bands, while the upper one indicates the fit Eq. (2.31) for the relative maxima.

words, to the onset of the inflaton decay, when the backreaction effects from excited daughter fields become non-negligible. In practice, we have determined z_{br} as the moment when the (conformal) energy of the mother field drops $\sim 5\%$ with respect its initial amplitude.

In Fig. 2.3 we have plotted the different z_{br}'s obtained from our simulations, for several resonance parameters in the range $0.4 < q < 500$. We observe that $z_{\mathrm{br}}(q)$ follows a clear oscillatory pattern, in clear correspondence with the particular structure of resonance bands shown in Fig. 2.1. In general, the wider the resonance band in the Lamé equation for a given q, the shorter z_{br} is. For those values of q emplaced within resonance bands, we find in fact an almost constant value

$$z_{\mathrm{br}}(q) \sim 40 \,, \quad q \in (1,3), (6,10) \dots \tag{2.30}$$

On the other hand, the behavior of z_{br} for q values outside the resonance bands, i.e. for $q \in [3,6], [10,15], \dots$, is quite different. For q values that are in the left extreme of these intervals, i.e. $q \simeq 3, 10, \dots$, z_{br} takes its maximum value, as this corresponds to the right end of a resonance band at $\kappa = 0$, see Fig. 2.1. We provide the following phenomenological fit to these relative maxima (excluding the particular case $q = 3$), which we also plot in the Figure,

$$z_{\mathrm{br}}(q) \approx 552 e^{-|\log_{10} q|^{0.48}} \,, \quad q = 10, 21, 36 \dots \tag{2.31}$$

As q increases inside one of the intervals outside the resonance bands, z_{br} decreases until hitting $z_{br}(q) \sim 40$ at the center (more or less) of the nearest resonance band, see Fig. 2.3. In conclusion, we observe a direct translation of the resonance structure of Fig. 2.1 into the lattice simulations. This happens because for $z \lesssim z_{br}$, the backreaction effects of χ onto the φ are negligible, and hence the Lamé equation (2.20) is really at work.

Let us compare now this result with the analytical calculation from Section 2.3.1. For the range of q values shown in Fig. 2.3, we obtain $z_{eff} \sim 78$ from Eq. (2.28), so the analytical prediction only overestimates in a factor ~ 2 the actual number $z_{br} \sim 40$, found in the simulations at the onset of backreaction. Failing in a factor ~ 2 is not surprising, as the estimation of z_{eff} in Eq. (2.28) involved in fact many approximations. However, the relevant point is that z_{eff} should not be identified with a decay time, but rather, with the moment when the linear approximation breaks down. The time scale for determining the end of the transfer of energy from the mother field into the decay products, which we shall identified as the truly 'decay time' scale of the inflaton, will be referred to as z_{dec}. As we shall see, it corresponds in fact to a much longer time scale, $z_{dec} \gg z_{eff}, z_{br}$, which cannot be estimated analytically, as the dynamics at $z \gtrsim z_{br}$ become non-linear.

To follow the post-inflationary dynamics in the non-linear regime, it is useful to see how the different contributions to the total energy of the system evolve as a function of time. The total energy can be written as a sum of its different contributions as

$$\rho_t(z) \equiv \frac{\lambda \phi_i^4}{a^4} E_t \equiv \frac{\lambda \phi_i^4}{a^4} \left(E_{K,\varphi} + E_{K,\chi} + E_{G,\varphi} + E_{G,\chi} + E_{int} + E_V \right), \quad (2.32)$$

with

$$E_{K,f} = \frac{1}{2} \left(f' - f \frac{a'}{a} \right)^2, \quad E_{G,f} = \frac{1}{2} |\nabla_y f|^2, \quad E_{int} = \frac{1}{2} q \varphi^2 \chi^2, \quad E_V = \frac{1}{4} \varphi^4, \quad (2.33)$$

where $E_{K,f}$ and $E_{G,f}$ are the kinetic and gradient energy of the fields ϕ, χ, and E_{int} and E_V are the interaction and potential energies, all written in terms of the natural variables of Eq. (2.15) (i.e. in terms of the field variables $f = \varphi, \chi$ and derivatives of these with respect z^μ).

In the left panel of Fig. 2.4 we show the evolution of the volume-averaged amplitude of the different energy components of the system. We can clearly observe how, at first, the inflaton energy dominates the energy budget of the system, alternating between kinetic and potential energies as the oscillations go on. Short after the onset of the simulation, the rest of energies start growing (including the inflaton gradient energy, which indicates the formation of inhomogeneities), becoming very soon an important part of the total energy. At time z_{br}, these energies have grown enough and start backreacting onto the inflaton condensate, inducing its decay (i.e. the decrease of the inflaton kinetic and potential energies). This can also be
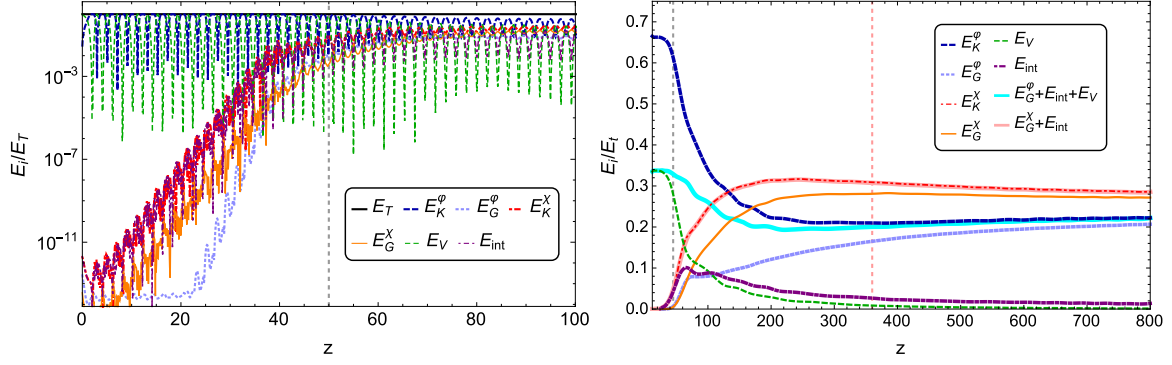
Figure 2.4.: Evolution of the different energy components of the system as a function of time, see Eq. (2.32), for the inflationary scenario $V(\phi) \propto \phi^4$, where $q = 500$. Left: We plot E_i/E_t for the initial stages of the inflaton decay, and we have indicated z_{br} with a vertical dashed red line. Right: We plot the same case for later times. To see better how the equipartition regime holds, we have removed the oscillations by taking the oscillation average of the different functions. We have added two new lines that indicate the sums $E_{G,\varphi} + E_{int} + E_V$ and $E_{G,\chi} + E_{int}$, see Eq. (2.35).

appreciated in Fig. 2.2, where from $z \gtrsim z_{br}$ the (conformal) inflaton amplitude starts decreasing significantly.

Let us note that the energy fractions at $z \simeq z_{br}$ are quite independent of the resonance parameter. From the numerical outcome we find

Energy Fractions at z_{br}:

$$
\begin{aligned}
\frac{E_{K,\varphi}}{E_t} &\simeq (62.5 \pm 2.4)\%, & \frac{E_V}{E_t} &\simeq (29.0 \pm 2.7)\%, \\
\frac{E_{K,\chi}}{E_t} &\simeq (4.1 \pm 2.5)\%, & \frac{E_{int}}{E_t} &\simeq (3.6 \pm 2.2)\%,
\end{aligned}
\tag{2.34}
$$

with the errors $\pm \Delta E_x/E_t$, simply reflecting a small scattering of energies with q. We see from this that at $z = z_{br}$, most of the energy remains yet in the inflaton. However, we also learn that backreaction really becomes noticeable when $\sim 1\%$ of the total energy has been transferred into the daughter field(s). The other energy components $E_{G,\varphi}, E_{G,\chi}$ remain always at sub-percentage levels during $0 < z \lesssim z_{br}$.

At times $z \gtrsim z_{br}$, the energy components evolve substantially from the given values in Eq. (2.34). In particular, the energies evolve towards an 'equiparted' distribution among components, until the system eventually reaches a stationary regime, where the energy components do not change appreciably. This is observed in the right panel of Fig. 2.4, where we have removed the oscillations by taking the oscillation average of the different energies. We observe different equipartition identities for the φ and χ fields respectively,

$$
E_{K,\varphi} \simeq E_{G,\varphi} + E_{int} + E_V, \qquad E_{K,\chi} \simeq E_{G,\chi} + E_{int}.
\tag{2.35}
$$
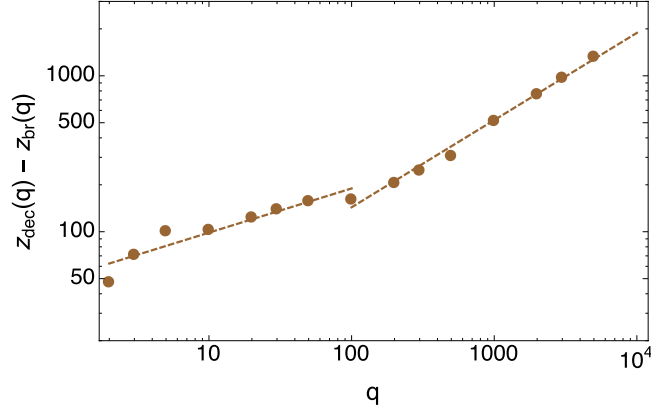
Figure 2.5.: Points show the different z_{dec} obtained for different lattice simulations with different values of q, for preheating with quartic potential. The dashed line indicates the best fit (2.36).

As it can be appreciated in Fig. 2.4, the second identity holds almost exactly for all times, while the first one only holds for late times (though it is not a bad approximation at earlier times).

From the analysis of the energies we see that a new time scale, much longer than z_{br}, can be naturally identified with the decay time of the mother field. This scale can be defined by how long it takes the system to relax from $z \gtrsim z_{\mathrm{br}}$ into the stationary regime. We denote this time scale as z_{dec}. It is this time, and not z_{br}, that signals the true end of the inflaton decay, because it is at $z \gtrsim z_{\mathrm{dec}}$ that there is no (appreciable) transfer of energy anymore from the inflaton into the daughter field(s). Although the exact definition of z_{dec} is more arbitrary than z_{br}, we find appropriate to provide an operative definition based on the level of accuracy of equipartition. In particular, at the moment when the inflaton equipartition energy holds at a better level than 2%, i.e. $(E_{K,\varphi} - E_{G,\varphi} - E_{\mathrm{int}} - E_V)/(E_{K,\varphi} + E_{G,\varphi} + E_{\mathrm{int}} + E_V) \gtrsim 0.02$, the inflaton kinetic and gradient energies are stabilized and do not evolve appreciably further, see Fig. 2.4.

We show in Fig. 2.5 the value of $z_{\mathrm{dec}} - z_{\mathrm{br}}$ as a function of q, as extracted from our lattice simulations with different q's. We see that z_{dec} grows with the resonance parameter q, following a simple power-law fit. We obtain

$$
z_{\mathrm{dec}}(q) - z_{\mathrm{br}}(q) = \begin{cases} 51q^{0.28} & \text{if } q < 100 \,, \\ 11q^{0.56} & \text{if } q \geq 100 \,, \end{cases} \tag{2.36}
$$

which we also show in Fig. 2.5. Note that for $q \lesssim 100$, the scales z_{br} and z_{dec} are not particularly separated, with $|z_{\mathrm{dec}} - z_{\mathrm{br}}| \lesssim z_{\mathrm{br}}$. This explains why these point must be fitted with a different power law. Note that the inflaton decay takes longer the greater the resonance parameter (i.e. the larger the mother-daughter coupling), which is in principle counter-intuitive. This is a direct consequence of the non-linearities of the system.

As mentioned, we can only obtain our fits for resonance parameters up to $q \sim 10^4$ due to the limitations of the lattice approach. However there is nothing specially different in the physics of parametric resonance for $q \gg 10^4$. Therefore, there is no impediment, in principle, to extrapolate the scaling law (2.36) to higher q's.

Let us note that the energy fractions at $z \gtrsim z_{\rm dec}$ do not change appreciably any more in our simulations. Some small change should be expected nonetheless, as the system approaches equilibrium. However this is not captured in our simulations. The energy from the end of the inflaton decay onwards are actually rather independent of q, given by the fractions

Energy Fractions at $z \gtrsim z_{\rm dec}$:

$$\frac{E_{K,\chi}}{E_t} \simeq (29.5 \pm 3.3)\%\,, \quad \frac{E_{K,\varphi}}{E_t} \simeq (22.6 \pm 3.4)\%\,, \quad \frac{E_{G,\chi}}{E_t} \simeq (26.2 \pm 3.4)\%\,, \tag{2.37}$$

$$\frac{E_{G,\varphi}}{E_t} \simeq (17.7 \pm 3.0)\%\,, \quad \frac{E_{\rm int}}{E_t} \simeq (3.2 \pm 0.7)\%\,, \quad \frac{E_V}{E_t} \simeq (0.8 \pm 0.2)\%\,, \tag{2.38}$$

again with the errors $\pm \Delta E_j / E_t$ reflecting some (rather random) scattering of the energies with q. We see from this that at $z \gtrsim z_{\rm dec}$, the energy is almost 'democratically' split between the mother and the daughter field(s), though with some more energy stored in the latter, with $E_\chi / E_t \simeq (E_{G,\chi} + E_{K,\chi})/E_t \sim (54.7 \pm 4.7)\%$, $E_\varphi / E_t \equiv (E_{K,\varphi} + E_{G,\varphi} + E_V)/E_t \simeq (41.1 \pm 4.5)\%$, and $E_{\rm int}/E_t \simeq (4.3 \pm 0.5)\%$. At these moments it is also verified the approximate equipartition $E_{K,\varphi}/E_t \simeq (E_{G,\varphi} + E_{\rm int} + E_V)/E_t \sim 21\% - 23\%$ and $E_{K,\chi}/E_t \simeq (E_{G,\chi} + E_{\rm int})/E_t \sim 29\% - 30\%$.

2.4. Preheating with quadratic potential

2.4.1. Analysis in the linear regime

Let us now consider preheating in the case of an inflaton with quadratic potential,

$$V_{\rm inf}(\phi) = \frac{1}{2}m^2\phi^2\,, \tag{2.39}$$

where $m \approx 6 \times 10^{-6} m_p$ is the appropriate mass scale for chaotic inflation, and the inflaton is coupled to another scalar field X with an interaction term $g^2\phi^2 X^2$. For field values $\phi \gg m_p$, the slow-roll conditions (1.39) are fulfilled, and the potential energy sustains inflation. In this regime, the inflaton slowly rolls down its potential, and when $\phi \sim m_p$, the slow-roll conditions break and preheating starts. We defined the time $t_{\rm i}$ of the onset of the inflaton oscillatory regime when the condition (2.5) holds, which in this case is simply $H(t_{\rm i}) = m$. We can obtain the inflaton amplitude at $t = t_{\rm i}$ by imposing the slow-roll conditions at $\phi \gg m_p$, and solving

numerically Eqs. (1.25) and (1.26) self-consistently. We find

$$\phi_i \equiv \phi(t_i) \approx 2.32 m_p \, , \quad \dot{\phi}(t_i) \approx -0.78 m m_p \, . \tag{2.40}$$

It is convenient to define a new set of natural variables, as we did in Eq. (2.7). From Eq. (2.6), we see that the frequency of oscillation is simply $\omega_* = m$. Hence, we define the following dimensionless field and spacetime variables as

$$\varphi = \frac{1}{\phi_i} a^{3/2} \phi \, , \quad \chi = \frac{1}{\phi_i} a^{3/2} X \, , \quad z \equiv mt \, , \quad \vec{z} \equiv m\vec{x} \, , \quad \kappa \equiv \frac{k}{m} \, . \tag{2.41}$$

As before, we indicate differentiation with respect dimensionless time as $' \equiv d/dz$, and define ∇_y as the laplacian with respect dimensionless space variables. Note also that here, we have decided to keep using (dimensionless) cosmic time, instead of changing to (dimensionless) conformal time, as we did in in Eq. (2.7). This is convenient in this case, because this way, the inflaton oscillation period is constant. The fields' EOM in these variables are

$$\varphi'' - \left(\frac{3}{4} \frac{a'^2}{a^2} + \frac{3}{2} \frac{a''}{a} \right) \varphi - \frac{1}{a^2} \nabla_y^2 \varphi + \left(1 + \frac{4}{a^3} q_i \chi^2 \right) \varphi = 0 \, , \tag{2.42}$$

$$\chi'' - \left(\frac{3}{4} \frac{a'^2}{a^2} + \frac{3}{2} \frac{a''}{a} \right) \chi - \frac{1}{a^2} \nabla_y^2 \chi + \frac{4}{a^3} q_i \varphi^2 \chi = 0 \, , \tag{2.43}$$

where the resonance parameter is defined this time as

$$q_i = \frac{g^2 \phi_i^2}{4m^2} \, . \tag{2.44}$$

Note that this definition includes an extra factor $1/4$ with respect the general definition in Eq. (2.9). As discussed there, this is simply conventional, and what matters is the dimensionless ratio $\propto g^2 \phi_i^2 / m^2$.

Let us focus first on the case of a non-expanding universe, so we set $a = 1$ and $a' = a'' = 0$ in the above equations. At initial times, we can safely neglect the interaction and gradient terms, $\propto \chi^2 \varphi$ and $\propto \nabla_y^2 \varphi$, in the inflaton EOM (2.42). In this case it becomes $\varphi'' + \varphi = 0$, whose solution is, for initial conditions $\varphi(0) = 1$ and $\varphi'(0) = 0$, simply $\varphi = \cos(z)$. In this case, the mode equation of the daughter fields χ_k, Eq. (2.43), can be written as

$$\frac{d^2 \chi_k}{dz^2} + (A_k - 2q_i \cos 2z) \chi_k = 0 \, , \quad A_k = \kappa^2 + 2q_i \, . \tag{2.45}$$

This is the *Mathieu* equation, which similarly to the *Lamé* equation, is characterized by a well-known structure of resonance bands [25]. For some regions in the (q_i, κ) plane, there is a solution of the type $\chi_k \sim e^{\mu_\kappa z}$ with $\mathfrak{Re}[\mu_\kappa] > 0$, where μ_k is the so-called Floquet index. Again, the instability of the field modes means a strong growth of the occupation number $n_k \sim |\chi_k|^2 \propto e^{2\mu_k z}$, which can be intrepreted as a strong regime of particle creation. Depending

on the particular value of q_i, we can distinguish two different kinds of resonance. If $q_i < 1$, the width $\Delta\kappa$ of the resonance bands is very narrow, with $\Delta\kappa/\kappa \ll 1$. This regime is referred as *narrow resonance*. On the other hand, for $q_i \gg 1$, the width of the resonance bands is significantly larger, $\Delta\kappa/\kappa \sim \mathcal{O}(1)$, and the resonance is, consequently, much stronger. This regime is referred as *broad resonance*.

Let us now include the expansion of the Universe in our analysis. In the quadratic model, the energy density of the inflaton (again after oscillations-averaging) evolves as in a MD background, with $\rho_\phi \propto 1/a^3$, and the scale factor evolves correspondingly as $a(t) \sim t^{2/3}$ [52]. In this case, the amplitude of the inflaton oscilations decrease with time, and at late times, the inflaton approaches the following asymptotic solution [25],

$$\phi(t) \simeq \Phi(t)\sin(mt)\,, \quad \Phi(t) \equiv \frac{M_p}{\sqrt{3\pi}mt}\,. \tag{2.46}$$

The equation of motion of the daughter field modes can also be written as the Mathieu equation (2.45), but in this case, with the following time-dependent parameters,

$$A_k(z) = \frac{\kappa^2}{a^2} + 2q_{\text{eff}}(z)\,, \quad q_{\text{eff}}(z) \equiv \frac{q_i}{a^3}\,. \tag{2.47}$$

Hence, when the expansion of the universe is introduced, the scale factor affects the EOM of φ in a non-trivial way: even if the system starts in broad resonance with $q_i \gg 1$, as the Universe expands, the system rapidly redshifts towards neighboring bands of lower resonance parameter. This is due to the term $q_i a^{-3}$ in Eq. (2.43), which makes the effective resonance parameter $q_{\text{eff}} \equiv q_i a^{-3}$ decrease as time goes by. Therefore, the system does not remain in a single resonance band, but redshifts due to the expansion of the universe. As a consequence, even if the system starts in a broad resonance regime, it can only be maintained as such for some finite time, until it ends up in a narrow resonance regime.

For a detailed analysis of the behavior of the mode functions obeying the Mathieu equation, both in Minkowski and in an expanding Universe, we recommend to read the seminal work [25]. In that work, it was found that the maximum momentum excited during parametric resonance in broad resonance is approximately

$$k \lesssim k_M \equiv \sqrt{\frac{2}{\pi}}q_i^{1/4}m\,. \tag{2.48}$$

In Section 2.3.1 we presented, for parametric resonance with quartic potential, an estimation for the time scale z_{eff}, which indicates when a significant energy transfer from the mother to the daughter field has occurred. A similar computation was carried out in Ref. [25] for a mother field with a quadratic potential $V(\phi) = \frac{1}{2}m^2\phi^2$. The details are more cumbersome in this case, because contrary to the quartic model previously described, in the quadratic case the
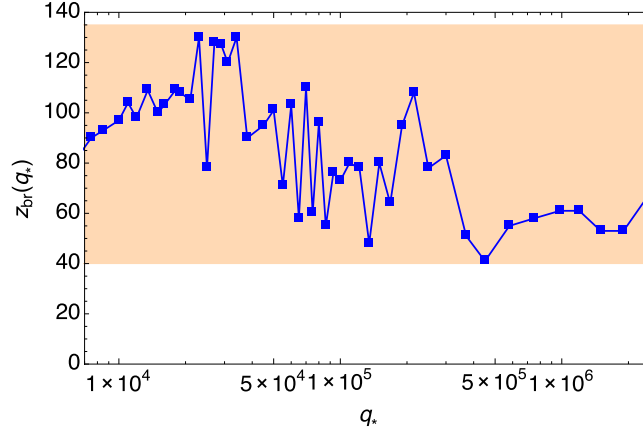
Figure 2.6.: We plot the different times z_{br} obtained from the lattice simulations of the $m^2\phi^2$ inflationary model with different resonance parameters. We have joined the points with a straight line, and the orange band corresponds to the values of Eq. (2.50).

Floquet index is not fixed for a given mode: each mode scans several resonance bands due to the expansion of the Universe, and the evolution of a resonant mode function χ_k is stochastic. Taking $\bar{\mu} \simeq 0.15$ as a reasonable averaged value of the stochastic Floquet index μ_κ, for chaotic inflation with $V(\phi) \propto \phi^2$, Eq. (112) of [25] is equivalent to

$$z_{eff} \simeq 8.3(15.1 - 1.1 \log_{10} q_i) \quad \Rightarrow \quad 89 \gtrsim z_{eff} \gtrsim 34, \text{ for } q_i \in [10^4, 10^{10}], \tag{2.49}$$

with $q_i \equiv g^2 \phi_i^2 / (4m^2)$. As in the quartic case, this time scale is always of the order of $z_{eff} \sim \mathcal{O}(10)$, changing only logarithmically with the resonance parameter.

In our discussion we have ignored the backreaction effects coming from the non-linear interaction terms $\propto \chi^2 \varphi$ and $\propto \varphi^2 \chi$ in the field EOM (2.41). To fully capture the dynamics of the system, we will present results from a set of lattice simulations of the preheating process in the next subsection.

2.4.2. Lattice simulations of preheating with quadratic potential

We now present the results from our lattice simulations of preheating with quadratic potential. We have simulated cases in the interval $q_i \in [7.5 \times 10^3, 2.5 \times 10^6]$, which are the ones that we can capture well in the lattice.

In Fig. 2.6 we show the backreaction time z_{br} as a function of q_i, obtained from our lattice simulations. We define z_{br} again as the moment when the inflaton conformal amplitude φ starts decreasing abruptly. For all simulations, we obtain

$$z_{br} \in [40, 135] . \tag{2.50}$$

We do not observe a clear pattern for z_{br} as a function of q_i, as we saw in the $\lambda \varphi^4$ case. This is, however, expected. The reason is that, in the present case, we cannot differentiate whether a mode is placed in the middle of a resonance band or not. On the contrary, the resonance in this system is stochastic, because each mode experiences a rapid scanning of bands due to the expansion of the Universe [25]. The 'wiggly' pattern of z_{br} as a function of q_i is, therefore, just a reflection of the stochastic nature of the resonance in this system. To our knowledge, the pattern depicted in Fig. 2.6 has never been shown before. Due to the stochastic nature of the resonance, one cannot predict exactly z_{br} for a specific initial resonance parameter q_i.

Looking at Fig. 2.6, we appreciate that the onset of the backreaction, and hence the start of the inflaton decay, happens always at a time $z_{br} \sim$ few $\times \mathcal{O}(10)$. On the other hand, the analytical estimate of Eq. (2.49) gives, for $q_i \sim 10^4 - 10^6$, the range of values $68 \lesssim z_{eff} \lesssim 86$. As in the quartic case, we see that z_{eff} is a good estimation of the back-reaction time z_{br} (ignoring of course the stochastic pattern seen in Fig. 2.6). It is not, however, a good approximation to the decay time z_{dec} of the inflaton, which we estimate next.

We can understand better the post-inflationary dynamics at $z \gg z_{br}$ if we analyze again how the different energy contributions evolve as a function of time. The total energy can be written as a sum of its components as

$$\rho = \frac{m^2 \phi_i^2}{a^3} E_t = \frac{m^2 \phi_i^2}{a^3} \left(E_{K,\varphi} + E_{K,\chi} + E_{G,\varphi} + E_{G,\chi} + E_{int} + E_V \right), \tag{2.51}$$

with

$$E_{K,f} = \frac{1}{2} \left(f' - \frac{3}{2} \frac{a'}{a} f \right)^2, \quad E_{G,f} = \frac{1}{2a^2} |\nabla_y f|^2, \quad E_{int} = \frac{2q_i}{a^3} \chi^2 \varphi^2, \quad E_V = \frac{1}{2} \varphi^2, \tag{2.52}$$

where $E_{K,f}$ and $E_{G,f}$ are the kinetic and gradient energy of the fields φ, X ($f = \varphi, \chi$ labelling their conformal amplitude), and E_{int} and E_V are the interaction and potential energies.

In Fig. 2.7 we show the evolution of the energy contributions as a function of time for a particular resonance parameter. We take, as before, the oscillation average of the different functions. One of the most interesting properties of this system is that the equipartition identities

$$E_{K,\varphi} \simeq E_{G,\varphi} + E_{int} + E_V, \quad E_{K,\chi} \simeq E_{G,\chi} + E_{int}, \tag{2.53}$$

hold for all times. This can be observed in Fig. 2.7.

Let us begin by noting that, despite the spiky patter of z_{br} exhibited in Fig. 2.6, the dominant energy fractions at $z \simeq z_{br}$ show much less scattering with q_i than in the case of ϕ^4. The energy fractions are mostly independent of the resonance parameter, and are given by

Energy Fractions at z_{br}:
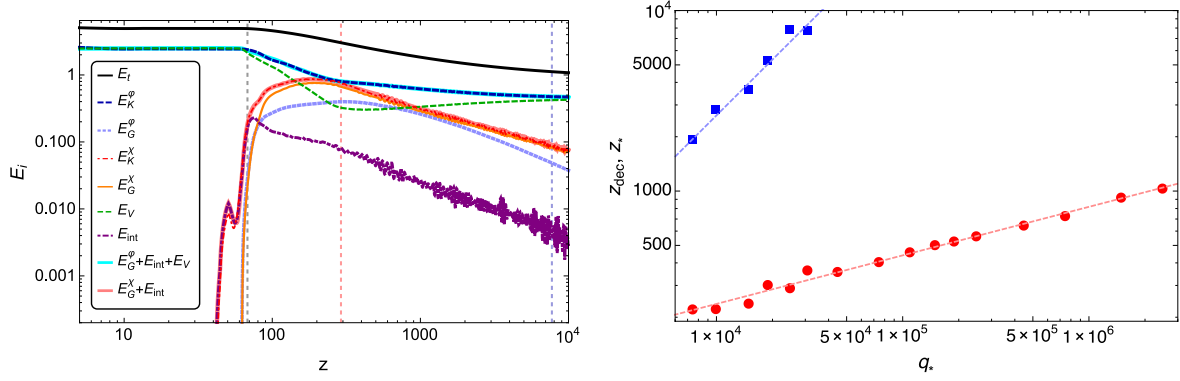
Figure 2.7.: Left: We show for the quadratic preheating case and $q_i = 25000$, the evolution of the different energy components of the system as a function of time, see Eq. (2.53). We normalize them to the total energy at initial times, $E_t(t_i)$. The grey, red, and blue vertical dashed lines indicate the times z_{br}, z_{dec} and $z_{0.80}$. Right: We show the times z_{dec} (red circles) and $z_{0.80}$ (blue squares) as a function of q_i obtained from lattice simulations.

$$\frac{E_{K,\varphi}}{E_t} \simeq (49.4 \pm 0.1)\%, \quad \frac{E_V}{E_t} \simeq (48.7 \pm 0.6),$$
$$\frac{E_{K,\chi}}{E_t} \simeq (0.9 \pm 0.3)\%, \quad \frac{E_{int}}{E_t} \simeq (0.8 \pm 0.3)\%. \tag{2.54}$$

The errors $\pm \Delta E_x / E_t$ simply reflect the (random) scattering of energies with q_i. We see again that at $z = z_{br}$, almost all of the energy remains yet in the inflaton. When the inflaton transfers $\sim 0.5\%$ of its energy, backreaction becomes noticeable, and the inflaton amplitude starts decaying. The other energy components, $E_{G,\varphi}/E_t$, $E_{G,\chi}/E_t$, remain always at less than $\sim 0.1\%$ levels during $0 < z \lesssim z_{br}$, independently of q_i.

We can define again a time scale z_{dec} that characterizes the moment when the system enters into a stationary regime. As equipartition holds all the time, we cannot determine now a specific moment when equipartition is verified to better than a certain degree (as we did in the inflationary $\lambda \phi^4$ case). However, we can define z_{dec} at the onset of the stationary regime, understanding the latter now as the regime when the inflaton kinetic and potential energies do not evolve appreciably anymore within one inflaton oscillation period. In practice, we define z_{dec} at the moment when these energies do not change more than $\sim 0.5\%$ within one oscillation. Let us note, that this does not mean that these energies do not evolve in time at $z \gtrsim z_{dec}$. Actually they evolve smoothly, but the relative change (within an oscillation time scale) is simply very small. Extracting z_{dec} that way from our lattice simulations, we find the data to be very well fitted (see right panel of Fig. 2.7) by,

$$z_{dec}(q_i) \approx 19.9 \, q_i^{0.27}. \tag{2.55}$$

Once again, we see that the larger the resonance parameter q_i, the longer it takes the flow of energy from the inflaton to the daughter fields to cease. At this time, the dominant energy components are actually rather independent of the resonance parameter for $q_i \gtrsim 5 \cdot 10^4$. Their relative fractions are given by

Dominant Energy Fractions at $z \gtrsim z_{\text{dec}}$ ($q_i \gtrsim 5 \cdot 10^4$):

$$\frac{E_{K,\chi}}{E_t} \simeq (25.2 \pm 2.2)\%, \quad \frac{E_{K,\varphi}}{E_t} \simeq (26.0 \pm 2.3)\%, \quad \frac{E_{G,\chi}}{E_t} \simeq (22.9 \pm 2.5)\%, \tag{2.56}$$

again with the errors $\pm \Delta E_j / E_t$ reflecting some scattering of the energies with q_i. The interaction energy E_{int}/E_t is a very sub-dominant component, which remains also almost constant after $z \gtrsim z_{\text{dec}}$. The inflaton gradient energy $E_{G,\varphi}/E_t$ and the potential energy density E_V/E_t are also sub-dominant components, but show some trend of energy exchange: as q_i increases, $E_{G,\varphi}/E_t$ grows and E_V/E_t decreases. We provide the following estimations based on fits obtained within the range $q_i \in [7500, 2.5 \cdot 10^6]$,

Sub-dominant Energy Fractions at $z \approx z_{\text{dec}}$ ($q_i \gtrsim 7 \cdot 10^3$):

$$\frac{E_{G,\varphi}}{E_t} \simeq \frac{19}{(1 + 30000/q_i)^{1/2}}\%, \quad \frac{E_V}{E_t} \simeq \frac{27}{(q_i/2000 - 1)^{1/3}}\%, \quad \frac{E_{\text{int}}}{E_t} \simeq (2.3 \pm 0.5)\% \quad . \tag{2.57}$$

For $q_i \gtrsim 5 \cdot 10^5$, we observe that the potential energy becomes marginal, with $E_V/E_t \lesssim 5\%$, while the inflaton gradient energy seems to saturate to a fraction $E_{G,\varphi}/E_t \simeq 19\% - 20\%$, which still remains subdominant as compared to $E_{K,\chi}, E_{G,\chi}, E_{K,\varphi}$. In other words, at $z \approx z_{\text{dec}}$, the energy is 'democratically' split between the mother and the daughter fields, with final fractions given as $E_\chi/E_t \sim E_\varphi/E_t \sim 50\%$, where we have defined $E_\chi \equiv (E_{K,\chi} + E_{G,\chi} + \frac{1}{2}E_{\text{int}})$ and $E_\varphi \equiv (E_{K,\varphi} + E_{G,\varphi} + E_V + \frac{1}{2}E_{\text{int}})$.

Finally, let us note that at times $z > z_{\text{dec}}$, the energy fractions $E_{K,\varphi}/E_t$ and E_V/E_t still evolve: they grow slowly, but monotonically. At this stage, the total energy density is not scaling anymore as $1/a^3$, so the total contribution $E_t = E_{K,\varphi} + E_{K,\chi} + E_{G,\varphi} + E_{G,\chi} + E_{\text{int}} + E_V$ [see Eq. (2.51)] decreases further in time after $z \gtrsim z_{\text{dec}}$. This is clearly seen in the left panel of Fig. 2.7. Actually, at very late times $z \gg z_{\text{dec}}$, the inflaton dominant energies seem to evolve very slowly towards some value close to (but presumably smaller than) $E_{K,\varphi}/E_t \simeq 50\%$, $E_V/E_t \simeq 50\%$. Correspondingly, the rest of energy fractions decrease gradually to very small values. Our simulations however do not capture the very long times required to probe the final asymptotic values of the inflaton energy components. It is very likely that neither $E_{K,\varphi}/E_t$ or E_V/E_t really reach 50%, but a somewhat smaller value. To quantify this, we have introduced a new time scale z_X, indicating the time it takes for the inflaton energy components (kinetic and potential energies) to represent a given $X\%$ of the total energy of the system. Within our simulation capabilities, the latest time we have been able to reach is $z_{0.80}$, when $(E_{K,\varphi} + E_V)/E_t \simeq 80\%$

(i.e. when $E_{K,\varphi}/E_t$ and E_V/E_t reach individually $\sim 40\%$, as there is equipartition). Even though 80% does not represent the final asymptotic value of the inflaton energy, it clearly signals a moment where the total energy density is well dominated by the inflaton. We observe in our simulations that the rate of growth of the inflaton energy components (between some time after $z_{\rm dec}$ and $z_{0.80}$) follows a well defined power-law in time. Extrapolating such growth to later times, we can in principle predict the moment $z_{0.99}$. In Eqs. (2.58) we provide fits to $z_{0.80}$ and to $z_{0.99}$. Whereas $z_{0.80}$ is measured directly from the numerical simulations, $z_{0.99}$ should be taken only as indicative, as it is only an extrapolation based on the growth of the inflaton energy components at $z \leq z_{0.80}$. In reality, we do not know if eventually the inflaton will dominate up to $\sim 99\%$, or whether it will saturate (most likely) to a somewhat smaller fraction. The time scales are

$$z_{0.80} \simeq 0.26 \, q_{\rm i} \; (\text{measured}) \qquad \rightarrow \qquad z_{0.99} \sim 30 \, q_{\rm i} \; (\text{extrapolated}) \,. \tag{2.58}$$

The values of $z_{0.80}$ follow a well defined power law, see right panel of Fig. 2.7. The fit is obtained only for the cases $q_{\rm i} \lesssim 40000$, since for bigger resonance parameters we cannot reach $z_{0.80}$ in our simulations. Assuming the fit of $z_{0.80}$ in Eq. (2.58) is valid for every resonance parameter, we then expect $z_{0.80} \sim 10^5$ for $q_{\rm i} \sim 10^5$, or $z_{0.80} \sim 10^6$ for $q_{\rm i} \sim 10^6$.

In conclusion, even though the system manages to transfer approximately $\sim 50\%$ of the inflaton energy into the daughter field(s) at $z_{\rm dec}$, unless some new ingredient is added into the scenario (e.g. new coupling to new particle species), the system tends to go back, slowly but systematically, to a complete inflaton energy domination in the long term $z \gg z_{\rm dec}$. Contrary to the ϕ^4 case, the energy density in the daughter field(s) is eventually red-shifted away.

2.5. Lattice simulations: Decay of spectator fields

We move now into the study of scenarios where the oscillating field ϕ does not dominate the energy budget of the Universe. This is the case of any scalar field with a monomial potential that was a spectator field during inflation. We will assume again that ϕ is coupled to some extra species, in particular to another scalar field X, with coupling $g^2\phi^2 X^2$. A paradigmatic example of a spectator-field in cosmology is the curvaton [37, 38, 39], which is typically assumed to have a quadratic potential,

$$V(\phi) = \frac{1}{2}m^2\phi^2 \,. \tag{2.59}$$

We will restrict our numerical study to this case. This scenario can be analyzed in a very similar way to the quadratic preheating case studied in Section 2.4. If we redefine the spacetime and field variables as in Eq. (2.41), the field EOM are identical to Eqs. (2.42)-(2.43), with the

resonance parameter defined as (we rewrite Eq. (2.44) for convenience)

$$q_{\mathrm{i}} = \frac{g^2}{4} \left(\frac{\phi_{\mathrm{i}}}{m} \right)^2 . \qquad (2.60)$$

As before, we choose the initial time of our simulations at the onset of the oscillatory regime of the spectator field, which we set when $H(t = t_{\mathrm{i}}) \equiv H_{\mathrm{i}} = m$.

There are two essential differences with respect to the analogue inflationary case. In the latter, we obtain the time-evolution of the scale factor by solving the Friedmann equations self-consistently with the fields' EOM. However, in our present scenario neither of the fields ϕ or X dominate the energy content of the Universe. The evolution of the background expansion rate is determined by the inflationary sector, which we do not model explicitly. We will simply fix the expansion rate as a power law characterized by an equation of state w, i.e.

$$a(t) = a_{\mathrm{i}} \left(1 + \frac{1}{p} H_{\mathrm{i}}(t - t_{\mathrm{i}}) \right)^p = \left(1 + \frac{1}{p} z \right)^p , \qquad p = \frac{2}{3(1 + w)} . \qquad (2.61)$$

We will consider $w = 1/3$ for a RD background, and $w = 0$ for a MD background. In practice, for the quadratic potential scenario we will focus mostly in the RD case, as this represents the most relevant cosmological case of viable curvaton [37, 38, 39]. For completeness, we will present some results of the quadratic spectator field in a MD background, even if this case seems not to have any cosmological relevance.

The second difference with respect the quadratic inflaton is that now there are more free parameters, which makes the parametrization of the system in principle more complex. In the inflationary case the mass m and the amplitude ϕ_{i} were constrained by the CMB observations, whereas now these are free parameters. Fortunately, if we look at the EOM Eqs. (2.42)-(2.43), we notice that the dynamics only depends on the combination $g^2(\phi_{\mathrm{i}}/m)^2$ through q_{i}. At the same time, one can check that the spectrum of the initial modes mimicking quantum fluctuations, when written in natural units, only depends on the ratio ϕ_{i}/m. Therefore, the system only depends ultimately on two independent parameters, ϕ_{i}/m and g^2 (or alternatively ϕ_{i}/m and q_{i}). Whereas in the inflationary case ϕ_{i}/m was fixed, now this ratio represents an extra free parameter. Finally, the velocity of the field at the onset of the oscillatory regime is determined from the slow-roll condition, which still holds approximately when $H_{\mathrm{i}} = m$. We take therefore as initial velocity the approximation $\dot{\phi}_{\mathrm{i}} \simeq -m^2\phi/(3H_{\mathrm{i}}) = -m\phi_{\mathrm{i}}/3$.

Fig. 2.8 is a diagram of the $(q_{\mathrm{i}}, m/\phi_{\mathrm{i}})$ parameter space, where the coupling strength can be read as $g = 2(m/\phi_{\mathrm{i}})\sqrt{q_{\mathrm{i}}}$. We have excluded the region $g > 1$, depicted in grey in the figure, as this corresponds to non-perturbative coupling strengths. There are different regions in the parameter space $(q_{\mathrm{i}}, m/\phi_{\mathrm{i}})$, according to the different dynamics of the system discussed in Section 2.4. The narrow resonance region correspond to values $q_{\mathrm{i}} < 1$, which lattice simulations cannot capture well. For $1 < q_{\mathrm{i}} \lesssim 10^4$, the inflaton is in broad resonance regime initially, but
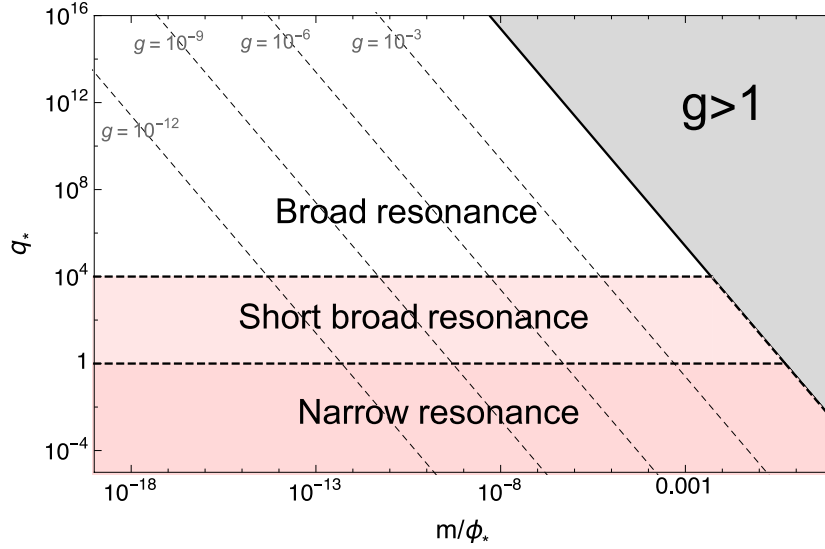
Figure 2.8.: We show different regions in the $(q_i, m/\phi_i)$ parameter space of a spectator field with $\propto \phi^2$ potential, according to their different dynamics. Note that the coupling is $g = 2(m/\phi_i)\sqrt{q_i}$ from (2.60). Explanation of the meaning of these regions is given in the bulk text.

due to the expansion of the Universe, it enters into narrow resonance before backreaction effects from the daughter field activate the decay of the mother field. Hence, we denote this region as 'short broad resonance'. A broad resonance regime sustained for a sufficiently long time, corresponds to $q_i \gtrsim 10^4$ values. We will only study in the lattice this regime, sampling q_i from $\sim 10^4$ to $\sim 10^7$.

We will parametrize the system as a function of g^2 and m/ϕ_i, in light of the previous discussion. In the left panel of Fig. 2.9 we show the backreaction time z_{br}, as a function of the coupling g, for different combinations of q_i and post-inflationary expansion rates. We see that the dependence of z_{br} on g is mostly insensitive (within some scatter) to the choice of q_i and expansion rate. We find the following fit to the data,

$$z_{br}(g) \approx 16.9 - 20.9 \log_{10} g \ . \tag{2.62}$$

As detailed in Section 2.4.1, the logarithmic dependence appears as a consequence of the initial linear behavior of the mode functions, which obey the Mathieu equation until their backreaction into ϕ is noticed. The reason why we see now the logarithmic dependence in this Figure, is that now we have varied g across many orders of magnitude, unlike in the inflationary case (recall Fig. 2.6).

In the right panel of Fig. 2.9 we plot z_{dec} as a function of q_i. In this case, we only provide fits for the RD case. We see that independently of the numerical value of (m/ϕ_i), all points can
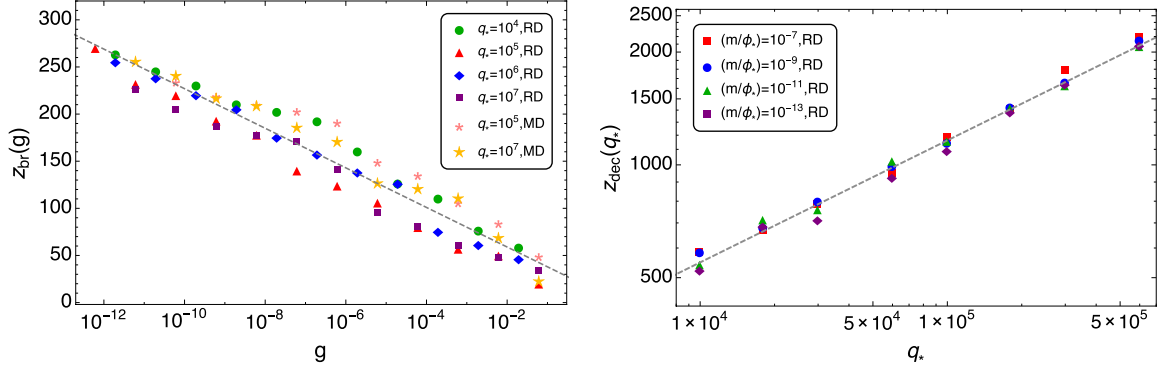
Figure 2.9.: Left: We show z_{br} as a function of coupling g obtained from lattice simulations, for an oscillating spectator-field with quadratic potential. Each symbol corresponds to a specific resonance parameter q_i and expansion rate (RD or MD). We see that independently of the particular case, all values coincide approximately in a single straight line, which we fit in Eq. (2.62) and show with a dashed line. Right: We plot z_{dec} as a function of q_i, for an oscillating spectator-field with quadratic potential and a RD Universe. We consider different values of m/ϕ_i. The dashed line corresponds to the fit of z_{dec}, Eq. (2.63).

be fitted very well to

$$z_{dec}(q_i) \approx 27.3 q_i^{0.33} \, . \tag{2.63}$$

The energy of this system can be written in terms of its different contributions in the same way as in the quadratic preheating case [Eqs. (2.51) and (2.52)]. Their time-evolution is also very similar to the one seen in Fig. 2.7 for chaotic inflation, so we just specify the different energy contributions at both z_{br} and z_{dec}. We find that the numbers are quite independent from ϕ_i/m and q_i. At z_{br}, we have

Energy Fractions at $z \approx z_{br}$ ($q_i \gtrsim 10^4$) :

$$\frac{E_{K,\varphi}}{E_t} \simeq (49.8 \pm 0.5)\% \, , \quad \frac{E_V}{E_t} \simeq (48.7 \pm 1.0)\% \, , \tag{2.64}$$

$$\frac{E_{K,\chi}}{E_t} \simeq (0.7 \pm 0.7)\% \, , \quad \frac{E_{int}}{E_t} \simeq (0.7 \pm 0.7)\% \, , \tag{2.65}$$

with the other energies contributing less than 0.1%. The error bars $\Delta E_i/E_t$ account for the dispersion due to different choices of q_i and ϕ_i/m. As in the quadratic preheating case, at z_{br} most of the energy is stored in the mother field (in the kinetic and potential energies), while only $\sim 1\%$ is stored in the daughter field. This percentage is enough to induce the onset of the mother field decay due to backreaction effects.

On the other hand, at z_{dec}, the energies are distributed in the following manner,

Dominant Energy Fractions at $z_{\rm dec}$ ($q_{\rm i} \gtrsim 10^4$):

$$\frac{E_{K,\varphi}}{E_t} \simeq (24.3 \pm 0.9)\%\,, \quad \frac{E_{G,\varphi}}{E_t} \simeq (20.0 \pm 0.8)\%\,, \tag{2.66}$$

$$\frac{E_{K,\chi}}{E_t} \simeq (26.4 \pm 1.0)\%\,, \quad \frac{E_{G,\chi}}{E_t} \simeq (24.8 \pm 1.2)\%\,, \tag{2.67}$$

which are also approximately independent on $q_{\rm i}$ and $\phi_{\rm i}/m$. The other two energies are sub-dominant and have a certain dependence in $q_{\rm i}$, which we have fitted as

Sub-dominant Energy Fractions at $z \approx z_{\rm dec}$ ($q_{\rm i} \gtrsim 10^4$):

$$\frac{E_V}{E_t} \simeq \frac{80}{(1+q_{\rm i})^{0.3}}\%\,, \quad \frac{E_{\rm int}}{E_t} \simeq \frac{13}{(1+q_{\rm i})^{0.2}}\%\,. \tag{2.68}$$

Note that, unlike the quadratic preheating case, for the spectator-field both the potential and interaction energy contributions have a decreasing behavior with $q_{\rm i}$.

At $z \gtrsim z_{\rm dec}$ the system enters into a stationary regime, where the energies $E_{K,\varphi}$ and E_V evolve very slowly in time. However, similarly to the analogous preheating scenario, each of the energy fractions $E_{K,\varphi}/E_t$ and E_V/E_t still grow, slowly but monotonically, towards some value of the order of, but (presumably) somewhat smaller than, $\sim 50\%$. This asymptotic regime is however attained at very large times, much larger than in the quadratic inflaton case for the same $q_{\rm i}$'s. Due to this, we have only been able to capture partially this regime in our lattice simulations with spectator fields. We define z_X as the moment when the mother field energy components represent a fraction $X\%$ of the total energy of the mother-daughter fields system, analogously as in the preheating case. We can only reach up to $z_{0.40}$ in our numerical simulations of spectator fields (let us recall that in the case of preheating we reached $z_{0.80}$). However the trend of growth of $E_{K,\varphi}/E_t$ and E_V/E_t between $z_{\rm dec}$ and $z_{0.40}$ follows again a well defined power-law, which is expected to hold at later times. Thus, extrapolating the behavior of the energy fractions at later times, we can predict again $z_{0.99}$. The fits we obtain are

$$z_{0.4} \simeq 0.18\,q_{\rm i}\ \text{(measured)} \quad \rightarrow \quad z_{0.99} \sim 8 \cdot 10^{-6}\,q_{\rm i}^3\ \text{(extrapolated)}\,. \tag{2.69}$$

In reality, as in the preheating case, we do not know to which final value $E_{K,\varphi}/E_t$ and E_V/E_t settle eventually down, and hence the extrapolated $z_{0.99}$ must be considered only as indicative of the time scale of the final asymptotic state.

2.6. Summary

In this chapter we have studied parametric resonance using classical real time field theory lattice simulations. We have simulated an oscillating mother field ϕ coupled to a daughter

field X, which is excited due to an interaction term $g^2\phi^2 X^2$. We have considered two main scenarios. First, when the mother field is the inflaton field, oscillating around the minimum of its potential after inflation. We have considered the case of chaotic inflation with $V \propto \phi^2$ and $V \propto \phi^4$ potentials. In a second type of scenarios, the oscillating field was just a spectator-field during inflation with $V \propto \phi^2$ potential, playing no dynamical role on the expansion of the Universe.

Our results show very clearly that the computation in the linear regime of the moment of efficient transfer of energy z_{eff}, see Eqs. (2.29), (2.49), does not represent a good estimation of the decay time scale z_{dec} of the mother field. Instead, z_{eff} indicates well (up to $\mathcal{O}(1)$ factors) the onset of the mother field decay at z_{br}, when the back-reaction of the daughter field becomes noticeable. Despite the exponential transfer of energy into the daughter fields during the time $z < z_{\mathrm{br}}$, the daughter field fluctuations follow a linear equation, whilst the mother field amplitude remains almost unperturbed. At $z \gtrsim z_{\mathrm{br}}$, the presence of the excited daughter fields makes the amplitude and energy of the mother field to abruptly decrease. At $z \gtrsim z_{\mathrm{br}}$ the dynamics become non-linear, and there is a noticeable transfer of energy between the mother and the daughter fields. Eventually, at $z \gtrsim z_{\mathrm{dec}}$ the amplitude of the fields settle down to stationary values, with the energy equiparted among the different components. As for $z \geq z_{\mathrm{dec}}$ the dominant energy components do not evolve any more noticeably, we identify the onset of that stationary stage as the truly time scale of the decay of the mother field. In the case of a quadratic potential, at $z \gtrsim z_{\mathrm{dec}}$, in reality only the mother field kinetic and potential (conformal) terms remain almost constant, as the (conformal) energy components of the daughter fields decay slowly at long times.

The linear calculation of $z_{\mathrm{eff}} \sim z_{\mathrm{br}}$ indicates that the stronger the coupling between mother and daughter fields, the faster the system becomes non-linear. However, the dependence is only logarithmic, so in practice z_{br} only changes by a factor $\mathcal{O}(1)$ when varying the strength of the coupling in more than 10 orders of magnitude, see e.g. the left panel of Fig. 2.9. Nevertheless, as the system becomes non-linear after $z \gtrsim z_{\mathrm{br}}$, our numerical results show a rather counter-intuitive result, opposite to the intuition gained from the analytic estimations: the stronger the mother-daughter coupling, the longer the time decay z_{dec} scale is, with a typical power-law behavior with respect the resonance parameter, $z_{\mathrm{dec}} \propto q^r$, with $r \sim 1/4, 1/3$ or $1/2$, depending on the case.

Let us note that we have defined and obtained the decay time scale z_{dec} at the onset of the stationary regime, but we have not analyzed the evolution of the equation of state or the departure from thermal equilibrium. For a study of the subsequent evolution of the system at $z \gtrsim z_{\mathrm{dec}}$ towards thermalization, see [57, 58, 59, 60]. We have found nonetheless a remarkable result: in the case of quadratic potentials, the energy components of the daughter field tend to decay at the very late times $z \gg z_{\mathrm{dec}}$, so that slowly but monotonically the mother field tends to dominate the energy budget of the mother-daughter system.

Let us remark that in this chapter we have considered the decay products to be scalar fields. However, parametric resonance can also take place for all bosonic species, including gauge fields (either Abelian and non-Abelian). There are many scenarios where the decay products are gauge fields, see e.g. [61, 62, 63, 64, 65, 66, 67, 68, 69, 70, 71, 72], although not in all of them the driving particle production mechanism is parametric resonance. We will demonstrate in Chapter 4 that the dynamics of parametric resonance into Abelian gauge fields (at least for a mother field with quartic potential), is only slightly modified in the linear regime, i.e. z_{br} changes slightly. The late time non-linear dynamics remain however basically unchanged. Therefore, in principle, our fitted formulas can be applied equally to the case of parametric resonance of gauge bosons.

There are some scenarios of preheating where the daughter fields are scalar fields, but the mechanism responsible for the particle production is not parametric resonance, e.g. hybrid preheating [73, 74, 75, 76, 77, 78, 79, 80]. Our fitted formulas, unfortunately, cannot be applied to these scenarios. The case of trilinear or non-renormalizable interactions between the mother and the daughter field(s) [81, 82, 83, 84] are neither captured by our analysis. The case of oscillations of a multi-component field is neither captured well by our analysis, see e.g. [85, 86, 87, 88, 89]. We speculate nonetheless, that the non-linear dynamics after the initial excitation in all these scenarios, is probably very similar to the one after parametric resonance. However, only proper lattice simulations can prove this.

Chapter 3.

Gravitational wave production from preheating: parameter dependence

Parametric resonance is among the most efficient phenomena generating gravitational waves (GWs) in the early Universe. The dynamics of parametric resonance, and hence of the GWs, depend exclusively on the resonance parameter q. The latter is determined by the properties of each scenario: the initial amplitude and potential curvature of the oscillating field, and its coupling to other species. Previous works have only studied the GW production for fixed value(s) of q. In this chapter we study the production of GW in post-inflationary preheating scenarios driven by parametric resonance, by running lattice simulations for a wide range of q values. We present simple fits for the final amplitude and position of the local maxima in the GW spectrum. Our parametrization allows to predict the location and amplitude of the GW background today, for an arbitrary q. The GW signal can be rather large, as $h^2\Omega_{GW}(f_p) \lesssim 10^{-11}$, but it is always peaked at high frequencies $f_p \gtrsim 10^7 \text{Hz}$. We also discuss the case of spectator-field scenarios, where the oscillatory field can be e.g. a curvaton.

Results presented in this Chapter have been published in Ref. [5].

3.1. Introduction

Gravitational waves (GW) are ripples of the spacetime which propagate at the speed of light. Since the first direct detection of two GW signal coming from the collision of astrophysical binaries [90], a new window into the Universe has opened, which allows us to probe astrophysical and cosmological environments previously inaccessible. In particular, the Universe is presumed to be permeated by various GW backgrounds of cosmological origin. For example, we expect an almost scale-invariant background from inflation [91]. We also expect a strong production of GW from non-equilibrium phenomena after inflation, such as (p)reheating [92, 93, 94, 78, 79, 95, 80], phase transitions [96, 97, 98, 99, 100], or cosmic de-

fects [67, 101, 102, 103, 104, 105]. A direct detection of these backgrounds would probe physical phenomena at energies beyond the reach of particle colliders. For a recent review on gravitational wave backgrounds of cosmological origin, see Ref. [106].

Parametric resonance is a non-perturbative, non-linear, and out-of-equilibrium phenomenon. Due to this, the violent excitation of field species via parametric resonance is expected to produce a significant amount of gravitational waves [92, 94, 107, 78, 79, 95, 80, 108, 109, 110]. Our aim in this chapter is, precisely, to parametrize the production of GW from parametric resonance in the early Universe[1]. This is a natural continuation of the research results presented in Chapter 2, where we have parametrized the mother and daughter field dynamics, in different preheating and spectator-field scenarios where parametric resonance is naturally expected to occur.

In this chapter we focus on the paradigmatic cases of preheating after chaotic inflation models, though our results can be extended to other cases, as long as they exhibit a potential with a monomial shape during the stages following inflation. We will also briefly comment the case of parametric resonance from inflationary spectator fields, and in particular, their inability to produce a large amount of GW. We have characterized the GW production from parametric resonance during all its relevant stages, from the initial linear growth of the daughter field fluctuations, through the intermediate non-linear stage, till the relaxation towards a stationary distribution. We have also parametrized the GW spectra by surveying the relevant circumstances and parameters in each case. For this, we have used massively parallelized lattice simulations, obtaining simple fits to the most significant quantities, like the characteristic peak scales and associated amplitudes of the matter and GW spectra.

The chapter is divided as follows. In Section 3.2 we present an estimation of the frequency and amplitude of the GW background produced during parametric resonance, based on the analytic understanding of the linear stage of the daughter field(s) excitation. In Section 3.3 we present our results from numerical lattice simulations of preheating for a quartic inflaton potential, and in Section 3.4 for a quadratic inflation potential. In Section 3.5 we briefly study the production of GW from spectator fields undergoing parametric resonance. In Section 3.6 we summarize our results and conclude.

---

[1]Note that we do not consider the case of 'oscillons', which correspond to stable field configurations formed whenever a field oscillates around the minimum of its potential, as long as the potential shape meets certain circumstances, see e.g. [111, 112]. For the GW production from oscillons see [113, 114, 115, 116].

3.2. Gravitational waves from parametric resonance: scenarios and analytical calculations

In this section, we consider the gravitational waves produced by a scalar field, being excited due to a parametric resonance process. We consider the same scenario as in Section 2.2, where the potential of the mother field is monomial. In this case, the mother field starts oscillating around the minimum of its potential after inflation. In this situation, the equation of the daughter field modes, Eq. (2.12), admits unstable solutions of the type $X_\kappa^{(c)} \sim e^{\mu_q(\kappa)z}$, with $\mathfrak{Re}[\mu_q] > 0$ for certain regions in the (κ, q) parameter space. This exponential growth of certain daughter field modes, is what we understand as parametric resonance. As we shall see, this generates a significant anisotropic stress $\Pi_{ij} \sim \partial_i X_c \partial_j X_c$, which in turn creates GW.

Gravitational waves correspond to the transverse and traceless (TT) degrees of freedom of metric perturbations,

$$ds^2 = a^2(\tau)\left(-d\tau^2 + \delta_{ij} + h_{ij}\right) dx^i dx^j \,, \tag{3.1}$$

where $d\tau = dt/a(t)$ is conformal time, and h_{ij} verify the conditions $\partial_i h_{ij} = 0$ (transversality) and $h_i^i = 0$ (tracelessness). Linearizing the Einstein equations (1.1) lays down the EOM for the generation and propagation of GW in a FLRW background,

$$h_{ij}'' + 2\mathcal{H}h_{ij}' - \nabla^2 h_{ij} = \frac{2}{m_p^2}\,\Pi_{ij}^{\mathrm{TT}} \,, \tag{3.2}$$

where $' \equiv d/d\tau$ represents derivatives with respect to conformal time, and we have defined $\mathcal{H} \equiv a'/a$ as the comoving Hubble rate. The source of GW, Π_{ij}^{TT}, is the TT-part of the anisotropic stress of the system, defined as

$$\Pi_{ij}^{\mathrm{TT}} \equiv \left\{\partial_i X \partial_j X\right\}^{\mathrm{TT}} = \frac{1}{a^2}\left\{\partial_i X_c\,\partial_j X_c\right\}^{\mathrm{TT}} \,. \tag{3.3}$$

The anisotropic stress should really be sourced by the gradients of all excited fields, including the mother field term $\partial_i\phi\partial_j\phi$. However, we take the mother field as approximately homogeneous at initial times, so we ignore such term for the moment. The contribution of the mother field will be automatically included in the lattice simulations that we will present in sections 3.3 and 3.4.

Obtaining the TT-part of a tensor in configuration space amounts to a non-local operation, so it is more convenient to work in Fourier space, where a geometrical TT-projection can be easily built. The EOM of the GW in Fourier space reads

$$h_{ij}''(\mathbf{k}, \tau) + 2\mathcal{H}h_{ij}'(\mathbf{k}, \tau) + k^2 h_{ij}(\mathbf{k}, \tau) = \frac{2}{m_p^2}\Pi_{lm}^{\mathrm{TT}}(\mathbf{k}, \tau) \,. \tag{3.4}$$

In momentum space, the TT operation is defined as $\Pi_{lm}^{\rm TT}(\mathbf{k}, \tau) \equiv \Lambda_{ij,lm}(\hat{\mathbf{k}})\Pi_{lm}(\mathbf{k}, \tau)$, with $\Pi_{ij}(\mathbf{k}, \tau)$ the Fourier transform of $\Pi_{ij}(\mathbf{x}, \tau)$, and $\Lambda_{ij,lm}(\hat{\mathbf{k}})$ a projector defined as[2]

$$\Lambda_{ij,lm}(\hat{\mathbf{k}}) \equiv P_{il}(\hat{\mathbf{k}})P_{jm}(\hat{\mathbf{k}}) - \frac{1}{2}P_{ij}(\hat{\mathbf{k}})P_{lm}(\hat{\mathbf{k}}), \quad P_{ij} = \delta_{ij} - \hat{k}_i\hat{k}_j, \quad \hat{k}_i = k_i/k. \tag{3.5}$$

The energy density spectrum of a stochastic (isotropic) background of GW (at subhorizon scales) takes the form [106]

$$\frac{d\rho_{\rm GW}}{d\log k} = \frac{k^3 m_p^2}{8\pi^2 a^2}\mathcal{P}_{h'}(k, \tau), \tag{3.6}$$

where $\langle h'(\mathbf{k}, \tau)h^{*'}(\mathbf{k}', \tau)\rangle = (2\pi)^3\mathcal{P}_{h'}(\kappa, \tau)\delta^{(3)}(\mathbf{k} - \mathbf{k}')$. This can be written as an explicit function of the source matter fields as

$$\frac{d\rho_{\rm GW}}{d\log k}(k, \tau) = \frac{1}{4\pi^2 a^4(\tau)}\frac{k^3}{m_p^2}\int_{\tau_i}^{\tau}d\tau'\int_{\tau_i}^{\tau}d\tau''\, a(\tau')\, a(\tau'')\cos[k(\tau' - \tau'')]\,\Pi^2(k, \tau', \tau''), \tag{3.7}$$

where Π^2 is the Unequal-Time-Correlator (UTC) of the source of $\Pi_{ij}^{\rm TT}$, defined as

$$\langle 0|\Pi_{ij}^{\rm TT}(\mathbf{k}, \tau)\Pi_{ij}^{\rm TT^*}(\mathbf{k}', \tau')|0\rangle \equiv (2\pi)^3\Pi^2(k, \tau, \tau')\delta^{(3)}(\mathbf{k} - \mathbf{k}). \tag{3.8}$$

Substituting the quantized field Eq. (2.10) into Eq. (3.3), leads to the expression in Fourier space,

$$\Pi_{ij}^{\rm TT}(\mathbf{k}, \tau) = \tag{3.9}$$

$$\frac{\Lambda_{ij,lm}(\hat{k})}{(2\pi)^3 a^2(\tau)}\int d\mathbf{p}\, p_l p_m\left(\hat{a}_{\mathbf{p}}X_{\mathbf{p}}^{(c)}(\tau) + \hat{a}_{-\mathbf{p}}^\dagger X_{\mathbf{p}}^{(c)^*}(\tau)\right)\left(\hat{a}_{\mathbf{k}-\mathbf{p}}X_{\mathbf{k}-\mathbf{p}}^{(c)}(\tau) + \hat{a}_{-(\mathbf{k}-\mathbf{p})}^\dagger X_{\mathbf{k}-\mathbf{p}}^{(c)^*}(\tau)\right).$$

The only combinations of creation/annihilation operators which contribute to the expectation value in Eq. (3.8), turn out to be

$$\langle 0|\hat{a}_{\mathbf{p}}\hat{a}_{\mathbf{k}-\mathbf{p}}\hat{a}_{\mathbf{q}}^\dagger\hat{a}_{\mathbf{k}'-\mathbf{q}}^\dagger|0\rangle = (2\pi)^6\left[\delta^{(3)}(\mathbf{k} - \mathbf{p} - \mathbf{q}) + \delta^{(3)}(\mathbf{p} - \mathbf{q})\right]\delta^{(3)}(\mathbf{k} - \mathbf{k}'), \tag{3.10}$$

$$\langle 0|\hat{a}_{\mathbf{p}}\hat{a}_{-(\mathbf{k}-\mathbf{p})}^\dagger\hat{a}_{\mathbf{q}}\hat{a}_{-(\mathbf{k}'-\mathbf{q})}^\dagger|0\rangle = (2\pi)^6\delta^{(3)}(\mathbf{k})\delta^{(3)}(\mathbf{k}' - \mathbf{k}), \tag{3.11}$$

where we have used the commutation rule in Eq. (2.11). Since the second term Eq. (3.11) can be re-written as proportional to $\delta^{(3)}(\mathbf{k})\delta^{(3)}(\mathbf{k}')$, it does not contribute to $\Pi^2(k, t, t')$ at finite momenta $k = k' \neq 0$. Thus, only the term Eq. (3.10) contributes to the final expression of the UTC, which reads

$$\Pi^2(k, \tau, \tau') = \frac{1}{4\pi^2 a^2(\tau)a^2(\tau')}\int dp\, d\theta\, p^6\sin^5\theta\, X_{\mathbf{p}}^{(c)}(\tau)X_{\mathbf{k}-\mathbf{p}}^{(c)}(\tau)X_{\mathbf{k}-\mathbf{p}}^{(c)^*}(\tau')X_{\mathbf{p}}^{(c)^*}(\tau'), \tag{3.12}$$

---

[2]Note that when we define the analogous TT-projector on a lattice grid for numerical simulations, this requires a different definition than that in Eq. (3.5) for the continuum, see Ref. [108] for more details.

where we have used the result $\Lambda_{ij,lm}(\hat{k})\left(p_i(k-p)_j(k-p)_l p_m + p_i(k-p)_j p_l(k-p)_m\right) = p^4 \sin^4\theta$, with θ the angle between $\mathbf{p}$ and $\mathbf{k}$. The spectrum of GW Eq. (3.7) is finally given by

$$\frac{d\rho_{\text{GW}}}{d\log k}(k,t) = \frac{Gk^3}{2\pi^3}\int dp\, d\theta\, p^6 \sin^5\theta\left(\left|I_{(c)}(k,p,\theta,\tau)\right|^2 + \left|I_{(s)}(k,p,\theta,\tau)\right|^2\right),\qquad (3.13)$$

with

$$I_{(c)} \equiv \int_{\tau_i}^{\tau}\frac{d\tau'}{a(\tau')}\cos(k\tau')X_{\mathbf{k}-\mathbf{p}}^{(c)}(\tau')X_{\mathbf{p}}^{(c)}(\tau'),\quad I_{(s)} \equiv \int_{\tau_i}^{\tau}\frac{d\tau'}{a(\tau')}\sin(k\tau')X_{\mathbf{k}-\mathbf{p}}^{(c)}(\tau')X_{\mathbf{p}}^{(c)}(\tau').\quad (3.14)$$

Eqs. (3.13) and (3.14) are the master formulae that allow to compute the Gravitational Wave production, as a function of the field modes undergoing parametric resonance.

3.2.1. Redshift of gravitational wave backgrounds

Let us derive now how a GW background generated in the early universe redshifts till today. Since GW decouple immediately after production, we simply need to redshift appropriately the frequency and amplitude of the spectrum computed at the end of the GW generation. Let us denote as t_i the initial time at the onset of GW production, t_f as the end of GW production, t_{RD} as the first moment when the Universe becomes radiation dominated (RD), and finally t_o as the present time. The ratio between the scale factors at the end of inflaton and today can be written as

$$\frac{a_i}{a_o} = \frac{a_i}{a_{\text{RD}}}\frac{a_{\text{RD}}}{a_o} = \epsilon_i^{1/4}\left(\frac{g_{s,o}}{g_{s,\text{RD}}}\right)^{\frac{1}{3}}\left(\frac{g_o}{g_{\text{RD}}}\right)^{-\frac{1}{4}}\left(\frac{\rho_o}{\rho_i}\right)^{\frac{1}{4}}. \qquad (3.15)$$

In the second equality, we have used that during the thermal phase of the Universe, $\rho \propto g_t T^4$ and $aT \propto g_{s,t}^{-1/3}$, with $g_{s,t}$ and g_t the entropic and relativistic degrees of freedom respectively at a time t, and T the temperature. We have also used that between t_i and t_{RD}, the energy density scales as $\rho \propto a^{-3(1+w)}$ with $w = p/\rho$ the effective equation of state (pressure-to-density ratio) of the Universe. We have introduced the factor

$$\epsilon_i \equiv \left(\frac{a_i}{a_{\text{RD}}}\right)^{(1-3w)}, \qquad (3.16)$$

which quantifies the (averaged) expansion rate of the Universe between t_i and t_{RD}. Taking into account that $g_{s,t} \sim g_t$, we see that $(g_{s,o}/g_{s,\text{RD}})^{1/3}(g_o/g_{\text{RD}})^{-1/4} \sim (g_o/g_{\text{RD}})^{1/12} \sim \mathcal{O}(1)$ [≈ 1.77 if $g_o/g_{\text{RD}} = 10^3$, ≈ 1.47 if $g_o/g_{\text{RD}} = 10^2$]. Putting all together, and using the energy density of relativistic species today $\rho_o \approx 2\cdot 10^{-15}\text{eV}^4$, the frequency today associated to a co-moving

mode k of a GW background created in the early universe between t_i and t_f, reads

$$f \equiv \left(\frac{a_i}{a_o}\right)\frac{k}{2\pi} = \epsilon_i^{1/4}\left(\frac{g_{s,o}}{g_{s,RD}}\right)^{\frac{1}{3}}\left(\frac{g_o}{g_{RD}}\right)^{-\frac{1}{4}}\left(\frac{\rho_o}{\rho_i}\right)^{\frac{1}{4}}\frac{k}{2\pi}$$

$$\simeq \epsilon_i^{1/4}\left(\frac{k}{\rho_i^{1/4}}\right) \times 8 \cdot 10^9 \text{ Hz} . \tag{3.17}$$

On the other hand, the spectral amplitude of the GW background today, normalized to the actual critical energy density ρ_c, can be obtained as

$$h^2\Omega_{GW} \equiv \frac{h^2}{\rho_c}\frac{d\rho_{GW}}{d\log k} = h^2\Omega_{rad}\left(\frac{a_f}{a_{RD}}\right)^{1-3w}\left(\frac{g_{s,o}}{g_{s,RD}}\right)^{\frac{4}{3}}\left(\frac{g_{RD}}{g_o}\right)\Omega_{GW}^{(f)}$$

$$\simeq h^2\Omega_{rad}\left(\frac{g_o}{g_{RD}}\right)^{1/3} \times \epsilon_i\left(\frac{a_f}{a_i}\right)^{1-3w}\Omega_{GW}^{(f)}$$

$$\approx \mathcal{O}(10^{-6}) \times 4\epsilon_i\left(\frac{a_f}{a_i}\right)^{1-3w}\Omega_{GW}^{(f)} , \tag{3.18}$$

where $\Omega_{GW}^{(f)} \equiv \frac{1}{\rho_f}\left(\frac{d\rho_{GW}}{d\log k}\right)_f$. For this derivation, in the second line we have used that $g_{s,t} \sim g_t$, and in the third line that $h^2\Omega_{rad} \simeq 4 \cdot 10^{-5}$ and $(g_o/g_{RD})^{1/3} \sim \mathcal{O}(0.1)$.

If the Universe is in a RD phase already at the onset of GW production at t_i (i.e. $t_{RD} \leq t_i$), then $w = \frac{1}{3}$, and the expansion history factors in Eqs. (3.17) and (3.18) are simply $\epsilon_i = 1$ and $(a_f/a_i)^{1-3w} = 1$. This is the case, e.g. for preheating from an inflaton with potential $V(\phi) \propto \phi^4$, as discussed in Section 2.3. However, if the Universe is in an expanding phase with $w < \frac{1}{3}$ between t_i and t_{RD}, then there is always a frequency shift to the IR by a factor $\epsilon_i^{1/4} < 1$, as well as an amplitude suppression by a factor $\epsilon_i(a_f/a_i)^{(1-3w)} = (a_f/a_{RD})^{(1-3w)} \equiv \epsilon_f < 1$. This is the case for example for preheating with quadratic potential $V(\phi) \propto \phi^2$, as discussed in Section 2.4. If on the contrary, the equation of state is *stiff* with $w > 1/3$, then the frequency shifts to the UV, while the amplitude of the GW background is enhanced by a factor $\epsilon_i(a_f/a_i)^{(1-3w)} = (a_f/a_{RD})^{(1-3w)} \equiv \epsilon_f > 1$.

3.2.2. Estimation of the GW production from parametric resonance

In this section, we present an estimation of the gravitational waves produced during parametric resonance after inflation. Gravitational waves are sourced by field gradients, so it is useful to understand first the dynamics of parametric resonance in momentum space. A scalar field undergoing broad resonance with $q > 1$, experiences an excitation of the field modes up to a

given (comoving) cut-off $\kappa \lesssim \kappa_*$, which for quartic and quadratic potentials, it is given by

$$
\begin{cases}
\kappa_* \sim q^{1/4} & , \ V(\phi) \propto \phi^4 \, , \\
\kappa_* \sim (a/a_{\mathrm{i}})^{1/4} q_{\mathrm{i}}^{1/4} & , \ V(\phi) \propto \phi^2 \, ,
\end{cases}
\tag{3.19}
$$

(see Eqs. (2.48) and (2.21) respectively). Here, q is the resonance parameter in each case, $\kappa \equiv k/\omega_*$ is momentum, and a_i is the scale factor at the end of inflation. In other words, the excitation of a field in broad resonance consists in the development of large field amplitudes for modes with momentum inside a radius $\kappa \lesssim \kappa_*$. We will refer to this configuration as a 'Bose-sphere', outside which ($\kappa > \kappa_*$) the field occupation number vanishes, hence suppressing the GW production. Consequently, GW will only be created inside the Bose-sphere $\kappa < \kappa_*$. Of course, after a number of oscillations of the mother field, the excited daughter field backreacts into the former. This results in an excitation of finite modes of the mother field, breaking apart its homogeneous condition. From that moment onward, the two-field system becomes non-linear, and one expects higher modes $\kappa \gtrsim \kappa_*$ of the daughter field to be excited. This re-scattering effect enhances the radius of the Bose-sphere as $\kappa_* \longrightarrow \alpha(q)\kappa_*$, with $\alpha(q)$ a function of q. For moderate q values, a factor $\mathcal{O}(1) \lesssim \alpha(q) \lesssim \mathcal{O}(10)$ is typically observed.

We expect on general grounds, that the GW spectrum will have a peak at some scale $\kappa = \kappa_p$, located roughly around the maximally excited momentum of the scalar field spectrum, i.e. $\kappa_p \sim \kappa_*$. On the other hand, we found in Eq. (3.17) an expression for the redshift of the frequency of a GW background produced after inflation. Substituting (3.19) into Eq. (3.17), we find the following estimate for the frequency of the peak in the GW background,

$$
f_p \ \sim \ 8 \cdot 10^9 \left(\frac{\omega_*}{\rho_{\mathrm{i}}^{1/4}} \right) \epsilon_i^{\frac{1}{4}} \, q^{\frac{1}{4}+\eta} \ \mathrm{Hz} \times
\begin{cases}
1 & , \ V(\phi) \propto \phi^4 \, , \\
\left(\frac{a_{\mathrm{f}}}{a_{\mathrm{i}}} \right)^{\frac{1}{4}} & , \ V(\phi) \propto \phi^2 \, .
\end{cases}
\tag{3.20}
$$

We have introduced a parameter η to quantify the goodness of our analytical estimation, and in particular, of our assumption $\kappa_p \sim \kappa_* \propto q^{1/4}$. As our derivation ignores the enhancement effect $\kappa_* \to \alpha(q)\kappa_*$ mentioned before, it is likely that the scaling of f_p as $\propto q^{1/4}$ does not hold, as $\alpha(q)$ is in general expected to be a function of the resonance parameter q. Only when confronting Eq. (3.20) with our lattice simulations, we will be able to quantify whether η represents only a small correction.

We also found an estimation for the q-dependence of the GW amplitude in Ref. [5]. These estimations are based on Eqs. (3.13) and (3.18), as well as dimensional arguments, and are more complicated to obtain. Here we simply quote our results: the interested reader can find all the details of the derivation in the indicated reference.

In particular, in Ref. [5] we found that, during the linear stage of parametric resonance, the peak of the daughter field spectrum $k^3|X_k^{(c)}|^2$ should scale as

$$k_*^3|X_{k_*}^{(c)}|^2 \propto q^{-1/2}. \tag{3.21}$$

As we will show, our numerical simulations display precisely this behavior. Moreover, we found that the GW peak amplitude at the end of GW production is given by

$$\Omega_{\mathrm{GW}}^{(\mathrm{f})}(\kappa_p) = \frac{C^2}{8\pi^4}\frac{\omega_*^6}{\rho_i m_p^2}\, q^{-\frac{1}{2}+\delta}\,, \tag{3.22}$$

with C a dimensionless constant, and δ another parameter quantifying the goodness of the estimation as a function of q. Substituting this into Eq. (3.18), the corresponding amplitude of the GW peak today can be written as

$$h^2\Omega_{\mathrm{GW}}(f_p) \sim \mathcal{O}(10^{-9}) \times \epsilon_{\mathrm{i}}\, C^2 \frac{\omega_*^6}{\rho_i m_p^2}\, q^{-\frac{1}{2}+\delta}\,, \tag{3.23}$$

where we have used $\frac{1}{8\pi^4} \sim 1.3\cdot 10^{-3}$, and absorbed the factor $1.3\cdot 4\cdot(a_{\mathrm{f}}/a_{\mathrm{i}})^{1-3\omega}$ into the C^2 constant.

We shall compare our prediction for the q-dependence of the GW amplitude and frequency, given in Eqs. (3.20) and (3.23), with the results from our lattice simulations, presented in the next two sections.

3.3. Lattice simulations: gravitational waves from preheating with quartic potential

In this section we study GW production during preheating, when the inflaton has a quartic potential $V_{\mathrm{inf}}(\phi) = \frac{1}{4}\lambda\phi^4$. We have carried out several lattice simulations of the preheating process, including in this case the tensor fields representing the GW as extra dynamical fields. We have considered different values of the resonance parameter q in the interval $0.4 < q < 5000$. Lower values cannot be simulated because the resonance bands are too narrow to be captured in the lattice, while any larger values cannot be considered due to a lack of a good UV coverage. All the results presented in this section have been obtained from simulations with $N^3 = (256)^3$ points, and minimum momenta $\kappa_{\mathrm{min}} \sim \mathcal{O}(0.1)$, the specific number depending on the particular case.

Before moving on to the analysis of the GW production in these scenarios, it is interesting to see first how the times z_{br} and z_{dec} are reflected in the matter field spectra. In Fig. 3.1 we
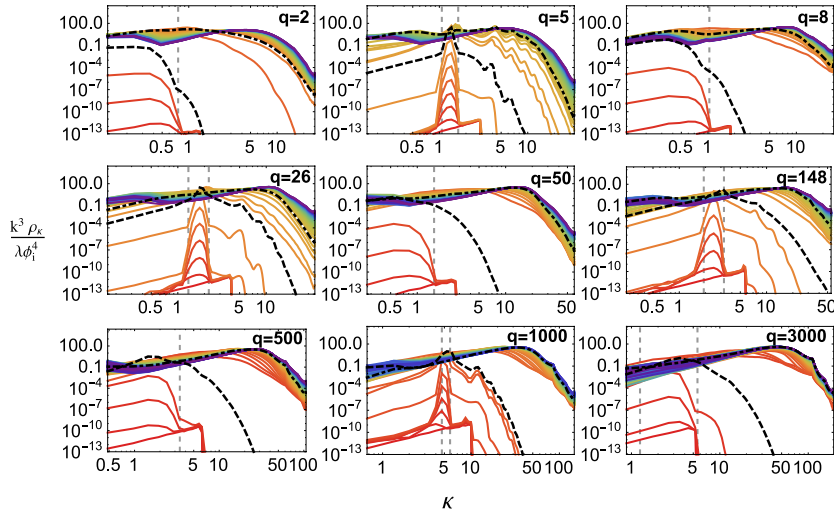
Figure 3.1.: We show the time-evolution of the daughter-field energy density spectra $\kappa^3 \rho_{\kappa,\chi}/(\lambda \phi_i^4)$ [Eq. (3.24)] as a function of the momentum, for different values of the resonance parameter q. The spectra correspond to times $z = 0, 10, 20, \ldots$, with red lines corresponding to early times, and purple lines to late times. In panels $q = 5, 26, 148, 1000, 3000$, which correspond to cases with a main resonance band of the type $\kappa_- < \kappa < \kappa_+$, we indicate κ_- and κ_+ with dashed, vertical lines. In the rest of panels, in which the main band has the form $0 < \kappa < \kappa_+$, we simply indicate the position of κ_+. The values of $\kappa_\pm$ have been obtained from the numerical properties of the *Lamé* equation. We also show with black dashed and black dot-dashed curves the spectra at times $z \approx z_{br}$ and $z \approx z_{dec}$ respectively.

show the time-evolution of the energy density spectra of the daughter field, defined as

$$k^3 \rho_{k,\chi} = \frac{\lambda \phi_i^4}{2} \kappa^3 \left(|\chi_\kappa'|^2 + \omega_{\kappa,\chi}^2 |\chi_\kappa|^2 \right) , \quad \omega_{\kappa,\chi} = \sqrt{\kappa^2 + q\varphi^2 - (a''/a)} , \qquad (3.24)$$

obtained from lattice simulations, and for different values of the resonance parameter q. For $q = 5, 26, 148, 1000, 3000$, the main resonance band is of the form $\kappa_- < \kappa < \kappa_+$, while for $q = 2, 8, 50, 500$, the band is of the type $0 < \kappa < \kappa_+$. As expected, for initial times $z \lesssim z_{br}$, the linear analysis is approximately valid, and the growth of the daughter field takes place mainly inside the resonance bands delimited with dashed, vertical lines. This generates a structure of peaks in the field spectra, due to the particular structure of resonance bands of the *Lamé* equation, (2.20). However, for late times $z \gtrsim z_{br}$, i.e. when the backreaction effects on the inflaton condensate are already significant, the spectra grow outside these bands, washing out the structure of peaks created during the initial stages. The daughter field populates modes of higher-momenta, due to the scattering among modes induced by the coupling between
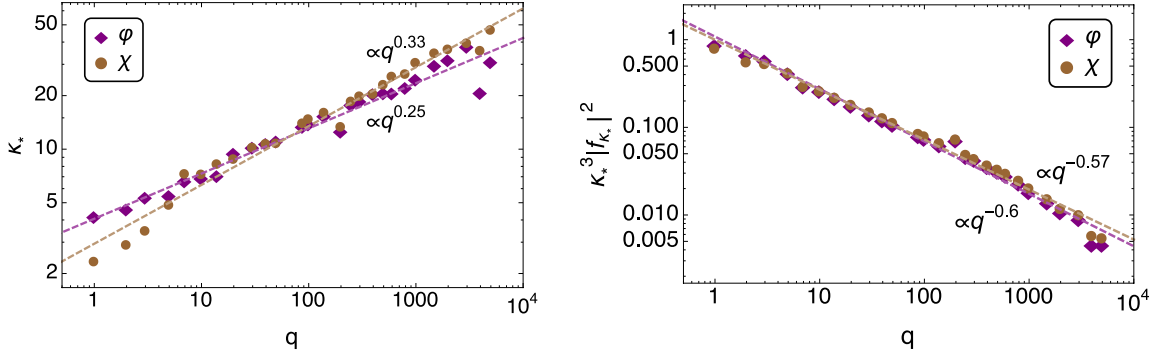
Figure 3.2.: *Left:* Position of the peak κ_* as a function of q, for the inflaton and daughter fields, when a final saturated amplitude has already been reached. Right: Spectral amplitude $\kappa_*^3 |f_{\kappa_*}|^2$ at the peak position κ_*, for both the inflaton and the daughter fields ($f = \varphi, \chi$). In both panels, each point corresponds to a single lattice simulation, and the dashed straight lines correspond to the fits in Eq. (3.25).

fields. When the stationary regime is achieved at times $z \gtrsim z_{\text{dec}}$, the spectra does not evolve appreciably anymore, and its amplitude reaches a final saturated value[3].

Let us check whether the matter spectra obtained from lattice simulations obey the scaling with q presented in Section 3.2. Essentially, due to the structure of resonance bands, the position of the peak should scale as $\kappa_* \propto q^{1/4}$ [Eq. (3.19)], while according to our calculations, the amplitude of such peak should scale as $\kappa_*^3 |\chi_{\kappa_*}|^2 \propto q^{-1/2}$ [Eq. (3.21)]. In Fig. 3.2 we plot both quantities as a function of q, extracted from our lattice simulations when the fields spectra have saturated. We obtain the following fits,

$$\text{Daughter field } \chi: \quad \kappa_* \approx 13 \left(\frac{q}{100} \right)^{0.33}, \quad \kappa_*^3 |\chi_{\kappa_*}|^2 \approx 7 \cdot 10^{-2} \left(\frac{q}{100} \right)^{-0.57},$$

$$\text{Mother field } \varphi: \quad \kappa_* \approx 13 \left(\frac{q}{100} \right)^{0.25}, \quad \kappa_*^3 |\varphi_{\kappa_*}|^2 \approx 7 \cdot 10^{-2} \left(\frac{q}{100} \right)^{-0.60}. \quad (3.25)$$

The power-law scaling for the daughter field spectral peak, obtained from lattice simulations, coincides quite well with the theoretical prediction $\propto q^{-1/2}$ [Eq. (3.21)] , with a deviation of the mean exponent with respect the theoretical value of only $100 \times \frac{(0.57-0.5)}{0.5} \sim 14\%$. On the other hand, the theoretical location of the daughter field's peak at $\kappa_* \sim q^{1/4}$ [Eq. (3.19)] is realized with a correction of the exponent of $100 \times \frac{(0.33-0.25)}{0.25} \sim 30\%$. This deviation from the theoretical expectation should not be seen as surprising: strictly speaking, such predictions are only expected to be valid during the linear regime of the daughter fluctuations growth. The spectra fitted in Eq. (3.25), however, are measured at $z \gtrsim z_{\text{dec}}$, so non-linear effects cannot be ignored.

---

[3]In reality, the 'saturated' amplitudes will evolve smoothly at times $z \gg z_{\text{dec}}$, as the field distributions adapt themselves on their way towards equilibrium, as seen in Chapter 2. However, during this regime no GW are emitted, so we are not interested in this late stage right now.

It is also remarkable that the mother field φ follows a similar scaling as the daughter field, even though we did not have a clear expectation in this respect. The (mean value of the) peak position of the mother field spectra is actually located exactly at $\sim q^{1/4}$, whereas the exponent of the spectral peak amplitude presents only a deviation of $100 \times \frac{(0.6-0.5)}{0.5} \sim 20\%$ with respect the theoretical predicted scaling. We think this is due to the coupling between the daughter and the mother fields: slightly before $z \simeq z_{\mathrm{br}}$, when the daughter field modes have already grown significantly (following the resonance pattern of the linear analysis), the same modes of the mother field are excited, thanks to the interaction term. This 'dragging' effect is clearly seen in the inflaton spectra, see e.g. Fig 11 (top panels) in Appendix A of Ref. [3].

3.3.1. Gravitational wave parametrization

Let us discuss now the production of GW during preheating with quartic potential. Let us define a rescaled tensor field as $\bar{h}_{ij} \equiv a h_{ij}$. Using the rescalings defined in Eq. (2.15), the equation of motion of the GW Eq. (3.2) takes the form

$$\bar{h}_{ij}'' - \nabla_y^2 \bar{h}_{ij} - \frac{a''}{a}\bar{h}_{ij} = \frac{2\phi_i^2}{am_p^2}\left[\partial_i\varphi\partial_j\varphi + \partial_i\chi\partial_j\chi\right]^{\mathrm{TT}}. \tag{3.26}$$

The total energy of the system ρ_t (contributed by the matter fields, as the GW are energetically very sub-dominant) can be written as

$$\rho_t(z) = \frac{\lambda\phi_i^4}{a^4} \times \left[\frac{1}{2}\sum_{f=\chi,\varphi}\left(f' - f\frac{a'}{a}\right) + \frac{1}{2}\sum_{f=\chi,\varphi}|\nabla_y f|^2 + \frac{1}{2}q\varphi^2\chi^2 + \frac{1}{4}\varphi^4\right] \equiv \frac{\lambda\phi_i^4}{a^4}E_t. \tag{3.27}$$

The spectrum of GW in Eq. (3.6), normalized over the total energy density of the system, can be written as

$$\Omega_{\mathrm{GW}}(\kappa,z) \equiv \frac{1}{\rho_t(z)}\frac{d\rho_{\mathrm{GW}}}{d\log k}(\kappa,z) = \frac{m_p^2}{\phi_i^2}\frac{(\sqrt{\lambda}\phi_i\kappa)^3}{8\pi^2 V E_t(z)}\int\frac{d\Omega_k}{4\pi}\left|(\bar{h}_{ij}' - \mathcal{H}\bar{h}_{ij})(\kappa,z)\right|^2. \tag{3.28}$$

We show in Fig. 3.3 the time-evolution of the GW spectra for the resonance parameters $q = 5, 30, 200, 500$, obtained from our lattice simulations. We observe that the GW spectra grow several orders of magnitude in a short time $\Delta z \sim \mathcal{O}(10)$, saturating eventually at a given time scale z_f, which signals the end of GW production. We have observed that typically, $z_{\mathrm{br}} < z_f < z_{\mathrm{dec}}$, with the last order-of-magnitude growth of the GW spectrum amplitude taking place when the non-linear effects are becoming noticeable $z \gtrsim z_{\mathrm{br}}$. For the given parameters of the figure, the final amplitude of the GW after saturation is $\Omega_{\mathrm{GW}}^{(f)} \sim \mathcal{O}(10^{-5}) - \mathcal{O}(10^{-6})$ approximately, relative to the total energy at reheating.
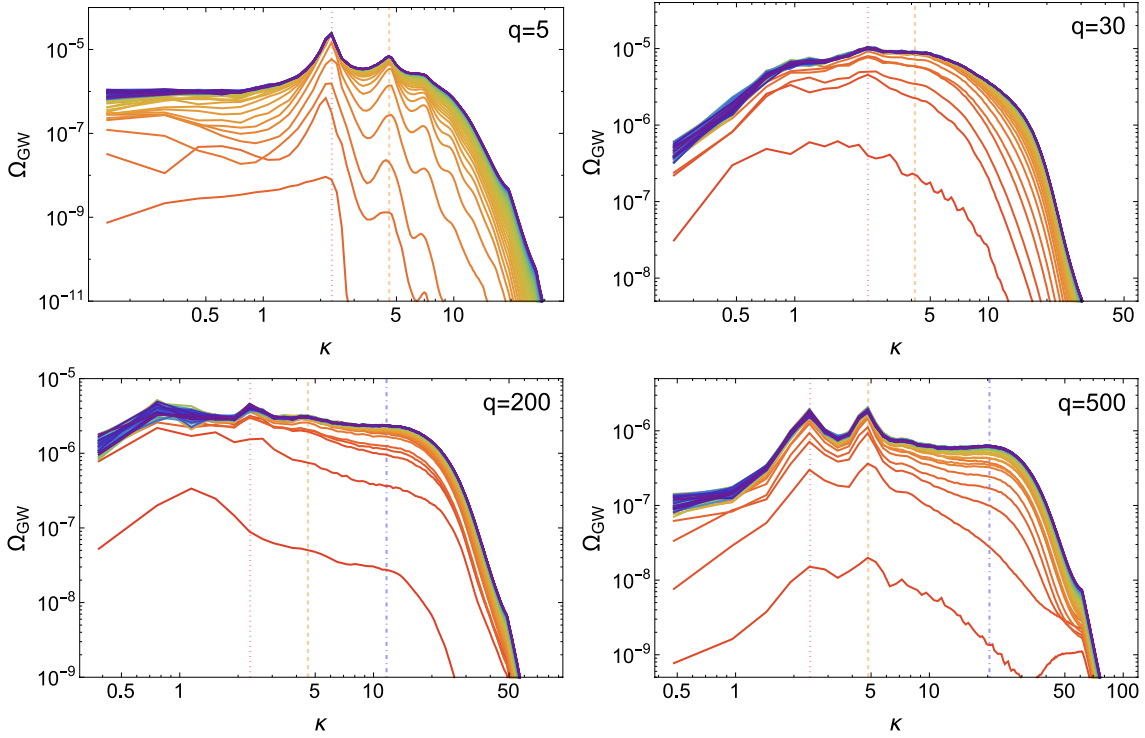
Figure 3.3.: Numerical spectra of GW $\Omega_{GW}(\kappa, z)$, Eq. (3.28), as a function of the momentum $\kappa \equiv k/(\sqrt{\lambda}\phi_i)$, for the resonance parameters $q = 5$, $q = 30$, $q = 200$ and $q = 500$. In all panels, the spectra go from red at early times, to purple at late times, measured at regular intervals $\Delta z = 10$, from $z = 10$ up to $z = 690$. The vertical lines indicate the position of the peaks in the final saturated spectra, with the red dotted, yellow dashed, and blue dot-dashed lines indicating the position of κ_1, κ_2, and κ_{hb} respectively (see bulk text).

Let us note that certain peaks emerge in the GW spectra during its evolution towards saturation, and some of these remain as features in the final saturated spectra (whereas others disappear). As seen in the EOM of the GW (3.26), GW are sourced by the matter fields, or more specifically, by their gradients. Therefore, one should be capable to explain the origin of the peaks in the GW spectra, in terms of the dynamics of the matter fields in momentum space. For this, let us us look at Fig. 3.4, where we show both the matter and GW spectra for two different resonance parameters, $q = 5$ and $q = 300$, at different times.

Let us focus first in the case $q = 5$ shown in the top two panels of Fig. 3.4. The first spectra in the left-top panel is measured at $z = 70$ ($< z_{br} \approx 80$), when the backreaction effects from the daughter field have not yet affected significantly the inflaton homogeneous condensate. As expected, the daughter field is excited inside its main resonance band, while the inflaton fluctuations are still sub-dominant. At this time, the GW amplitude is of the order $\Omega_{GW} \sim \mathcal{O}(10^{-9})$, as shown by the first spectra in the top-right panel. The second spectra in the top-left panel is measured at the time $z = 105$ ($> z_{br} \approx 80$), some time after the onset of backreaction, when the dynamics of the system is already fully non-linear. At that moment,
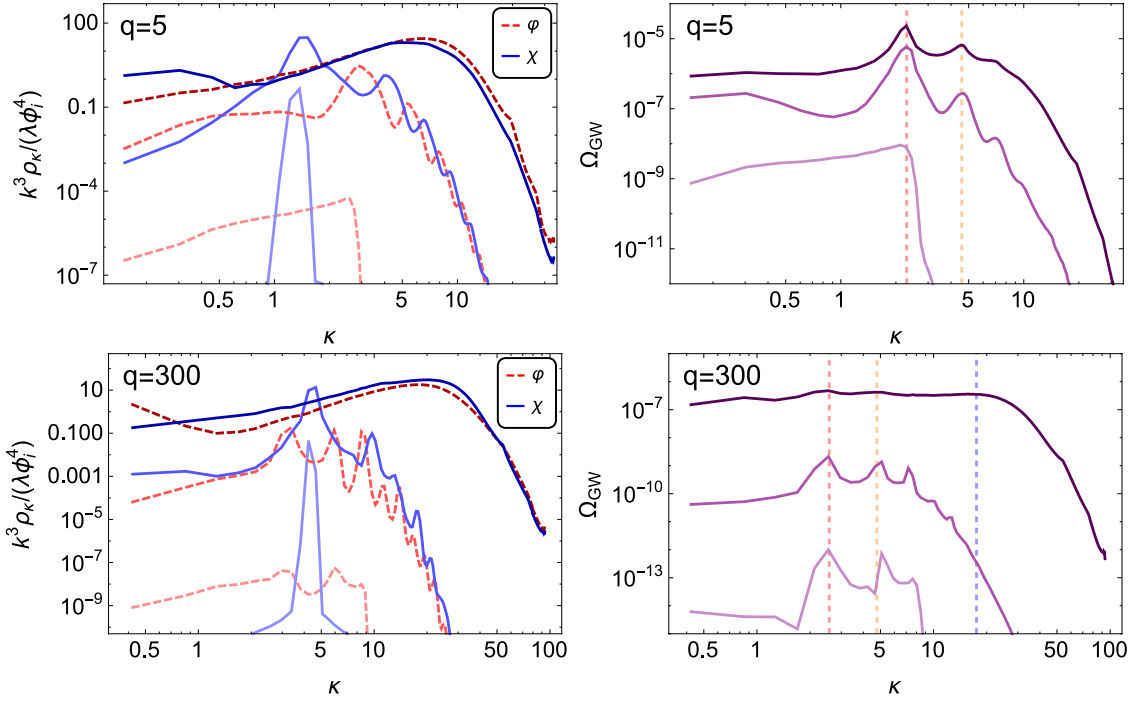
Figure 3.4.: In the top-left panel we show, for $q = 5$, the energy density spectra of the inflaton and daughter fields [Eq. (3.24)] at times $z = 70, 105, 340$. The same spectra are shown in the bottom-left panel for the same times, but for the resonance parameter $q = 300$. The right panels show the corresponding GW spectra at the same times. We also show here with dashed vertical lines the position of the peaks in the final saturated spectra: κ_1 in red, κ_2 in orange, and κ_{hb} in blue (explanations for these quantities are given in the bulk text).

we can observe two important features in the field spectra: first, the spectral amplitude of the inflaton and daughter fields have become comparable for all modes, and second, a detailed structure of peaks have appeared in both spectra. Such structures get imprinted in the GW spectra, which also show different peaks, whose position is correlated with the one of the peaks of the matter fields. The amplitude of the corresponding GW spectra has become much larger at this time, of the order $\Omega_{GW} \sim \mathcal{O}(10^{-6})$ at its maximum. Finally, the last spectra in the top-left panel are measured at time $z = 340$ ($> z_{\text{dec}} \approx 160$). At this time, the initial peaks in the matter spectra have disappeared. Moreover, due to the mode-to-mode coupling generated by the non-linearities of the system, both spectra have transferred power to higher modes, developing a peak at shorter scales with a characteristic *hunchback* shape. Correspondingly, the GW spectral power has also moved towards the UV, and its amplitude has gained a final order of magnitude growth, with the maximum reaching up to $\Omega_{GW} \sim \mathcal{O}(10^{-5})$. Let us remark that even though the structure of peaks is partially maintained in the final spectrum of GW (specifically, the peaks indicated with red and orange vertical dashed lines), it is also partially washed out, as the peaks at the shorter scales are smoothed-out.

A similar analysis can be done for the case $q = 300$, shown in the lower panels of Fig. 3.4. In the bottom-left panel we show the spectra of the matter fields, again for times $z = 70, 105, 340$. As in the previous $q = 5$ case, we observe a couple of peaks that are generated during the initial dynamics of the system. We indicate these peaks with red and orange dashed lines in the figure. We can clearly see that these peaks are still maintained in the last spectra, at $z = 340$ ($> z_{dec} \approx 160$). On the other hand, as observed in the bottom-right panel, the largest amplitude of the final saturated GW spectra [shown again at the time $z = 340$] is of the order $\Omega_{GW} \sim \mathcal{O}(10^{-6})$. The main difference with respect to the previous case $q = 5$, is that now the 'displacement' of the matter spectra towards the UV, creates an additional peak in the GW spectra at short scales, with the same *hunchback* shape as for the matter fields. This peak is indicated with a blue dashed line in the GW spectra shown in the lower panels of Fig. 3.3 and right-bottom panel of Fig. 3.4. This peak is absent for lower values of q, like those in the top panels of Fig. 3.3 and right-top panel of Fig. 3.4. The hunchback peak is clearly generated during the late dynamics of the system, due to the mode-to-mode coupling between short and long modes, when the system is fully non-linear.

The location of the *hunchback* peak grows monotonically with q, and hence only when q is sufficiently large, it becomes a well separated peak from the other more IR peaks. Phenomenologically, we have found that such threshold is precisely $q \gtrsim 60$. On the other hand, the IR peaks in the GW spectra are, remarkably, always placed at the same position, independently of q (see location of red and yellow dashed vertical lines in Figs. 3.3 and 3.4).

Let us try to explain the origin and q-dependence of these peaks. As said, we observe IR peaks at fixed scales, plus an extra peak in the UV at a q-dependent scale. We think this is due to a combination of effects: on the one hand, the daughter field spectrum is peaked at $\kappa \sim q^{1/4}$, as we already discussed and quantified in Eq. (3.25). As we also discussed and quantified in Eq. (3.25), the large and rapidly growing amplitude of the daughter fluctuations 'drags', via the interaction term, the inflaton fluctuations at the same scale $\kappa \sim q^{1/4}$. Secondly, at the same time, the inflaton, due to its own self-interactions, possesses a self-resonance for $q = 3$ [26]. Thus, the inflaton fluctuations start growing at some fixed IR scales due to its self-resonance, and the inflaton spectrum develops a structure of peaks, located always at the same scales, independently of q. However, since the two fields are coupled, the interaction term between them, leads eventually to the development of the same pattern of peaks in both daughter and mother field spectra. This happens mostly when the system becomes fully non-linear around $z \gtrsim z_{br}$, so it is hard to develop an analytical description of it. However we note that, phenomenologically, we always observe this effect, independently of the value of q. For instance, this is clearly seen in the spectra at time $z \approx 105$, plotted in the top-left and bottom-left panels of Fig. 3.4. As a consequence, the GW spectrum ends also exhibiting some peaks in the IR at fixed positions. On the other hand, if the resonance parameter is sufficiently large ($q > 60$), then also a hunchback peak appears in the GW spectrum, at shorter scales. The hunchback
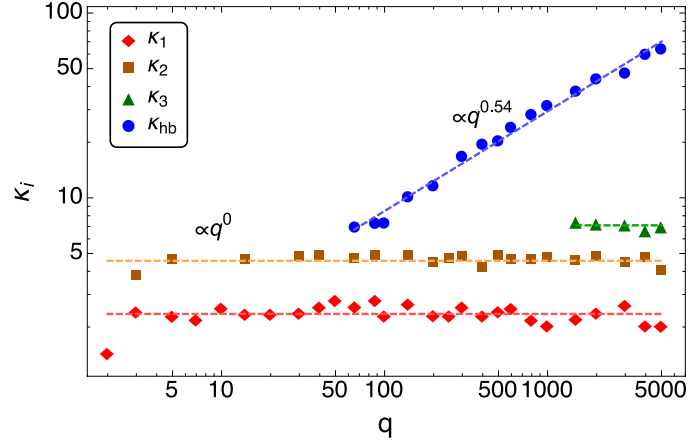
Figure 3.5.: Left: We show the position $\kappa_i \equiv k_i/(\sqrt{\lambda}\phi_i)$ of the different peaks in the saturated GW spectra, for the peaks κ_1 (red diamonds), κ_2 (orange squares), κ_3 (green triangles), and κ_{hb} (blue circles). The dashed lines indicate the fits Eqs. (3.29)-(3.32) to these quantities.

peak becomes prominent mostly when the system becomes non-linear at $z \gtrsim z_{br}$. We expect that, due to the non-linear interactions among modes, the q-dependence of the location of the hunchback peak may differ from the linear prediction. Presumably, given that it grows out of the initial peak developed at $\kappa \sim q^{1/4}$, it will still depend on q. However, given that it evolves significantly during to the non-linear stages of the system, some new q-dependence will most likely arise. Only by fitting the outcome of our simulations, we can figure out the final q-dependence of the hunchback peak.

In light of the discussion above, we proceed to parametrize the peaks in the final GW spectra $\Omega_{GW}^{(f)}$, as a function of the resonance parameter q. Our main results are presented in Figs. 3.5 and 3.6. Let us start with Fig. 3.5, where we show the position of the peaks in the GW spectra, as obtained from the lattice simulations. We first observe two peaks, the location of which we denote as κ_1 and κ_2, whose position is clearly independent on the choice of q. These peaks appear for the whole range of resonance parameters simulated ($q \in [1, 5000]$), although in some cases the scales or the two peaks are so near that only one of them can be distinguished. These peaks are formed during the initial linear regime of the system, as described in the previous paragraph. An additional third peak is also observed in the (few) simulations done for $q \gtrsim 1000$, whose position is also independent on the particular choice of q. We denote the location of this peak as κ_3. We have fitted the position of these IR peaks as

$$\kappa_1 \approx 2.4 \pm 0.3, \tag{3.29}$$

$$\kappa_2 \approx 4.6 \pm 0.3, \tag{3.30}$$

$$\kappa_3 \approx 7.1 \pm 0.3, \quad (q \gtrsim 1000), \tag{3.31}$$

with the error indicating some random scattering with q.
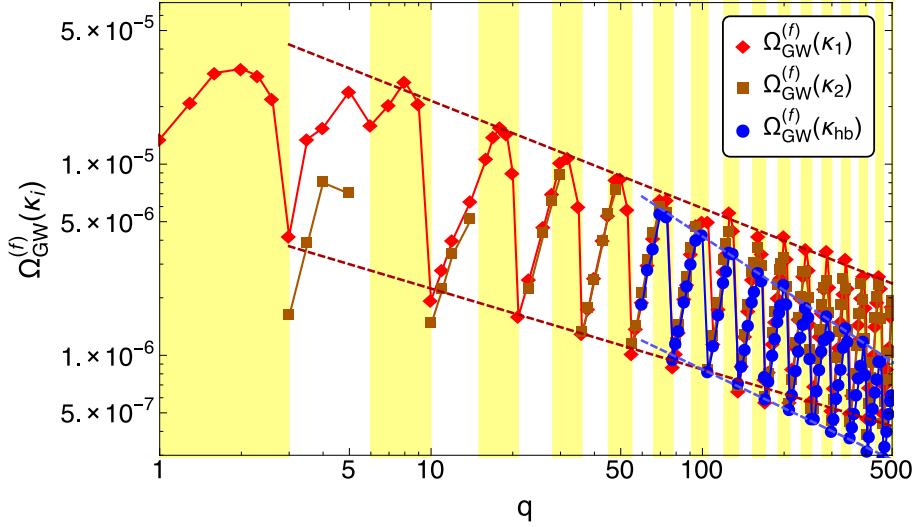
Figure 3.6.: We show the amplitude of the GW spectra $\Omega_{GW}^{(f)}$ at peaks κ_1 (red diamonds), κ_2 (orange squares), and κ_{hb} (blue circles), as a function of q, in the interval $1 < q < 500$. The yellow vertical bands indicate the values of q in which the main resonance band of the corresponding *Lamé* equations is of the type $0 < \kappa < \kappa_+$. The diagonal dashed lines indicate the upper and lower bounds, whose fit we provide in Eqs. (3.33)-(3.34).

On the other hand, for $q \gtrsim 60$ we observe an additional peak in the spectra, with its location growing monotonically with q. This is the peak with a *hunchback* shape that we reported before, for instance for the case $q = 300$ shown in the right-bottom panel of Fig. 3.4. This peak emerges visibly in the GW spectrum during the non-linear dynamics of the system. We denote its position as κ_{hb}, and we find the following power-law fit in the range $q \gtrsim 60$,

$$\kappa_{hb} \approx 8.5 \left(\frac{q}{100} \right)^{0.54} , \quad (q \gtrsim 60) . \tag{3.32}$$

As said, for $q \lesssim 60$, we cannot differentiate this peak from the others. The location of the hunchback peak depends on q, but as expected, it does not scale accordingly to the linear theory as $\sim q^{1/4}$. It rather scales as $\kappa_{hb} \sim q^{1/2}$, demonstrating – as argued above – that the non-linear dynamics changes the location of this peak in a non-trivial way. The monotonic dependence on q implies that the GW spectra exhibit a clear separation between IR and UV scale features, which grows with the strength of the interaction coupling. This is, in fact, one of the main reasons why it is unfeasible to simulate systems with arbitrarily large resonance parameter above $q \gtrsim 10^4$. Besides, the reason for κ_3 to only appear when q is sufficiently large becomes now clear: only for $q > 10^3$, the hunchback peak is separated enough in the UV, so that its IR tail does not exceed the amplitude of the peak κ_3.

Let us now analyze how the amplitude of these peaks depend on the resonance parameter. In Fig. 3.6 we show the GW amplitudes $\Omega_{GW}^{(f)}(\kappa_1)$, $\Omega_{GW}^{(f)}(\kappa_2)$ and $\Omega_{GW}^{(f)}(\kappa_{hb})$ as a function of q in

the interval $1 < q < 500$, obtained directly from lattice simulations. We have also indicated, with yellow bands, the values of q for which the main resonance band is of the type $0 < \kappa < \kappa_+$, where the resonance is stronger (i.e. $q \in [1,3], [6,10], \cdots$).

First, we observe that $\Omega_{\mathrm{GW}}^{(\mathrm{f})}(\kappa_{\mathrm{hb}})$ follows a clear oscillatory pattern, with a dependence on q correlated with the structure of resonance bands of the Lamé equation. This was clearly expected, as the strength of the resonance of the daughter field determines the strength of the source of the GW, and consequently the strength of the GW final amplitude. Interestingly, both $\Omega_{\mathrm{GW}}^{(\mathrm{f})}(\kappa_1)$ and $\Omega_{\mathrm{GW}}^{(\mathrm{f})}(\kappa_2)$ also follow the same oscillatory pattern, correlated again with the structure of resonance bands of the Lamé equation. Quite remarkably, the IR structure of peaks developed in the GW spectrum is then such that: on the one hand, the location of the peaks is fixed (as determined initially by the inflaton resonance bands for $q = 3$), while on the other hand, the amplitude of the peaks is modulated by the strength of the resonance of the daughter field, as dictated by the *Lamé* equation (for the given resonance parameter q). In other words, for the IR peaks, the GW production becomes stronger (larger amplitude) the stronger the resonance of the daughter field is. Let us note that, even though $\Omega_{\mathrm{GW}}^{(\mathrm{f})}(\kappa_2)$ follows the same oscillatory pattern as $\Omega_{\mathrm{GW}}^{(\mathrm{f})}(\kappa_1)$, for values $q \lesssim 50$ it can be difficult to differentiate the two peaks, and hence the smaller number of data points associated to κ_2 in both Figs. 3.5, 3.6.

In all cases, the peak amplitudes Ω_{GW} decay with q. In particular, the upper and lower envelopes of the oscillatory pattern of the Ω_{GW} peak amplitudes, can be fitted as a decaying power-law with q. The decaying behavior of the amplitude is expected from the analytical prediction in Eq. (3.22). The exponent of the power-law decay differs however from the analytical result $\Omega_{\mathrm{GW}} \propto q^{-1/2}$. We have fitted the upper and lower envelopes of the amplitude oscillations, from the numerical data measured at the relative maxima and minima. The fits are

$$8.4 \cdot 10^{-7} \left(\frac{q}{100}\right)^{-0.42} \lesssim \Omega_{\mathrm{GW}}^{(\mathrm{f})}(\kappa_1, \kappa_2) \lesssim 5.9 \cdot 10^{-6} \left(\frac{q}{100}\right)^{-0.56} , \quad (q > 1) , \quad (3.33)$$

$$8.4 \cdot 10^{-7} \left(\frac{q}{100}\right)^{-0.68} \lesssim \Omega_{\mathrm{GW}}^{(\mathrm{f})}(\kappa_{\mathrm{hb}}) \lesssim 4.2 \cdot 10^{-6} \left(\frac{q}{100}\right)^{-0.94} , \quad (q > 60) . \quad (3.34)$$

Note that we find $\Omega_{\mathrm{GW}}^{(\mathrm{f})}(\kappa_2) \approx \Omega_{\mathrm{GW}}^{(\mathrm{f})}(\kappa_1)$ (when κ_2 can be distinguished from κ_1), while the amplitude of the peak κ_3 is observed to be $\Omega_{\mathrm{GW}}^{(\mathrm{f})}(\kappa_3) \approx 10^{-7}$, i.e. always sub-dominant with respect the peaks at κ_1 and κ_2.

As the analytical prediction $\frac{d \log \Omega_{\mathrm{GW}}}{d \log q} = -\frac{1}{2}$ is based on the linear regime analysis, it is not surprising that the real dependence of the GW amplitudes at the saturation time, bounded by Eqs. (3.33)-(3.34), differs from it. Yet, it is nice to observe that the GW amplitudes follow, at least, a decaying power-law with q. The deviation of the measured exponents $-0.42 \lesssim \frac{d \log \Omega_{\mathrm{GW}}}{d \log q} \lesssim -0.94$ with respect to the linear prediction -0.5 is attributed to the non-linear dynamics, and could have not been predicted *a priori* without numerical simulations.

We can now redshift the amplitude and position of the GW peaks. Using Eq. (3.17) we obtain the following frequencies today

$$f_p = \kappa_p \times 6 \cdot 10^6 \text{ Hz} . \tag{3.35}$$

Substituting Eqs. (3.29)-(3.34) into Eq. (3.35), we obtain that the exact frequencies of the peaks today are

$$f_1 \approx 1.5 \cdot 10^7 \text{ Hz} , \tag{3.36}$$

$$f_2 \approx 2.8 \cdot 10^7 \text{ Hz} , \tag{3.37}$$

$$f_3 \approx 4.5 \cdot 10^7 \text{ Hz} , \quad (\text{only for } q \gtrsim 10^3) , \tag{3.38}$$

$$f_{\text{hb}} \approx \left(\frac{q}{100}\right)^{0.54} \times 5.3 \cdot 10^7 \text{ Hz} , \quad (\text{only for } q \gtrsim 60) . \tag{3.39}$$

Using Eq. (3.18) we also find that the redshifted amplitude(s) today of this background is $h^2\Omega_{\text{GW}}(f_p) \simeq 4 \cdot 10^{-6}\Omega_{\text{GW}}^{(\text{f})}(\kappa_p)$. This translates into the following (interval of) amplitudes for the measured peaks,

$$3.4 \cdot 10^{-12} \left(\frac{q}{100}\right)^{-0.42} \lesssim h^2\Omega_{\text{GW}}(f_{1,2}) \lesssim 2.4 \cdot 10^{-11} \left(\frac{q}{100}\right)^{-0.56} , \tag{3.40}$$

$$3.4 \cdot 10^{-12} \left(\frac{q}{100}\right)^{-0.68} \lesssim h^2\Omega_{\text{GW}}(f_{\text{hb}}) \lesssim 1.6 \cdot 10^{-11} \left(\frac{q}{100}\right)^{-0.94} . \tag{3.41}$$

These amplitudes are in perfect agreement with the background amplitudes computed in the past for this scenario in the case $g^2/\lambda = 120$, where it was also obtained $h^2\Omega_{\text{GW}} \sim 10^{-11}$ [107, 79, 117, 118].

Even though our analytical prediction in Eq. (3.23) was based on the linear analysis, we can still calibrate it based on the numerical outcome. In particular, we can use the highest GW signal, occurring at the local maxima of the oscillatory pattern in Fig. 3.6, to extract the parameters C^2 and δ characterizing the theoretical prediction. In particular, as $\epsilon_i = 1$, $\omega_*^2 \equiv \lambda\phi_i^2$, and $\rho_i \approx \frac{\lambda}{4}\phi_i^4$, from equating

$$\Omega_{\text{GW}}\big|_{\text{th}} \simeq 10^{-9} \times \epsilon_i C^2 \frac{\omega_*^6}{\rho_i m_p^2} q^{-\frac{1}{2}+\delta} = \Omega_{\text{GW}}\big|_{\text{num}} \simeq 1.6 \cdot 10^{-11} \left(\frac{q}{100}\right)^{-0.94} , \tag{3.42}$$

we deduce,

$$\delta \gtrsim -0.44 , \quad \text{and} \quad C \simeq \frac{0.61}{\lambda} \left(\frac{m_p}{\phi_i}\right) . \tag{3.43}$$
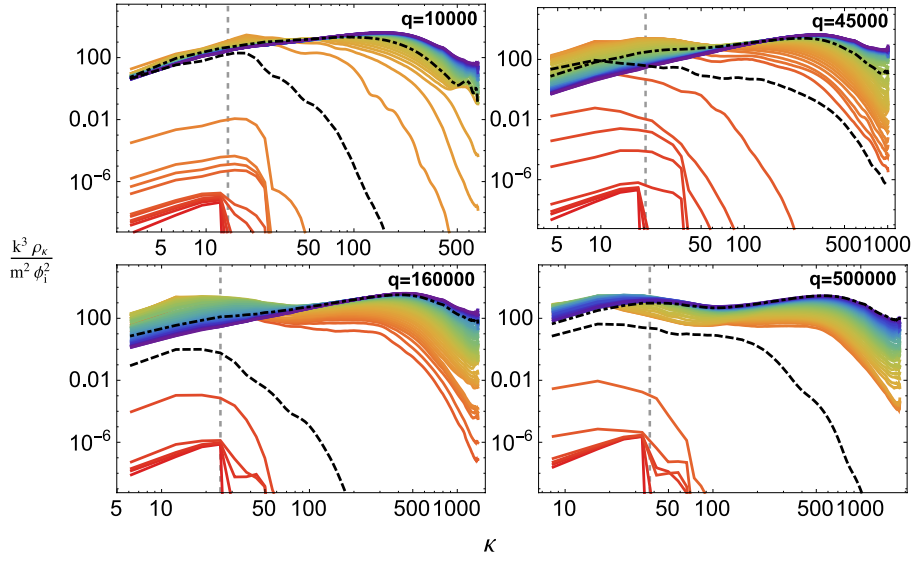
Figure 3.7.: We show the time-evolution of the daughter-field energy density spectra $\rho_{\kappa,\chi}$ [Eq. (3.44)] as a function of the momentum, for the resonance parameters $q = 10000, 45000, 160000, 500000$. The spectra are measured at equally spaced times $z = 10, 20, \ldots$, with red lines corresponding to early times, and purple lines to late times (after a stationary regime has been established). The gray, vertical dashed lines indicate the position of the maximum momentum excited according to the linear analysis, which scales as $\propto q^{1/4}$. We also show with black dashed and dot-dashed lines the spectra at times $z \approx z_{\mathrm{br}}$ and $z \approx z_{\mathrm{dec}}$.

3.4. Lattice simulations: gravitational waves from preheating with quadratic potential

We switch now to study the production of GW during preheating with quadratic potential, $V_{\mathrm{inf}}(\phi) = \frac{1}{2}m^2\phi^2$, in the case where the inflaton is coupled to another scalar daughter field with coupling $g^2\phi^2X^2$. We have done real-time classical lattice simulations of the preheating process, and computed the associated GW production. Our simulations have been done in lattice cubes of $N^3 = 256^3$ points, and their size has been chosen so that the lattice captures all the relevant momenta for the dynamics. We have run simulations varying the resonance parameter within the interval $q_{\mathrm{i}} \in [6 \cdot 10^3, 10^6]$.

We will parametrize the GW production from preheating with quadratic potential below. However, before moving on, let us briefly analyze and parametrize the matter field spectra in this scenario. In Fig. 3.7 we plot the time-evolution of the energy density spectra of the daughter field as a function of the momentum,

$$k^3\rho_{k,\chi} = \frac{m^2\phi_{\mathrm{i}}^2}{2}\kappa^3 a \left(|\chi_\kappa' - \frac{a'}{2a}\chi_\kappa|^2 + \omega_{\kappa,\chi}^2|\chi_\kappa|^2 \right) \,, \quad \omega_{\kappa,\chi} = \sqrt{\frac{\kappa^2}{a^2} + \frac{4}{a^3}q_i\varphi^2} \,, \quad (3.44)$$
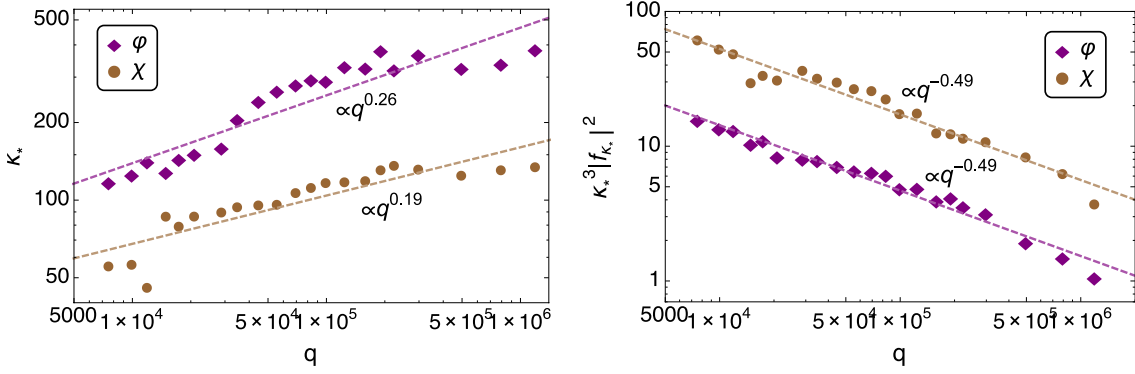
Figure 3.8.: We plot, for the inflaton and daughter fields, the position of the peak κ_* in the spectra after saturation as a function of q (left panel), and the corresponding amplitude $\kappa_*^3|f_{\kappa_*}|^2$ ($f = \varphi, \chi$) (right panel). Dashed lines in both panels correspond to the fits in Eq. (3.45).

for four different resonance parameters. We have highlighted the spectra at times z_{br} and z_{dec} with dashed black lines. As expected, we clearly observe that before $z \lesssim z_{\mathrm{br}}$, the excitation of the field modes occurs mainly inside the resonance band $\kappa < \kappa_{\mathrm{M}} \propto q_i^{1/4}$, while for $z \gtrsim z_{\mathrm{br}}$ the system becomes non-linear and power is transferred to higher modes in the UV. At $z \approx z_{\mathrm{dec}}$, the spectra have already saturated, as the fields have just reached a stationary regime, and hence do not source GW anymore. During the process, only a single peak emerges in the matter spectra, and consequently, only a single peak is expected in the GW spectra. In Fig. 3.8 we show the position κ_* where a peak appears in the fields spectra $\kappa^3|f_\kappa|^2$ (left panel), as well as the corresponding peak amplitude $\kappa_*^3|f_{\kappa_*}|^2$ (right panel), obtained from our lattice simulations for different choices of q. We obtain the following fits for these quantities,

$$\text{Daughter field } \chi: \quad \kappa_* \approx 69 \left(\frac{q_i}{10^4}\right)^{0.19}, \quad \kappa_*^3|\chi_{\kappa_*}|^2 \approx 53 \left(\frac{q_i}{10^4}\right)^{-0.49},$$

$$\text{Mother field } \varphi: \quad \kappa_* \approx 136 \left(\frac{q_i}{10^4}\right)^{0.26}, \quad \kappa_*^3|\varphi_{\kappa_*}|^2 \approx 14 \left(\frac{q_i}{10^4}\right)^{-0.49}. \quad (3.45)$$

As in the case of a quartic inflationary potential, the expected power-law scaling $\propto q_i^{-1/2}$ for the daughter spectral peak holds also quite well (within the sampling), with a deviation of the mean exponent with respect the theoretical prediction of only $100 \times \frac{|0.49-0.5|}{0.5} \sim 2\%$. The theoretical location of the daughter field's peak at $\kappa_* \sim q_i^{1/4}$ is however only realized with a correction (of the exponent) of $100 \times \frac{|0.19-0.25|}{0.25} \sim 24\%$. The fact that the location of the peak of the daughter field spectra deviates to some extent from the theoretical expectation is actually expected, as strictly speaking such prediction is only valid when the linear regime applies. The spectra fitted in Eq. (3.45) are however measured at $z \simeq z_{\mathrm{dec}}$, after the system went non-linear. The fact that the amplitude of the spectrum follows so well the theoretical scaling as $\propto q_i^{-1/2}$ is certainly remarkable.

Analogously to the quartic case, the mother field φ also follows a similar scaling as the daughter field. The (mean value of the) peak position of the mother field spectra is actually located almost exactly at the theoretical expectation $\sim q_i^{1/4}$, whereas the exponent of the spectral peak amplitude presents only a deviation of $100 \times \frac{(0.49-0.5)}{0.5} \sim 2\%$. This can only be explained, again, due to the coupling between the daughter and the mother fields: slightly before $z \simeq z_{\mathrm{br}}$, when the daughter field mode amplitudes have grown significantly (following the linear analysis resonance), the modes of the mother field become excited through the interaction term. This 'dragging' effect excites exactly the same inflaton modes as in the daughter field spectra.

3.4.1. Gravitational wave parametrization

We now proceed to study the GW production in the quadratic potential model. To do so, let us define a rescaled GW field as $\bar{h}_{ij} \equiv a^{3/2} h_{ij}$. The EOM of the GW, Eq. (3.2), can then be written as

$$\bar{h}_{ij}'' - \nabla_y^2 \bar{h}_{ij} - \left(\frac{3}{4} \frac{a'^2}{a^2} + \frac{3}{2} \frac{a''}{a} \right) \bar{h}_{ij} = \frac{2\phi_i^2}{m_p^2 a^{7/2}} (\partial_i \varphi \partial_j \varphi + \partial_i \chi \partial_j \chi)^{\mathrm{TT}} . \tag{3.46}$$

The total energy ρ_t of the system contributed by the matter fields (the contribution from the GW is negligible) is

$$\rho_t = \frac{m^2 \phi_i^2}{2a^3} \times \left[\sum_{f=\varphi,\chi} \left(f' - \frac{3}{2} \frac{a'}{a} f \right)^2 + \frac{1}{a^2} \sum_{f=\varphi,\chi} |\nabla_y f|^2 + \left(1 + \frac{4q}{a^3} \chi^2 \right) \varphi^2 \right] \equiv \frac{m^2 \phi_i^2}{2a^3} E_t . \tag{3.47}$$

The amplitude of the stochastic background of GW is then, from Eq. (3.6),

$$\Omega_{\mathrm{GW}}(k,z) = \frac{1}{\rho_t} \frac{d\rho_{\mathrm{GW}}}{d\log k}(k,z) = \frac{m_p^2}{\phi_i^2} \frac{(m\kappa)^3}{4\pi^2 V E_t(z)} \int \frac{d\Omega_k}{4\pi} \left| \bar{h}_{ij}' - \frac{3}{2} \mathcal{H} \bar{h}_{ij} \right|^2 . \tag{3.48}$$

In the top panels of Fig. 3.9 we show the time-evolution of the GW spectra produced during preheating, for the cases $q_i = 2.1 \cdot 10^4$ and $q_i = 10^5$. We observe that the initial fluctuations imposed in the matter fields generate an initial GW amplitude of the order $\Omega_{\mathrm{GW}} \sim 10^{-22}$. During the subsequent preheating stage, the amplitude grows fifteen orders of magnitude, saturating at an amplitude of the order $\Omega_{\mathrm{GW}}^{(f)} \sim 10^{-6}$ at the end of GW production. During the GW creation there is a significant population of higher modes beyond the initial cut-off scale Eq. (2.48). Therefore, a significant displacement of the GW spectra towards UV scales occurs, as higher modes of the GW are also populated. During this displacement, a peak forms at a given scale $\kappa_p > \kappa_M$. We will refer to the final amplitude of this peak as $\Omega_{\mathrm{GW}}^{(f)}(\kappa_p)$. As the position of this peak cannot be properly observed in the top panels of Fig. 3.9, we have plotted the same spectra in the bottom panels, zooming in the last stages of GW production. The position κ_p
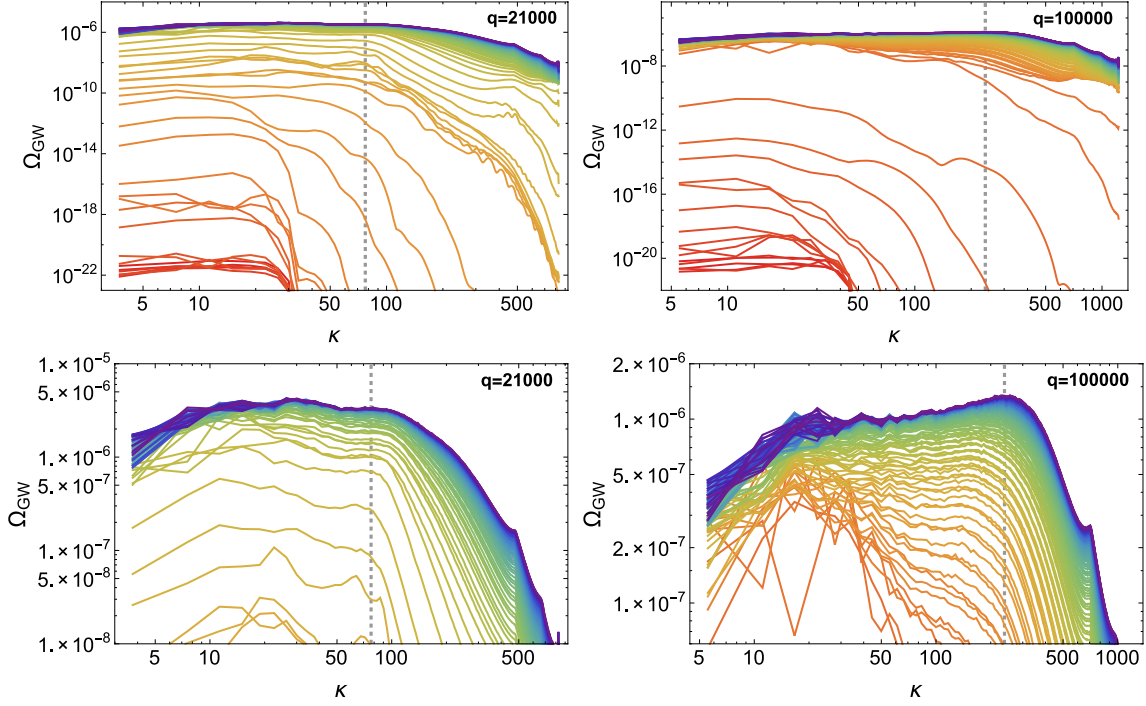
Figure 3.9.: The top panels show the time-evolution of the GW spectra $\Omega_{\mathrm{GW}}(\kappa, z)$ for the quadratic preheating model, for both $q = 21000$ (top-left) and $q = 100000$ (top-right). The spectra are depicted at times $z = 0, 5, 10, \ldots$, and go from red (early times) to blue (late times). The bottom panels show the same quantities, but zoomed to observe the peak better.

clearly indicates the transition from short to large momenta, so that for $\kappa > \kappa_p$, the amplitude of the GW spectra starts decreasing significantly. It constitutes therefore an estimate of the maximum momenta attained by the GW spectra, due to the population of UV modes outside the initial radius $\kappa \lesssim \kappa_M$, when the system becomes non-linear at $z \gtrsim z_{\mathrm{br}}$.

In Fig. 3.10 we show the position κ_p and amplitude $\Omega_{\mathrm{GW}}(\kappa_p)$ of the peak in the GW spectra, extracted from our lattice simulations for different values of q. We observe that as we increase q, the position of the peak κ_p in the saturated spectra moves to the UV, while the amplitude of the peak decreases. We have found the following fits to the peak amplitude and position,

$$\kappa_p \approx 48 \left(\frac{q}{10^4} \right)^{0.67}, \quad \Omega_{\mathrm{GW}}^{(\mathrm{f})}(\kappa_p) \approx 3.8 \times 10^{-6} \left(\frac{q}{10^4} \right)^{-0.43}. \tag{3.49}$$

Not surprisingly, we see that the linear prediction for the peak position at $\kappa_p \sim q^{1/4}$ is not well verified, given that the fit in Eq. (3.49) is measured after the system becomes non-linear and ceases to source GW. The mentioned shift of power into shorter scales by the matter fields, translates into a different q-dependence of the peak position $k_p \propto q^{2/3}$, which cannot be predicted with the linear theory. This is a direct result of the non-linearities in the system, and can only be obtained with numerical simulations like ours. At the same time, the amplitude of
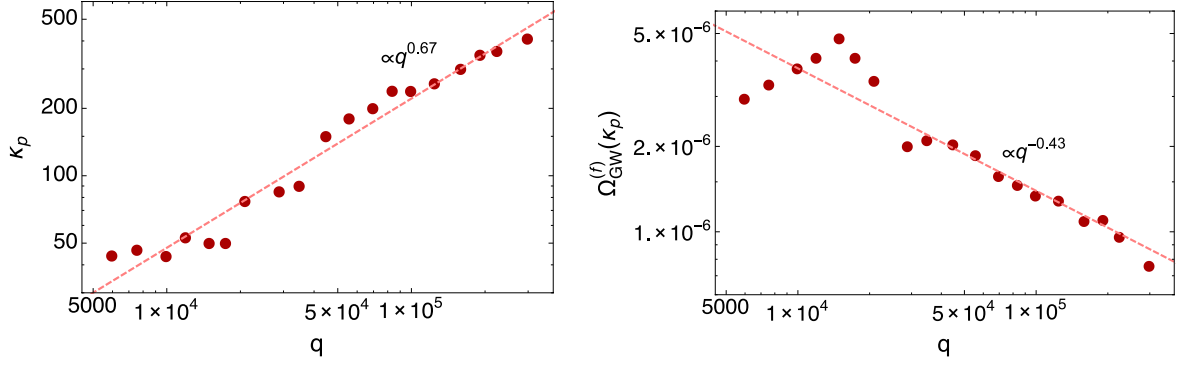
Figure 3.10.: We show, for the quadratic preheating model, the position of the peak κ_p in the saturated GW spectra (left panel) as a function of q, as well as its corresponding amplitude $\Omega_{\mathrm{GW}}^{(\mathrm{f})}(\kappa_p)$ (right panel). Each point corresponds to a lattice simulation. The fits to both quantities [Eq. (3.49)] are shown with dashed lines.

the peak approaches very well the theoretical scaling predicted by the linear theory $\frac{d\log\Omega_{\mathrm{GW}}}{d\log q} = -\frac{1}{2}$, with a deviation of the measured exponent of only $100 \times (|0.43 - 0.5|/0.5) = 14\%$. We believe the reason for this is that the scaling of the GW amplitude with q is set during the linear stage, when the GW grow exponentially fast due to the resonance of the daughter field. Hence, during the non-linear regime, the peak position is modified non-trivially from $\kappa_p \sim q^{1/4}$ to $\kappa_p \sim q^{2/3}$, but the amplitude receives only a boost that is independent of the resonance parameter q. This behavior is certainly remarkable, and certainly could not be anticipated by the linear theory.

Let us finally compute the redshifted GW spectra today. In this scenario, the post-inflationary expansion rate corresponds to a matter-dominated Universe [52], as the inflaton energy density after averaging over its oscillations, behaves as $\rho_\phi \propto 1/a^3$. The equation of state is then $\omega \simeq 0$, so the redshifting factor from Section 3.2, [defined in Eq. (3.16)], becomes

$$\epsilon_i \equiv \left(\frac{a_i}{a_{\mathrm{RD}}}\right) = \left(\frac{a_i}{a_f}\right)\epsilon_f, \qquad \text{with} \quad \epsilon_f \equiv \left(\frac{a_f}{a_{\mathrm{RD}}}\right). \tag{3.50}$$

From our simulations we measure directly the final time of GW production t_f, and hence determine the pre-factor (a_i/a_f), which is typically of the order of $\sim \mathcal{O}(10^{-2})$. Therefore, it is better to express the amplitude and frequency today, Eqs. (3.17)- (3.18), in terms of ϵ_f:

$$f \simeq \epsilon_f^{1/4}\left(\frac{k}{\rho_i^{1/4}}\right) \times 2.5 \cdot 10^9 \,\mathrm{Hz}\,, \qquad h^2\Omega_{\mathrm{GW}} \simeq 4 \cdot 10^{-6}\epsilon_f \times \Omega_{\mathrm{GW}}^{(\mathrm{f})}. \tag{3.51}$$

Plugging our fits in Eq. (3.49) into Eq. (3.51), we obtain

$$f_p = \epsilon_f^{1/4}\left(\frac{q}{10^4}\right)^{0.67} \times 2.0 \cdot 10^8 \,\mathrm{Hz}\,, \tag{3.52}$$

$$h^2\Omega_{\mathrm{GW}}(f_p) = \epsilon_f\left(\frac{q}{10^4}\right)^{-0.43} \times 1.5 \cdot 10^{-11}\,, \quad (q_i \gtrsim 6 \cdot 10^3)\,. \tag{3.53}$$

The longer the Universe takes to reach a RD stage, the smaller the factor ϵ_{f} is. This means that the longer the post-inflationary matter-dominated expansion phase lasts, the more the GW peak moves to the IR, but the more suppressed its amplitude becomes.

Based on the numerical outcome, we can calibrate our analytical prediction of Section 3.2. Knowing that $\omega_*^2 \equiv m^2$, and $\rho_i \simeq \frac{1}{2}m^2\phi_i^2$, we can extract the parameters C^2 and δ characterizing the theoretical GW amplitude in Eq. (3.23). In particular, equating

$$\Omega_{\mathrm{GW}}\big|_{\mathrm{th}} \simeq 2 \cdot 10^{-11} \times \epsilon_f C^2 \frac{m^4}{\phi_i^2 m_p^2} q_i^{-\frac{1}{2}+\delta} \quad = \quad \Omega_{\mathrm{GW}}\big|_{\mathrm{num}} \simeq \epsilon_f \left(\frac{q_i}{10^4}\right)^{-0.43} \times 1.5 \cdot 10^{-11} \,, \quad (3.54)$$

we deduce

$$\delta \simeq 0.06 \,, \quad \text{and} \quad C \simeq 6.3\left(\frac{m_p \phi_i}{m^2}\right) \,. \tag{3.55}$$

3.5. Gravitational waves from parametric resonance in spectator field scenarios

Finally, let us briefly consider gravitational wave production from parametric resonance scenarios, in the case where the energy of the mother and daughter fields are subdominant with respect the total energy of the Universe. This is the case, for example, of the curvaton scenarios discussed in Section 2.5, as well as the SM Higgs after inflation, analyzed in Part II.

The EOM of the GW Eq. (3.2), can be written symbolically as

$$\Box h_{**} = \frac{2}{m_p^2}\Pi_{**}^{\mathrm{TT}} \,, \qquad \Pi_{**}^{\mathrm{TT}} = \left\{\frac{\partial\phi}{\partial x^*}\frac{\partial\phi}{\partial x^*}\right\}^{\mathrm{TT}} \,, \tag{3.56}$$

where ϕ is some field involved in the process of parametric resonance. For the sake of the argument, let us consider ϕ as the mother field. This field will only start oscillating after inflation, when its (effective) mass becomes of the order of the Hubble rate $\sim H$. Let us denote ϕ_{i} as the initial amplitude of the oscillations. We can then 'parametrically' re-scale the source of GW as

$$\Pi_{**}^{\mathrm{TT}} \sim H^2\phi_{\mathrm{i}}^2 \times \left\{\frac{\partial\varphi}{\partial y^*}\frac{\partial\varphi}{\partial y^*}\right\}^{\mathrm{TT}} \sim H^2\phi_i^2 \,, \tag{3.57}$$

with $\vec{y} \equiv H\vec{x}$, $\varphi \equiv \phi/\phi_{\mathrm{i}}$, and where we have (crudely) estimated that $\{\frac{\partial\varphi}{\partial y^*}\frac{\partial\varphi}{\partial y^*}\}^{\mathrm{TT}} \sim (\Delta\varphi/\Delta y)^2 \sim \mathcal{O}(1)$, as within a spatial scale $\Delta y \sim \mathcal{O}(1)$, the field amplitude typically oscillates (in real space), and hence $\Delta\varphi \sim \varphi \sim \mathcal{O}(1)$. As crude as our estimation of $\{\frac{\partial\varphi}{\partial y^*}\frac{\partial\varphi}{\partial y^*}\}^{\mathrm{TT}}$ might be, this does not change the fact that the amplitude of the source of the GW is parametrically controlled

by $\propto H^2 \phi_i^2$. Thus, in order to estimate the GW production from a spectator field, we need to determine first the typical amplitude ϕ_i of such a field.

The amplitude of a spectator field excited during (pure *de Sitter*) inflation is [119]

$$\langle \phi^2 \rangle = \frac{3H^2}{8\pi^2} \left(\frac{H}{m}\right)^2 \left(1 - \exp\left\{-\frac{2}{3}\frac{m^2}{H^2}N\right\}\right) \longrightarrow \begin{cases} \frac{H^2}{4\pi^2}N \,, \ N \ll \frac{H^2}{m^2} \\[2mm] \frac{3H^4}{8\pi^2 m^2} \,, \ N \gg \frac{H^2}{m^2} \end{cases} , \qquad (3.58)$$

where we have implicitly assumed that the initial field amplitude (say at the onset of inflation) is zero, and the mass is bounded as $0 \leq m \ll H$. The typical amplitude of a strictly massless spectator field is then of the order of $\phi_{\rm rms} \simeq \mathcal{O}(1)H(N/100)^{1/2}$. In other words, $\phi_{\rm rms} \sim H$, modulo some mild dependence on the number of e-folds. For a massive but light field with $m < H$, after a (typically large) number of efolds $N \gg (H/m)^2$, the spectator field reaches its saturation amplitude $\phi_{\rm rms} \to \mathcal{O}(0.1)(H/m)H$.

Unless $N \ggg 1$ and $m/H \lll 1$, it is fair to say that the typical amplitude of a spectator field is, roughly speaking, $\phi \sim H$. Using this fact and Eq. (3.57), we conclude that the source of GW, in the case of a spectator field (with initially vanishing amplitude) is bounded as $\Pi_{**}^{\rm TT} \lesssim H^4$ (modulo some mild dependence on the number of efolds).

Let us note that $\Pi_{**}^{\rm TT} \lesssim H^4$ is in reality an upper bound because in reality, the initial source of GW in any process of parametric resonance, are the daughter field(s) rather than the mother field. The mother field typically contributes to the GW production when it finally develops sizeable time-dependent gradients. This happens when the daughter field backreacts over the mother field, manifesting the truly non-linear nature of the field dynamics due to the coupling between the field species. The daughter fields, however, never become significantly more energetic than the mother field (see, for example, Figs. 2.4 and 2.7). Therefore, even though the parametrization of the GW source due to the daughter field(s) may differ from Eq. (3.57), Eq. (3.57) should still represent a good estimation of an upper bound for the GW source in a process of parametric resonance.

As the energy density spectrum of GW is proportional to $(\Pi_{**}^{\rm TT})^2$, see Eqs. (3.7), (3.8), we can estimate now the GW production of fields in parametric resonance when the mother field is a spectator field. More specifically, we can parametrically compare it to the GW production when parametric resonance is due to the oscillations of an inflaton. In the latter case, the estimation Eq. (3.57) also applies, though in this occasion the typical amplitude of the inflaton at the end of (large-field) inflation is $\phi_i \sim m_p$. The GW source of parametric resonance during inflationary preheating, using Eq. (3.57), is then bounded as $\Pi_{**}^{\rm TT} \lesssim m_p^2 H^2$. The ratio of the GW energy density produced by parametric resonance due to the oscillations of a spectator field, $\Omega_{\rm GW}^{(s)}$, to the GW energy density created (for the same daughter-mother coupling) by the oscillations of

an inflaton, $\Omega_{\rm GW}^{\rm (i)}$, can be parametrically estimated as

$$\frac{\Omega_{\rm GW}^{\rm (s)}}{\Omega_{\rm GW}^{\rm (i)}} \sim \frac{(\Pi_{**}^{\rm (s)})^2}{(\Pi_{**}^{\rm (i)})^2} \sim \left(\frac{H}{m_p}\right)^4 \ll 1 \,. \tag{3.59}$$

The GW production due to parametric resonance from a spectator field (with initially vanishing amplitude), can then only be much smaller than that of the analogous production from the parametric resonance of an inflaton field (with a large amplitude like in single-field slow-roll inflation). This result is actually expected, as the typical energy of a spectator field is always very sub-dominant compared to the inflaton energy. If the fraction of energy converted in GW in the process of parametric resonance is fixed by the daughter-mother coupling, it is therefore natural to expect that the absolute GW production from the parametric resonance of a spectator field, is very sub-dominant as compared to the analogous GW production from an inflaton field, as the latter exceeds the energy budget of the spectator field.

3.6. Summary

Preheating in the early Universe is expected to generate a large amount of gravitational waves (GW). The non-equilibrium dynamics of the fields after inflation develop energy gradients, which source very efficiently tensor perturbations. When the fields relax into a stationary state, the GW production ceases, and GW decouple and travel freely ever since, redshifting until now. One of the most paradigmatic situations is when the inflaton field exhibits a monomial potential as $V(\phi) \propto \phi^n$ after the end of inflation. Following the end of inflation, when the inflaton (mother field) oscillates around the minimum of its potential, it provides a non-adiabatic time-dependent mass to all field species (daughter fields) coupled to it. As a result, the fluctuations of such species grow exponentially in the process known as parametric resonance. This sources a significantly large background of GW.

In this chapter we have studied and parametrized the production of GW during parametric resonance in standard preheating scenarios. The dynamics of the matter fields is characterized in terms of the dimensionless resonance parameter q, which depends on the coupling strength, as well as on the initial amplitude and curvature potential of the mother field. We have carried out lattice simulations of two main scenarios where parametric resonance takes place: preheating with quartic $V(\phi) \propto \phi^4$ potential in Section 3.3 and preheating with quadratic $V(\phi) \propto \phi^2$ potential in Section 3.4. We have computed and parametrized the spectra of both GW and matter fields, and confronted the numerical results with analytical estimations.

In Section 3.3 we focused in the quartic case. We observed that there are two types of peaks imprinted in the GW spectra: infrared peaks located at fixed scales independently of q, and a higher frequency peak located at a scale $\kappa \sim q^{1/2}$. In all cases, the amplitude shows

a characteristic oscillatory pattern between $-0.42 \lesssim \frac{d \log \Omega_{\rm GW}}{d \log q} \lesssim -0.94$, depending on the strength of the resonance (which is determined by q). See Eqs. (3.33)-(3.34). In the range explored numerically of resonance parameters, $q \in [1, 5000]$, we find all peaks at around $f_p \approx \mathcal{O}(10^7) - \mathcal{O}(10^8)$ Hz, and the amplitude today as $h^2 \Omega_{\rm GW} \approx \mathcal{O}(10^{-11}) - \mathcal{O}(10^{-13})$. See Eqs. (3.40)-(3.41). In Section 3.4 we focused in the quadratic case. In this scenario we observe just a single peak in the GW spectrum, with an amplitude scaling with the resonance parameter as $\propto q^{-0.43}$. See Eqs. (3.52)-(3.53). The final position and amplitude of the spectrum today are however more uncertain than in the quartic case, as there is a dependence on the unknown duration of the period following the end of GW production, during which the universe maintains an expansion rate different than RD. Assuming that such period does not last for long after GW generation ceases, the redshifted amplitude can reach amplitudes today up to $h^2 \Omega_{\rm GW} \approx \mathcal{O}(10^{-11}) - \mathcal{O}(10^{-13})$ (for the simulated range $6000 \lesssim q \lesssim 2.5 \cdot 10^6$). For larger q's, as the amplitude decays as $\sim q^{-1/2}$, the signal becomes weaker and weaker.

One of the most remarkable results we have obtained is that the peak amplitudes of the GW background decrease with increasingly larger resonance parameters q. Naively, one would expect the opposite, as the larger the q, the broader the resonance. However, although more (daughter field) modes are excited for larger values of q, there is also less power transferred per mode: the daughter field spectrum may be wider, but it is also lower in amplitude. The two effects combine in such a way, that both the spectra of the fields, and of the GW, decrease in amplitude with increasingly bigger values of q. This is to be contrasted with the case when the daughter fields experiencing a parametric excitation (due to the oscillations of some coherent field) are either gauge fields [64, 65, 66, 67, 68, 69, 70, 71, 72] or fermions [29, 30, 31, 32, 33, 34, 120, 121, 122]. For both gauge and fermion species, it is found that the corresponding GW background scales as $\Omega_{\rm GW} \sim q^{3/2+\delta}$, with $\delta \ll 1$ some small correction. In the case of gauge bosons, this can be easily explained: even though they experience the same dynamics as scalar fields when coupled to an oscillatory (homogeneous) field (this is explicitly demonstrated in Chapter 4 for Abelian gauge fields), their anisotropic stress (i.e. the source of GW) has a different structure than in the scalar field case. We will see an example of this behaviour in Chapter 5, where we study the GW produced during the post-inflationary decay of the SM Higgs after inflation into gauge bosons. In the case of fermionic daughter fields, the theoretical analysis also predicts that $\Omega_{\rm GW} \sim q^{3/2}$ [121, 122].

As a final remark, let us note that there are scenarios of preheating where our analysis cannot be applied. The case of trilinear or non-renormalizable interactions between the mother and the daughter field(s) [81, 82, 83, 84] are not captured well by our fitted formulae. The case of oscillations of a multi-component field is neither captured by our analysis, see e.g. [85, 86, 87, 88, 89, 123]. Besides, there are also scenarios where the mechanism responsible for the particle production is not parametric resonance, e.g. tachyonic preheating [74, 75, 76, 77, 78, 79, 80, 67, 124], in which case our analysis does obviously not apply.

Part II.

Standard Model dynamics after inflation

Chapter 4.

Decay of the Standard Model Higgs field after inflation

In this chapter we study the non-perturbative dynamics of the standard model (SM) after inflation, in the regime where the SM is decoupled from (or weakly coupled to) the inflationary sector. We use classical lattice simulations in an expanding box in (3+1) dimensions, modelling the SM gauge interactions with both global and Abelian-Higgs analogue scenarios. We consider different postinflationary expansion rates. During inflation, the Higgs forms a condensate, which starts oscillating soon after inflation ends. Via nonperturbative effects, the oscillations lead to a fast decay of the Higgs into the SM species, transferring most of the energy into Z and W± bosons. All species are initially excited far away from equilibrium, but their interactions lead them into a stationary stage, with exact equipartition among the different energy components. From there on, the system eventually reaches equilibrium. We have characterized in detail, in the different expansion histories considered, the evolution of the Higgs and of its dominant decay products until equipartition is established. We provide a useful mapping between simulations with different parameters, from which we derive a master formula for the Higgs decay time as a function of the coupling constants, Higgs initial amplitude and postinflationary expansion rate.

Results presented in this Chapter have been published in Ref. [1].

4.1. Introduction

The discovery of the standard model (SM) Higgs in the *Large Hadron Collider* (LHC) [125, 126] initiated the quest for understanding its cosmological implications. The Higgs could have played different roles in the early Universe, depending for example on the running of the Higgs potential at large scales, or the existence of interactions between the Higgs and the inflationary sector or the scalar curvature. One interesting possibility is *Higgs-inflation*, where the SM Higgs

is the field responsible for the inflation of the Universe. In this case, the Higgs must have a non-minimal coupling to spacetime curvature, which is fixed by the amplitude of the CMB anisotropies [19].

In the following three chapters, we will rather explore a different route for the role of the Higgs during and after inflation. We will merely assume that inflation was driven by a very slowly evolving energy density, without specifying the nature of the field responsible for it. We will also assume that the SM Higgs is not coupled directly to the inflationary sector [127, 56, 55, 128]. Under these circumstances, the Higgs behaves during inflation as a spectator field living in a (quasi-)de Sitter background. Consequently, the Higgs fluctuates, with the effective potential of the Higgs ultimately dictating its behavior. If the instability scale of the Higgs potential is at sufficiently large energies, the Higgs field does not decay to the negative-energy vacuum during inflation, and forms a condensate with high amplitude. When inflation ends, the Higgs condensate starts oscillating around the minimum of its potential, and decays to the SM gauge bosons and fermions due to parametric effects.

In this chapter we investigate in detail the Higgs's decay into its most energetically dominant decay products, the SM electroweak gauge bosons, during the immediate stages following the end of inflation. This was previously studied in [55, 128], where analytical techniques were employed to study the same problem. In this thesis we use instead lattice simulations in an expanding box in (3+1) dimensions, modelling the SM interactions with global and Abelian-Higgs setups, which go beyond the assumptions behind any analytical calculation. Besides this, we also consider different Higgs initial amplitudes and postinflationary expansion rates. The analysis presented here will be followed, in Chapter 5, by an analysis of the gravitational waves produced during the Higgs decay process, based also on lattice simulations of an Abelian-Higgs setup. Afterwards, I will present in Chapter 6 a set of lattice simulations of the electroweak SU(2)× U(1) gauge sector of the SM, in order to quantify the effects on the non-Abelian interactions in the Higgs post-inflationary dynamics. Finally, I will discuss in Chapter 7 the effects of a non-minimal Higgs-curvature coupling in the Higgs and gauge post-inflationary dynamics, and its implications for vacuum stability after inflation.

This chapter is organized in such a way that we increase progressively the complexity of the different approaches used to describe the dynamics of the system, approximating the structure of the SM interactions better and better at each new step. In Section 4.2 we first present a brief analysis of the behavior of the Higgs after inflation, ignoring its coupling to the rest of the SM species. In Section 4.3 we switch on the coupling to the SM fields, but ignore the gauge nature of the interactions. We obtain analytical estimates for a later comparison with numerical simulations. In Section 4.4 we present the first set of lattice simulations, where we follow the Higgs and its decay products, yet under the assumption that the gauge nature of the SM interactions can be neglected. In Section 4.5 we finally incorporate gauge interactions into the simulations, by modelling the SM with an Abelian-Higgs setup. This is just an approximation

to the gauge structure of the SM, but the outcome of these simulations fully incorporates the nonlinear and nonperturbative effects of the SM, while considering the gauge nature of its interactions. In Section 4.6 we present a useful mapping between simulations with different parameters, from which we obtain a characterization of the Higgs decay width as a function of the coupling constants, initial Higgs amplitude, and postinflationary expansion rate. In Section 4.7 we summarize our results and conclude.

4.2. Higgs dynamics during and after inflation

In this section we consider the dynamics of the Standard Model Higgs during and after inflation. The relevant part of the SM Lagrangian is

$$S_{\mathrm{SM}} \supset \int d^4 x \sqrt{-g} \left(|D_\mu \Phi|^2 + \xi R |\Phi|^2 + V(\Phi) \right) , \qquad (4.1)$$

where g is the determinant of the spacetime metric, Φ is the Higgs field (a complex doublet), and D_μ is the gauge covariant derivative. We have also included a coupling of the Higgs to the scalar curvature $\xi R |\Phi|^2$, which is necessary for renormalization in curved spacetime. We will consider for the moment the minimal scenario $\xi = 0$, and postpone to Chapter 7 the discussion about the effects of such term in the Higgs dynamics[1]. The SM Higgs doublet can be parametrized in the unitary gauge by a single scalar real degree of freedom, $\Phi \equiv \varphi / \sqrt{2}$. The Higgs potential is, at tree level,

$$V(\Phi) \equiv \frac{\lambda}{4} (\varphi^\dagger \varphi - v^2)^2 , \qquad (4.2)$$

where $v \equiv 246 \mathrm{GeV}$ is the electroweak scale. In this thesis, we will always consider Higgs amplitudes $\varphi \gg v$, so we can safely ignore the vacuum term in Eq. (4.2).

When the theory is renormalized, the different coupling constants run with energy. Let us focus on the Higgs self-coupling. The renormalized-group-improved Higgs potential can be written as

$$V(\varphi) = \frac{\lambda(\varphi)}{4} |\varphi|^4 , \qquad (4.3)$$

where $\lambda(\varphi)$ is the renormalised Higgs self-coupling at the renormalization scale $\mu = \varphi$. The running behavior has been computed up to three loops in Minkowski spacetime [131, 132]. The running is very sensitive to the strong coupling constant α_s, the Higgs mass m_h, and the Yukawa top coupling y_t, the latter being currently the strongest source of uncertainty. We show in the

---

[1]In reality, when the theory is renormalized, $\xi = \xi(\mu)$ runs with energy, so it cannot be set exactly to 0 at all scales. For example, according to the calculation of Ref. [129] at one-loop level, a value $\xi(v) = 0$ at the electroweak scale $v \sim \mathcal{O}(10^2) \mathrm{GeV}$ corresponds to $\xi(H_*) \approx -0.03$ at the scale $H_* \sim 10^{14} \mathrm{GeV}$.
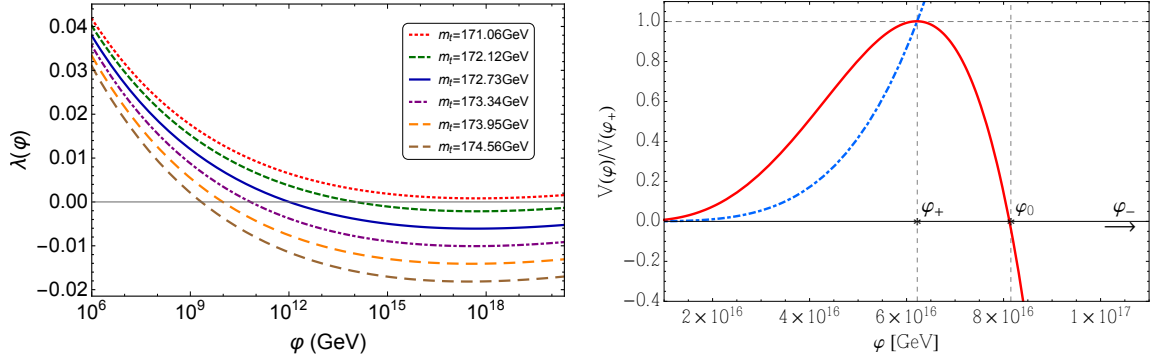
Figure 4.1.: Left: Running of $\lambda(\varphi)$ as a function of the Higgs field φ for $\alpha_s = 0.1184$, $m_h = 125.5$GeV, and different values of the top quark mass m_t, obtained from the public package provided in Ref. [130]. Right: Improved renormalized Higgs potential at next-to-next-to-leading order (red continuous line) computed for $\alpha_s = 0.1184$, $m_H = 125.5$ GeV, and $m_t = 171.2$ GeV. Also shown, from comparison, the function $\frac{1}{4}\lambda_+\varphi^4$ (blue dashed line), where $\lambda_+ \equiv \lambda(\mu_+) \simeq 3 \times 10^{-5}$.

left panel of Fig. 4.1 the running of $\lambda(\varphi)$ for the central values $\alpha_s = 0.1184$, $m_h = 125.5$GeV, and different values of the top quark mass. The figure has been obtained with the public package of [130]. We observe that, for top quark masses larger than $m_t \geq m_{t,c} \approx 171.1$GeV, the Higgs self-coupling (and hence the effective Higgs potential) becomes negative for amplitudes $\varphi > \varphi_0$, with φ_0 a certain scale. In the right panel of Fig. 4.1, we have plotted the Higgs potential for the particular case $m_t = 171.2$GeV $\geq m_{t,c}$. The effective potential develops a barrier at large field amplitudes, reaching a maximum height at some scale $\varphi = \varphi_+$, so that at higher energies $\varphi > \varphi_+$ the effective potential goes down, crosses zero at $\varphi = \varphi_0$, and becomes negative, possibly reaching a (negative) minimum at some scale $\varphi_- \gg \varphi_0$. We indicate the scales φ_+ and φ_0 for different choices of the top quark mass in Table 4.1. For the world-average top quark mass $m_t = 172.44^{\pm 0.13(\text{stat})}_{\pm 0.47(\text{syst})}$GeV [133], the instability scale is $\varphi_0 \approx 10^{11}$GeV. This may have important implications for the stability of the Higgs vacuum in the early Universe, because the Higgs field could achieve these amplitudes during or after inflation. However, for top quark masses $m_t < m_{t,c}$, the Higgs potential is positive at all scales, and there is not a second negative-energy vacuum at large amplitudes.

In this chapter and the next two ones, we will consider that the Higgs amplitude during inflation remains always in the 'safe' side of the effective potential, where $\lambda(\varphi)$ is positive. This can be guaranteed if φ_+ is sufficiently large compared to the inflationary scale, or alternatively, if beyond-the-SM physics stabilizes the potential at high energies. With these considerations, the Higgs fluctuates during inflation, like any light degree of freedom. The fluctuations then pile up at super-Hubble scales, creating a condensate [134, 119]. The amplitude of the Higgs condensate, however, does not grow unbounded with the numbers of e-folds, as it happens in the case of a massless free field. On the contrary, the Higgs self-interactions provide an effective (sub-Hubble) mass to the fluctuations, which eventually saturates the growth of the

m_t(GeV)	φ_+(GeV)	φ_0(GeV)
172.12	7.83×10^{11}	1.01×10^{12}
172.73	5.20×10^{10}	6.70×10^{10}
173.34	7.49×10^{9}	9.65×10^{9}
173.95	1.67×10^{9}	2.15×10^{9}
174.56	4.92×10^{8}	6.34×10^{8}

Table 4.1.: The values of the Higgs field where the potential Eq. (4.3) has a maximum (φ_+) and crosses zero (φ_0), obtained for $\alpha_s = 0.1184$, $m_h = 125.5$GeV, and different values of the top quark mass. These quantities have been obtained with the public package of [130].

condensate amplitude [54]. In particular, the Higgs amplitude during inflation reaches, within few e-folds, the equilibrium distribution [54]

$$P_{\rm eq}(\varphi) = \mathcal{N} \exp\left\{ -\frac{2\pi^2}{3} \frac{\lambda \varphi^4}{H_*^4} \right\}, \quad \mathcal{N} \equiv \frac{2^{\frac{1}{4}} \lambda^{\frac{1}{4}} \sqrt{4\pi}}{3^{\frac{1}{4}} \Gamma(\frac{1}{4}) H_*}, \tag{4.4}$$

where $H_* \gg v$ is the Hubble rate of inflation, characterized as a de Sitter period.

The correlation length, i.e. the physical scale above which the Higgs amplitude φ fluctuates according to Eq. (4.4), is given by $l_* \approx \exp\{3.8/\sqrt{\lambda}\} H_*^{-1}$ [54], so it is exponentially larger than the inflationary Hubble radius H_*^{-1}. After the equilibrium distribution is reached at some point during inflation, the correlation length remains invariant until the end of the exponential expansion. Hence, immediately after inflation, the Higgs amplitude φ can safely be considered homogeneous within any volume of size $l \ll l_*$. The Higgs amplitude varies randomly according to Eq. (4.4), but only at scales $l \gg l_*$, much larger than the correlation length.

A typical Higgs amplitude at the end of inflation is given by the *root mean square* (rms),

$$\varphi_{\rm rms} = \sqrt{\langle \varphi^2 \rangle} \simeq 1.15 \, H_* \left(\frac{0.01}{\lambda} \right)^{-1/4}. \tag{4.5}$$

For reasonable values $\lambda \in [10^{-2}, 10^{-5}]$ (see left panel of Fig. 4.1), the typical Higgs amplitudes are of the order $\varphi_{\rm rms} \sim H_*$. We do not know the actual value of φ within the 'progenitor' patch from which our visible Universe grew up. Actually, we do not know the value of the Higgs condensate within any patch, we just know that typically $\varphi/H_* \sim \mathcal{O}(0.01) - \mathcal{O}(1)$ for reasonable values of λ. That means that just after inflation, within any patch of size $l \lesssim l_*$, the Higgs has a nonzero amplitude that could be really large, almost as big as H_* depending on its realization. The most updated upper bound for the inflationary Hubble rate is [16]

$$H_* \le H_*^{\rm (max)} \simeq 8.4 \times 10^{13} \text{GeV},$$

so the Higgs amplitude at the end of inflation could be ranging around $|\varphi| \lesssim (10^{12} - 10^{14})$ GeV $\times (H_* / H_*^{(\text{max})})$.

Before moving on, let us note that we have not considered a coupling between the Higgs field and the inflationary sector. The need to reheat the Universe after inflation requires somehow a coupling between the SM and the inflationary sector, though there is no particular constraint on this. Therefore, effective operators are expected to connect the Higgs with the inflaton when integrating out some possible mediator field(s). However, as we will show in the following sections, the Higgs decays very fast after inflation into all SM species. Hence, even if there is a Higgs-inflaton effective coupling, we will assume in practice that its effects are negligible.

4.2.1. Higgs oscillations after inflation

The amplitude of the Higgs after inflation is nonzero, and given that the Higgs potential is symmetric, the Higgs condensate is forced to oscillate around its minimum at $\varphi = 0$. As we shall see, the larger the Higgs amplitude, the sooner the oscillations will start after the end of inflation. The EOM (equation of motion) of the Higgs just after inflation is

$$\ddot{\varphi} + 2\mathcal{H}\dot{\varphi} + a^2 \lambda \varphi^3 = \nabla^2 \varphi, \tag{4.6}$$

where $\cdot \equiv d/dt$, with t being conformal time, and $\mathcal{H} = \dot{a}/a$ being the comoving Hubble rate.

In order to analyze the dynamics of the Higgs after inflation, it is necessary first to fix the postinflationary expansion rate. Since we do not specify the nature of the inflationary sector here, we can parametrize the scale factor after inflation like

$$a(t) = a_* \left(1 + \frac{1}{p} a_* H_* (t - t_*) \right)^p, \qquad p \equiv \frac{2}{(1 + 3w)}, \tag{4.7}$$

with a_* being the scale factor at the initial time $t = t_*$ (i.e. at the end of inflation), and w being the equation of state of the Universe characterizing the expansion rate of the period following inflation[2]. For instance, if the inflationary sector is described by an inflaton with a quadratic potential, the Universe expands as in a matter-domination (MD) regime after inflation, so $w = 0$ and $p = 2$. If it is described by an inflaton with a quartic potential, the Universe expands as in a radiation-domination (RD) regime, with $w = 1/3$ and $p = 1$. We are also free to consider other possibilities, such as a kination-domination (KD) regime, with $w = 1$ and $p = 1/2$, obtained when an abrupt drop of the inflaton potential takes place at the end of inflation, transferring all

---

[2]Note that for $t \approx t_*$, there should be a transition period between (quasi) de Sitter and power-law expansion, which we do not take into account.

the energy into kinetic degrees of freedom [135, 136]. The Hubble rate is then given by

$$\mathcal{H}(t) \equiv \frac{\dot{a}}{a} = \frac{a_* H_*}{[1 + p^{-1} a_* H_* (t - t_*)]} \equiv \frac{a_* H_*}{\sqrt[p]{a(t)/a_*}} \, . \tag{4.8}$$

We will consider the evolution of the Higgs in an arbitrary patch, inside which its amplitude [randomly drawn from Eq. (4.4)] can be regarded as homogeneous. The correlation length is exponentially bigger compared to the Hubble radius, so if we just follow the Higgs within a causal domain of initial size $l \sim 1/H_* \ll l_*$, then we can drop the Laplacian term on the *rhs* of Eq. (4.6). It is convenient to define dimensionless conformal time and Higgs field variables as

$$z \equiv a_* H_* (t - t_*) \, , \quad h(z) \equiv \frac{a}{a_*} \frac{\varphi}{\varphi_*} \, , \tag{4.9}$$

with φ_* being the initial amplitude of the Higgs. The scale factor can then be written as $a(z) = a_* (1 + p^{-1} z)^p$. Hence, we can write the Higgs EOM in a more convenient form as

$$h'' + \beta^2 h^3 = \frac{a''}{a} h \, , \quad \beta^2 \equiv \frac{\lambda \varphi_*^2}{H_*^2} \, , \tag{4.10}$$

where $' \equiv d/dz$, and β characterizes the frequency of oscillations. The term on the rhs scales as $a''/a \sim (a_*/a)^{2/p}$, and hence it becomes irrelevant very soon, since it decays as $a''/a \sim z^{-2/p} \ll 1$. The initial condition for the Higgs amplitude in the new variables is, by construction, $h_* \equiv 1$. The initial condition for the derivative $h'_* \equiv dh_*/dz$, taking into account that the Higgs was in slow roll during inflation [i.e. $\dot{\varphi}(t_*) = -\lambda a_*^2 \varphi_*^3 / 2 H_*$], reads out $h'_* \equiv 1 - \beta^2/2$.

We have plotted in Fig. 4.2 different solutions to the Higgs Eq. (4.10), for a RD background and different values of β. We observe that the initial velocity of the Higgs and the frequency of its oscillations (in the dimensionless variables) both depend, through β, on the initial amplitude of the Higgs φ_*, and the actual value of λ. Therefore, at different patches of the Universe (separated at distances larger than the correlation length $l \gg l_*$), the Higgs will start oscillating with different amplitudes, and the oscillation frequency will also be different.

At the end of inflation, the Higgs has, within any arbitrary patch of size smaller than l_*, an initial velocity in slow roll and a nonzero amplitude as large as $\varphi/H_* \sim \mathcal{O}(0.01) - \mathcal{O}(1)$. This amplitude remains 'frozen' for a finite time until the start of the oscillations. Looking at Eq. (4.6), and denoting as $z_{\rm osc}(\beta)$ the time at which oscillations start at each patch, we see that the condition for the onset of oscillations is $a(z_{\rm osc}) \sqrt{\lambda} \varphi(z_{\rm osc}) = \mathcal{H}(z_{\rm osc})$. For simplicity, we will set the initial value of the scale factor to unity $a_* \equiv a(t_*) = 1$, so that $\mathcal{H}_* \equiv H_*$, $z \equiv H_*(t - t_*)$, and $a(z) = (1 + z/p)^p$. We will also denote any quantity evaluated at $z_{\rm osc}$ with the suffix $_{\rm osc}$, so for example $a_{\rm osc} \equiv a(z_{\rm osc})$. It follows that $a_{\rm osc} \sqrt{\lambda} \varphi_{\rm osc} = a_{\rm osc} H_{\rm osc} = H_* / a_{\rm osc}^{1/p}$, from which we
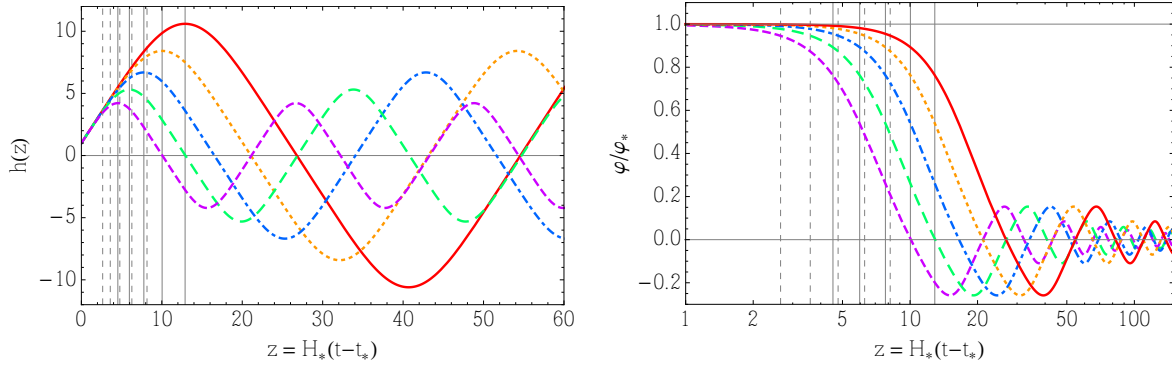
Figure 4.2.: Evolution of the Higgs field for $\beta = 10^{-2}, 2.5 \times 10^{-2}, 5.0 \times 10^{-2}, 7.5 \times 10^{-2}$ and 10^{-1} (corresponding to the red solid, orange dotted, blue dotted-dashed, green long-dashed and purple short-dashed lines, respectively). The background is RD, so $w = 1/3$. Dashed vertical lines mark the time $z_{\rm osc}(\beta)$ when the oscillation condition is attained, $a\sqrt{\lambda}\varphi \equiv \mathcal{H}$, whereas continuous vertical lines mark the time $z_M(\beta)$ when the first maximum in the oscillations is reached, characterized by the condition $h'(z_M) \equiv 0$. Left: Evolution of $h(z)$. Right: Evolution of the physical Higgs φ/φ_*, which is initially frozen until the oscillations start, and then decreases as $\propto 1/a$ afterwards, as it oscillates.

find

$$\varphi_{\rm osc} \equiv \frac{H_*}{\sqrt{\lambda}} \frac{1}{\left(a_{\rm osc}\right)^{1+\frac{1}{p}}} \quad \Rightarrow \quad \sqrt[p]{a_{\rm osc}}\, \beta\, h_{\rm osc} = 1 \,. \tag{4.11}$$

We have obtained fits for $z_{\rm osc}, h_{\rm osc}$ as a function of β and ω. These fits will turn out to be useful later on. We find

$$h_{\rm osc} = 0.98\, \beta^{-\frac{2}{3(1+w)}} \,, \tag{4.12}$$

$$z_{\rm osc} = \frac{2}{(1+3w)} \left(1.02\, \beta^{-\frac{(1+3w)}{3(1+w)}} - 1\right) \,. \tag{4.13}$$

On the other hand, let us define z_M as the time when $h(z)$ reaches its first maximum [characterized by $h'(z_M) = 0$], as well as the oscillation period as Z_T. We can show that $h(z_M)$ and Z_T also depend on β and the post-inflationary equation of state w, according to the following fits,

$$h(z_M) = A h_{\rm osc} \,, \quad Z_T = B\beta^{-\frac{(1+3w)}{3(1+w)}} \,, \tag{4.14}$$

where the constants A and B are $(A, B) \simeq (1.28, 6.30), (1.22, 6.25), (1.17, 6.25)$ for $w = 0, 1/3$, and 1, respectively.

At the end of inflation, the Higgs energy density at a given patch is mostly dominated by its potential energy,

$$V_* \equiv \frac{\lambda \varphi_*^4}{4}, \tag{4.15}$$

which represents a very small contribution of the total energy budget at that moment. In particular, averaging over realizations, we find

$$\frac{\langle V_* \rangle}{3 m_p^2 H_*^2} \simeq 4 \times 10^{-12} \left(\frac{H_*}{H_*^{(\mathrm{max})}} \right)^2 \ll 1. \tag{4.16}$$

At the onset of oscillations, part of the potential energy will become kinetic, with the two contributions – kinetic and potential – becoming of the same magnitude. In order to see this, let us first write the total energy density of the Higgs as

$$\rho_\varphi = \frac{1}{2a^2} \dot{\varphi}^2 + \frac{\lambda}{4} \varphi^4 = \frac{V_*}{a^4(z)} E(z, \beta), \tag{4.17}$$

with the kinetic and potential contributions given by

$$E(z, \beta) = \frac{1}{\beta^2} \left(h' - \frac{a'}{a} h \right)^2 + h^4 \equiv E_K(z, \beta) + E_V(z, \beta). \tag{4.18}$$

We can then take the average over the Higgs oscillations as[3]

$$\overline{\rho}_\varphi(z, \beta) = \frac{V_*}{a^4(z)} \overline{E}(\beta), \quad \overline{E}(\beta) = \frac{1}{Z_T(\beta)} \int_z^{z + Z_T(\beta)} dz' E(z', \beta), \tag{4.19}$$

and again split the result into potential and kinetic contributions, $\overline{E}(\beta) = \overline{E}_K(\beta) + \overline{E}_V(\beta)$, where

$$\overline{E}_V(\beta) \equiv \frac{1}{Z_T(\beta)} \int_z^{z + Z_T(\beta)} h^4(z') dz' = \frac{1}{3} \overline{E}(\beta), \tag{4.20}$$

$$\overline{E}_K(\beta) \equiv \frac{1}{Z_T(\beta)} \int_z^{z + Z_T(\beta)} dz' \frac{1}{\beta^2} \left(h' - \frac{a'}{a} h \right)^2 = \frac{2}{3} \overline{E}(\beta). \tag{4.21}$$

$$\tag{4.22}$$

The averaged components verify $\overline{E}_V(\beta) = \frac{1}{3} \overline{E}(\beta)$ and $\overline{E}_K(\beta) = \frac{2}{3} \overline{E}(\beta)$. We observe that the Higgs energy density scales as a^{-4} with the expansion of the Universe [52], behaving as if it were a fluid of relativistic species.

---

[3]Note that we are not including in the average the prefactor $1/a^4(t)$ factorized out in Eq. (4.17), since the scale factor changes only marginally during each oscillation. Therefore, we are only averaging the contribution due to the Higgs oscillatory behavior.

4.3. Higgs decay: Analytical estimates

As just explained, the Higgs oscillates everywhere in the Universe, although the time to start the oscillations depends sensitively on the initial condensate amplitude, which varies from patch to patch according to $P_{\text{eq}}(\varphi)$ [Eq. (4.4)]. Once the oscillations have begun within a given patch, all fields coupled directly to the Higgs are excited every time the Higgs goes through the minimum of its potential. In the case of bosonic species, this occurs through a process of parametric resonance, similar to the one described in Section 2.3.1 in the context of preheating. Consequently, there is a resonant growth of the number density of species due to a cumulative effect [21, 22, 25, 26, 137, 55, 128]. In the case of fermionic species there is no parametric resonance, but an interesting effect occurs, since modes with successively higher momenta are excited as the oscillations carry on [29, 138, 32, 30, 31, 122].

First, all charged leptons of the SM are directly coupled to the Higgs via a Yukawa interaction, so all fermions of the SM will be excited during the oscillations of the Higgs [122], with the possible exception of neutrinos. Among the SM fermions, the top quark has the largest coupling to the Higgs, so most of the energy transferred into fermions goes into top quarks. The $SU(2)_L$ gauge bosons are also coupled directly to the Higgs, and indeed the strength of their coupling is very similar to that of the Yukawa top quark. When two species, one fermionic and another bosonic, are coupled with the same strength to an oscillatory homogeneous field, the first burst of particle production is actually spin independent, and hence an equal number of bosons and fermions are created [33]. However, the successive particle creation bursts at each Higgs zero crossing take place on top of an already existing number density of previously created species. The spin statistics becomes then crucial, differentiating bosons from fermions in a noticeable way: bosonic occupation numbers start growing exponentially as the oscillations accumulate, whereas the fermion occupation numbers are always Pauli-blocked, forcing the transfer of energy into modes with higher and higher momenta. Due to this, the transfer of energy is much more efficient into the bosonic species [32] than into fermions. Therefore, in the following three chapters we will only focus on the production of the $W^{\pm}$ and Z gauge bosons, which are the most energetically dominant species among the Higgs decay products. Besides, in the context under study here – the decay of the Higgs after inflation –, the subdominant production of the SM charged leptons has been already addressed in [122].

In order to study the dynamics after inflation of the Higgs and its most energetic decay products, one should in principle consider the full $SU(2) \times U(1)$ gauge structure of the SM electroweak sector. However, one can make reasonable approximations for both analytical and computational purposes. In this chapter we consider the following approximate schemes, mimicking the structure of the SM interactions:

i) *Abelian model*. This consists in modelling the interactions between the electroweak gauge bosons and the Higgs with an Abelian-Higgs set-up. Since gauge fields are initially

excited by the Higgs from the vacuum, it is clear that nonlinearities due to the truly non-Abelian nature of $SU(2)$ are expected to be negligible during the initial growth of the gauge field occupation numbers [63]. The authors of Ref. [128] have shown, using the Hartree approximation, that the effective contribution induced by the created gauge bosons onto themselves (due to the non-Abelian nonlinearities) can be neglected as long as the backreaction from the gauge fields onto the Higgs does not become significant. We shall see in Section 4.5.1 that this fact justifies, in principle, ignoring the non-Abelian structure of the SM interactions, while maintaining only the Abelian dominant part.

ii) Global model. A more crude approximation can yet be done, by ignoring the gauge structure of the interactions. This does not mean that we ignore the interactions themselves, but rather that we consider them as if they were dictated by a global symmetry, instead of a gauge one. In this scenario, one simply solves the mode equations of various scalar fields coupled to the Higgs with a quadratic interaction. Each of these scalar fields mimics a component of the gauge fields, with the quadratic interactions reproducing the coupling of the gauge bosons and the Higgs obtained from the SM gauge covariant derivative terms. This way, one can presumably capture the initial stages of the parametric resonance of $W^{\pm}$ and Z bosons.

The approach *i* is our most precise modelling of the SM interactions, but also the most involved one. On the other hand, although the approach *ii* is less accurate, it allows for an analytical treatment. The order of presentation of our different approaches is thus based on increasing progressively the degree of proximity to the real system. First, in the remainder of this section, we start with the analytical treatment of the global modelling, ignoring all nonlinearities of the system. In Section 4.4 we implement the global model *ii)* on the lattice. Afterwards, in Section 4.5, we present a lattice implementation of the Abelian model *i)*. Finally, in Chapter 6 we will present lattice simulations of the exact SU(2)×U(1) gauge theory. We will then be able to accurately assess the validity of the global and Abelian models.

4.3.1. Analytical approach to the Higgs decay in the global model

In this approach, we simply solve the mode equation for a scalar field χ, coupled to the Higgs with an interaction term of the form $\frac{e^2}{2}\chi^2\varphi^2$. In order to identify e^2 with the gauge coupling g^2 between the Higgs and a gauge field, we need to make the identification $e^2 \to g^2/4$, with g^2 the gauge coupling g_Z^2 or g_W^2 of either the Z or the $W^{\pm}$ gauge bosons. This matches correctly the interaction derived from the covariant gauge derivative of the electroweak sector of the SM. Analytical results following this approach were previously presented in Ref. [55]. We develop nevertheless some new formulas which will be useful later on.

The equation for the Fourier modes of the field χ, after an appropriate conformal redefinition $\chi_k \equiv X_k/a$, and assuming RD, can be mapped into [26]

$$X_k'' + \left(\kappa^2 + q(h/h_{\mathrm{osc}})^2\right) X_k = 0 \,, \qquad q \equiv \frac{e^2}{\lambda} \,, \tag{4.23}$$

with q being the resonance parameter, $\kappa \equiv k/(\sqrt{\lambda}\varphi_{\mathrm{osc}})$, $' \equiv d/dz$, and $z \equiv \mathcal{H}_{\mathrm{osc}}t$. Given the behavior of $h(z)$, dictated by the Higgs quartic potential, this equation corresponds indeed to the Lamé equation (2.20), which was studied in detail in Section 2.3.1 in the context of preheating with quartic potential. This equation has a well-understood structure of resonances. Whenever $q \in \frac{1}{2}[n(n+1),(n+1)(n+2)]$, with $n = 1, 3, 5, \ldots$ (i.e. $q \in [1,3], [6,10], \ldots$), there is an infrared band of resonance $0 \leq k \lesssim k_* \equiv \frac{1}{\sqrt{2}\pi}q^{1/4}\mathcal{H}_{\mathrm{osc}}$, for which $X_k \propto e^{\mu_k z}$ with $\mathfrak{Re}[\mu_k] > 0$. If the resonance parameter $q > 1$ is not within one of the resonant bands, but lies in between two adjacent bands, then there is still a resonance of the type $X_k \propto e^{\mu_k z}$, but within a shorter range of momenta $k_{\min} \leq k \lesssim k_*$ (with $k_{\min} > 0$), and hence with a smaller Floquet index μ_k. For resonant parameters $q \gg 1$, μ_k is typically of order $\sim \mathcal{O}(0.1)$.

Considering the range $10^{-2} \lesssim \lambda \lesssim 10^{-5}$, and taking into account the strength of the $W^{\pm}, Z$ gauge couplings at high energies, we obtain that the resonant parameters are within the range $\mathcal{O}(10) \lesssim q \lesssim \mathcal{O}(10^3)$. In particular, since at high energies $g^2 = g_W^2 \simeq 0.3$ for W gauge bosons, we obtain $q = 7.5$ for $\lambda = 10^{-2}$, and $q = 3000$ for $\lambda = 2.5 \times 10^{-5}$. For Z bosons we obtain resonance parameters twice as big. For completeness, we have sampled resonance parameters within the interval $q \in [5,3000]$, which corresponds to a range $\lambda = 1.5 \times 10^{-2} - 2.5 \times 10^{-5}$ for W bosons and $\lambda = 3.0 \times 10^{-2} - 5.0 \times 10^{-5}$ for Z bosons.

For simplicity, we will consider until the end of this section that the resonance parameter $q = e^2/\lambda$ always falls within one of the resonant bands, $q \in [1,3], [6,10], [15,21], \ldots$. This assumption is quite reasonable: note that the gauge couplings of the Z and $W^{\pm}$ gauge bosons verify $g_Z^2 \approx 2g_W^2 \approx 0.6$ at very high energies, so it is likely that either $q_W \equiv g_W^2/4\lambda$ or $q_Z \equiv g_Z^2/4\lambda \approx 2q_W$, will fall within one of the instability bands.

Let us find an estimate for the time scale z_{eff} at which an efficient transfer of energy has taken place from the Higgs into the gauge bosons, characterized by $\rho_A(z_{\mathrm{eff}}) = \rho_\varphi(z_{\mathrm{eff}})$, with ρ_i ($i = A, \varphi$) the energy density of each species. This will be just a crude estimate of the time scale of the Higgs decay, but it should provide, at least, a reasonable estimate of the order of magnitude. Note that this calculation will be very similar to the one carried out in Section 2.3.1 [see Eqs. (2.22) to (2.29)].

For our calculations, we represent the gauge field as if it were simply a collection of three scalar fields (one for each spatial component), all coupled with the same coupling strength g^2 to the Higgs. The growth of the fluctuations in the initial stages of resonance is described by the linearized Eq. (4.23). The energy density of the created particles due to the resonance is

then given by

$$\rho_A = \frac{3}{2\pi^2 a^3} \int dk k^2 n_k \omega_k \, , \quad \omega_k^2 \equiv \frac{k^2}{a^2} + \frac{g^2}{4}\overline{\varphi^2} \, , \tag{4.24}$$

with the factor 3 accounting for the three spatial components of a gauge field, and where we have introduced an oscillation-averaged effective mass for the gauge boson,

$$m_A^2 = \frac{g^2}{4}\overline{\varphi^2} = \frac{g^2}{4}\frac{\varphi_*^2}{a^2}\overline{h^2} \equiv \frac{g^2}{4}\frac{\varphi_*^2}{a^2}\frac{1}{Z_T(\beta)}\int_z^{z+Z_T(\beta)} dz' h^2(z') \tag{4.25}$$

For $q \gg 1$, the maximum (comoving) momentum possibly excited in broad resonance is given by

$$k_*^2 \equiv \frac{q^{1/2}}{2\pi^2}a_{\rm osc}^2 \lambda \varphi_{\rm osc}^2 = \frac{q^{1/2}}{2\pi^2}h_{\rm osc}^2 \lambda \varphi_*^2 \, , \tag{4.26}$$

from which, given that $\overline{h^2} \sim h_{\rm osc}^2$, we see that

$$\frac{m_A^2}{(k_*/a)^2} \sim \mathcal{O}(10)q^{1/2} \gg 1 \, . \tag{4.27}$$

In broad resonance $q \gg 1$, the decay products are always nonrelativistic, and we can approximate the effective mode frequency as $\omega_k \simeq m_A \sim \frac{g}{2}\frac{\varphi_*}{a}h_{\rm rms}$, where $h_{\rm rms} \equiv \sqrt{\overline{h^2}}$. It turns out that $h_{\rm rms} \simeq h_{\rm osc}$ independently of β. If q is within a resonant band, then all modes with momenta $0 \leq k \lesssim k_*$ are excited with some Floquet index varying within $[0, \mu_k^{(\rm max)}(q)]$. We can therefore model the occupation number of the excited modes simply as a step function $n_k = e^{2\overline{\mu}_k y}\Theta(1 - k/k_*)$, where $\overline{\mu}_k \sim \mathcal{O}(0.1)$ is the mean Floquet index of the resonance band, and $y \equiv \mathcal{H}_{\rm osc}(t - t_{\rm osc}) = a_{\rm osc}\sqrt{\lambda}(\varphi_{\rm osc}/H_*)(z - z_{\rm osc}) = (a_{\rm osc})^{-\frac{1}{p}}(z - z_{\rm osc})$, with $z = H_* t$. It follows that

$$
\begin{aligned}
\rho_A(z) &\simeq \frac{(h_{\rm rms}/h_{\rm osc})^2}{4\pi^2}\frac{1}{a^4}e^{\frac{2\overline{\mu}_k}{\sqrt[p]{a_{\rm osc}}}(z-z_{\rm osc})}g\varphi_* h_{\rm osc}k_*^3 \\
&\simeq q^{5/4}\frac{(h_{\rm rms}/h_{\rm osc})^2}{2^{5/2}\pi^5}e^{\frac{2\overline{\mu}_k}{\sqrt[p]{a_{\rm osc}}}(z-z_{\rm osc})}\frac{H_*^4}{(a\sqrt[p]{a_{\rm osc}})^4} \, ,
\end{aligned}
\tag{4.28}
$$

where we have used that $\beta h_{\rm osc} = 1/\sqrt[p]{a_{\rm osc}}$.

On the other hand, the energy of the Higgs, since the onset of the oscillations, decays as

$$\rho_\varphi(z) = V_*\frac{1}{a^4}3\overline{E}_V(\beta) = \frac{3}{4}\frac{\lambda\varphi_*^4}{a^4}\overline{h^4} = \frac{3}{4\lambda}\overline{(h/h_{\rm osc})^4}\frac{H_*^4}{(a\sqrt[p]{a_{\rm osc}})^4} \, , \tag{4.29}$$

where $\overline{(h/h_{\rm osc})^4} \sim \mathcal{O}(1)$. We can now find $z_{\rm eff}$ by simply equating Eqs. (4.28) and (4.29),

$$\frac{q^{1/4}}{2^{5/2}\pi^5}\sqrt{\overline{(h/h_{\rm osc})^2}}e^{\frac{2\overline{\mu}_k}{\sqrt[p]{a_{\rm osc}}}(z_{\rm eff}-z_{\rm osc})} = \frac{3}{g^2}\overline{(h/h_{\rm osc})^4} \, , \tag{4.30}$$

so that

$$z_{\text{eff}} = z_{\text{osc}} + \frac{\sqrt[p]{a_{\text{osc}}}}{2\overline{\mu}_k} \left[\log \left(\frac{\overline{(h/h_{\text{osc}})^4}}{(h_{\text{rms}}/h_{\text{osc}})} \right) + \log \left(\frac{3 \cdot 2^{5/2}\pi^5}{g^2} \right) - \frac{1}{4}\log q \right] . \tag{4.31}$$

Let us recall that $g^2 \simeq 0.3, 0.6$ at large energies, and $q \equiv g^2/(4\lambda) \sim \mathcal{O}(10) - \mathcal{O}(10^3)$, depending on the value of λ. Taking this into account, we find that the first term in the brackets of the rhs is always irrelevant, the second term is constant and of the order $\simeq 9$, and the last term is of order ~ -1. Therefore, we can approximate the above expression, using $\sqrt[p]{a_{\text{osc}}} = (1 + \frac{1}{p}z_{\text{osc}})$, as

$$z_{\text{eff}} \sim 20 \times \left(\frac{0.2}{\overline{\mu}_k} \right) \beta^{-\frac{(1+3w)}{3(1+w)}} . \tag{4.32}$$

Moreover, using Eq. (4.7), the scale factor at $z = z_{\text{eff}}$ is given by

$$a_{\text{eff}} \equiv a(z_{\text{eff}}) \sim (20(1 + 3w))^{\frac{2}{(1+3w)}} \cdot \beta^{-\frac{2}{3(1+w)}} . \tag{4.33}$$

It is clear that depending on how small the initial value of β is within a given path of the Universe, the longer it takes for the Higgs to transfer energy efficiently into the gauge bosons, simply because the longer it takes (since the end of inflation) to start oscillating. Since $\beta_{\text{rms}} \sim \mathcal{O}(0.1)$, we see that typically the Higgs decays at a time $z_{\text{eff}}(\beta_{\text{rms}}) \sim \mathcal{O}(10^2)$. Although the time varies from patch to patch depending on the values of β, it is clear that the Higgs tends to decay really fast after inflation, within a few dozens of oscillations. In the following sections we will check the validity of this estimate by comparing it with the outcome obtained from lattice simulations.

4.4. Lattice simulations, Part 1: Global modelling

In this section, we model the SM interactions with a set of scalar fields. More specifically, we consider the Lagrangian

$$-\mathcal{L} = \frac{1}{2}\partial_\mu\varphi\partial^\mu\varphi + \frac{1}{2}\partial_\mu\chi_i\partial^\mu\chi_i + \frac{\lambda}{4}\varphi^4 + \frac{e^2}{2}\varphi^2\sum_i\chi_i^2 , \tag{4.34}$$

with $i = 1, 2, 3$. Varying the action $S = \int d^4x\,\mathcal{L}$ leads to the classical EOM

$$\ddot{\varphi} + 2\mathcal{H}\dot{\varphi} - \nabla^2\varphi + a^2(\lambda\varphi^2 + e^2\sum_i\chi_i^2)\varphi = 0 , \tag{4.35}$$

$$\ddot{\chi}_i + 2\mathcal{H}\dot{\chi}_i - \nabla^2\chi_i + a^2e^2\varphi^2\chi_i = 0 . \tag{4.36}$$

The term $e^2 \varphi^2 \chi_i$, under the identification $e^2 = g^2/4$, mimics precisely the interaction term from the covariant derivative of the EW gauge bosons, $\frac{g^2}{2} \Phi^\dagger \Phi A_\mu$, where A_μ stands for either Z_μ or $W_\mu^\pm$, and Φ is the Higgs doublet. More concretely, choosing the unitary gauge for the Higgs $\Phi = (0, \varphi/\sqrt{2})$, and fixing $A_0 = 0$, we can identify each χ_i with each spatial component of the gauge boson A_i, and φ with the unitary representation of the Higgs. This way, by solving the system of scalar field equations (4.35) and (4.36), we can study the properties of the Higgs interactions with gauge bosons in an approximative way.

We now present the main results of the lattice simulations carried out for this scenario. Let us define new field variables as

$$h \equiv \frac{a}{a_*} \frac{\varphi}{\varphi_*}, \quad X_i \equiv \frac{\chi_i}{H_*} \frac{a}{a_*}. \tag{4.37}$$

It is also convenient to redefine new spacetime coordinates $z^\mu = (z^0, z^i)$ with respect to the conformal ones $x^\mu = (x^0, x^i) \equiv (t, x^i)$, as

$$z \equiv z^0 = H_* t, \quad z^i = H_* x^i. \tag{4.38}$$

With these redefinitions, we eliminate the friction terms in Eqs. (4.35) and (4.36), and produce the following equivalent set of dynamical equations,

$$h'' - \nabla^2 h + \beta^2 h^3 + e^2 h \sum_j X_j^2 = \frac{a''}{a} h, \tag{4.39}$$

$$X_i'' - \nabla^2 X_i + q\beta^2 h^2 X_i = \frac{a''}{a} X_i, \tag{4.40}$$

with $' \equiv d/dz$, and the spatial derivatives taken with respect to the z^i variables. The resonance parameter that appears naturally in Eq. (4.40), $q \equiv \frac{e^2}{\lambda}$, should therefore be interpreted as $q \equiv \frac{g^2}{4\lambda}$.

We have solved Eqs. (4.39) and (4.40) in three-dimensional lattices with periodic boundary conditions. We consider initial conditions given by a homogeneous Higgs mode $h(0) \equiv 1$ and $h'(0) \equiv 1 - \beta^2/2$ (as described in Section 4.2), and a null zero mode for the scalar fields coupled to the Higgs, $X_i(0) = 0$ and $X_i'(0) = 0$. We add, on top of the homogeneous contributions, a set of Fourier modes with spectrum $\langle |f_k|^2 \rangle = \frac{1}{2a^2 \omega_k}$ (in physical variables), mimicking the quantum vacuum fluctuations of the ground state of a scalar field in a FRW background. Let us recall that the Higgs is frozen in slow roll until the oscillation condition Eq. (4.11) is attained at $z = z_{\text{osc}}$; see the right panel of Fig. 4.2. Hence, during the time $0 \leq z < z_{\text{osc}}$, we only evolve in the lattice Eq. (4.39), corresponding to the slow rolling of the Higgs field (the homogeneous mode of the χ_i fields is kept to zero). At $z = z_{\text{osc}}$, we add the small inhomogeneous Fourier modes to all fields, and from then on, we evolve together Eqs. (4.39) and (4.40).
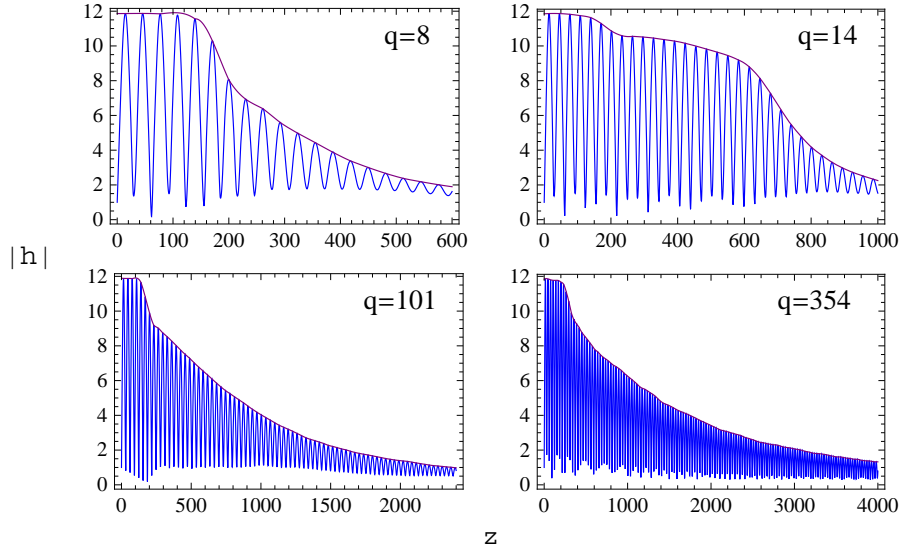
Figure 4.3.: Volume-averaged value of the Higgs field $|h|$ as a function of time, for four different resonance parameters, $q = 8, 14, 101$ and 354. Also plotted, the corresponding envelope functions of the oscillations. All cases correspond to $\beta = 0.01$.

Our simulations depend on three parameters: q, β, and w. We have run simulations for $\beta = 0.5, 0.1, 10^{-2}, 10^{-3}$ and 10^{-4}, and for each value of β, we have chosen a set of 26 resonance parameters $q \equiv \frac{g^2}{4\lambda}$, logarithmically spaced between $q = 5$ and $q = 3000$. This corresponds to sampling the Higgs self-coupling from $\lambda \sim 10^{-5}$ to $\lambda \sim 10^{-2}$. Scanning this way β and q lead us to characterize the behavior of the system, scrutinizing all possible different outcomes depending on λ and φ_*. We have guaranteed that we include both the cases in which q is within a resonance band of the Lamé equation, or in the middle of two bands (see Section 2.3.1). We have also run different simulations for three different expansion rates: a MD universe ($w = 0$), a RD universe ($w = 1/3$), and a KD universe ($w = 1$).

We now present the main results of the lattice simulations carried out for this scenario. The following results will be presented for a RD background ($w = 1/3$) and $\beta = 0.01$, the generalization to other expansion rates will be considered in Section 4.6. We have run simulations on a lattice with $N = 128$ points per dimension, with periodic boundary conditions. We have made sure that our results are not sensitive to the lattice spacing and time step.

In Fig. 4.3 we plot, as a function of time, the volume-average of the modulus of the (conformally transformed) Higgs field $|h|$. In this figure, we show the outcome corresponding to $\beta = 0.01$, and four different resonance parameters, $q = 8, 14, 101$ and 354. One conclusion is immediately clear: the time scale of the Higgs amplitude decay depends noticeably on q. Looking at the different panels of Fig. 4.3, it seems that the Higgs decay is slower the greater the resonance parameter q is. This is very opposite to the intuition gained by the study of the Lamé equation in Section 4.3, which dictates that the larger the q, the shorter the decay time of the Higgs [see Eq. (4.31)]. We thus see on this the first difference between the simplified study
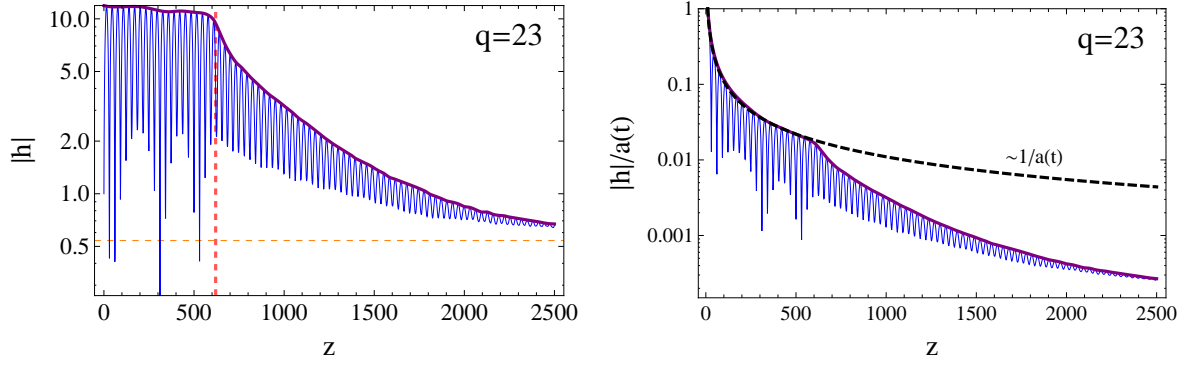
Figure 4.4.: We plot in the left panel the volume-averaged value of the Higgs modulus for $q = 23$, $\beta = 0.01$ and RD. We indicate the time $z = z_{\mathrm{br}}$ with a vertical dashed line. We plot in the right panel the corresponding physical Higgs amplitude $|\varphi|/\varphi_* = |h|/a$. The decay of the Higgs into the other fields at later times is manifested by a significant decrement of $|\varphi|$ well below the $1/a$ decaying envelope.

of the system of scalar fields in the linear regime, and the real outcome when nonlinearities are incorporated in lattice simulations. We will further comment on this issue later on.

One can distinguish two different stages in each decay process. Let us look, for instance, at the left panel of Fig. 4.4, where the conformal Higgs modulus $|h|$ is plotted for $q = 23$, and where we also include the envelope curve of the oscillations. One can clearly appreciate that initially, and for some time, the envelope is approximately constant. This is observed as a *plateau* feature in the upper panel of Fig. 4.4. The vertical dashed line in the figure indicates the end of this initial behavior, after which a second stage of rapid decay follows. Note, however, that the amplitude of the physical Higgs $\varphi/\varphi_* = h/a(t)$ is always decaying with the scale factor, no matter what its coupling to other species is. Before the second stage starts, the physical Higgs amplitude φ decays mostly due to the expansion of the Universe, and not because of an efficient transfer of energy into the scalars. However, both effects are combined afterwards, producing an even more sharp decay of the physical amplitude. This is clearly seen in the right panel of Fig. 4.4.

In order to understand better this two-stage behavior, we plot the different contributions to the total energy of the system as a function of time. The energy density can be conveniently written as

$$\rho(z) = V_* \frac{E_t(z)}{a(z)^4} \, , \quad V_* \equiv \frac{\lambda \varphi_*^4}{4} \, , \tag{4.41}$$

$$E_t(z) = E_K^\varphi + E_V + E_G^\varphi + E_K^\chi + E_G^\chi + E_{\mathrm{int}} \, , \tag{4.42}$$
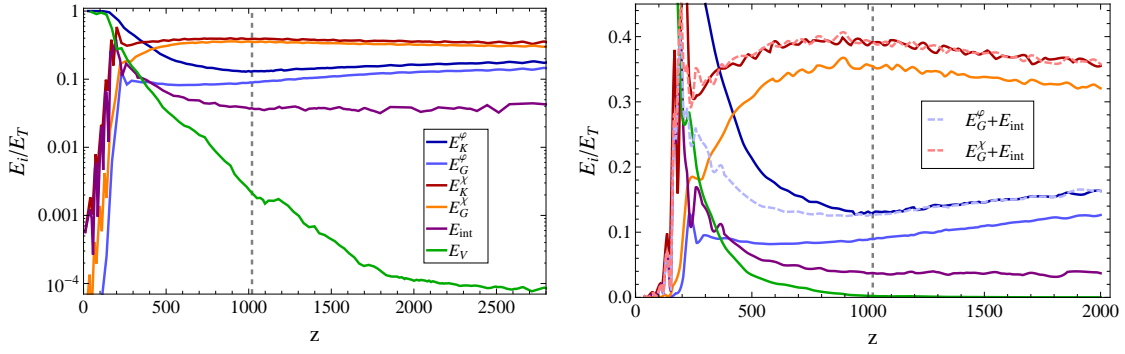
Figure 4.5.: Left: We show the envelope curves of the oscillations of the different contributions to the total energy $E_t(z)$, obtained for $q = 8$, $\beta = 0.01$ and RD. The vertical dashed line corresponds to the decay time z_{dec}. Bottom: Same quantities as in the upper figure (same color coding), but zooming in the area of interest. We also add two new lines, a pink one corresponding to the sum of the Higgs gradient energy and the interaction energy, and a light blue line, representing the sum of the χ fields' gradient energy plus the interaction energy.

where, for our choice of variables, the Higgs and χ field contributions to the kinetic (K) energy are given by ($\dot{} \equiv d/dt$, $' \equiv d/dz$)

$$E_K^\varphi = \frac{2}{\beta^2}\left(h' - h\frac{a'}{a}\right)^2 , \quad E_K^\chi = \frac{2\lambda}{\beta^4}\sum_{i=1}^{3}\left(X_i' - X_i\frac{a'}{a}\right)^2 , \tag{4.43}$$

the gradient (G) contributions by

$$E_G^\varphi = \frac{2}{\beta^2}|\vec{\nabla}h|^2 , \quad E_G^\chi = \frac{2\lambda}{\beta^4}\sum_{i=1}^{3}|\vec{\nabla}X_i|^2 , \tag{4.44}$$

and finally, the Higgs potential (V) energy and the interaction (int) term, by

$$E_V = h^4 , \quad E_{\text{int}} = \frac{2e^2}{\beta^2}h^2\sum_i X_i^2 . \tag{4.45}$$

In Fig. 4.5 we have plotted the different contributions to $E_t(z)$ for the parameters $\beta = 0.01$ and $q = 8$. Initially, the system is dominated by the kinetic and potential energy densities of the Higgs. This corresponds to the regime of anharmonic oscillations of the Higgs condensate described in Section 4.2.1, for when the coupling to other fields was ignored ($g^2 \to 0$). However, in reality, as soon as the Higgs starts to oscillate, there is an energy transfer into any species coupled to the Higgs. Each time the Higgs crosses zero, a fraction of its energy goes into the χ fields. Initially, the amount of energy transferred at each zero crossing is small relative to the total energy stored in the Higgs, so it takes some time until the transfer becomes noticeable. Eventually, at the time $z = z_{\text{br}}$, the energy transferred into the χ fields becomes significant enough compared to the Higgs energy itself, so the Higgs condensate becomes affected. From

then onwards, the Higgs continues pumping energy into the other fields at $z > z_{br}$, but the amount of energy transferred at each zero crossing is no longer a small fraction of the energy available in the Higgs condensate itself. Therefore, soon after backreaction becomes noticeable at $z = z_{br}$, the previously exponential growth of the χ fields energy densities stops, eventually saturating to a fixed amplitude. This is clearly seen in Fig. 4.5, where the gradient and kinetic energy densities of the χ fields saturate to an almost constant amplitude. At the same time, immediately after $z = z_{br}$, the energy of the Higgs (mostly dominated by the kinetic contribution) drops abruptly, as can be clearly seen, for instance, from $z \approx 175$ to $z \approx 900$, for the case depicted in Fig. 4.5.

A very relevant aspect to note is that when all the energy contributions stop growing or decreasing abruptly (with the exception of the Higgs potential energy, which keeps on falling for a long time), the energy components reach equipartition. In particular, at some time $z > z_{br}$, the kinetic energy E_K^φ of the Higgs becomes equal to the sum of the Higgs gradient energy plus the interaction energy, $E_G^\varphi + E_{int}$; see the lower panel of Fig. 4.5. In other words, equipartition in the Higgs sector holds[4] as $E_K^\varphi = E_G^\varphi + E_{int}$. Similarly, in the χ fields, the sum of their gradient energy plus the interaction term achieves equipartition with their kinetic energy, $E_K^\chi = E_G^\chi + E_{int}$, as can also be well appreciated in the lower panel of Fig. 4.5.

All features described so far are, of course, not specific to the particular case $q = 8$, $\beta = 0.01$ and RD, shown in Fig. 4.5. A similar behavior is observed in the outcome of the field distribution for other choices of β, q and ω, although the duration of the different stages changes. In particular, the duration of the initial plateau is directly dependent on the band structure of the Lamé equation.

We have characterized the dependence of z_{br} with the resonant parameter q; see Fig. 4.6. Let us recall that z_{br} corresponds to the moment when the energy transferred into the χ fields is sufficiently large so that the Higgs amplitude and energy density starts to decrease. Therefore, this is the moment that should be compared to the analytical estimate Eq. (4.32) of the Higgs decay time z_{eff}, derived in Section 4.3.1. The $z_{br}(q)$ behavior can be characterized by

$$
z_{br}(q) \sim \begin{cases} 160 & , \quad q \in \text{Resonant Band} , \\ 869 - 92 \log q & , \quad q \notin \text{Resonant Band} . \end{cases} \tag{4.46}
$$

If a given q is within a resonant band, $z_{br}(q)$ is almost independent of q, as appreciated in the left panel of Fig. 4.6. For RD and $\beta = 0.01$, our analytical estimate Eq. (4.32) predicts $z_{eff} \simeq 200$, which is reasonably similar to the fit found from our numerical outcome, $z_{br}(q) \approx 160$. The analytical estimates are only an approximation to the real dynamics, and one cannot expect anything more than a reasonable order-of-magnitude prediction, as is indeed the case.

---

[4]In reality, it should be $E_K^\varphi = E_G^\varphi + E_{int} + E_V$, but E_V is so small by then, that it does not make a difference to add it or not.
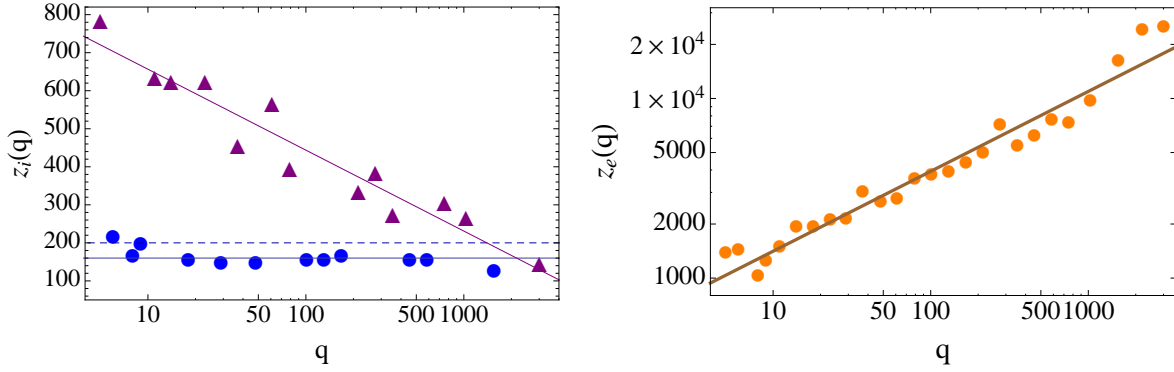
Figure 4.6.: Left: The different times $z_{\mathrm{br}}(q)$ obtained from our simulations, for RD ($\omega = 1/3$) and $\beta = 0.01$. Purple triangles and blue circles correspond to q parameters inside or outside a resonance band of the Lamé equation respectively. The blue and purple continuous lines correspond to the best fit to the circles and triangles respectively; Eq. (4.46). The dashed line corresponds to the analytical estimate $z_{\mathrm{eff}} \approx 200$, obtained from Eq. (4.32) with $\bar{\mu}_k = 0.2$. Right: The different points show the Higgs time decay $z_{\mathrm{dec}}(q)$ as a function of q obtained from our simulations for the same (ω, β) values as the upper panel. The brown line corresponds to the best fit, Eq. (4.47).

More importantly, the analytical calculation predicts that z_{eff} should be only dependent on q logarithmically [Eq. (4.31)], which implies that for mildly broad resonance parameters as the ones we have, $q \sim \mathcal{O}(10) - \mathcal{O}(10^3)$, z_{eff} is essentially independent of q, as is indeed well appreciated in Fig. 4.6.

The dependence of $z_{\mathrm{br}}(q)$ with q's outside resonance bands is also logarithmic, though with a big coefficient. As it can be appreciated in the upper panel of Fig. 4.6, for $q \lesssim 10^2$ it is a factor $\sim$2-4 larger than the analytical prediction Eq. (4.32), but becomes of the same order for $q \sim 10^2 - 10^3$, modulo a factor $\sim$1-2. Possibly, for $q \gg 10^3$, $z_{\mathrm{br}}(q)$ will become smaller, but as said before, such regime is never valid in our case of study.

In light of the results of this section, we see that the Higgs decay should be identified, rather than with z_{br}, with the abrupt drop of the Higgs energy density, some time afterwards at $z > z_{\mathrm{br}}$. After the drop, the kinetic contribution E_K^{φ} (which is the dominant energy component of the Higgs) enters into a stationary regime, equipartitioned with $E_G^{\varphi} + E_{\mathrm{int}}$. The onset of this regime signals the end of the decrease of the Higgs kinetic energy. We therefore provide a definition of the decay time of the Higgs, z_{dec}, as the moment when equipartition (within the Higgs sector) holds better than a given percentage. In practice, we operationally determine z_{dec} as the moment when the equality $E_K^{\varphi} \simeq E_G^{\varphi} + E_{\mathrm{int}}$ holds to better than 1%. Defining the Higgs decay like this might seem arbitrary, but when looking carefully at the evolution of the energy components, we see that the end of the drop of the Higgs kinetic energy E_K^{φ}, coincides always with the onset of its equipartition with $E_G^{\varphi} + E_{\mathrm{int}}$, for all resonant parameters. From then onwards, i.e. for $z > z_{\mathrm{dec}}$, all energy components (with the exception of the Higgs
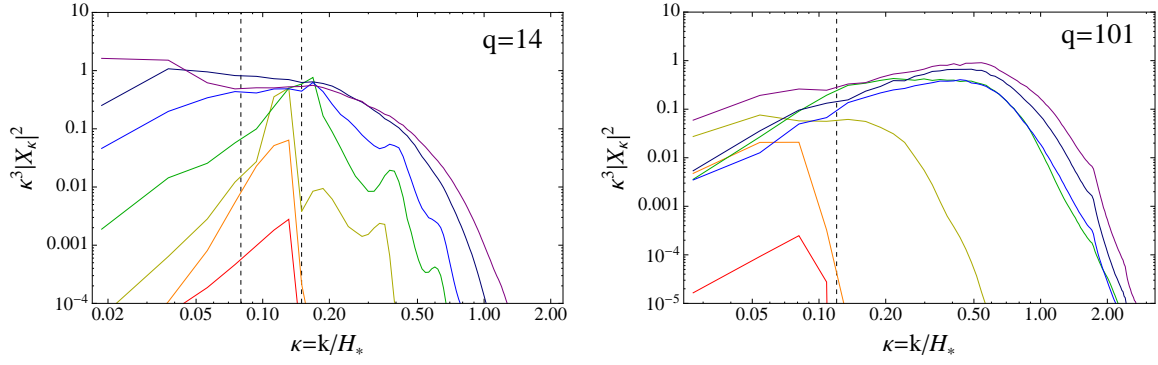
Figure 4.7.: Left: Spectra for $q = 14$ of one of the scalar fields, χ_1, plotted at times $z = 11, 94, 258, 504, 668, 1160, 2308$. Right: Same spectra for $q = 101$, plotted at times $z = 11, 94, 174, 254, 335, 657, 1302$. The dashed vertical lines in the four figures indicate the position of the corresponding band of the Lamé equation.

potential) enter into a stationary regime, evolving very slowly, and preserving all the time the equipartition condition, $E_K^\varphi \simeq E_G^\varphi + E_{\text{int}}$ and $E_K^\chi \simeq E_G^\chi + E_{\text{int}}$.

The dependence of the decay time scale z_{dec} versus q is shown in the right panel of Fig. 4.6. A fit to this relation is given by

$$z_{\text{dec}}(q) = 507 q^{0.44} \ . \tag{4.47}$$

This is valid for $\beta = 0.01$ and for a RD ($w = 1/3$) background. As we shall explain in Section 4.6, this fit can be generalized to other β values within our range of interest, and to other expansion rates (characterized by the equation of state w), as

$$z_{\text{dec}}(q) \approx 50.7 \beta^{\frac{-(1+3\omega)}{3(1+\omega)}} q^{0.44} \ . \tag{4.48}$$

As we can see, the behavior of $z_{\text{dec}}(q)$ is actually independent of whether q is within or outside a resonance band. More remarkably, the growth of $z_{\text{dec}}(q)$ with q is actually quite contrary to the intuition obtained from solving the Lamé equation. In the linear regime, when the Lamé equation is valid, we expect that the larger the resonance parameter, the faster the transfer of energy from the Higgs to its decay products [see Eq. (4.32)]. However, the behavior of z_{dec} is set by the nonlinearities of the problem, as opposed to z_{br}, which is determined by the linear regime. This results in a completely opposite trend to z_{br}, given the growth of z_{dec} with q.

To conclude the section, we will briefly describe the dynamics of the system in the spectral domain. During the initial stages, the modes that are excited correspond to those in the band structure of the Lamé equation. We clearly see this for $z < z_{\text{br}}(q)$ in Fig. 4.7, where we plot, for $q = 14$ and $q = 101$, the field spectra $k^3 |X_k|^2$. We also indicate with dashed lines the resonance bands. As the amplitude of the modes within the resonance bands grows, the system becomes more and more nonlinear. Rescattering among modes occurs, and the bands become wider.

Due to the coupling of the modes through Eqs. (4.39) and (4.40), the initial parametric resonance of the χ_k modes within the resonance bands, excite at the same time Higgs modes $\varphi_{k'}$, which then rescatter off other modes $\chi_{k''}$, and so on. As a consequence, the power spectrum of the fields grows exponentially and widens, with a typical width $0 \leq k \lesssim \mathcal{O}(10)k_L$. As we have discussed in detail, at late times $z \gtrsim z_{\text{dec}}$ the fields enter into a stationary stage, characterized by equipartition and a very slow evolution of the energy densities.

In the next section, we will present a similar analysis of the properties of the Higgs decay process, but finally introducing the gauge nature of the interactions. Before we move on, let us recall again that all our results of Section 4.4, correspond to RD and were obtained for a fixed value $\beta = 0.01$. We will devote Section 4.6 to an analysis of how the results change when varying the Higgs initial amplitude (i.e. β) and the background expansion rate (i.e. w).

4.5. Lattice Simulations, Part 2: Abelian-Higgs modelling

In this section, we study the properties of the Higgs decay, modelling the system with an Abelian-Higgs framework. In this approach, and in contrast with the global scenario, we introduce a gauge structure in the interactions. We will approximate the action of the electroweak sector of the standard model, invariant under the local SU(2)$\times$U(1) symmetry group, by a local U(1) gauge theory. In Section 4.5.1, we will see that the corrections due to the non-Abelian nature of the SM interactions are not expected to play any significant role, at least at initial times. Let us also note that we will continue considering a system where the Higgs is only coupled to a single gauge boson, with resonance parameter $q = g^2/4\lambda$. In Section 4.5.2 we will consider the real case of the Higgs decaying simultaneously into the three gauge bosons W^+, W^- and Z.

The Abelian-Higgs model with one gauge boson is described by the action $S = \int \mathcal{L} \, d^4x$, with Lagrangian

$$-\mathcal{L} = (D_\mu \Phi)^* (D^\mu \Phi) + \frac{1}{4e^2} F_{\mu\nu} F^{\mu\nu} + \lambda (\Phi^* \Phi)^2 , \tag{4.49}$$

where the covariant derivative is $D_\mu = \partial_\mu - iA_\mu$, the field strength is $F_{\mu\nu} \equiv \partial_\mu A_\nu - \partial_\nu A_\mu$, and e is the Abelian coupling strength representing the coupling of either one of the $W^\pm$ or Z gauge fields. As before, in order to mimic correctly the Higgs-gauge interactions, we need to take $e^2 = g^2/4$, with $g^2 = g_W^2$ or g_Z^2, respectively for W or Z bosons. The Higgs is here a complex field written in terms of its real components as

$$\Phi \equiv \frac{1}{\sqrt{2}} \varphi \equiv \frac{1}{\sqrt{2}} (\varphi_1 + i\varphi_2) , \quad \varphi_i \in \mathfrak{Re} . \tag{4.50}$$

From action (4.49) we derive the following equations of motion

$$\ddot{\Phi} - D_i D_i \Phi + 2\mathcal{H}\dot{\Phi} + 2\lambda a^2(t)|\Phi|^2\Phi = 0, \tag{4.51}$$

$$\partial_0 F_{\mu 0} - \partial_i F_{\mu i} + 2e^2 a^2(t)\mathfrak{Im}[\Phi^* D_\mu \Phi] = 0. \tag{4.52}$$

As we are dealing with a gauge theory, we have a gauge freedom in the choice of the field components. This allows us to set, from now on, the condition $A_0 = 0$. In this case, the EOM of the gauge fields, Eq. (4.52), can be written in terms of its components as

$$\ddot{A}_j + \partial_j \partial_i A_i - \partial_i \partial_i A_j = 2e^2 a^2(t)\mathfrak{Im}[\Phi^* D_j \Phi], \tag{4.53}$$

$$\partial_i \dot{A}_i = 2e^2 a^2(t)\mathfrak{Im}[\Phi^* \Phi]. \tag{4.54}$$

Eq. (4.54) is the Gauss law, which represents a constraint that the solution to Eqs. (4.51) and (4.53) must preserve at all times. We also define the gauge-invariant electric and magnetic fields as usual, $E_i \equiv \dot{A}_i$ and $B_i = \frac{1}{2}\epsilon_{ijk}(\partial_j A_k - \partial_k A_j)$.

As in the global scenario, it is really useful to redefine the spacetime and field variables. On the one hand, we change to the same set of dimensionless spacetime coordinates $z^\mu = (z^0, z^i)$ introduced in Section 4.4,

$$z \equiv z^0 = H_* t, \quad z^i = H_* x^i, \tag{4.55}$$

and on the other hand, we define new Higgs and gauge field dimensionless variables as

$$h_j \equiv \frac{a(z)}{a_*} \frac{\varphi_j}{\varphi_*}, \qquad V_i \equiv \frac{1}{H_*} A_i. \tag{4.56}$$

(with $j = 1, 2; i = 1, 2, 3$) where $\varphi_* \equiv |\varphi(t_*)|$ is the initial modulus of the complex Higgs field at the end of inflation. To distinguish between different variables, we use a dot or a prime to denote differentiation with respect conformal or natural variables ($\dot{} \equiv d/dt, ' \equiv d/dz$), respectively. From now on, all spatial derivatives will also be with respect the new variables, unless otherwise stated. We also define a dimensionless covariant derivative as

$$\mathcal{D}_i \equiv \frac{\partial}{\partial z} - iV_i.$$

With these changes, Eqs. (4.51)-(4.54) can be written as

$$h_1'' - \mathfrak{Re}[\mathcal{D}_i \mathcal{D}_i(h_1 + ih_2)] + \beta^2(h_1^2 + h_2^2)h_1 = h_1 \frac{a''}{a}, \tag{4.57}$$

$$h_2'' - \mathfrak{Im}[\mathcal{D}_i \mathcal{D}_i(h_1 + ih_2)] + \beta^2(h_1^2 + h_2^2)h_2 = h_2 \frac{a''}{a}, \tag{4.58}$$

$$V_j'' + \partial_j \partial_i V_i - \partial_i \partial_i V_j = j_i(z), \tag{4.59}$$

$$\partial_i V_i' = j_0(z), \tag{4.60}$$

where the current $j_\mu(x)$ is defined as

$$j_\mu(x) \equiv q\beta^2 \mathfrak{Im}[(h_1 - ih_2)\mathcal{D}_\mu(h_1 + ih_2)] . \tag{4.61}$$

Finally, we also define dimensionless electric and magnetic fields as

$$\mathcal{E}_i \equiv V_i' = \frac{E_i}{H_*^2} , \qquad \mathcal{B}_i \equiv \frac{1}{2}\epsilon_{ijk}(\partial_j V_k - \partial_k V_j) = \frac{B_i}{H_*^2} . \tag{4.62}$$

Let us consider now the initial conditions of the different fields. For the homogenous mode of the Higgs field, we have, from Eq. (4.56) and by construction, $|h_*| \equiv |h(t_*)| = \sqrt{h_{1*}^2 + h_{2*}^2} = 1$ at the end of inflation. As long as this condition is satisfied, we can freely distribute this initial value between the components $h_{i*} \equiv h_i(t_*)$, thanks to the symmetries of the model. A convenient choice is $h_{1*} = 1$ and $h_{2*} = 0$. Moreover, as we are evolving the system of equations from the end of inflation, the Higgs initial velocity must obey the slow-roll condition $\dot{\varphi}_i(t_*) = -\lambda a_*^2 \varphi_*^2 \varphi_i / 2H_*$. With the previous choice for h_{1*} and h_{2*}, the slow-roll condition reads $h_{1*}' = 1 - \frac{\beta^2}{2}$ and $h_{2*}' = 0$. We also set the homogeneous mode of the gauge bosons to zero, $V_{i*} = V_{i*}' = 0$, until the onset of the oscillations at $z = z_{\text{osc}}$.

In this chapter, we have solved the system of Eqs. (4.57)-(4.60) in three-dimensional lattices. More specifically, we have solved a gauge-invariant set of analogous equations in a discrete spacetime. In all simulations, we have ensured that the lattice analogue of the Gauss conservation law Eq. (4.60) is preserved by the time evolution of the system to the machine precision. More details of the lattice formulation of the theory, as well as the preservation of the Gauss laws, are given in Appendix A of the thesis.

The system is solved in the following way. First, for the times $0 < z < z_{\text{osc}}$, we only evolve the homogeneous Higgs field with Eqs. (4.57) and (4.58), while the homogeneous gauge fields are kept to zero. At $z = z_{\text{osc}}$, we add fluctuations on top of the homogeneous modes of the different fields, allowing the gauge boson production to take place. Over the homogeneous mode of each Higgs component, we add Fourier modes with a spectrum $\langle |f_k|^2 \rangle = \frac{1}{2a^2\omega_k}$ (in physical variables), which mimics again the vacuum fluctuations of the ground state of a scalar field in a FRW background. On the other hand, the initialization of the gauge fields is more subtle and delicate than in the case of scalar fields. In this case, the fluctuations we add to the gauge fields must preserve the Gauss constraint Eq. (4.60) initially at every lattice point. We fix the gauge fields' amplitude in momentum space as

$$V_i'(\vec{k}, z_{\text{osc}}) = i\frac{k_i}{k^2} j_0(\vec{k}, z_{osc}) , \tag{4.63}$$

where in the lattice this is done with the corresponding lattice momenta. The implementation of these initial conditions is described in more detail in Section A.2.4 of Appendix A. From
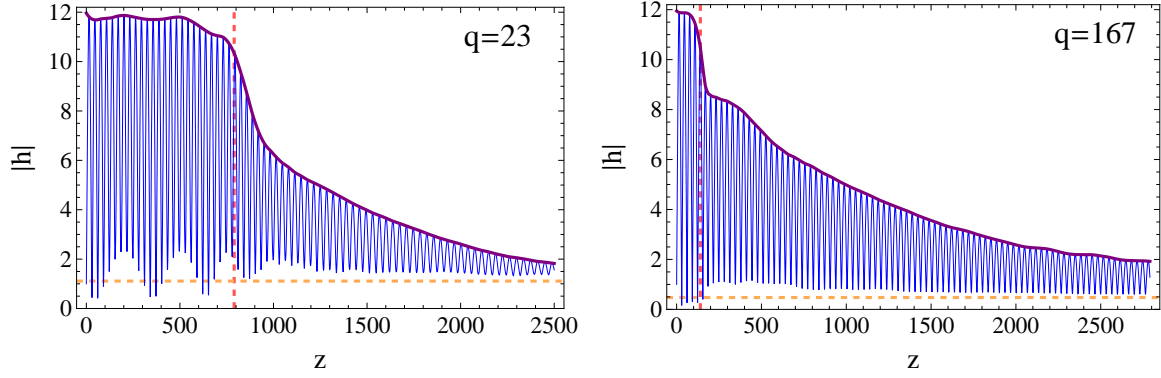
Figure 4.8.: We show in blue the volume-average value of the conformal Higgs field $|h|$ as a function of time for the resonance parameters $q = 23$ and $q = 167$, and in purple the maximum amplitude of the oscillations. The dashed vertical line indicates the approximate time at which the initial plateau finishes and the Higgs decay starts.

$z \geq z_{\text{osc}}$ onwards, the Gauss law is then preserved to machine precision by the gauge-invariant evolution of the system.

We now present the main results of the lattice simulations carried out for the Abelian-Higgs model. Like in the global scenario of Section 4.4, we have run simulations for several resonance parameters ranging from $q = 5$ to $q = 3000$. These values correspond to λ values between 2.5×10^{-5} and 1.5×10^{-2} for the W boson, and 5×10^{-5} and 3×10^{-2} for the Z boson. All results presented in this section will be obtained for a RD background ($w = 1/3$) and for $\beta = 0.01$. In Section 4.6 we will explain how these results can be extrapolated to other values of ω and β.

One of the main differences of the Abelian-Higgs model with respect to the global scenario is that now the Higgs field is described by a set of two components h_1, h_2, combined in a complex variable $h = h_1 + ih_2$. The quantity of interest that we must study is then the average value of the Higgs modulus, $|h| \equiv \sqrt{h_1^2 + h_2^2}$. We have plotted in Fig. 4.8 the volume-average of the Higgs modulus $|h|$ as a function of time, for the two resonance parameters $q = 23$ and $q = 167$. We find that the Higgs amplitude behaves qualitatively in a similar way as in the global scenario. This can be rapidly seen by comparing Fig. 4.8 to the equivalent Fig. 4.4 of the global scenario. In both scenarios, there is first a stage of few oscillations during which the (conformal) Higgs amplitude does not decay, corresponding to a *plateau* in the envelope function. After that, at times $z \gtrsim z_{\text{br}}(q)$, the Higgs amplitude starts decaying strongly. This time is indicated in both panels of Fig. 4.8 with a red dashed vertical line.

The time scale $z_{\text{br}}(q)$ signals, as in the global modelling, the moment at which the decay products (in this case, gauge bosons) have accumulated sufficient energy to start affecting the dynamics of the Higgs condensate. As before, this is understood better if we plot the different contributions to the energy, as a function of time. The energy density of the Abelian-Higgs

model is found to be

$$\rho(z) = \frac{V_*}{a^4(z)} E_t(z), \quad V_* \equiv \frac{\lambda}{4} |\varphi_*|^4, \tag{4.64}$$

where V_* is the value of the Higgs potential at the end of inflation. The function $E_t(z)$ is formed by the sum of the following contributions:

$$E_t(z) = E_K + E_{GD} + E_E + E_M + E_V. \tag{4.65}$$

Here E_K and E_V are the kinetic and potential energies of the Higgs field

$$E_K^\varphi = \frac{2}{\beta^2} \sum_i^2 \left(h_i' - h_i \frac{a'}{a} \right)^2, \quad E_V = (h_1^2 + h_2^2)^2,$$

E_{GD} is a gauge-invariant term formed by the product of two covariant derivatives of the Higgs field (hence containing the spatial Higgs gradients plus the interaction terms)

$$E_{GD} = \frac{2}{\beta^2} \sum_i \mathfrak{Re}[(\mathcal{D}_i(h_1 + ih_2))^* \mathcal{D}_i(h_1 + ih_2)], \tag{4.66}$$

and E_E and E_M are the electric and magnetic energy densities

$$E_E = \frac{2}{q\beta^4} \sum_i \mathcal{E}_i^2, \quad E_M = \frac{2}{q\beta^4} \sum_i \mathcal{B}_i^2. \tag{4.67}$$

We have plotted in the left panel of Fig. 4.9 the volume-averaged quantities as a function of time for the resonance parameter $q = 9$. We also show in the right panel of Fig. 4.9 the contribution of each energy component to the total, E_i/E_t, removing the oscillations of each component, and hence showing only the corresponding envelope functions. We see that initially the dominant contributions come from the kinetic and potential energies of the Higgs field. This corresponds to the oscillations of the condensate around the minimum of its potential, before it 'feels' the gauge fields. Meanwhile, the other components of the energy, E_E, E_M and E_{GD}, grow really fast, due to the energy transfer from the Higgs into the gauge fields. Note that for the whole evolution of the system (until equipartition is reached), the electric energy clearly dominates over the magnetic energy.

As in the global analogue, although gauge bosons are being strongly created, the Higgs condensate is at first unaffected. At $z \approx z_{br}(q)$ (indicated by a dashed red vertical line in the figures) the gauge energy has grown enough to start affecting significantly the Higgs condensate, and a sharp decrease of both the Higgs potential and kinetic energy start from then on. Physically, this happens when the fraction $\delta \equiv E_E/E_t < 1$ becomes sizeable, of the order $\delta \gtrsim 0.1$
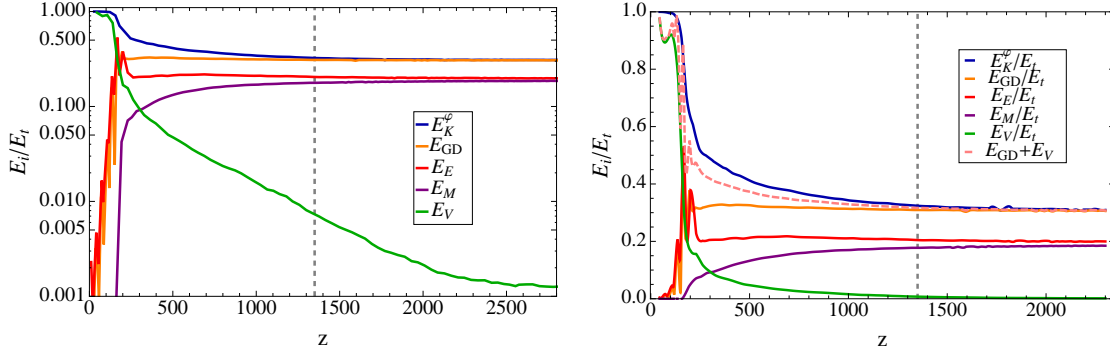
Figure 4.9.: Left panel: We plot the different contributions to the total energy of the system as a function of time, E_i/E_t [see Eq. (4.65)], for $q = 9$. All functions are oscillating, so we take the envelope of the corresponding oscillations for clarity. The dashed vertical line signals the Higgs decay time $z_{\text{dec}}(q)$. Right panel: We plot the same quantities with the same color code as in the upper panel, but now E_{GD} and E_V appear dashed, and we have added a new pink line corresponding to $E_{\text{GD}} + E_V$, which is the quantity that equipartitionates with E_K. Let us note that equipartition in the gauge sector, between the electric and magnetic contributions, is achieved later than in the scalar sector, at some time $z > z_{\text{dec}}(q)$.

As in the global scenario, for $z \gtrsim z_{\text{br}}(q)$ the Higgs kinetic and potential energies decrease sharply. The potential energy very soon becomes irrelevant compared to the other energy contributions, while the kinetic energy approaches an almost constant amplitude. Simultaneously, E_{GD} and E_E stop their growth, and also saturate to almost constant values. However, the magnetic energy continues to grow even after E_{GD} and E_E have been stabilized. Finally, at $z = z_{\text{dec}}$, the system arrives again at a stationary regime, in which equipartition between different components is clearly achieved. In this regime, 30% of the total energy goes to the Higgs kinetic part, 30% to E_{GD}, 20% to electric energy E_E, and 20% to magnetic energy E_M. The potential energy E_V also saturates to a constant, but it is very subdominant with respect to the other contributions. Quite remarkably, these numerical percentages are independent of the values q and β taken in our simulations. In other words, the final fractions of energies are universal within the Abelian-Higgs formulation[5].

We observe that the kinetic energy of the Higgs field E_K eventually becomes equal to $E_{\text{GD}} + E_V$. Since E_{GD} is gauge invariant, it contains both the Higgs gradient terms plus the Higgs interactions with the gauge fields. The evolution of the different energy components and the achievement of equipartition can be well appreciated in Fig. 4.9. Note that the quantity $E_{\text{GD}} + E_V$ can be naturally identified, in the global scenario, with the quantity $E_G^\varphi + E_{\text{int}} + E_V$. In that case we also observed equipartition according to the analogous equality $E_K \approx E_G^\varphi + E_{\text{int}} + E_V$.

---

[5]We shall see in Chapter 6 that this is still true if the non-Abelian nature of the interactions is considered.
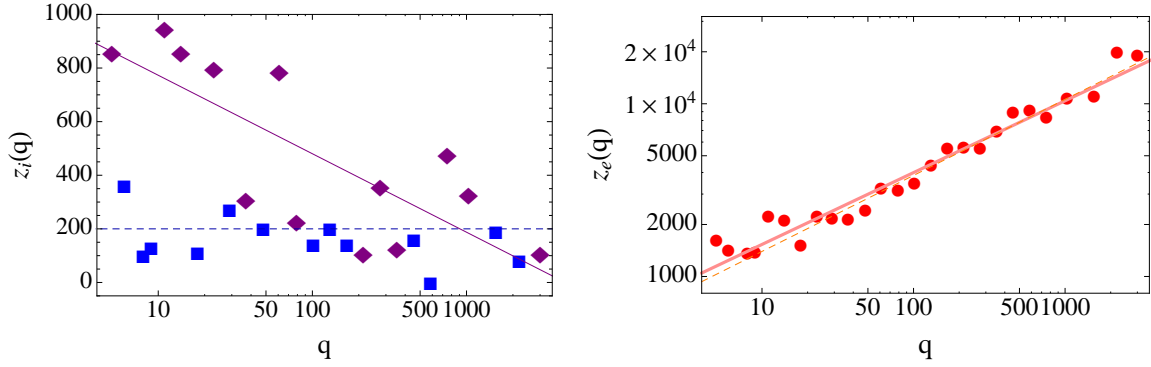
Figure 4.10.: Left: Different values of $z_{br}(q)$ obtained for different resonance parameters q, for a RD universe and for $\beta = 0.01$. Blue squares correspond to q values that are within a resonance band of the Lamé equation, while purple diamonds are points which are not. The purple line corresponds to the best fit (4.68), while the dashed blue line corresponds to the analytical estimate $z_{eff} \approx 200$, obtained from Eq. (4.32) ($\bar{\mu}_k = 0.2$). Right: Red points indicate the obtained Higgs decay times $z_{dec}(q)$ as a function of q, for the same Abelian-Higgs simulations, while the red thick line shows the best fit (4.69). The dashed yellow line shows the best fit of this same quantity obtained from the global simulations in Eq. (4.47).

It is useful to define the Higgs decay time as the moment when the Higgs kinetic energy results stabilized at the onset of the stationary regime. As in the global scenario, we will call this quantity $z_{dec}(q)$. Naturally, there is again some degree of arbitrariness in this definition. In the global scenario, we observed that a good operative criterion for defining z_{dec} was based on the degree of equipartition achieved. In our present gauge context, we have observed that an appropriate criterion is to take the moment when the relative difference between E_K and the sum $E_{GD} + E_V$ becomes less than 1%. We have indicated this time in Fig. 4.9, with a dashed vertical line. As we can observe in Fig. 4.9, our criterion $E_K \simeq E_{GD} + E_V$ holding better than 1%, coincides very well with the moment when all relevant energy densities have just stopped either growing or decreasing. Hence it defines very well what we mean by the end of the Higgs decay.

We have characterized again the dependence of z_{br} and z_{dec} with the different q's considered. We show in the upper panel of Fig. 4.10 the behavior of $z_{br}(q)$. In the figure, blue squares correspond to q values within a resonance band, and purple circles correspond to values outside bands. We see a clear trend, such that simulations with q within resonance bands have a smaller $z_{br}(q)$ than those with q between adjacent bands. Like in the global scenario, the order of magnitude of z_{br} for blue squares is approximated quite well with the analytical estimate $z_{eff} \approx 200$, obtained from Eq. (4.32), with $\bar{\mu}_k = 0.2$. At the same time, the purple circles can be fitted as

$$z_{br}(q) \sim 1066 - 127 \log q \,, \quad q \notin \text{Resonant Band} \,, \tag{4.68}$$
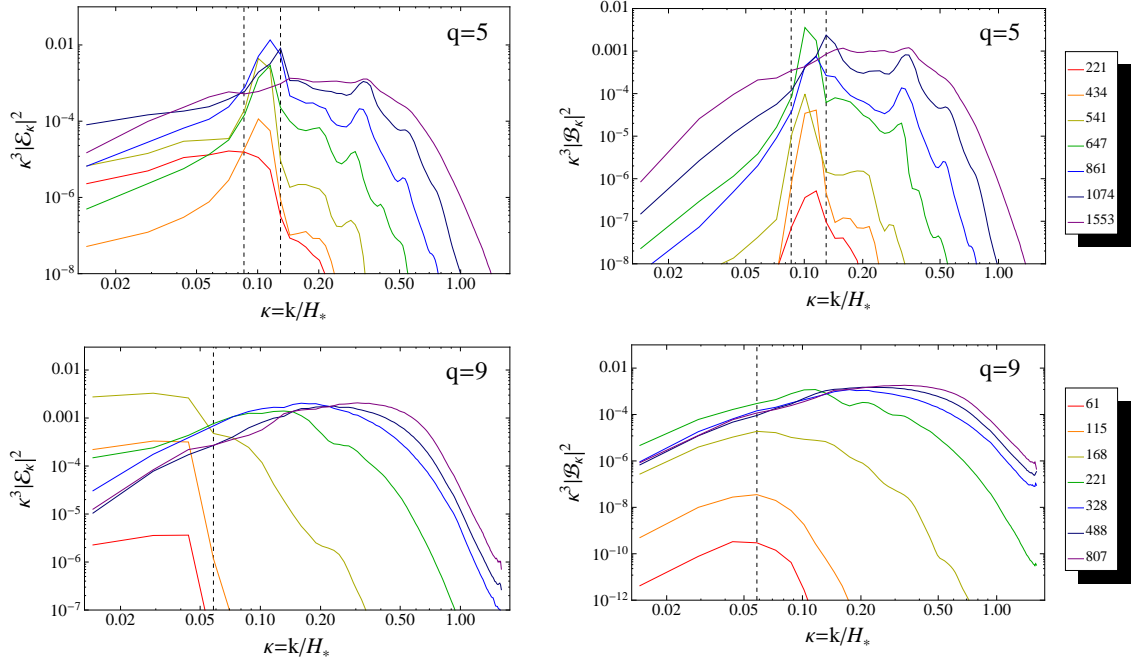
Figure 4.11.: Electric spectra $k^3|\mathcal{E}_k|^2$ and magnetic spectra $k^3|\mathcal{B}_k|^2$ for different times and for $q = 5$ (upper panels) and $q = 9$ (lower panels). The dashed, vertical lines indicate the corresponding position of the resonance band. The corresponding times at which the spectra are plotted are written at the right.

but their dispersion is much worse than in the global case (recall the left panel of Fig. 4.6).

In the right panel of Fig. 4.10, we also plot z_{dec} as a function of the resonance parameter q. We have obtained the following phenomenological fit

$$z_{\text{dec}}(q) = 588q^{0.42}, \tag{4.69}$$

indicated in the figure with a red continuous line. Note that we have plotted as well the corresponding fit obtained from the global simulations, Eq. (4.47), with a dashed line. Both fits coincide pretty well, indicating that the Higgs decay time $z_{\text{dec}}(q)$ obtained in the global scenario constitutes already a very good estimation. To some extent this is surprising, since one could expect that the extra terms in the gauge field's EOM could play some role, like for example modulating the decay time $z_{\text{dec}}(q)$ differently than in the case of only scalar fields. However, our results prove that this is not the case. In fact, they imply that the interaction term $g^2 A_\mu A^\mu \varphi^2$ (which is the only one kept in the global scenario) is the most relevant one when determining the Higgs decay time scale and the onset of the stationary regime.

Let us note again that the fit Eq. (4.69) is only valid for $\beta = 0.01$ and for a RD background. Using the theoretical extrapolation that we will present in Section 4.6, this can be generalized

to other β and w values as

$$z_{\text{dec}}(q) \approx 58.8\beta^{\frac{-(1+3\omega)}{3(1+\omega)}} q^{0.42} . \tag{4.70}$$

An alternative source of information about the Abelian-Higgs system comes from the spectra of the different fields. Since we are dealing with a gauge theory, all quantities of physical interest must be gauge invariant. We then plot in Fig. 4.11 the spectra of the electric and magnetic fields $k^3|\mathcal{E}_k|^2$ and $k^3|\mathcal{B}_k|^2$ for two different resonance parameters, $q = 5$ and $q = 9$. The latter is placed in the middle of a resonance bands, while the former is between the first and second resonance bands. The dashed vertical lines in the figures indicate the position of the resonantly excited momenta in each case. In the case $q = 5$, a peak clearly appears in both spectra at initial times, centered in the corresponding main resonance band. This confirms that the behavior derived from the Lamé equation describes well enough the real dynamics during the initial stages, even for the gauge theory. When the gauge bosons start to affect significantly the Higgs condensate, i.e. for $z \gtrsim z_{\text{br}}(q)$, both spectra start to displace to the right, populating modes of higher momenta. In this process, new subdominant peaks appear. As time goes on, the peaks disappear, and when the Higgs condensate has decayed [i.e for $z \gtrsim z_{\text{dec}}(q)$], the stationary state is established. For the case $q = 9$, the band of excited momenta is much wider (including modes down to $k = 0$), and consequently, the time scale $z_{\text{br}}(q) \approx 150$ is much smaller than for $q = 5$. For $q = 9$, the population of higher modes is much faster than for $q = 5$, and we do not observe additional subdominant peaks in the spectra.

4.5.1. Beyond the Abelian-Higgs

The real nature of the SM interactions is non-Abelian, since the EW sector of the SM is SU(2)$\times$ U(1) gauge invariant. In the EOM of the gauge bosons there are therefore nonlinear terms[6] of the form $\sim g^2 A^3, g A \partial A, g \partial A^2$, where we omit charge and Lorentz indices for simplicity. Following [128], one obtains that within the Hartree approximation, the terms $\sim g A \partial A, g \partial A^2$ vanish, so that in principle only the terms $\sim g^2 A^3$ contribute effectively to the dynamics of the gauge fields. We can write the effective mass entering into the gauge fields' EOM, as given by their interactions with the Higgs, plus a contribution from their own non-Abelian self-interactions. Symbolically, we will write this as

$$m_A^2 = g^2 \varphi^2 + \langle A^2 \rangle . \tag{4.71}$$

The Abelian-Higgs simulations capture the first term $g^2 \varphi^2$, which is due to the interaction with the Higgs, and is responsible for the resonant excitation of the gauge fields. The self-

---

[6]For the sake of clarity of the physics, we switch back to physical variables in the discussion of this subsection.

induced mass due to the gauge-field self-interactions is, of course, not present in the Abelian approach. This second term describes the nonlinearities of the non-Abelian nature of the SM interactions. Hence, only when the gauge fields have been excited with a sufficiently high amplitude $\langle A^2 \rangle \gtrsim g^2 \varphi^2$ may their presence have any relevance. The question is then: when do the gauge fields reach the critical amplitude $A \sim A_c \equiv g\varphi$?

The answer can be easily found by analyzing the effective mass of the Higgs. The non-Abelian nature of the interactions does not add any extra contribution into the effective mass of the Higgs field, given by

$$m_\varphi^2 = \lambda \varphi^2 + g^2 \left\langle A^2 \right\rangle . \tag{4.72}$$

These terms are already captured in our simulations, so the only difference in a non-Abelian simulation would come from the fact that A_μ is affected by the nonlinearities of its own EOM. The gauge fields backreact into the Higgs dynamics at the time $z = z_{\text{br}}(q)$, which corresponds physically with the moment when the amplitude of the gauge fields has grown – due to parametric resonance – up to $\langle A^2 \rangle \gtrsim \lambda \varphi^2 / g^2$. This condition corresponds, however, to a typical amplitude of the gauge fields $A \sim A(z_{\text{br}}) \equiv \sqrt{\lambda}\varphi / g$, which is much smaller than A_c. In particular, $\frac{A(z_{\text{br}})}{A_c} \sim \frac{1}{g\sqrt{q}} < 1$, for the typical broad resonant parameters $q \sim \mathcal{O}(10) - \mathcal{O}(10^3)$. The effective mass of the gauge bosons at $z \approx z_{\text{br}}$ is

$$m_A^2(z_{\text{br}}) \;=\; g^2 \varphi^2 + \left\langle A^2 \right\rangle_{z_{\text{br}}} \approx g^2 \varphi^2 \left(1 + \frac{1}{g^2 q} \right) , \tag{4.73}$$

where $\frac{1}{g^2 q} \ll 1$ for the typical values in this scenario. It is then clear that $m_A^2(z_{\text{br}}) \approx g^2 \varphi^2$, as if there were no effect from the gauge-field self-interactions. By the time the gauge-field resonant production backreacts on the Higgs dynamics, the gauge fields stop growing, as explained in detail in Section 4.5. Therefore, the non-Abelian terms (neglected in the Abelian-Higgs approach), are not expected to play any significant role in the dynamics of the system, except for low resonance parameters of the order $q \sim \mathcal{O}(10)$. It is, however, likely that the presence of the non-Abelian terms will possibly change the details of the achievement of the equipartition regime. Therefore, although we do not expect the time scale $z_{\text{br}}(q)$ to change significantly, the time scale $z_{\text{dec}}(q)$ will probably change moderately in the presence of non-Abelian corrections. In light of this analysis, we see *a posteriori* that neglecting the nonlinearities due to the non-Abelian nature of the SM interactions can be justified.

In any case, note that only lattice simulations of a SU(2)×U(1) gauge system can really assess whether the approach of ignoring the non-Abelianities is correct, or they have a sizeable effect in the Higgs and gauge post-inflationary dynamics. We will present such simulations in Chapter 6.

4.5.2. Abelian-Higgs model with three gauge fields

So far, we have studied the postinflationary Higgs dynamics in the lattice, mimicking its interaction with a single gauge boson using an Abelian-Higgs modelling. This has allowed us to obtain a bunch of interesting results, which depend greatly on the choice of the gauge boson resonance parameter, $q \equiv g^2/(4\lambda)$, with g^2 being the corresponding standard model coupling of either W or Z bosons. Naturally, we should include the three massive gauge bosons in our simulations (i.e. the W^+, W^- and Z), as in the EW sector of the standard model. Remarkably, the results presented so far for a single gauge field can be easily translated into the three-boson case, with an appropriate field redefinition. We explain this in what follows.

In the case of a Higgs decaying into three Abelian gauge fields, the Higgs equation can be written as

$$h'' - \mathcal{D}_i\mathcal{D}_i h + \beta^2|h|^2 h = h\frac{a''}{a} \,, \tag{4.74}$$

where $h \equiv h_1 + ih_2$, and the covariant derivative is now

$$\mathcal{D}_i \equiv \frac{\partial}{\partial z^i} - i(W_i^+ + W_i^- + Z_i) \,. \tag{4.75}$$

Here, W_μ^+, W_μ^-, and Z_μ are the corresponding fields of the W^+, W^-, and Z bosons, respectively. We describe the three fields in the temporal gauge, so that their 0 components are null. The EOMs of either of the W bosons are then

$$W_j'' + \partial_j\partial_i W_i - \partial_i\partial_i W_j = q_W\beta^2\mathfrak{Im}[h^*\mathcal{D}_i h] \,, \tag{4.76}$$

$$\partial_i W_i' = q_W\beta^2\mathfrak{Im}[h^*h'] \,, \tag{4.77}$$

with $q_W \equiv g_W^2/(4\lambda)$. Equivalently, the EOMs of the Z boson are

$$Z_j'' + \partial_j\partial_i Z_i - \partial_i\partial_i Z_j = q_Z\beta^2\mathfrak{Im}[h^*\mathcal{D}_i h] \,, \tag{4.78}$$

$$\partial_i Z_i' = q_Z\beta^2\mathfrak{Im}[h^*h'] \,, \tag{4.79}$$

with $q_Z \equiv g_Z^2/(4\lambda)$. Note that there is a Gauss law for each gauge field, representing as before, dynamical constraints of the system. Interestingly, this system can be reduced, with an appropriate redefinition of the gauge fields, to the case of a Higgs decaying into a single gauge field studied above. To see this, let us define the following effective gauge field and resonance parameter,

$$S_\mu \equiv W_\mu^+ + W_\mu^- + Z_\mu \,, \quad q \equiv q_Z + 2q_W = \frac{g_Z^2 + 2g_W^2}{4\lambda} \,. \tag{4.80}$$

If we consider the mapping

$$W_\mu^\pm \equiv \frac{q_W}{q} S_\mu \,, \quad Z_\mu \equiv \frac{q_Z}{q} S_\mu \,, \tag{4.81}$$

automatically $S_0 = 0$, and we can then reduce both the W EOM (4.76)-(4.77) and the Z EOM (4.78)-(4.79) to just

$$S_j'' + \partial_j \partial_i S_i - \partial_i \partial_i S_j = q\beta^2 \mathfrak{Im}[h^* \mathcal{D}_i h] \,, \tag{4.82}$$

$$\partial_i S_i' = q\beta^2 \mathfrak{Im}[h^* h'] \,, \tag{4.83}$$

where the covariant derivative of Eq. (4.75) is now simply $\mathcal{D}_\mu \equiv \partial_\mu - iS_\mu$.

Therefore, the three gauge bosons can be described[7] by a single *effective* gauge boson S_i, coupled to the Higgs with the resonance parameter q of Eq. (4.80). This property is very useful, since we just need to introduce only one effective gauge field, Eq. (4.80), and the system is then fully described by Eqs. (4.74), (4.82) and (4.83). As an example, if we have $q_W = 14$ and $q_Z \simeq 2q_W = 28$, all three gauge bosons can be described by the EOM of a single gauge field with resonance parameter $q = 28 + 14 + 14 = 56$. In other words, the system behaves in such a way that the three gauge bosons have the same effective resonance parameter. From Eq. (4.81), we find the following relation between the W and Z amplitudes

$$Z_i(z) = \frac{q_Z}{q_W} W_i^+(z) = \frac{q_Z}{q_W} W_i^-(z) \,, \tag{4.84}$$

which at very high energies, when $q_Z \approx 2q_W$, reduces simply to $Z_i(z) \approx 2W_i^+(z) \approx 2W_i^-(z)$. Eq. (4.84) follows in all spacetime (and in the lattice, in all sites at all times).

We have just seen that the dynamical equations of the Higgs coupled to three gauge bosons can be reduced to a system with the Higgs coupled to only one gauge boson, with resonance parameter $q = q_Z + 2q_W$. However, strictly speaking, both scenarios are not really identical, if we compare them for the same q and β. On the one hand, in the simulations with just one gauge boson (say the W boson), the Higgs self-coupling is simply $\lambda = \lambda_{1B} \equiv g_W^2/4q$. On the other hand, in the simulations with three gauge bosons, it is $\lambda = \lambda_{3B} \equiv (2g_W^2 + g_Z^2)/4q$ [see Eq. (4.80)], which differs in a factor $(2 + (g_Z/g_W)^2)$ with respect to λ_{1B}. The spectrum of initial fluctuations of the Higgs field depends explicitly on λ, so initial conditions change, and consequently, both systems are not exactly equivalent. It is crucial, then, that we figure out the importance of these differences. For this, we have run a new set of lattice simulations, including one effective gauge boson S_μ, with the appropriate Higgs self-coupling $\lambda = \lambda_{3B}$ (which as explained, exactly imitates the three Abelian gauge bosons). We have then compared our results with the ones obtained previously, for a single gauge boson with coupling $\lambda = \lambda_{1B}$.

---

[7]As we shall see in Section 6.2, this property can be generalized to the case of an arbitrary number of Abelian gauge bosons.
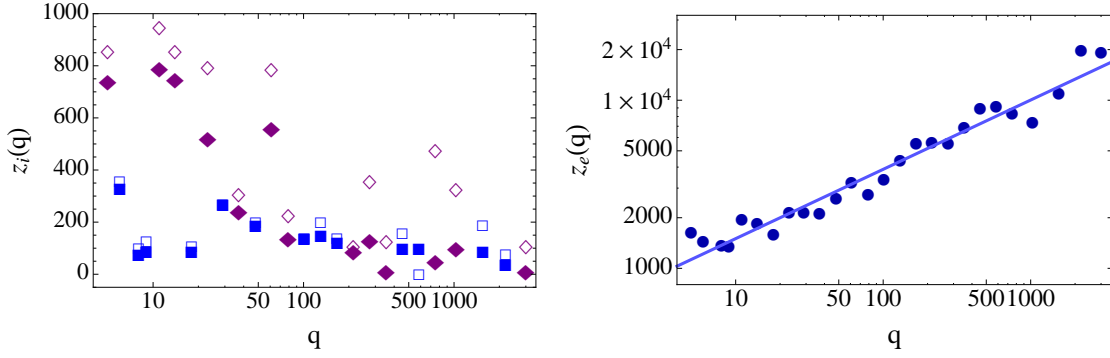
Figure 4.12.: Left: Filled points show the $z_{\text{br}}(q)$ times obtained from simulations with an effective gauge boson S_μ, whereas empty points show the analogous results from simulations with a single W_μ boson shown in Fig. 4.10. Blue squares and purple diamonds correspond to q values inside and outside a resonance band of the Lamé equation. Right: points represent the $z_{\text{dec}}(q)$ values obtained for the effective S_μ boson, whereas the blue line corresponds to the phenomenological fit of Eq. (4.85).

In Fig. 4.12 we have plotted the new time scales z_{br} (left panel) and z_{dec} (right panel) as a function of q, obtained from the simulations with $\lambda = \lambda_{3B}$. In the first panel, we have also plotted the results for z_{br}, obtained above from the simulations with $\lambda = \lambda_{1B}$. We observe that the times z_{br} at which the plateau ends are reduced slightly with respect to the W-boson case when q is outside a resonance band, but they are almost identical when it is within a band; see Fig. 4.12. There are, however, virtually no differences in the time scale z_{dec}, which signals again both the end of the Higgs decay and the onset of equipartition. The new fit of z_{dec} from the simulations with an effective gauge boson S_μ is

$$z_{\text{dec}}(q) = 581q^{0.42} = 581(q_Z + 2q_W)^{0.42} \,, \qquad (4.85)$$

very similar to the old fit Eq. (4.69). Note that, as mentioned before, this fit is done for a RD universe with $\beta = 0.01$. Anticipating again the results that we will explain in Section 4.6, the generalization of this fit to other β values and expansion rates (characterized by ω) is

$$z_{\text{dec}}(q) \approx 58.1\beta^{\frac{-(1+3\omega)}{3(1+\omega)}}(2q_W + q_Z)^{0.42} \,, \qquad (4.86)$$

This equation probably represents the most relevant result of this chapter. We see that the real decay time z_{dec} of the Higgs into the three gauge bosons $W^\pm, Z$ is, using again the approximate high-energy relation $q_Z \approx 2q_W$, a factor $((q_Z + 2q_W)/q_W)^{0.42} \approx 4^{0.42} \approx 1.79$ times longer than if we only considered the decay of the Higgs into a single W boson [equivalently, a factor $((q_Z + 2q_W)/q_Z)^{0.42} \approx 2^{0.42} \approx 1.34$ longer if we considered the decay of the Higgs into a Z boson].

It seems surprising at first glance, that the decay takes longer when the resonance parameter is effectively larger, $q = 2q_W + q_Z > q_W$; naively one would expect a faster decay if there are

more bosons into which to decay. This is, however, a reflection again of the nonlinear behavior of the system at $z \gtrsim z_{br}$, responsible for the previously discussed counterintuitive growth of $z_{dec}(q)$ with q.

We have also observed that the energy equipartition does not to change with respect to the single W boson case. The final equipartition state is identical to the previously studied case of one single boson, reaching at late times,

$$\frac{E_K}{E_t} \approx 0.3 \, , \quad \frac{E_{GD}}{E_t} \approx 0.3 \, , \quad \frac{E_E}{E_t} \approx 0.2 \, , \quad \frac{E_M}{E_t} \approx 0.2 \, , \tag{4.87}$$

and $E_V/E_t \ll 1$. Note also that, in the case of three gauge bosons, we have three different electric and magnetic fields. From the relation $Z_i(z) = 2W_i(z)$ (valid at high energies), and given the definition of the electric and magnetic energies, we see that 50% of the total electric energy corresponds to the Z boson, while the other 50% is divided equally between the other two W bosons. The same distribution takes place for the magnetic energy.

4.6. Varying the Higgs initial amplitude and the expansion rate

All results from sections 4.4 and 4.5 have been presented for a scale factor evolving in a RD universe ($\omega = 1/3$), and for $\beta = 0.01$. Naturally, in order to fully understand the dynamical properties of the Higgs decay after inflation, we have explored other β parameters, and we have also considered other expansion rates such as MD ($\omega = 0$) or KD ($\omega = 1$). Fortunately, one can easily extrapolate the results from one particular set of parameters, say (β_1, ω_1), to another set (β_2, ω_2), using the analytical properties of the Higgs equation described in Section 4.2.

More specifically, we saw in Eq. (4.14) that in the case of no coupling to the gauge bosons, the conformal period Z_T and the value of the transformed Higgs field at the first maximum $h(z_M)$, can be approximated as $Z_T = c_1 \beta^{\frac{-(1+3\omega)}{3(1+\omega)}}$ and $h(z_M) = c_2 \beta^{-\frac{2}{3(1+\omega)}}$, where c_1 and c_2 are constants independent of ω and β. From these properties we can see that, if for a given set of values (ω_1, β_1), the volume-averaged Higgs field takes the value $h(\beta_1, \omega_1)$ at the time $z(\beta_1, \omega_1)$, then for (ω_2, β_2) the Higgs field at the time

$$z(\beta_2, \omega_2) \simeq \beta_2^{\frac{-(1+3\omega_2)}{3(1+\omega_2)}} \beta_1^{\frac{(1+3\omega_1)}{3(1+\omega_1)}} z(\beta_1, \omega_1) \, , \tag{4.88}$$

should take the value

$$h(\beta_2, \omega_2) \approx \beta_2^{\frac{-2}{3(1+\omega_2)}} \beta_1^{\frac{2}{3(1+\omega_1)}} h(\beta_1, \omega_1) \, . \tag{4.89}$$
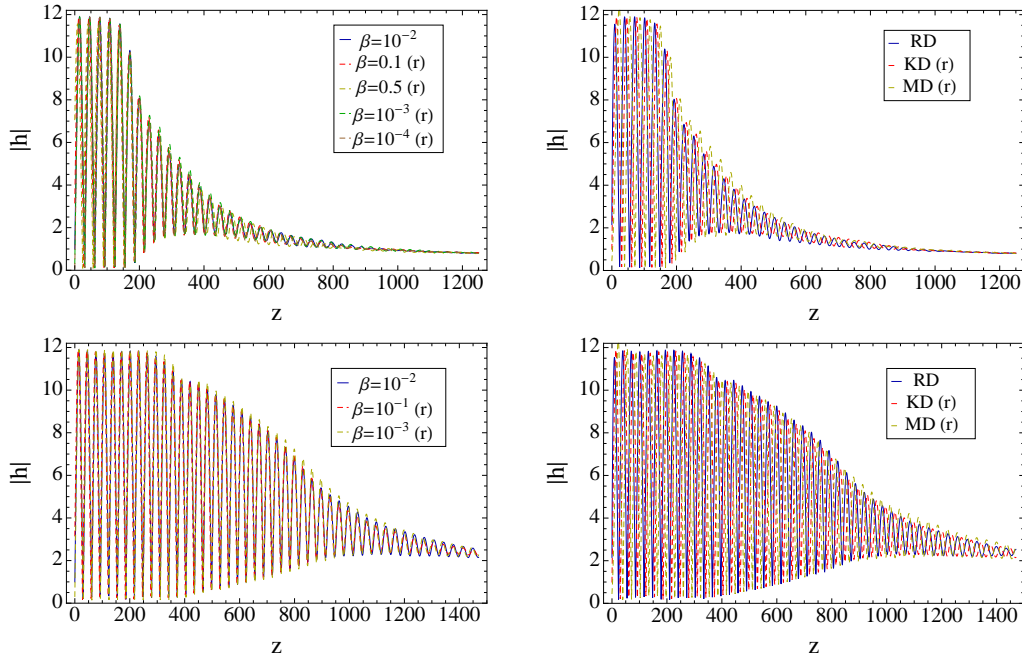
Figure 4.13.: We plot the volume-averaged value of the Higgs conformal field $|h|$ as a function of time, obtained directly from our simulations, for either different β parameters or expansion rates. Lines with the symbol '(r)' have been extrapolated, using an inversion of Eqs. (4.88) and (4.89), to obtain a theoretical prediction of the results of a RD universe ($\omega = 1/3$) with $\beta = 0.01$. The top panels correspond to global simulations with $q = 8$, and the bottom panels correspond to Abelian-Higgs simulations with $q = 6$. In the left panels, we vary β, while in the right panels, we vary ω. We see that the lattice results for $(\omega, \beta) = (1/3, 0.01)$ coincide quite well with the different theoretical extrapolations obtained from the lattice results for other (ω, β) parameters.

Notably, this property is maintained quite well even in the presence of a Higgs coupling to its decay products (either scalars in the global simulations or gauge bosons in the Abelian-Higgs simulations). This extrapolation is therefore very powerful[8]. In Fig. 4.13, we have plotted the volume-averaged value of $|h|$ as a function of time, for both global (top panels) and Abelian-Higgs simulations (bottom panels). Let us focus for instance on the top-left panel. We have obtained for $q = 8$ the behavior of $|h|$ as a function of time for $\beta = 10^{-4}, 10^{-3}, 10^{-2}, 10^{-1}$, and 0.5, directly from the simulations. Using the outcome from these simulations with different β parameters, we have then inverted Eqs. (4.88) and (4.89), and obtained the (extrapolated) behavior corresponding to $\beta = 0.01$. These are different predictions for the Higgs decay when $\beta = 0.01$, but obtained from the real data from simulations with different β values. We see that the four different extrapolated theoretical predictions obtained for $\beta = 10^{-4}, 10^{-3}, 10^{-1}$ and 0.5 coincide very well with the real simulation for $\beta = 0.01$.

---

[8]As we shall see in Chapter 6, this extrapolation also works in the lattice simulations of the SU(2)$\times$U(1) gauge-invariant system.

The same is done in the top-right panel, but changing the scale factor instead of β (which we fix in this figure as $\beta = 0.01$). There, we compare the result of the Higgs decay for $w = 1/3$ (RD), on one hand obtained directly from simulations with $\omega = 1/3$, and on the other hand from the corresponding extrapolated predictions from the lattice simulations with $\omega = 0$ (MD) and $\omega = 1$ (KD). The three lines also coincide very well. The same analysis is repeated for Abelian-Higgs simulations in the two bottom figures, with identical conclusions.

This property allows us to extrapolate easily the results for the Higgs decay time for a RD universe with $\beta = 0.01$, presented in the last two sections, to another set of (ω, β) parameters. In particular, from Eq. (4.47) we obtain Eq. (4.48), from Eq. (4.69) we obtain Eq. (4.70), and from Eq. (4.85) we obtain Eq. (4.86).

4.7. Summary

If the EW vacuum is stable with the Higgs self-coupling kept positive, the Higgs typically develops a large VEV during inflation, representing a classical condensate, homogeneous over scales exponentially larger than the inflationary radius $1/H_*$. In this chapter we have studied the relaxation of the Higgs, i.e. its decay, during the stages following immediately after inflation. We have used different methods of progressive complexity, accuracy and proximity to the real case of the SM. We have modelled the SM interactions in a two-step manner. First, considering a global scenario, ignoring the gauge structure of the SM, and representing the gauge fields as a collection of scalar fields appropriately coupled to the Higgs. Secondly, we have considered an Abelian gauge scenario, with the gauge fields and the Higgs embedded within an Abelian-Higgs framework, but ignoring the nonlinearities due to the truly non-Abelian nature of the SM. For the global model we have presented both analytical (Section 4.3.1) and lattice calculations (Section 4.4), whereas in the most precise and involved gauge modelling, we have just presented the outcome from lattice simulations (Section 4.5).

The analytical results of the global modelling estimate correctly the right order of magnitude of the Higgs decay time. When studying such scenario in the lattice, including all nonlinearities within such a scheme, we find that the actual Higgs decay takes longer, typically a factor $z_{\text{dec}}/z_{\text{eff}} \sim 3.17 q^{0.44}$ larger: see Eq. (4.48) for z_{dec} and Eq. (4.32) for z_{eff}. This is because the analytical calculations are only capable of estimating the order of magnitude of the time scale when sufficient energy has been transferred into the extra scalar fields (mimicking the EW gauge bosons). However, that time only signals the moment $z = z_{\text{br}}(q)$ when the Higgs condensate really starts noticing that it is coupled to extra species. From then on, at times $z \gtrsim z_{\text{br}}(q)$, the Higgs energy density begins to decrease in a noticeable manner, being transferred to the most strongly coupled species, the EW gauge bosons. It is this decrease of the energy of the Higgs that should be interpreted as the decay of the Higgs. Eventually, the Higgs energy density

saturates to an approximately constant value, at some moment $z_{dec}(q) > z_{br}(q)$. Around the same time, the energy of the species coupled to the Higgs has also stopped growing, and saturates into slowly evolving magnitudes.

Very interestingly, the same pattern and time scales are observed in the gauge scenario, though the final fractions of energies are different. The time scale $z_{dec}(q)$ that characterizes the end of the Higgs decay in the gauge case is given by Eq. (4.70), which represents a factor $z_{dec}/z_{eff} \sim 3.68q^{0.42}$ larger than the analytical prediction z_{eff} of Eq. (4.32). We see therefore that, at the end, the differences between the global and gauge modelings are not so relevant, at least in terms of the estimation of the Higgs decay time $z_{dec}(q)$. It is worth stressing that $z_{dec}(q)$ grows with q (both in the global and gauge scenarios), which could be thought as being a counter-intuitive fact. This is due to the nonlinearities characteristic of the system, which become relevant from $z \gtrsim z_{br}$ onwards.

One of our more interesting results is the extrapolation laws Eqs. (4.88),(4.89). We have seen that the dynamics of the system depend basically on three parameters: q, β, and the expanding background equation of state ω. Eqs. (4.88),(4.89) allow us to extrapolate the lattice results for parameters (ω_1, β_1) into a very good approximation of the results of another set of parameters (ω_2, β_2). This technique works very well indeed for both global and Abelian-Higgs simulations (see Fig. 4.13), and as we shall see in Chapter 6, it also works in the simulations of the SU(2)×U(1) system. This has led us to obtain the generic formula for the Higgs decay time z_{dec}, Eq. (4.86), as a function of β, q and ω.

Remarkably, we have also shown that the case of the SM, where the Higgs is coupled simultaneously to the three EW gauge bosons W^+, W^- and Z, behaves identically to the case in which the Higgs is only coupled to one *effective* gauge boson, with resonance parameter $q = q_Z + 2q_W$. We have found that when the three gauge bosons are considered, $z_{dec}(q) = 581(q_Z + 2q_W)^{0.42}$ [Eq. (4.85)]. The decay of the Higgs takes then a factor $(2 + q_Z/q_W)^{0.42}$ larger than if the Higgs were coupled to only one W boson, or equivalently $(1 + 2q_W/q_Z)^{0.42}$ times larger than if it were coupled to only Z gauge bosons. Again, this counterintuitive result is due to the nonlinearities that dominate the system at $z \gtrsim z_{br}$.

Interestingly, at the time $z \approx z_{dec}(q)$, in both in the global and gauge scenarios, we see that the distributions of fields reach equipartition. In the global model we find that the kinetic energy of the Higgs becomes equal to the sum of the gradient energy of the Higgs plus the interaction with the χ_i fields, $E_K^\varphi \simeq E_G^\varphi + E_{int}$. This equality holds to better than 1 % from $z \gtrsim z_{dec}$ onwards. In the gauge scenario, we find that the kinetic energy of the Higgs becomes equal to the sum of the covariant gradient energy (which includes the Higgs-gauge interactions) plus the Higgs potential, $E_K \simeq E_{GD} + E_V$. This equality also holds to better than 1% from $z \gtrsim z_{dec}(q)$ onwards. At some later time $z \gtrsim z_{dec}$, the electric and magnetic energy densities also reach equipartition to better than 1%, $E_E \simeq E_M$. The distribution of energy in the gauge

scenario is actually universal, since the system always reaches equipartition, with $E_K \simeq E_{GD}$ representing 30% of the total energy, and $E_E \approx E_M$ representing 20% each. In both global and gauge scenarios, once in the stationary equipartitioned regime, the potential energy becomes gradually more and more irrelevant.

The decay of the Higgs condensate during the early postinflationary stages constitutes an important event in the evolution of the Universe, which might have interesting cosmological consequences. For example, the possibility has been proposed in Ref. [139, 140] of realizing baryogenesis via leptogenesis, thanks to the Higgs oscillatory behavior. Also, if dark matter is a gauge singlet field coupled to the Higgs, it is also possible that the Higgs oscillations could produce the right amount of dark matter, such that its distribution could account for the correct relic abundance [141]. Finally, as we shall see in the next chapter, the fields excited from the decay of the Higgs may act as a source of gravitational waves.

Chapter 5.

Gravitational wave production from the Higgs decay after inflation

We study in this chapter the gravitational waves produced during the post-inflationary decay of the SM Higgs after inflation. The out-of-equilibrium dynamics of the process converts a fraction of the available energy into gravitational waves (GW). We study this process with classical lattice simulations in an expanding box, following the energetically dominant electroweak gauge bosons $W^\pm$ and Z. We characterize the GW spectrum as a function of the running couplings, Higgs initial amplitude, and post-inflationary expansion rate. Our study demonstrates the efficiency of GW emission by gauge fields undergoing parametric resonance. The initial energy of the Higgs condensate represents however, only a tiny fraction of the inflationary energy. Consequently, the resulting background is very suppressed, with an amplitude $h^2\Omega_{\rm GW}^{\rm (o)} \lesssim 10^{-29}$ today. The amplitude can be boosted to $h^2\Omega_{\rm GW}^{\rm (o)} \lesssim 10^{-16}$, if following inflation the universe undergoes a kination-domination stage; however the background is shifted in this case to high frequencies $f_p \lesssim 10^{11}$Hz. In all cases the signal is out of the range of current or planned GW detectors. This background will therefore remain, most likely, as a curiosity of the SM.

Results presented in this Chapter have been published in Ref. [2].

5.1. Introduction

In this chapter we study the production of gravitational waves within the framework of the Standard Model of particle physics. We consider the same scenario as in Chapter 4: we assume that the Higgs fluctuates during inflation, and forms a condensate at the end of inflation with typical amplitude given by Eq. (4.5). After inflation, the Higgs condensate starts oscillating around the minimum of its potential. This gives rise to its decay into all the species of the SM, as the latter are non-perturbatively excited through parametric effects. All the SM species coupled directly to the Higgs, i.e. the electroweak gauge bosons $W^\pm$, Z, and the massive fermions

(quarks and charged leptons), are all highly excited. This is a violent non-equilibrium process, that create large time-dependent matter density inhomogeneities, which therefore act as a classical source of gravitational waves.

The GW production coming form the decay of the Higgs field into fermions was studied in [122], following the formalism of [120, 121]. Fermions are excited through parametric effects [29, 30], though the growth of their occupation numbers is Pauli blocked. The most energetic fermion species excited is the top quark, since its Yukawa coupling is the largest one within the SM. In this chapter we focus instead in the production of GW by the gauge bosons. The gauge field production is expected indeed to be more efficient than that of fermions, as their occupation numbers grow exponentially through a process of parametric resonance. Most of the energy of the Higgs condensate is actually transferred into the electroweak $W^{\pm}, Z$ gauge bosons. Therefore, even if the final GW background is contributed by all the Higgs decay product species, the gauge fields we study here represent in fact the dominant contributors.

In Chapter 4 we presented a full set of lattice simulations of the Higgs decay process into gauge bosons, modeling the SM gauge interactions with both global and Abelian-Higgs setups. In this chapter, we will study the GW production, again with lattice simulations of an Abelian-Higgs setup. This is just an approximation to the gauge structure of the electroweak interactions. However, as analyzed in Section 4.5.1, the non-Abelian corrections are suppressed by the smallness of the Higgs self-coupling. In high-energy inflationary models, the Higgs self-coupling runs in fact into small values [132, 131], making the non-Abelian corrections less relevant. In this chapter we are mostly interested in scenarios with the highest possible energy scale of inflation, as this enhances the production of GW in the system. Therefore, the use of an Abelian modeling will suffice for our aim to study the GW production from the SM fields after inflation.

The structure of this chapter is as follows. In Section 5.2 we discuss our formalism to study GW production in this process. In Section 5.3 we present our results, describing the general features of the GW spectra obtained from our lattice simulations. In Section 5.4 we parametrize the GW spectra as a function of the Higgs initial amplitude, Higgs self-coupling, and post-inflationary expansion rate, and discuss how the GW background redshifts until today. Finally, in Section 5.5 we wrap up our results and conclude.

5.2. Gravitational wave production

Gravitational waves (GW) follow the equations of motion

$$\ddot{h}_{ij} + 2\frac{\dot{a}}{a}\dot{h}_{ij} - \partial_k \partial_k h_{ij} = \frac{2}{m_p^2}\Pi_{ij}^{\mathrm{TT}} , \tag{5.1}$$

where the source of GW, $\Pi_{ij}^{\rm TT}$, is the *transverse-traceless* (TT) part of the anisotropic stress tensor Π_{ij}. In this Chapter, we will mimic the interactions between the Higgs and gauge fields with the Abelian-Higgs modelling described in Section 4.5. The action of the theory was written in Eq. (4.49), and the corresponding field equations of motion were displayed in Eqs. (4.51)-(4.54). In our case, in the presence of both scalar and vector fields, the source is effectively given by [142]

$$\Pi_{ij}^{\rm TT} = \left\{ 2\mathfrak{Re}[(D_i\varphi)^*(D_j\varphi)] - \frac{1}{e^2 a^2}(E_i E_j + B_i B_j) \right\}^{\rm TT} , \tag{5.2}$$

where $\{...\}^{\rm TT}$ represents the TT part of the quantity inside the brackets. Here, we fix $e^2 = (2g_W^2 + g_Z^2)/4$, , so that the gauge field A_μ effectively describes the simultaneous decay of the Higgs field into the the Z and $W^\pm$ bosons (see Section 4.5.2 for an extensive discussion about this). From Eq. (5.2), we clearly see that both the Higgs and the gauge bosons contribute as a source of GW.

It is convenient to redefine the tensor mode amplitude through a conformal redefinition like $h_{ij} \equiv \bar{h}_{ij}/a$ (recall that initially we take $a_* = 1$), so that Eq. (5.1) can be written in terms of the dimensionless variables Eqs. (4.55) and (4.56) as

$$\bar{h}_{ij}'' - \left(\partial_k \partial_k + \frac{a''}{a} \right) \bar{h}_{ij} = \frac{2}{a}\frac{1}{\lambda}\left(\frac{H_*}{m_p} \right)^2 \mathcal{P}_{ij}^{\rm TT} , \tag{5.3}$$

with

$$\mathcal{P}_{ij} = \mathcal{P}_{ij}^{[h]} + \mathcal{P}_{ij}^{[g]} , \tag{5.4}$$

$$\mathcal{P}_{ij}^{[h]} \equiv \beta^2 \mathfrak{Re}[(D_i h)^*(D_j h)] , \qquad \mathcal{P}_{ij}^{[g]} \equiv -\frac{1}{q}(\mathcal{E}_i \mathcal{E}_j + \mathcal{B}_i \mathcal{B}_j) . \tag{5.5}$$

Here, $\mathcal{E}_i$ and $\mathcal{B}_i$ are the natural electric and magnetic fields, defined in Eq. (4.62), and the effective resonance parameter is $q \equiv (2g_W^2 + g_Z^2)/(4\lambda)$.

The spectrum of the GW energy density contained within a volume V, and normalized to the total energy density $\rho_{\rm tot}$ of the Universe (at the time of GW production), can be written in the continuum as

$$\Omega_{\rm GW}(k,z) \equiv \frac{1}{\rho_{\rm tot}}\frac{d\rho_{\rm GW}}{d\log k}(k,z) = \frac{1}{8\pi^2 a^2}\frac{m_p^2}{\rho_{\rm tot}}\frac{k^3}{V}\left\langle \dot{h}_{ij}^*(k,z)\dot{h}_{ij}(k,z) \right\rangle_{4\pi} \tag{5.6}$$

where $\langle...\rangle_{4\pi} \equiv \frac{1}{4\pi}\int d\Omega_k ...$, with $d\Omega_k$ a solid angle differential in **k**-space. In light of the parameters factorized out in the source term of Eq. (5.3), it is convenient to define a new gravitational wave variable ω_{ij} as

$$\bar{h}_{ij}(k,z) \equiv \frac{2}{\lambda}\left(\frac{H_*}{m_p} \right)^2 w_{ij}(k,z) . \tag{5.7}$$

We can hence express $\Omega_{\mathrm{GW}}(k,z)$ in terms of the natural variables of the problem as

$$\Omega_{\mathrm{GW}}(k,z) \equiv \delta_* \, \epsilon_w(a) \, \Theta_{\mathrm{GW}}(k,z) \,, \quad \delta_* \equiv \left(\frac{H_*}{m_p}\right)^4 \,, \quad \epsilon_w(a) \equiv \left(\frac{a}{a_*}\right)^{3w-1} \,, \quad (5.8)$$

where we define

$$\Theta_{\mathrm{GW}}(k,z) \equiv \frac{k^3}{6\pi^2\lambda^2} \frac{1}{V} \left\langle (w'_{ij} - \mathcal{H}w_{ij})(w'_{ij} - \mathcal{H}w_{ij}) \right\rangle_{4\pi} \,. \quad (5.9)$$

with $\mathcal{H} \equiv a'/a$. This way, we have factorized out the dependence with the Hubble scale H_* and the background expansion rate. In order to derive Eqs. (5.8)-(5.9), we have used that the total energy density of the Universe can be expressed as $\rho_{\mathrm{tot}} = 3m_p^2 H_*^2 a^{-3(1+w)}$, with w the post-inflationary equation of state. The factorization $\Omega_{\mathrm{GW}} = \delta_*\epsilon_w\Theta_{\mathrm{GW}}$ in Eq. (5.8) is indeed very convenient: the dependence on $\{q_s, \beta, w\}$ of $\Theta_{\mathrm{GW}}(k,z)$, comes only from the effect of these parameters on the solution of the field *eom*, Eqs. (4.57)-(4.60).

Note that the prefactor δ_* in Eq. (5.8), implies a suppression of the GW (energy density) as $\sim (H_*/m_p)^4 \lll 1$. This effect is related to the fact that the typical initial amplitude of the Higgs condensate is $\varphi_*^2 \sim \varphi_{\mathrm{rms}}^2 \sim H_*^2$, which is then suppressed by the appearance of a Planck mass factor as $1/m_p^2$ in the *rhs* of the GWs' Eq. (5.1). The scaling $\propto \delta_*$ is ultimately responsible for the smallness of the GW background today, as we will emphasize later on in section 5.4.1. Note that in standard preheating scenarios, say after chaotic inflation, the inflaton and preheat fields dominate the energy budget of the universe, and have typically much larger field amplitudes. Therefore, there is no such suppression in standard preheating via parametric resonance. However, the production of GW from subdominant field(s), like inflationary spectator fields as in our case, will be always suppressed by the smallness of the fields amplitude $\varphi \sim H_* \ll m_p$, as seen in Section 3.5.

Depending on whether the post-inflationary equation of state is stiff, $w > 1/3$, or not, $w \leq 1/3$, the background energy density of the Universe will correspondingly decrease slower or faster than relativistic species. The prefactor $\epsilon_w = (a/a_*)^{3w-1}$ in Eq. (5.9) will, therefore, either suppress the GW background as $\propto \epsilon_w < 1$ for $w < 1/3$ (e.g. $w = 0$ for MD), or enhance it as $\propto \epsilon_w > 1$ for $w > 1/3$ (e.g. $w = 1$ for KD). For $w = 1/3$ the background energy density corresponds to a RD Universe, and hence $\epsilon_w = 1$, so that there is neither a suppression nor an enhancement. In a KD scenario with $w = +1$, the amplitude of the GW background will be maximally enhanced since $\epsilon_w \gg 1$. However, as we shall see in Section 5.4.1, the large suppression due to $\delta_* \ll 1$ will still dominate over this enhancement, so that the overall modulation of the signal is $\Omega_{\mathrm{GW}} \propto \delta_*\epsilon_w \sim (H_*/m_p)^2$, which still represents a suppression, though a milder one.

In order to solve the *eom* Eq. (5.3) for the GW, we have followed the standard procedure first introduced in [79], solving a relativistic wave-like equation in real space sourced by the

full $\mathcal{P}_{ij}$, with no TT projection,

$$u_{ij}'' - \left(\partial_k \partial_k + \frac{a''}{a} \right) u_{ij} = \frac{1}{a} \mathcal{P}_{ij} \,. \tag{5.10}$$

We can then recover w_{ij} at any moment, in Fourier space, through the relation

$$w_{ij}(k,z) = u_{ij}^{\mathrm{TT}}(k,z) = \Lambda_{ij,lk}(\hat{k}) u_{lk}(k,z) \,, \tag{5.11}$$

$$\Lambda_{ij,lk}(\hat{k}) = P_{il} P_{jk} - \frac{1}{2} P_{ij} P_{lk} \,, \quad P_{ij} = \delta_{ij} - \hat{k}_i \hat{k}_j \,, \tag{5.12}$$

where $\Lambda_{ij,lk}(\hat{k})$ is a geometrical projector that filters out the TT degrees of freedom in Fourier space. Since $\Lambda_{ij,pq}(\hat{k}) \Lambda_{pq,lm}(\hat{k}) = \Lambda_{ij,lm}(\hat{k})$, the argument inside the angular-average $\langle ... \rangle$ in Eq. (5.9) can be computed as

$$\left(w_{ij}'(k,z) - \mathcal{H} w_{ij}(k,z) \right) \left(w_{ij}'(k,z) - \mathcal{H} w_{ij}(k,z) \right) =$$
$$\left(u_{ij}'(k,z) - \mathcal{H} u_{ij}(k,z) \right) \Lambda_{ij,lm}(\hat{k}) \left(u_{lm}'(k,z) - \mathcal{H} u_{lm}(k,z) \right) \,. \tag{5.13}$$

We have studied the GW creation process in lattices of $N = 256$ points per dimension. To solve the Higgs + gauge fields *eom* Eqs. (4.57) and (4.59), we have used the lattice formulation presented in Appendix A. For the discrete version of the GW EOM (5.10), we have simply substituted the continuous derivatives ∂_μ in Eq. (5.10), with standard forward/backward lattice derivatives. Also, in order to introduce a lattice version of the energy density spectrum of GW Eq. (5.9), we followed the prescription introduced in [108]. In our case, this translates into

$$\Theta_{\mathrm{GW}}(\tilde{\mathbf{n}}, z) = \frac{1}{6\pi^2 \lambda^2} \frac{d\tilde{x}^3 \kappa(\tilde{\mathbf{n}})^3}{N^3} \times \left\langle (u_{ij}' - \mathcal{H} u_{ij}) \Lambda_{ij,lm}^{(\mathrm{L})} (u_{lm}' - \mathcal{H} u_{lm}) \right\rangle_{4\pi} \,, \tag{5.14}$$

where $d\tilde{x} \equiv H_* dx$ is the dimensionless lattice spacing, $\kappa(\tilde{\mathbf{n}}) \equiv k(\tilde{\mathbf{n}})/H_*$ the dimensionless momenta, $k(\tilde{\mathbf{n}}) \equiv (2\pi/L)|\tilde{\mathbf{n}}|$ the momentum at the Fourier lattice site $\tilde{\mathbf{n}}$, L the length of the lattice box, and $w_{ij} \equiv w_{ij}(\tilde{\mathbf{n}}, z)$ the discrete Fourier transform of $w_{ij}(\mathbf{n}, z)$, with $\mathbf{n}$ labelling the lattice sites. Note that $\Lambda_{ij,lm}^{(\mathrm{L})}$ is a discretized version of the TT projector given in Eq. (5.12), and multiple choices are possible. We have chosen a lattice projector based on forward derivatives, noticing that other choices did not change the GW spectra appreciably, see [108] for a thoughtful discussion on this point. In all simulations we have ensured that the lattice resolution covers well the dynamical range of momenta excited in the process, for both the matter and the GW fields.

5.3. Results from lattice simulations

As described in Chapter 4, the exact dynamics of the Higgs decay process depend sensitively on three parameters: the resonance parameter q; the initial amplitude of the Higgs field φ_*, characterized by the parameter β defined in Eq. (4.10); and the post-inflationary equation of state w. Similarly, it is expected that the exact details of the GW spectra will also depend sensitively on q. However, the qualitative aspects of these spectra can be easily understood, without the need to specify the particular value of q. To see this, let us look at Fig. 5.1. There we show the temporal evolution of the spectrum $\Theta_{\mathrm{GW}}(k, z; q, \beta, w)$. The plots correspond to the resonance parameters $q = 61$ and 750, and for each case, to KD ($w = 1$), RD ($w = 1/3$) and MD ($w = 0$) post-inflationary expansion rates. Within each plot, each line corresponds to the GW spectra at a particular time, showing its evolution from approximately the start of the Higgs oscillations until well after the production of GW ceases. Note that in these plots we consider the particular value $\beta = 0.01$, but a scaling of the results to arbitrary β values will be presented in the next section.

Let us now discuss three qualitative aspects of the $\Theta_{\mathrm{GW}}(k, z; q, \beta, w)$ spectra shown in the figure: their time evolution, the amplitude when the GW stop growing, and the appearance of peaks.

Let us focus first on the time evolution of the spectra, and its relation with the time scales of the post-inflationary Higgs dynamics introduced in Section 4.5: z_{osc} (onset of the Higgs oscillatory regime), z_{br} (time at which the backreaction of the gauge bosons onto the Higgs condensate starts becoming effective), and z_{dec} (stabilization of the Higgs energy density and the onset of equipartition). We observe in Fig. 5.1 that the GW production begins shortly after the start of the Higgs oscillations, i.e. at the onset of parametric resonance at $z \gtrsim z_{\mathrm{osc}}$. From then on, we observe a significant growth of the GW amplitude during the linear stage $z \lesssim z_{\mathrm{br}}$. This is due to the initial exponential excitation of the gauge bosons, due to the parametric resonance induced by the Higgs condensate oscillations. However, the final amplitude of the spectra is mostly determined by the non-linear dynamics during some time after the onset of backreaction $z > z_{\mathrm{br}}$, while the Higgs condensate is decaying noticeably. We can define z_{GW} as the time scale at which GW stop being produced, so that Θ_{GW} saturates to a fixed amplitude. In general, one finds that $z_{\mathrm{GW}} < z_{\mathrm{dec}}$. In other words, the GW stop being produced before the onset of equipartition. This can be clearly observed in Fig. 5.1. Using Eq. (4.86), we find that for $q = 67$, we have $z_{\mathrm{dec}} \approx 1520, 3270, 7040$ for KD, RD and MD respectively, and for $q = 750$, we have $z_{\mathrm{dec}} \approx 4350, 9370, 20190$. Note that these times are much longer than the final times displayed in Fig. 5.1, when the spectra have already saturated.

The fact that $z_{\mathrm{GW}} < z_{\mathrm{dec}}$ is indeed not surprising. The precise moment when GW cease to be produced is better determined when the Higgs energy density stops dropping abruptly, and this happens sometime after $z = z_{\mathrm{br}}$ but before $z = z_{\mathrm{dec}}$. From this time onwards ($z > z_{\mathrm{GW}}$),
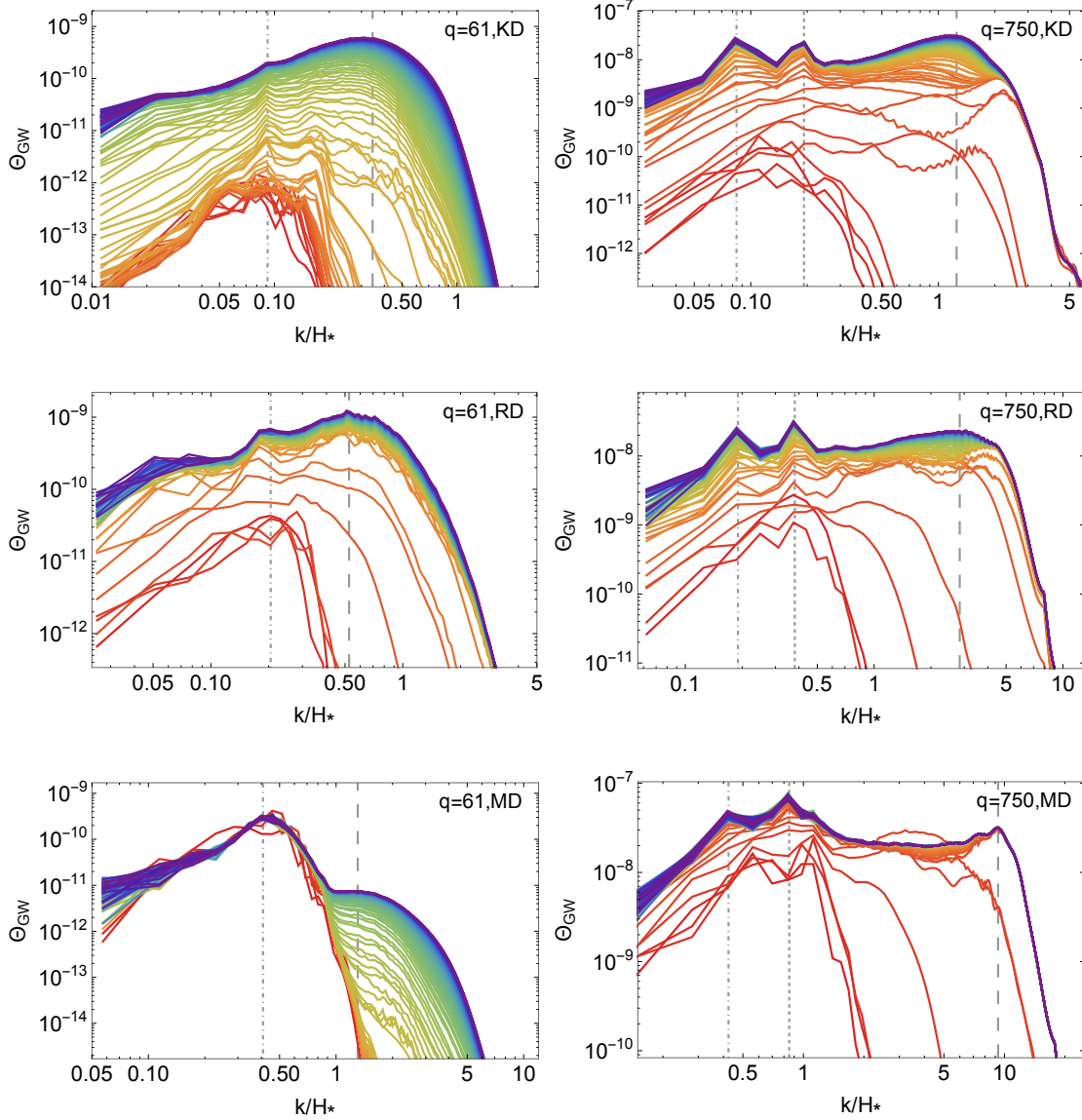
Figure 5.1.: Evolution in time of $\Theta_{GW}(k, z; q, \beta, w)$ as the GW are being created, computed for the resonance parameters $q = 61$ and 750, and for each parameter, for KD, RD and MD post-inflationary expansion rates. The time step between spectra is $\Delta z \approx 32.7$ for KD, $\Delta z \approx 15.5$ for RD, and $\Delta z \approx 7.3$ for MD. The last spectra plotted in each figure corresponds to the output time $z \approx 3280$ in KD, and to $z \approx 750$ in both RD and MD. The dotted-dashed, dashed, and dotted vertical lines indicate the position of various peaks k_1, k_2 and k_3 in the spectra, see bulk text.

even if the Higgs energy density is still decaying until the onset of equipartition at $z = z_{\text{dec}}$, the matter fields are only evolving smoothly, adjusting themselves towards equipartition. The time z_{dec} simply indicates when the Higgs (comoving) energy density is finally stabilized to a fixed amplitude, coinciding with the onset of equipartition. In conclusion, there is no more GW
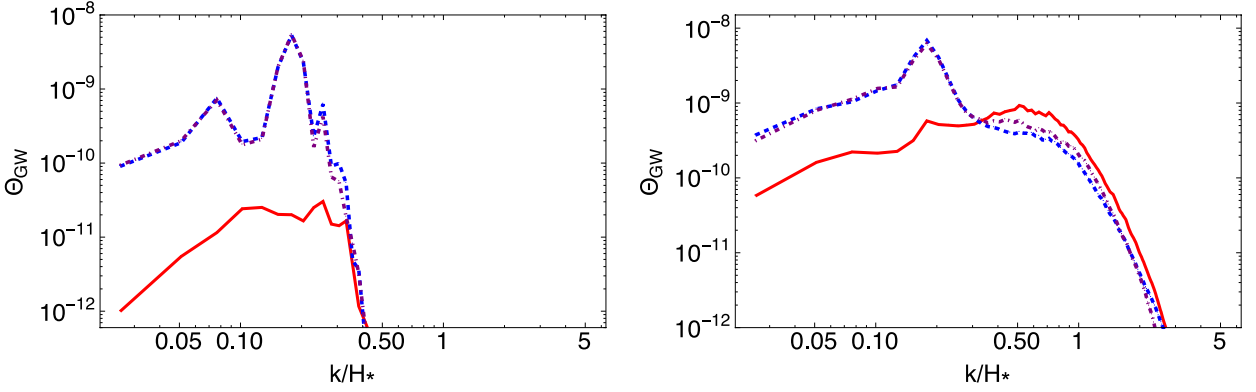
Figure 5.2.: We show Θ_{GW} (red continuous line), $\Theta_{\text{GW}}^{[h]}$ (dashed blue line) and $\Theta_{\text{GW}}^{[g]}$ (dotted-dashed purple line) at the times $z = 62$ (left figure) and $z = 373$ (right figure). The two figures correspond to $q = 61$ and $\beta = 0.01$.

production after $z = z_{\text{GW}}$. The growth of the GW spectra saturates at that moment, and the GW simply redshift from then on, due to the expansion of the Universe.

Let us now discuss the final amplitude of Θ_{GW} after it has saturated, i.e. for $z > z_{\text{GW}}$. If we focus on the panels where $q = 61$, we see that, independently of the chosen post-inflationary expansion rate (either KD, RD or MD), the maximum amplitude of the GW spectra is of the same order of magnitude, $\Theta_{\text{GW}} \sim \mathcal{O}(10^{-10})$. Of course, the particular shape of the final spectra is different in each case, but the final amplitude seems to very similar. The same happens if we focus on the $q = 750$ case, where for the three KD, RD and MD spectra, we have $\Theta_{\text{GW}} \sim \mathcal{O}(10^{-8})$. This indicates that the final amplitude of Θ_{GW} at saturation is roughly independent on the post-inflationary expansion rate. However, note that this should not be confused with the standard change of amplitude of the GW due to their nature as relativistic species. The prefactor ϵ_w in Eq. (5.8), which verifies $\epsilon_{w_1} > \epsilon_{w_2}$ if $w_1 > w_2$, accounts precisely for this effect. The final amplitude of the GW is indeed much more affected by their natural redshifting, than by the small dependence of Θ_{GW} on the rate of expansion.

Let us finally discuss the appearance of peaks in the GW spectra. In Fig. 5.1 we can see that, during the growth of the GW spectra, a structure of peaks develops. The GW are sourced by both the Higgs and gauge fields through the terms $\mathcal{P}_{ij}$ of Eq. (5.5), acting in the *rhs* of Eq. (5.3). In momentum space, the spectrum of GW is then sourced by a convolution of the Higgs and gauge fields spectra. Therefore, the position of the peaks is correlated with the appearance of peaks in the spectra of both the Higgs and the gauge fields.

To see this, let us denote by $u_{ij}^{[g]}$ the contribution to the GW sourced only by the gauge fields term $\mathcal{P}_{ij}^{[g]}(\mathcal{E}, \mathcal{B})$, and by $u_{ij}^{[h]}$ the contribution sourced by the Higgs covariant derivatives

$\mathcal{P}_{ij}^{[h]}(\mathcal{D}h)$, see Eq. (5.5). From the linearity of Eq. (5.10), it follows that

$$u_{ij}^{[g]''} - \left(\partial_k\partial_k + \frac{a''}{a}\right)u_{ij}^{[g]} = \frac{1}{a}\{\mathcal{P}_{ij}^{[g]}\}^{\mathrm{TT}}\,, \tag{5.15}$$

$$u_{ij}^{[h]''} - \left(\partial_k\partial_k + \frac{a''}{a}\right)u_{ij}^{[h]} = \frac{1}{a}\{\mathcal{P}_{ij}^{[h]}\}^{\mathrm{TT}}\,. \tag{5.16}$$

Similarly, let us denote as $\Theta_{\mathrm{GW}}^{[g]}$ and $\Theta_{\mathrm{GW}}^{[h]}$ the contribution to the GW spectra associated to these fields respectively. Clearly, as the GW spectrum is quadratic in u_{ij}, then $\Theta_{\mathrm{GW}} = \Theta_{\mathrm{GW}}^{[h]} + \Theta_{\mathrm{GW}}^{[g]} + \Theta_{\mathrm{GW}}^{[gh]}$, where $\Theta_{\mathrm{GW}}^{[gh]}$ represents an interference contribution from the convolution of a term like $\sim \mathcal{P}_{ij}^{[g]}\mathcal{P}_{ij}^{[h]}$. In Fig. 5.2 we show, for the case $q = 61$ and $\beta = 0.01$, both $\Theta_{\mathrm{GW}}^{[g]}$ and $\Theta_{\mathrm{GW}}^{[h]}$, as well as the total spectrum Θ_{GW} for two different times. One can see that $\Theta_{\mathrm{GW}}^{[g]}$ and $\Theta_{\mathrm{GW}}^{[h]}$ evolve in a similar manner, being almost identical, especially in the infrared regime. In particular, they both show some peaks at certain scales. This is a reflection of the dynamics of the system, which creates similar peaks in the spectra of $\mathcal{E}_i$, $\mathcal{B}_j$ and $\mathcal{D}_i h$, and transfers those peaks to $\mathcal{P}_{ij}^{[g]}$ and $\mathcal{P}_{ij}^{[h]}$. During the linear regime of parametric resonance, the fast creation of gauge bosons induces a similar growth of the electric and magnetic fields, as well as of the Higgs covariant derivatives. As a consequence, $\mathcal{P}_{ij}^{[g]}$ and $\mathcal{P}_{ij}^{[h]}$ contribute very similarly to the total spectrum of GW. This has a very interesting effect, as it produces a destructive interference in the infrared, suppressing the total amplitude Θ_{GW} with respect the individual amplitudes $\Theta_{\mathrm{GW}}^{[h]} \approx \Theta_{\mathrm{GW}}^{[g]}$. At the same time, this softens (in some cases it almost washes out) the peak structure, which becomes much more smoothed in the final spectrum. This is clearly shown by the continuous curves in Fig. 5.2, as compared with the dashed and dotted-dashed curves.

The origin of the peaks can be understood by examining the spectra of the matter fields, i.e. of the Higgs and gauge bosons. In particular, we plotted in Fig. 4.11 the electric and magnetic spectra for the resonance parameters $q = 5$ and $q = 9$. Looking at the initial stages of the process, a growth in both the Higgs and gauge fields spectra takes place in infrared scales (small k). In particular, peaks are generated in the matter fields spectra, according to the band structure of the Lamé equation, and these scales are essentially imprinted in the spectrum of the GW. The position of the most-infrared peak in the GW spectra, common to both the $q = 61$ and 750 cases in Fig. 5.1, is indicated with a dotted-dashed line. This peak corresponds to the initial resonance band in the spectra of the gauge fields. In the $q = 750$ case, there is even a second peak in the GW spectrum, indicated with a dotted line. It corresponds to another peak appearing in the spectrum of the Higgs field. When the system becomes fully non-linear, the spectra of both fields show a rescattering effect towards the ultraviolet, populating modes of higher and higher momenta. This generates a characteristic feature in the fields' spectra, which develop a relatively wide peak with a 'hunchback' shape in the ultraviolet scales. This last peak is shifted towards higher momenta according to how large the resonance parameter q is. Again, this scale is imprinted in the GW spectrum, and it is indicated with a dashed line in both cases $q = 61$ and 750 in Fig 5.1.
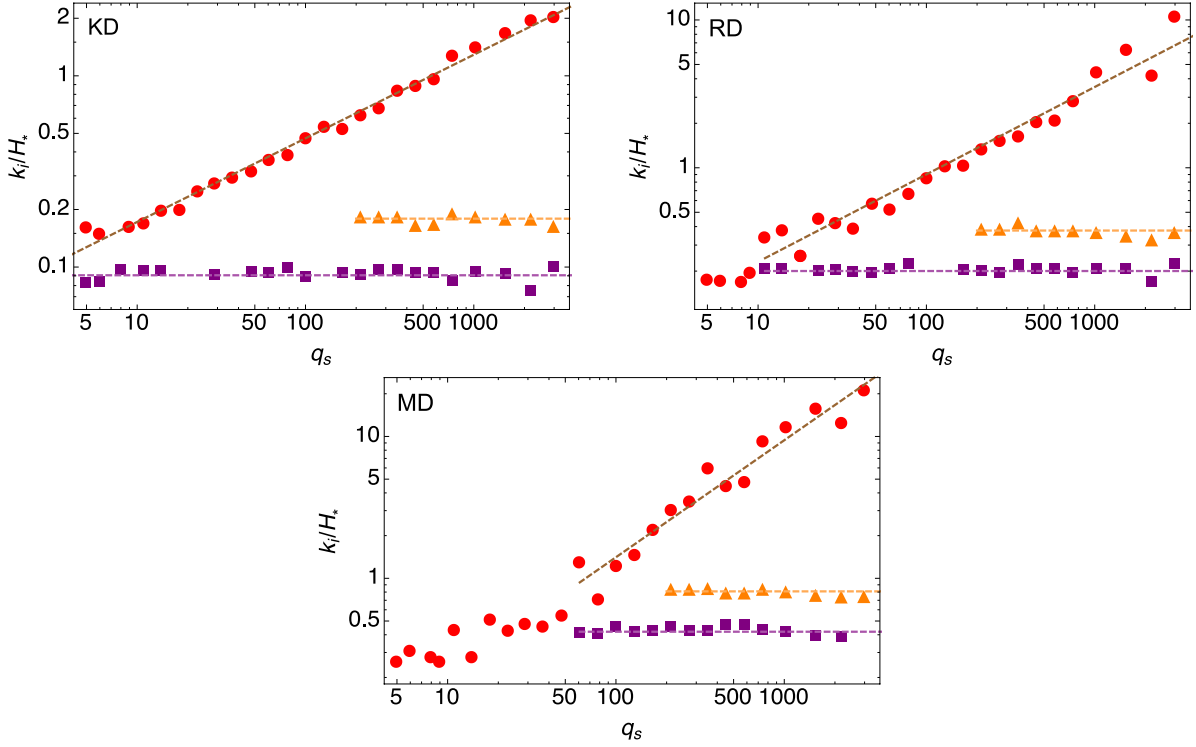
Figure 5.3.: Location of the different peaks k_i/H_* that appear in the GW spectra, as a function of the resonance parameter q. The panels correspond to KD (top), RD (middle) and MD (bottom), all obtained for $\beta = 0.01$. Red circles, purple squares and orange triangles correspond to k_1, k_2 and k_3, respectively. Dashed lines correspond to the best fits to k_1, k_2 and k_3, as given by Eqs. (5.17)- (5.21).

5.4. Parametrization of the gravitational wave spectra

In this section we parametrize the position and amplitude of the final peaks in the GW spectra as a function of q, w, and β. We will focus first on the particular case $\beta = 0.01$, and from this, we will apply the scaling found in Section 4.6 to extrapolate and generalize this parametrization to other β values.

Let us start with the position of the peaks. We show in Figure 5.3 the momenta k_i at which the peaks appear as a function of q, for the $\beta = 0.01$ case, and for the different expansion rates we have simulated: KD, RD and MD. The maximum number of peaks we can observe in the spectra is three: one associated to the hunchback, whose position we denote by k_3 (red circles), and two associated with the initial parametric resonance dynamics, whose position we denote by k_1 (purple squares) and k_2 (orange triangles). However, for some values of q we do not see all three peaks: for $q \lesssim 200$ the k_2 peak is not clearly observed, as it overlaps with either of the two. Also, for some q the peaks k_1 and k_3 are too near to each other, and hence it is difficult to attribute a particular peak to either of them. This explains why, for some specific values of q (particularly at low q), we just show the red circles corresponding to k_3.

The key idea is that, except for very low q, we appreciate a clear separation between the hunchback k_3 scale and the other scales k_1, k_2. This separation is appreciated in all the post-inflationary expansion rates. More specifically, the position of the hunchback peak increases with q, exhibiting a clear power-law dependence. We find the fit

$$k_3 \approx A_3 \, q^r H_* \tag{5.17}$$

with the parameter values (for $\beta = 0.01$) as

$$A_3 \approx \begin{cases} 0.0315, & \text{if KD} \\ 0.0593, & \text{if RD} \\ 0.0627, & \text{if MD} \end{cases} , \quad r \approx \begin{cases} 0.44, & \text{if KD} \\ 0.59, & \text{if RD} \\ 0.82, & \text{if MD} \end{cases} \tag{5.18}$$

On the other hand, the position of k_1 and k_2 are mostly independent on q. We find these peaks to be well fitted by

$$k_1 \approx A_1 H_* , \tag{5.19}$$
$$k_2 \approx A_2 H_* \; [q \gtrsim 200] , \tag{5.20}$$

with parameter values (again for $\beta = 0.01$) as

$$A_1 \approx \begin{cases} 0.091, & \text{if KD} \\ 0.20, & \text{if RD} \\ 0.42, & \text{if MD} \end{cases} , \quad A_2 \approx \begin{cases} 0.18, & \text{if KD} \\ 0.38 & \text{if RD} \\ 0.81, & \text{if MD} \end{cases} . \tag{5.21}$$

These fits are depicted with straight lines in Fig. 5.3.

On the other hand, we show in Fig. 5.4, the amplitude of the spectrum evaluated at the highest peak $\Theta_{\text{GW}}(k_p)$, for the different q considered, and for different post-inflationary expansion rates. For $\beta = 0.01$, we find the following phenomenological fit

$$\Theta_{\text{GW}}(k_p) \approx A_{\text{GW}} \left(\frac{q}{100} \right)^{\alpha_{\text{GW}}} , \qquad (\beta = 0.01) , \tag{5.22}$$

where

$$A_{\text{GW}} \approx \begin{cases} 3.1 \times 10^{-9}, & \text{if KD} \\ 2.4 \times 10^{-9}, & \text{if RD} \\ 2.1 \times 10^{-9}, & \text{if MD} \end{cases} , \quad \alpha_{\text{GW}} \approx \begin{cases} 1.50, & \text{if KD} \\ 1.58, & \text{if RD} \\ 1.61, & \text{if MD} \end{cases} . \tag{5.23}$$

This peak corresponds to the maximum amplitude of the GW at the moment when they stop being actively created, i.e., at $z = z_{\text{GW}}$. However, note that k_p does not necessarily correspond always to the same peak k_1, k_2 or k_3; rather, it alternates among these [for KD and RD expansion
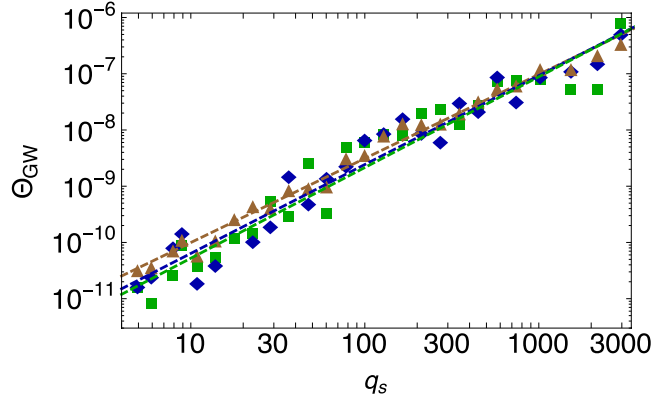
Figure 5.4.: Amplitudes Θ_{GW} of the highest peak of the GW spectra as a function of q, and for different post-inflationary expansion rates: KD (brown triangles), RD (blue diamonds) and MD (green squares). Dashed lines correspond to the best-fit functions of Eqs. (5.22)-(5.23).

rates we normally have $\Theta_{\mathrm{GW}}(k_p) \simeq \Theta_{\mathrm{GW}}(k_3)$, while for MD we have $\Theta_{\mathrm{GW}}(k_p) \simeq \Theta_{\mathrm{GW}}(k_1)$]. We see in Fig. 5.4 that the three fits for KD, RD, and MD coincide pretty well, confirming what we pointed out in the last section: the maximum amplitude of Θ_{GW} at saturation time z_{GW} is roughly independent of the post-inflationary expansion rate (the shape, however, is not; see Fig. 5.1).

These fits have been obtained for the particular $\beta = 0.01$ case, but a generic extrapolation to other β values can be easily carried out. We just need to use the rescaling laws that we found in Section 4.6, which connect scales and field amplitudes, from one simulation with Higgs initial amplitude and post-inflationary equation of state (β_1, w_1), to another simulation with different parameters (β_2, w_2). In particular, we found

$$z(\beta_2, \omega_2) \approx \beta_1^{p(\omega_1)} \beta_2^{-p(\omega_2)} z(\beta_1, \omega_1), \tag{5.24}$$

$$k(\beta_2, \omega_2) \approx \beta_1^{-p(\omega_1)} \beta_2^{p(\omega_2)} k(\beta_1, \omega_1), \tag{5.25}$$

$$h(\beta_2, \omega_2) \approx \beta_1^{p(\omega_1)-1} \beta_2^{1-p(\omega_2)} z(\beta_1, \omega_1), \tag{5.26}$$

where

$$p(w) \equiv \frac{1 + 3\omega}{3(1 + \omega)} = \begin{cases} 2/3, & \text{if KD} \\ 1/2, & \text{if RD} \\ 1/3, & \text{if MD} \end{cases}. \tag{5.27}$$

Using these rescaling laws, we predict the position of the peaks in the GW spectrum for arbitrary initial Higgs amplitudes β as

$$k_1 \approx A_1 \times \left(\frac{\beta}{0.01} \right)^{p(w)} H_*,$$
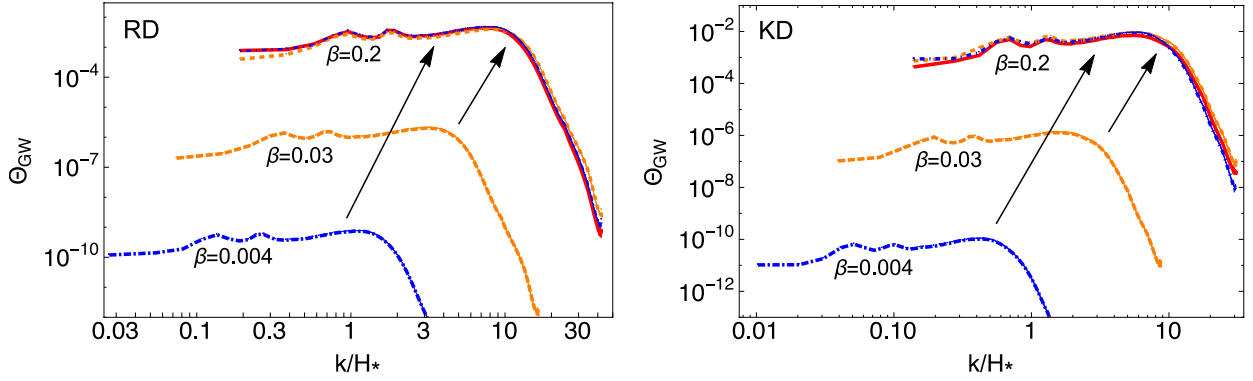
Figure 5.5.: We show the final spectra Θ_{GW} for the cases of $\beta = 0.2$, (continuous red line), of $\beta = 0.03$ (dashed yellow line), and of $\beta = 0.004$ (dot-dashed blue line), obtained directly from lattice simulations. This corresponds to the $q = 354$ case, and for RD (left panel) and KD (right panel). We also indicate with arrows the theoretical predictions for the $\beta = 0.2$ case, obtained from the $\beta = 0.03$ and $\beta = 0.004$ lattice results, using the extrapolation laws Eqs. (5.28), (5.29). We can see that the two extrapolated predictions match quite well the output of the real lattice simulations of the $\beta = 0.2$ case.

$$k_2 \approx A_2 \times \left(\frac{\beta}{0.01} \right)^{p(w)} H_* \,, \tag{5.28}$$

$$k_3 \approx A_3 \times \left(\frac{\beta}{0.01} \right)^{p(w)} q^r H_* \,.$$

On the other hand, rescaling the terms involved in the GW source Eq. (5.5) by means of Eqs. (5.24)-(5.26), we can predict now the scaling of Θ_{GW} [Eq. (5.14)], and, hence, how the amplitude of the background of GW scales with β. We find that

$$\Omega_{GW} \propto \Theta_{GW} \propto \beta^{4+v(w)} \,, \quad v(w) = 2 \frac{(w - 1/3)}{(w + 1)} \,. \tag{5.29}$$

We have confirmed the validity of these predictions by carrying out several lattice simulations with different β and w parameters. As an example, in Fig. 5.5 we show various spectra of GW for $q = 354$, for both RD ($w = 1/3$) and KD ($w = 1$). The continuous red, dashed yellow, and dotted-dashed blue lines, show the spectra for $\beta = 0.2, 0.03, 0.004$ respectively, obtained directly from lattice simulations. We indicate with arrows the theoretical predictions for $\beta = 0.2$, as obtained from the $\beta = 0.03$ and $\beta = 0.004$ lattice simulations, using the extrapolation laws Eqs. (5.28), (5.29). We see that the two extrapolated predictions match quite well the output of the real $\beta = 0.2$ lattice simulations within errors.

Using Eqs. (5.8), (5.22) and (5.29), we obtain that the maximum amplitude of the GW background at the end of the production stage, as a function of β, q, w, is given by

$$\Omega_{\text{GW}}(k_p) \approx A_{\text{GW}} \, \delta_* \, \epsilon_w \left(\frac{q}{100}\right)^{\alpha_{\text{GW}}} \left(\frac{\beta}{0.01}\right)^{4+v(w)}, \tag{5.30}$$

where ϵ_w, δ_* are given by Eq. (5.9), and $A_{\text{GW}}, \alpha_{\text{GW}}$ by Eq. (5.23). The amplitude in Eq. (5.30) constitutes one of the key results of our analysis. However, in order to quantify the amplitude of the signal today, we need to redshift its amplitude and frequency.

5.4.1. The gravitational wave background today

We now compute how the GW background redshifts until today. The highest peak of the GW spectrum today is of course characterized by the highest peak of Θ_{GW}, parametrized[1] by Eqs. (5.17), (5.22). Using Eqs. (3.17) and (3.18), the frequency and amplitude of highest peak today is found to be

$$f_p \simeq \epsilon_{\text{RD}}^{1/4} \left(\frac{H_*}{H_*^{(\text{max})}}\right)^{\frac{1}{2}} \left(\frac{\beta}{0.01}\right)^{p(w)} q^r \times 10^7 \text{ Hz}, \tag{5.31}$$

$$h^2 \Omega_{\text{GW}}^{(\text{o})}(f_p) \simeq 10^{-24} \times \epsilon_{\text{RD}} A_{\text{GW}} \left(\frac{q}{100}\right)^{\alpha_{\text{GW}}} \left(\frac{H_*}{H_*^{(\text{max})}}\right)^4 \left(\frac{\beta}{0.01}\right)^{4+v(w)}. \tag{5.32}$$

In order to understand what frequencies and amplitudes these expressions really imply, we need to consider specific cases. For instance, let us assume that the universe is RD after inflation, so that $\epsilon_{\text{RD}} = 1$, and let us consider that the inflationary Hubble rate is close to its upper bound, $H_* \lesssim H_*^{(\text{max})}$. Taking $q = 100$ and $\beta_{\text{rms}} \simeq 0.1$, we obtain

$$\text{RD}: h^2 \Omega_{\text{GW}}^{(\text{o})}(f_p) \lesssim 10^{-29}, \text{ at } f_p \lesssim 3 \cdot 10^8 \text{ Hz}. \tag{5.33}$$

This amplitude is tiny, so unfortunately there is not much hope to expect to detect it in the future, unless high-frequency GW detection technology undergoes unforeseen development. The main reason why this signal is so small lies in the suppression $\propto \delta_* = (H_*/m_p)^4 \sim 10^{-18}(H_*/H_*^{(\text{max})})^4 \ll 1$. As described in Section 3.5, this suppression of the GW amplitude is generic in scenarios where the energy of the oscillating field undergoing parametric resonance is subdominant with respect the total energy of the Universe, see Eq. (3.59). If the Universe was MD after inflation, the situation becomes even worse, because there is an extra dilution of the signal, as the latter is now proportional to some factor $\epsilon_{\text{RD}} \ll 1$. This dilution is simply a

---

[1] Although the highest-amplitude peak k_p is normally k_3, this is not always the case. However, when k_p is instead associated with k_1 or k_2 (typically for low q_s), the spectral amplitude at the k_3 peak is still very similar to that of the highest peak. Therefore, for simplicity, we are going to associate here the amplitude $\Theta_{\text{GW}}(k_p)$ [Eq. (5.22)] to the peak k_3 [Eq. (5.18)].

consequence of the fact that GW scale with the expansion of the Universe as relativistic species, $\rho_{GW} \propto 1/a^4$, whereas a MD background energy density dilutes slower as $\rho \propto 1/a^3$.

If the Universe is KD after inflation, the GW signal is, however, enhanced significantly. In particular, given the initial ratio of energies $\Delta \equiv V_*/\rho_* \sim 10^{-12}$ [Eq. (4.16)], the Universe will sustain a KD expansion rate until the moment when the relativistic SM fields become dominating the energy budget. This implies that the GW signal is enhanced by a factor $\propto \epsilon_{RD} = 1/\Delta \sim 10^{12}$. The scaling of the signal also goes as $\propto (\beta/0.01)^{4+v(1)}$ with $v(1) = 2/3$, instead of $v(1/3) = 0$ as in RD. Moreover, $A_{GW}^{KD} \gtrsim A_{GW}^{RD}$. Compared to a RD background, and for $\beta = 0.1$, there is therefore another enhancement (however milder) by a factor $(A_{GW}^{KD}/A_{GW}^{RD})(0.1/0.01)^{v(1)-v(1/3)} \sim 10$. Plugging all this into the redshifting formulas (cite), we obtain

$$\text{KD}: \ h^2\Omega_{GW}^{(o)}(f_p) \lesssim 10^{-16}, \ \text{at } f_p \lesssim 3 \cdot 10^{11} \text{ Hz.} \tag{5.34}$$

This corresponds yet to a small signal, but its amplitude is in fact comparable[2] to the standard scale-invariant inflationary background $h^2\Omega_{GW}^{(Inf)} \simeq 5 \cdot 10^{-16}(H_*/H_*^{(max)})^2$. However, the signal lies at extremely high frequencies $\sim 10^{11}$ Hz, beyond the range of planned GW detectors.

5.5. Summary

If the Higgs is decoupled from (or sufficiently weakly coupled to) the inflationary sector, a stochastic background of GW is expected due to the existence of the Standard Model Higgs. In particular, we expect the Higgs to be in the form of a condensate after inflation, decaying very rapidly – via non-perturbative effects – into the rest of the SM species. The resulting post-inflationary out-of-equilibrium dynamics of the SM fields generates, necessarily, a stochastic background of GW. The SM Higgs and the electroweak gauge bosons act as the dominant sources of the GW background, because their occupation numbers grow exponentially due to parametric resonance, unlike the case of fermions, which are Pauli blocked.

We have studied the details of the form of the GW spectrum, determining its frequency, amplitude and shape. We have characterized the dependence of the GW spectrum on the unknown parameters of the system, namely the Higgs initial amplitude at the end of inflation $\beta = \sqrt{\lambda}\varphi_*/H_*$, the equation of state w characterizing the post-inflationary expansion rate of the Universe, and the resonance parameter $q = (g_Z^2 + 2g_W^2)/4\lambda$. The running of the Higgs self-coupling at high energies is in fact quite uncertain within the experimental input, so λ can vary within the range $10^{-2} \lesssim \lambda < 10^{-5}$ (see Section 4.2). This translates into some uncertainty in

---

[2] In reality, the comparison to the inflationary signal is not fair here, as the KD regime after inflation would also boost the amplitude of the inflationary background by a factor $\propto \epsilon_{RD} \sim 10^{12}$.

the regime of the resonance parameter, which may vary within the range $q \sim \mathcal{O}(10) - \mathcal{O}(10^3)$. We have used real-time classical gauge field lattice simulations in an expanding box in $(3+1)$ dimensions. We now choose $N = 256$ points per dimension, ensuring that the relevant modes involved in this process were well captured within the dynamical range of the simulations.

Our results have been obtained within an Abelian-Higgs modeling. As explained in Section 4.5.1, this approach is expected to describe sufficiently well the system when $q \gg 1$. In fact, the largest amplitudes for the GW background are obtained when H_* is of the order of its current upper bound $H_*^{\text{(max)}} \sim 10^{14}$ GeV, which implies that λ runs to small values $\lambda < 10^{-2}$, hence making the resonance parameter large, $q > 10$. In light of this, the use of the Abelian approach is fully justified. In any case, the basic features of the fields dynamics and GW production, i.e. its dependence on q, β and w, are not expected to change drastically in the full non-Abelian scenario. Our study can be considered therefore as a good indicator of the GW amplitudes to expect in general, even if non-Abelian corrections were to be considered.

From our lattice simulations, we have obtained Eq. (5.30), which is a phenomenological fit of the amplitude of the GW spectra as a function of the different unknown parameters described above. We also obtain a parametrization of the observed redshifted amplitude until today in Eq. (5.32). If the Universe was RD after inflation, our calculations show in fact that this background is tiny, with an amplitude of $h^2 \Omega_{\text{GW}}^{\text{(o)}}(f_p) \lesssim 10^{-29}$, and peaked at high frequencies $f_p \sim 300$ MHz. The smallness of this background reflects simply the fact that the initial energy of the Higgs condensate represents only a tiny fraction of the inflationary energy. This is, in fact, a general feature of the GW produced from the decay of energetically subdominant fields after inflation. As seen in Section 3.5, the amplitude of the GW spectra is, in these scenarios, suppressed by a factor $(H_*/m_p)^4 \ll 1$ with respect an equivalent GW production from preheating [see Eq. (3.59)]. If the Universe was MD after inflation, although the background will be peaked at slightly smaller frequencies, its amplitude today can only be even smaller than in the RD case. The amplitude of the background is expected, however, to be enhanced significantly if the Universe underwent a KD regime after inflation. In that case, our calculations show that the background today could have an amplitude up to $h^2 \Omega_{\text{GW}}^{\text{(o)}}(f_p) \lesssim 10^{-16}$. This larger background is, however, peaked at very high frequencies, of the order of $f_p \lesssim 10^{11}$ Hz. Given that the background is always peaked at very high frequencies, and its amplitude today is very small, our prediction will remain, most likely, as a curiosity of the SM.

Chapter 6.

Non-Abelian corrections to the Higgs decay after inflation

We study the post-inflationary decay of the Standard Model Higgs into the electroweak SU(2)×U(1) gauge fields with classical lattice simulations. We consider the same scenario as in Chapter 4: we assume that the Higgs forms a condensate during inflation, which oscillates short after inflation ends, transferring most of its energy to the SM gauge bosons via parametric resonance. However, while in Chapter 4 we neglected the non-Abelian interaction terms between the Higgs and gauge fields, here we include explicitly the SU(2)×U(1) gauge structure in the lattice. We start by deriving theoretically the structure of resonance bands in parametric resonance, when the decay products are a combination of Abelian and non-Abelian gauge bosons. We then present the results from our lattice simulations, parametrizing this way the different time scales, energy ratios, and field spectra. We compare our results with the ones obtained with an equivalent Abelian-Higgs modelling of the system, and quantify the effects on the late Higgs+gauge dynamics coming from the non-Abelian interactions. We find that in the SU(2)×U(1) simulations, the Higgs transfers approximately 70% of its energy to gauge bosons, while in the Abelian approximation, the energy transfer is only 40%.

6.1. Introduction

In this chapter we continue the program initiated in chapters 4 and 5, where we studied the post-inflationary decay of the Higgs condensate into gauge bosons with lattice simulations. However, while there we made several approximations to the gauge structure of the SM electroweak sector, in this chapter we include explicitly the SU(2)×U(1) SM electroweak gauge group in our analysis, taking fully into account the non-Abelian interaction terms.

In particular, in Chapter 4 we modelled the electroweak gauge bosons in two different ways. First, we approximated the SM gauge bosons as scalar fields with appropriate interaction terms.

Second, we approximated the SM gauge bosons as Abelian gauge fields (i.e. we simulated an Abelian-Higgs model), including this way a gauge structure into the simulations. Both modellings provided similar results for the Higgs decay time and energy fractions. However, as said, in both cases we completely ignored the non-Abelian gauge interactions in the field EOM. As described in Section 4.5.1, this approach is justified at initial times, as the contribution of these terms is subdominant when the gauge energy is still a small fraction of the energy budget. However, at late times this is no longer true, and the non-Abelian terms may play a very important role, potentially changing the final results of the lattice simulations. In this chapter we want to understand and quantify precisely these effects.

We will start by studying parametric resonance when the resonantly excited decay products are a combination of Abelian and non-Abelian gauge bosons. We will derive an expression for the *effective resonance parameter*, which describes the dynamics of the process at initial times. We will then present the results from our lattice simulations, in which we introduce explicitely the SU(2)×U(1) gauge structure. We will analyze our results in light of the previous theoretical derivation, and compare them with respect an Abelian-Higgs modelling of the system. We will also quantify the effects that the non-Abelian interactions have in the Higgs and gauge post-inflationary dynamics.

The structure of this chapter is as follows. In Section 6.2 we describe the parametric resonance process generated by an oscillating scalar field coupled to Abelian and non-Abelian gauge fields. In Section 6.3 we present the results from our lattice simulations, putting special emphasis on the effect of the non-Abelian interactions in the system dynamics. In Section 6.4 we summarize our results and conclude.

6.2. Parametric resonance with gauge fields

In this section we explain how a combination of Abelian and non-Abelian gauge fields, resonantly excited due to a coupling to a time-dependent scalar field, can be effectively described with a single effective Abelian gauge boson at initial times.

Let us first consider the following gauge-invariant action under the U(1) group,

$$S = - \int d^4x \sqrt{-g} \left\{ \frac{1}{4} F_{\mu\nu} F^{\mu\nu} + |D_\mu \Phi|^2 + V(|\Phi|) \right\} , \qquad (6.1)$$

where here, $\Phi \equiv \frac{1}{\sqrt{2}} \varphi \equiv \frac{1}{\sqrt{2}} (\varphi_0 + i\varphi_1)$ is a complex scalar field (which we denote as *Higgs* from now on) with potential $V(|\Phi|)$, $F_{\mu\nu} \equiv \partial_\mu A_\nu - \partial_\nu A_\mu$ is the field strength of the Abelian gauge field A_μ, and $D_\mu \equiv \partial_\mu - i\frac{g_1}{2} A_\mu$ is the gauge covariant derivative with gauge coupling g_1. Minimization of this action with respect the Higgs and gauge variables give the following

equations of motion

$$\ddot{\varphi} - D_i D_i \varphi + 2\mathcal{H}\dot{\varphi} = -a^2 \frac{\partial V}{\partial \varphi^\dagger} , \qquad (6.2)$$

$$\partial_0 F_{0j} - \partial_i F_{ij} = \frac{g_1}{2} a^2 \mathfrak{Im}[\varphi^\dagger (D_j \varphi)] , \qquad (6.3)$$

$$\partial_i F_{0i} = \frac{g_1}{2} a^2 \mathfrak{Im}[\varphi^\dagger (D_0 \varphi)] , \qquad (6.4)$$

where t is conformal time, $\dot{} \equiv d/dt$, and $\mathcal{H} \equiv \dot{a}/a$ is the conformal Hubble rate. The first two expressions are dynamical equations of motion, while the third one is the Gauss constraint, which must be obeyed at all times. For simplicity, we impose the gauge conditions $A_0 = 0$ and $\partial_i \partial_j A_i = 0$. In this case, the EOM of the Abelian gauge fields, Eq. (6.3), becomes

$$\ddot{A}_j - \nabla^2 A_j = \frac{g_1}{2} a^2 \mathfrak{Im}[\varphi^* D_j \varphi] . \qquad (6.5)$$

Let us describe how parametric resonance takes place in this scenario. At initial times, gauge bosons have not been created in a significant number, so their backreaction effects onto the Higgs condensate can be neglected. In this regime, we can take the Higgs as a time-dependent homogeneous field, which oscillates around the minimum of its potential by following a linear trajectory in the Higgs complex plane. In particular, we can write the Higgs as

$$\varphi(t) \equiv (a + ib)|\varphi(t)| , \qquad (6.6)$$

where (a, b) are two real constant numbers that define the Higgs trajectory, and obey $a^2 + b^2 = 1$. Here, $|\varphi|$ is the modulus of the Higgs field, which is a solution to the Higgs EOM (6.2),

$$|\ddot{\varphi}| + 2\mathcal{H}|\dot{\varphi}| + a^2 \frac{\partial V}{\partial |\varphi|} = 0 . \qquad (6.7)$$

Let us consider potentials for the complex field of the type

$$V(|\varphi|) = \frac{1}{n} \lambda M^{4-n} |\varphi|^n , \qquad (6.8)$$

where $n = 2, 4, 6, \ldots$, M is some mass scale, and λ is a dimensionless coefficient. We saw in Section 2.2 that the solution of Eq. (6.7), with the potential given by (6.8), corresponds to an oscillating condensate with decaying amplitude, see Eq. (2.4). On the other hand, the equation for the Abelian gauge bosons, Eq. (6.5), can be written as

$$\ddot{A}_j - \nabla^2 A_j + \frac{g_1^2}{4} a^2(t)|\varphi|^2(t)|A_j = 0 . \qquad (6.9)$$

This equation does not depend on the constants a and b, but simply on the modulus of the Higgs field $|\varphi|$. Analogously to the discussion of Section 2.2, it is convenient to define new

spacetime and Higgs field variables as

$$\vec{x} \to \vec{y} \equiv \omega_* \vec{x}, \quad t \to z \equiv \omega_* t, \quad \varphi \to h \equiv a(t) \frac{\varphi}{\varphi_i}, \tag{6.10}$$

where $\omega_* = \sqrt{\lambda} M^{2-n/2} \varphi_i^{n/2-1}$ is the frequency of the oscillations [see Eq. (2.6)], and φ_i is the initial amplitude of the Higgs field. The gauge equation (6.5) can then be written as

$$\frac{d^2 A_j}{dz^2} + \left(qh^2 - \nabla_y^2 \right) A_j = 0, \tag{6.11}$$

where the *resonance parameter* is defined as

$$q \equiv \frac{g_1^2 \varphi_i^2}{4\omega_*^2}. \tag{6.12}$$

As discussed in Section 2.2, the solution of Eq. (6.11) has a structure of resonant bands, such that for some regions of the (κ, q) parameter space (with $\kappa \equiv k/\omega_*$), the gauge field modes have unstable solutions of the type $A_{j,\vec{k}} \sim e^{\mu_q(\kappa)z}$, with $\mathfrak{Re}[\mu_q(\kappa)] > 0$. This is exactly what we understand by *parametric resonance*. In the next section, we will work explicitly with the quartic potential of the SM, $V(\varphi) \equiv \frac{\lambda}{4}|\varphi|^4$. In such scenario, the oscillation frequency is simply $\omega_* = \sqrt{\lambda} \varphi_i$, and the resonance parameter becomes simply $q = g^2/(4\lambda)$.

Let us now consider a system of multiple Abelian gauge fields $A_\mu^{(n)}$ ($n = 1, 2, \ldots N$), coupled to the Higgs field through the covariant derivative term in the action, with gauge couplings $g_1^{(n)}$ ($n = 1, 2, \ldots N$). The gauge field equations of motion with gauge conditions $A_0^{(n)} = 0$ and $\partial_i \partial_j A_i^{(n)} = 0$ are

$$\ddot{A}_j^{(n)} - \nabla^2 A_j^{(n)} = \frac{g_1^{(n)}}{2} a^2 \mathfrak{Im}[\varphi^\dagger D_j \varphi],$$

$$D_j = \partial_\mu - \frac{i}{2} \sum_{n=1}^N g_1^{(n)} A_j^{(n)}. \tag{6.13}$$

In Section 4.5.2, we showed that this system can be identically described, at all times, with a single effective gauge boson S_j with gauge coupling g_{eff}, defined as

$$A_j^{(n)} = \frac{g_1^{(n)}}{g_{\text{eff}}} S_j, \quad g_{\text{eff}}^2 = \sum_{n=1}^N (g_1^{(n)})^2. \tag{6.14}$$

If we apply this transformation to each of the N equations in (6.13), we get

$$\ddot{S}_j - \nabla^2 S_j = \frac{g_{\text{eff}}}{2} a^2 \mathfrak{Im}[\varphi^\dagger D_j \varphi], \tag{6.15}$$

$$D_j = \partial_\mu - \frac{i}{2} g_{\text{eff}} S_j, \tag{6.16}$$

for all of them. This EOM is identical to the case of one Abelian gauge field, given in Eq. (6.5). The effective gauge boson can be written in terms of the individual ones as

$$
S_j \equiv \frac{1}{g_{\mathrm{eff}}} \sum_{n=1}^{N} g_1^{(n)} A_j^{(n)} \,.
\tag{6.17}
$$

Note that this transformation is exactly valid at all times, including also the later non-linear stage of parametric resonance. This is very useful when doing lattice simulations with multiple Abelian gauge bosons, as we only need to include one boson to capture completely the field dynamics. Analogously to Eq. (6.12), we can define an *effective resonance parameter* as

$$
q_{\mathrm{eff}} = \frac{g_{\mathrm{eff}}^2 \varphi_i^2}{4\omega_*^2} = \sum_{n=1}^{N} q^{(n)} \,, \qquad q^{(n)} = \frac{(g_1^{(n)})^2 \varphi_i^2}{4\omega_*^2} \,,
\tag{6.18}
$$

where $q^{(n)}$ are the resonance parameters of the individual Abelian gauge fields.

6.2.1. Parametric resonance with non-Abelian gauge fields

Let us now describe how parametric resonance works, when the excited fields are a combination of Abelian and non-Abelian gauge fields. Let us consider the following SU(2)×U(1) gauge-invariant action,

$$
S = -\int d^4x \sqrt{-g} \left\{ \frac{1}{4} (F_{\mu\nu} F^{\mu\nu} + G_{\mu\nu}^a G_a^{\mu\nu}) + (D_\mu \Phi)^\dagger (D^\mu \Phi) + V(|\Phi|) \right\} \,,
\tag{6.19}
$$

where $G_{\mu\nu}^a \equiv \partial_\mu B_\nu^a - \partial_\nu B_\mu^a + f^{abc} B_\mu^b B_\nu^c$ is the field strength of the non-Abelian gauge fields with $f_{abc} = 2\epsilon_{abc}$, $(D_\mu)_{\rho\sigma} \equiv \delta_{\rho\sigma} (\partial_\mu - i(g_1/2) A_\mu) - ig_2 B_\mu^a (T_a)_{\rho\sigma}$ is the covariant derivative $(\sigma, \lambda = 1, 2)$, with $T_a \equiv \sigma_a/2$ $(a = 1, 2, 3)$ the group generators, and the Higgs field Φ is now a complex doublet,

$$
\Phi \equiv \frac{1}{\sqrt{2}} \varphi = \frac{1}{\sqrt{2}} \begin{pmatrix} \varphi_0 + i\varphi_1 \\ \varphi_2 + i\varphi_3 \end{pmatrix} \,, \qquad \varphi_i \in \mathfrak{Re} \,.
\tag{6.20}
$$

The full dynamical equations of motion are

$$
\ddot{\varphi} - D_i D_i \varphi + 2\frac{\dot{a}}{a} \dot{\varphi} = -a^2 \frac{\partial V}{\partial \varphi^\dagger} \,,
\tag{6.21}
$$

$$
\partial_0 F_{0j} - \partial_i F_{ij} = \frac{g_1}{2} a^2 \mathfrak{Im}[\varphi^\dagger (D_j \varphi)] \,,
\tag{6.22}
$$

$$
\mathfrak{D}_0 G_{0j} - \mathfrak{D}_i G_{ij} = g_2 a^2 \mathfrak{Im}[\varphi^\dagger T_a (D_j \varphi)] \,,
\tag{6.23}
$$

with $(\mathfrak{D}_\nu)_{ab} O_b \equiv (\delta_{ab}\partial_\nu + \epsilon_{abc}B_\nu^c)O_b$. The Gauss constraints for the U(1) and SU(2) sectors are

$$\partial_i F_{0i} = \frac{g_1}{2}a^2 \mathfrak{Im}[\varphi^\dagger(D_0\varphi)] , \qquad (6.24)$$

$$(\mathcal{D}_i)_{ab}(G_{0i})^b = g_2 a^2 \mathfrak{Im}[\varphi^\dagger T_a(D_0\varphi)] . \qquad (6.25)$$

Let us impose the gauge conditions $A_0 = B_0^a = 0$ and $\partial_i\partial_j B_i^a = \partial_i\partial_j A_i = 0$. In this case, the dynamical equations of motion for the gauge fields, Eqs. (6.22) and (6.23), are written in terms of components as

$$\ddot{A}_j - \nabla^2 A_j = \frac{g_1}{2}a^2 \mathfrak{Im}[\varphi^\dagger D_j\varphi] , \qquad (6.26)$$

$$\ddot{B}_j^a - \nabla^2 B_j^a - \epsilon_{abc}\epsilon_{bde}B_i^c B_j^d B_i^e + \epsilon_{abc}\left(2B_i^c\partial_i B_j^b + B_j^b\partial_i B_i^c - B_i^c\partial_j B_i^b\right)$$
$$= g_2 a^2 \mathfrak{Im}[\varphi^\dagger T_a D_j\varphi]. \qquad (6.27)$$

In the SU(2)×U(1) gauge system, the Higgs doublet has four real components, see Eq. (6.20). As explained before, backreaction effects are negligible at initial times, and the Higgs oscillates in this regime along a linear trajectory in the (4-dimensional) space of Higgs components, so we can write the Higgs field in this regime as

$$\varphi(t) \equiv |\varphi(t)| \begin{pmatrix} a + ib \\ c + id \end{pmatrix} , \qquad (6.28)$$

where $a, b, c, d \in [0, 1]$ are four real constant numbers obeying $a^2 + b^2 + c^2 + d^2 = 1$, that indicate the axis of the Higgs trajectory, and $|\varphi(t)|$ is a solution to Eq. (6.7). Moreover, the non-Abelian interaction terms in Eq. (6.27) are non-linear, so we can also ignore them initially. In this approximation, Eqs. (6.26) and (6.27) are then written as

$$\ddot{A}_j - \nabla^2 A_j + a^2(t)\frac{|\varphi^2(t)|}{4}\left(g_1^2 A_j + g_1 g_2 \sum_{b=1}^{3} B_j^b x_b\right) = 0 , $$

$$\ddot{B}_j^a - \nabla^2 B_j^a + a^2(t)\frac{|\varphi^2(t)|}{4}\left(g_2^2 B_j^a + g_1 g_2 x_a A_j\right) = 0 , \qquad (6.29)$$

where x_a ($a = 1, 2, 3$) are three numbers that depend on the Higgs trajectory coefficients as

$$\left.\begin{aligned} x_1 &\equiv 2(ac + bd) \\ x_2 &\equiv 2(-bc + ad) \\ x_3 &\equiv a^2 + b^2 - c^2 - d^2 \end{aligned}\right\} \Rightarrow x_1^2 + x_2^2 + x_3^2 = 1 . \qquad (6.30)$$

As in the case of Abelian gauge fields discussed above, we can introduce an effective Abelian gauge boson S_μ and an effective gauge coupling g_{eff}, which mimic the dynamics of the system at initial times (i.e. when the approximation of neglecting the non-Abelian terms is valid). This

can be proven by substituting the following definitions into Eq. (6.29),

$$A_j = \frac{g_1}{g_{\text{eff}}} S_j \,, \quad B_j^a = \frac{g_2 x_a}{g_{\text{eff}}} S_j \,, \quad g_{\text{eff}}^2 \equiv g_1^2 + g_2^2 \,. \tag{6.31}$$

One can prove that, with this change, the four equations in (6.29) recover

$$\ddot{S}_j - \nabla^2 S_j + \frac{g_{\text{eff}}^2}{4} |\varphi^2(t)| a^2(t) S_j = 0 \,, \tag{6.32}$$

which is the equation of a single Abelian gauge boson S_j at initial times, coupled to the Higgs field with gauge coupling g_{eff}. Note also that, in this case, the effective gauge boson can be written as a function of the individual ones as

$$S_j \equiv \frac{1}{g_{\text{eff}}} \left(g_1 A_j + g_2 \sum_b B_j^b x_b \right) . \tag{6.33}$$

Let us assume now a power-law potential for the complex field, as written in Eq. (6.8). In this case, we can define an *effective resonance parameter* for the SU(2)×U(1) gauge system as

$$q_{\text{eff}} = \frac{g_{\text{eff}}^2 \varphi_i^2}{4\omega_*^2} = q_1 + q_2 \,, \tag{6.34}$$

where $q_1 \equiv g_1^2 \varphi_i^2 / (4\omega_*^2)$ and $q_2 \equiv g_2^2 \varphi_i^2 / (4\omega_*^2)$ are the independent resonance parameters of the U(1) and SU(2) sectors respectively. This is analogous to Eq. (6.12) for the case of N Abelian gauge bosons. This means that, at initial times, the system effectively behaves as a single gauge boson with resonance parameter q_{eff}. However, note that, unlike in the case of N Abelian gauge bosons, this approximation is only valid at initial times, when we are in the linear regime and can ignore the non-Abelian interactions in Eqs. (6.26) and (6.27). This approximation breaks up when the non-Abelian interaction terms become relevant at late times. To fully capture the effects of these interactions, we will present results from lattice simulations in the next section. In particular, we will consider the SM quartic potential $V(|\varphi|) = \frac{\lambda}{4} |\varphi|^4$. In this case, $\omega_* = \sqrt{\lambda}\varphi_i$, and the effective resonance parameter is simply $q_{\text{eff}} = (g_1^2 + g_2^2)/(4\lambda)$.

6.3. Lattice simulations of the Higgs decay into the SU(2)×U(1) gauge fields after inflation

In this section, we study the post-inflationary decay of the SM Higgs condensate into the SU(2)×U(1) electroweak gauge bosons. We will consider the same scenario as in Chapter 4, i.e. a Higgs field that 1) is not the inflaton, and 2) is decoupled from (or weakly coupled to) the inflationary sector.

In particular, we present results from a set of lattice simulations of the Higgs decay process. In Chapter 4, we mimicked the dynamics of the system with an Abelian-Higgs set-up. This way, we included a gauge structure into the lattice (unlike in the global set-up of Section 4.4), but ignored the effects coming from the presence of non-Abelian interaction terms. However, in this chapter we include explicitly the SU(2)×U(1) gauge structure in the lattice. We consider the action of Eq. (6.19), with the potential

$$V(|\varphi|) = \frac{\lambda}{4}|\varphi|^4 \,, \tag{6.35}$$

where λ is the Higgs self-coupling. In this context, φ represents the Higgs field, and A_μ and B_μ^a are the hypercharge and the W^a ($a = 1, 2, 3$) gauge fields respectively. The equations of motion are obtained from the minimization of this action, and have been written in Eqs. (6.21) and (6.23). The Higgs energy is subdominant with respect to the inflationary energy, as seen in Eq. (4.16), so we include the expansion of the Universe as a fixed time-evolving background, given by Eq. (4.7). We will follow and parametrize the dynamics from the end of inflation, including the initial linear parametric excitation and the following non-linear stage, until the system achieves a stationary regime. Our lattice formulation is based in a discretized version of action (6.19), which is explained in more detail in Appendix A.

As described in Section 4.3, the dynamics of the Higgs and gauge fields depend on several unknowns, which we must take into account when we parametrize the system: 1) the initial value of the Higgs amplitude in our patch, φ_*, which is given by the probability distribution of Eq. (4.4), 2) the value of the Hubble parameter during inflation H_*, 3) the values of the particle couplings (λ, g_1, g_2) at high-energy scales, and 4) the post-inflationary expansion rate. All these equations can be characterized by the β parameter [Eq. (4.10)], the post-inflationary equation of state w, and the resonance parameters q_1 and q_2 [Eq. (6.34)]. We will take in our simulations $g_1^2 \approx g_2^2 \approx 0.3$, which is a good approximation at inflationary scales, so the effective resonance parameter is $q_{\text{eff}} \equiv 2q_1 \equiv 2q_2 = g_1^2/(2\lambda)$. Consequently, we will parametrize the dynamics in terms of $(q_{\text{eff}}, \beta, w)$. However, let us remember that the Higgs solution follows a set of rescaling laws Eqs. (4.88) and (4.89), which allow to extrapole the results from a particular set of (β_1, w_1) parameters, to another set (β_2, w_2). This was proven in the Abelian-Higgs setup but, as we shall see below, this rescalings also holds in the SU(2)×U(1) lattice simulations. Therefore, in this section we first parametrize the system as a function of q_{eff} for the particular choice $\beta = 0.1$ and $w = 1/3$, and then generalize our results to other values of β and w using the rescaling laws.

As said, our results complete and complement the ones presented in Chapter 4, where we modelled the Higgs-gauge interactions with an Abelian-Higgs set-up. As seen in the previous section, the dynamics of a SU(2)×U(1) gauge sector undergoing parametric resonance can be approximated, at intial times, by the dynamics of a U(1) system with effective resonance parameter q_{eff}. However, the non-Abelian interactions are expected to play an essential role at

late times, and may affect the final energy distribution between the different species. In Section 6.3.1 we will study the validity of the Abelian approximation, and quantify the change in the dynamics induced by the non-Abelian interactions.

We have simulated the field dynamics in lattices of $N^3 = (128)^3$ points, and have adjusted the box size to cover the appropriate momentum scales during the initial resonant regime, as well as during the following non-linear propagation to the UV. The lattice formulation is explained in more detail in Appendix A. We also explain there how to set initial conditions for the different fields. There are four Gauss constraints, one for the U(1) group, and three for the SU(2) group [see Eqs. (6.24) and (6.25)]. In our lattice simulations, we have checked that these constraints are preserved at all times, except for the accumulated machine error during the time evolution. Moreover, in Eqs. (4.55) and (4.56), we defined a set of natural field and spacetime variables. Results will be quoted in terms of such variables.

Let us start by describing in a qualitative way the post-inflationary dynamics of the Higgs field and its decay products. Let us focus first on the particular case $q_{\text{eff}} = 50$, $\beta = 0.1$, and $w = 1/3$ (RD post-inflationary equation of state). We show in the left panel of Fig. 6.1 the volume-average of the Higgs conformal amplitude as a function of time, and in the right panel, the time-evolution of the different energy contributions of the system. The total energy of the Higgs+gauge system can be written as

$$\rho = \frac{\lambda \varphi_*^4}{4a^4} E_{\text{Tot}} \equiv \frac{\lambda \varphi_*^4}{4a^4} (E_K + E_V + E_G + E_{E,1} + E_{M,1} + E_{E,2} + E_{M,2}) \,, \tag{6.36}$$

where E_K, E_G and E_V are the Higgs kinetic, gradient, and potential energies,

$$E_K = \frac{2}{\beta^2} \left| h' - h\frac{a'}{a} \right|^2 \,, \quad E_G = \frac{2}{\beta^2} \sum_i |D_i h|^2 \,, \quad E_V = |h|^4 \,, \tag{6.37}$$

and $E_{E,a}$ and $E_{M,a}$ ($a = 1, 2$) are the electric and magnetic energies of the Abelian and non-Abelian sectors respectively,

$$E_{E,1} = \frac{2\lambda}{\beta^2} \sum_i \mathcal{E}_i^2 \,, \quad E_{E,2} = \frac{2\lambda}{\beta^2} \sum_{i,a} (\mathcal{E}_i^a)^2 \,, \tag{6.38}$$

$$E_{B,1} = \frac{2\lambda}{\beta^2} \sum_i \mathcal{B}_i^2 \,, \quad E_{B,2} = \frac{2\lambda}{\beta^2} \sum_i (\mathcal{B}_i^a)^2 \,. \tag{6.39}$$

Here, we have defined for convenience the dimensionless Abelian electric and magnetic fields as $\mathcal{E}_i \equiv F_{0i}/H_*^4$ and $\mathcal{B}_i \equiv \epsilon_{ijk}F_{jk}/H_*^4$ respectively, as well as the non-Abelian ones as $\mathcal{E}_i^a \equiv G_{0i}^a/H_*^4$ and $\mathcal{B}_i^a \equiv \epsilon_{ijk}G_{jk}^a/H_*^4$ respectively. Note that the total energy of the Higgs+gauge system evolves approximately as radiation at late times, $\rho \propto a^{-4}$, so E_{Tot} goes to a constant value at late times.
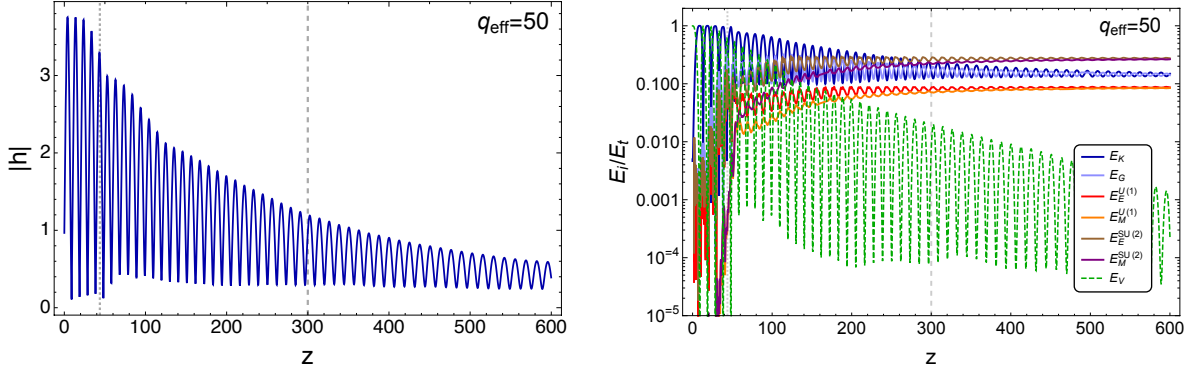
Figure 6.1.: Left: We show the volume-average of the Higgs conformal amplitude $|h| \equiv \sqrt{\sum_{n=0}^{3} h_n^2}$ as a function of time, for $q_{\text{eff}} = 50$, $\beta = 0.1$, and $w = 1/3$. Right: We show the different energy components of the Higgs+gauge energy [Eq. (6.36)] as a function of time, for the same parameters. In both panels, we indicate the time scales z_{br} and z_{dec} with dotted and dashed vertical lines respectively.

There are two relevant time scales in parametric resonance processes: the *backreaction time* z_{br}, which signals when the backreaction effects from the decay products start affecting the oscillating condensate, and the *decay time* z_{dec}, which signals when the system achieves a stationary/equipartition regime. For an explanation and a parametrization of these quantities in the context of preheating and scalar decay products, see Chapter 2. For times $z \lesssim z_{\text{br}}$, the Higgs field oscillates around the mininum of its potential, and simultaneously, the gauge energy grows exponentially due to resonant effects. However, the energy contribution from the gauge fields remains negligible with respect the Higgs energy at these times, so backreaction effects are irrelevant. However, at time $z \approx z_{\text{br}}$, when gauge energy becomes approximately ~10% of the total, backreaction effects from the gauge fields start affecting significantly the Higgs condensate, prompting its decay. For the case $q_{\text{eff}} = 50$, plotted in both panels of Fig. 6.1, this time is approximately $z_{\text{br}} \approx 50$. We have indicated such time with a vertical dotted line in the Figure. Afterwards, for times $z \gtrsim z_{\text{br}}$, the effects from the non-linear terms in the field EOM become important and can no longer be ignored. The different energy ratios evolve towards a stationary regime, and the second time scale z_{dec} gives an estimate of when this regime has been achieved. For the case $q_{\text{eff}} = 50$, this time corrresponds to $z_{\text{dec}} \approx 300$, and has been plotted with a dashed line in both panels of Fig. 6.1. Finally, at late times $z \gtrsim z_{\text{dec}}$, we see that the volume-average energies are approximately distributed according to the following equipartition identities,

$$E_K \approx E_G + E_V \,, \quad E_{E,1} \approx E_{M,1} \,, \quad E_{E,2} \approx E_{M,2} \,. \tag{6.40}$$

In other words, there is equipartition between the electric and magnetic energies in both the Abelian and non-Abelian sectors, as well as between the Higgs kinetic and gradient+potential energies. Note that in this second case, we have also included the Higgs potential energy on
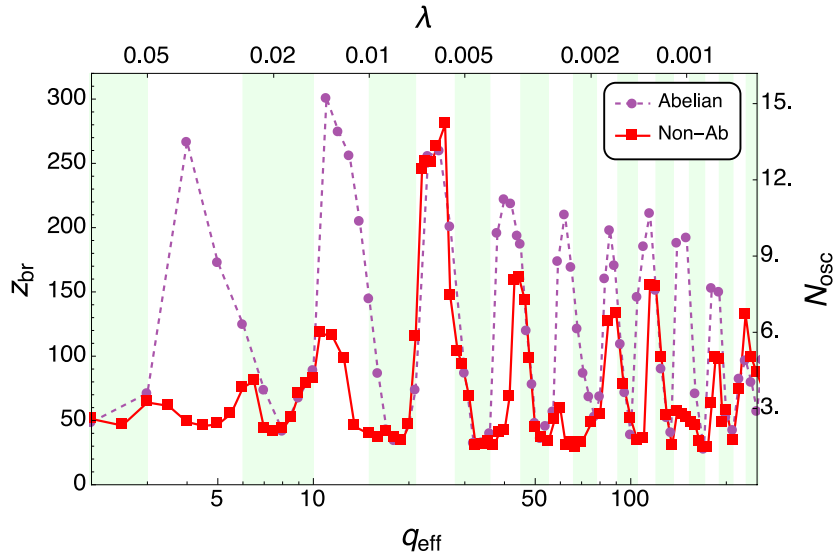
Figure 6.2.: We show z_{br} as a function of q_{eff}, for the lattice simulations of the SU(2)×U(1) gauge theory, and for the equivalent Abelian-Higgs approximation (see Section 6.3.1). We take $\beta = 0.1$ and $w = 1/3$ in both cases. Each point corresponds to a lattice simulation. The resonance parameters $q \in [1,3], [6,10] \ldots$ are indicated with green bands, while $q \in (3,6), (10,15) \ldots$ are indicated with white bands.

the right hand side of the equality: although it is subdominant at late times (see Fig. 6.1), its inclusion makes the equipartition identity better preserved.

Let us now parametrize the post-inflationary dynamics of the Higgs and gauge field as a function of q_{eff}, β, and w. We start by choosing the particular values $\beta = 0.1$ and $w = 1/3$, and parametrize how z_{br} and z_{dec} depend on q_{eff}. We will then generalize these results to arbitrary values of β and w, with the rescalings of Eqs. (4.88) and (4.89).

Let us start with the backreaction time z_{br}. This time scale can be defined in terms of the Higgs conformal amplitude, as the time when the envelope of the Higgs oscillations start decreasing abruptly (see left panel of Fig. 6.1). Conversely, it can also be defined in terms of energies, as the moment when the oscillation-average of the Higgs kinetic and potential energies start decreasing (see right panel of Fig. 6.1). Here we have decided to define z_{br} in terms of energy. In particular, at initial times ($z \ll z_{\mathrm{br}}$), the oscillation-average of the kinetic and potential energy ratios are respectively 66% and 33%, see Eqs. (4.20) and (4.21). We have technically defined z_{br} when the potential energy becomes 20% of the total.

We plot z_{br} as a function of q_{eff} in Fig. 6.2. Each point in the Figure corresponds to a single lattice simulation. We indicate with green bands the resonance parameters within the intervals $q_{\mathrm{eff}} \in [1,3], [6,10] \ldots$, for which, as explained in Section 4.3, the average Floquet index of the main resonance bands is larger, and the resonance is stronger. On the other hand, we indicate with white bands the values $q_{\mathrm{eff}} \in (3,6), (10,15)$, where the resonance is weaker. We also indicate in the top axis the value of λ through the relation $\lambda \equiv g_{\mathrm{eff}}^2/(2q_{\mathrm{eff}}) \equiv 0.3/(2q_{\mathrm{eff}})$, and

in the right axis the approximated Higgs number of oscillations, computed with the relation $N_{\text{osc}} \equiv z/Z_T$ with $Z_T \approx 19.8$ [see Eq. (4.14)]. We have also added a second set of simulations corresponding to an Abelian-Higgs model, which we will discuss in subsection 6.3.1.

We can clearly see that the structure of resonance bands gets imprinted in the behaviour of z_{br}: as expected, the stronger the resonance, the faster the gauge energy grows, and consequently, the shorter the backreaction time is. When q_{eff} is within a green band, the backreaction time attains a minimum with $z_{\text{br}} \approx 40$. However, when q_{eff} is within a white band, the value of z_{br} seems to vary randomly within the interval $z_{\text{br}} \in [40, 280]$. For example, in the first white band $q_{\text{eff}} \in (3, 6)$, we have $z_{\text{br}} \approx 50$, while for example in the interval $q_{\text{eff}} \in (21, 28)$, backreaction time attains the maximum $z_{\text{br}} \approx 280$. Hence, z_{br} can be parametrized as a function of q_{eff} (for $\beta = 0.1$ and $w = 1/3$) as

$$z_{\text{br}} \begin{cases} \approx 40 \,, & q_{\text{eff}} \in [1, 3], [6, 10] \dots \\ \in [40, 280] \,, & q_{\text{eff}} \in (3, 6), (10, 15) \dots \end{cases} \tag{6.41}$$

Note that a similar pattern for z_{br} as a function of q has also been observed in Fig. 2.3, in the context of parametric resonance with quartic potential, when the oscillating field is an inflaton and the decay products are scalars. A similar pattern has also been observed on Fig. 3.6, where we plotted the amplitude of the GWs generated during parametric resonance with quartic potential: for resonance paramaters $q \in [1, 3], [6, 10] \dots$, the resonance is stronger, and hence the GW amplitude is larger than for $q \in (3, 6), (10, 15) \dots$. However, this pattern is not observed for other potentials, such as quadratic: in this case, field modes redshift through many physical momenta due to the expansion of the Universe, and due to this, the dependence of z_{br} on q is stochastic (as seen in Fig. 2.6).

Let us now focus on the second quantity, z_{dec}. As described above, this quantity indicates the onset of the equipartition regime, according to the equipartition identities in Eq. (6.40). However, note that unlike the case of z_{br}, the definition of z_{dec} is much more ambiguous. Technically, we have decided to define z_{dec}, in this chapter, as the time when the Higgs equipartition identity holds at a 2% level, i.e., when the oscillation-average of the Higgs kinetic, gradient, and potential energies is $\frac{E_K - E_G + E_V}{E_K + E_G + E_V} = 0.02$. With this choice, z_{dec} gives an estimate of when the energies have more or less estabilished to their final numbers (as seen in the right panel of Fig. 6.1). However, note that choosing a smaller percentage would give larger values for z_{dec}. Note also that the different energies are still slightly oscillating for $z > z_{\text{dec}}$, so the situation at these times is still not totally stationary.

We plot z_{dec} as a function of q_{eff} in Fig. 6.3. Again, each point corresponds to a single lattice simulation. Note that we have decided to subtract the value of z_{br} from z_{dec} in each simulation: this way, we parametrize strictly the duration of the non-linear regime. We clearly see that for
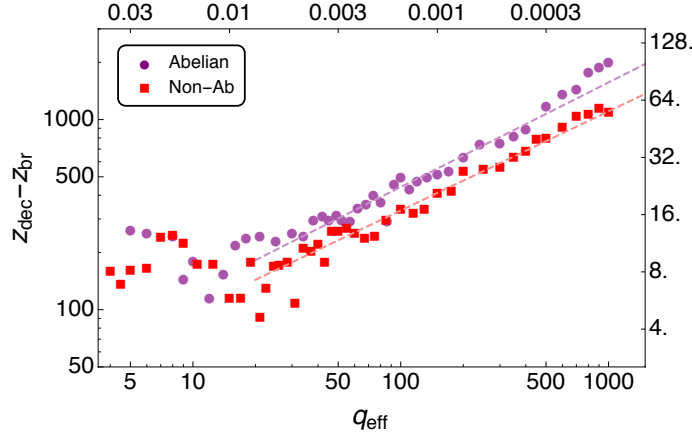
Figure 6.3.: We show z_{dec} as a function of q_{eff}, for $\beta = 0.1$ and $w = 1/3$. Red squares indicate results for the SU(2)×U(1) simulations, while purple squares indicate results from Abelian-Higgs simulations. Dashed lines indicates best fits (6.42) [SU(2)×U(1)] and (6.51) [Abelian-Higgs].

$q_{eff} \gtrsim 20$, z_{dec} has a power-law dependence on q_{eff}. We have obtained the following fit

$$z_{dec} = 330 \left(\frac{q_{eff}}{100}\right)^{0.53} + z_{br} \, , \quad (q_{eff} > 20, \beta = 0.1, \text{RD}) \, , \tag{6.42}$$

which we also show in Fig. 6.3. Note that this power-law form for the decay time, $z_{dec} \propto q^\alpha$, is quite generic in parametric resonance scenarios (see Chapter 2).

Until now, all our results have been presented for a RD post-inflationary expansion rate and $\beta = 0.1$. However, in Section 4.6 we presented a set of rescaling laws, Eqs. (4.88) and (4.89), that allowed to translate the results for the Higgs amplitude from lattice simulations, corresponding to one set of (β_1, w_1) values, to another (β_2, w_2). The validity of this extrapolation was assessed in Section 4.6, in the lattice simulations of the Abelian-Higgs set-up. Fortunately, this extrapolation also works when the gauge sector is formed by a SU(2)×U(1) group. In Fig. 6.4 we show the Higgs conformal amplitude obtained from lattice simulations for $q_{eff} = 24$, and for different choices of β and w. To check the validity of the rescaling laws, we have extrapolated all simulations to the $\beta = 0.1$, $w = 1/3$ case: all lines match approximately, proving this way the validity of the rescaling equations in this case. Then, the fitting formula for the backreaction time, Eq. (6.41), can be generalized as

$$z_{br} \begin{cases} \approx 13\beta^{\frac{-(1+3w)}{3(1+w)}} \, , & q_{eff} \in [1,3], [6,10] \dots \\ \in [13,89]\beta^{\frac{-(1+3w)}{3(1+w)}} \, , & q_{eff} \in (3,6), (10,15) \dots \, . \end{cases} \tag{6.43}$$

On the other hand, the formula for the decay time, Eq. (6.42), is generalized as

$$z_{dec} = 105 \left(\frac{q_{eff}}{100}\right)^{0.53} \beta^{\frac{-(1+3w)}{3(1+w)}} + z_{br} \, , \quad (q_{eff} > 20) \, . \tag{6.44}$$
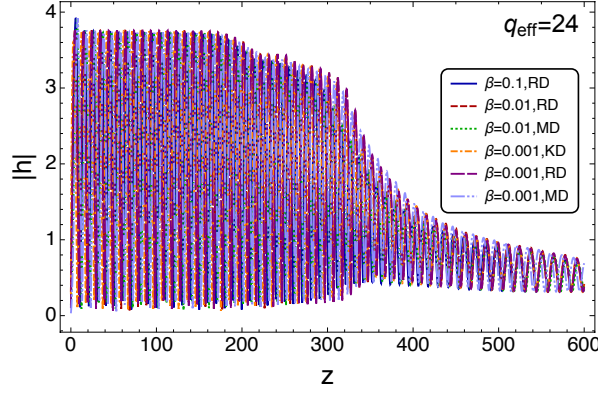
Figure 6.4.: We show the time-evolution of $|h|$, for different β and w parameters, obtained for different lattice simulations. All functions have been rescaled to $\beta = 0.1$ and $w = 1/3$ with Eqs. (4.88) and (4.89), to check their validity.

Let us finally study how the energy is distributed between its different components at late times, i.e. when the system is well within the stationary regime. We plot in Fig. 6.5 the different energy ratios E_i/E_{Tot} as a function of q_{eff} at late times $z > z_{\text{dec}}$. Definitions for E_{Tot} and the different E_i are provided in Eqs. (6.36)-(6.39). By definition, all ratios E_i/E_{Tot} sum one. In practice, we have plotted the ratios from the last time available in our simulations (always with $z > z_{\text{dec}}$), but choosing a slightly different time does not change significantly these results. Note that we have decided to sum E_V to E_G, so that we can check the equipartition identities (6.40) as precisely as possible. Note also that, for the electric and magnetic energies of the SU(2) sector, we have decided to divide the energies by 3 to account for the different colours.

We can clearly observe that the equipartition equalities (6.40) hold independently on the value of q_{eff}. Let us define the total Higgs and electromagnetic energies as

$$E_{\text{Hig}} = E_K + E_G + E_V \,, \tag{6.45}$$

$$E_{\text{EM}} = E_{E,1} + E_{M,1} + E_{E,2} + E_{M,2} \,. \tag{6.46}$$

Note that assigning E_G exclusively to the Higgs field is somewhat arbitrary, because E_G also contains gauge energy through the interaction term in the covariant derivative. In any case, we can clearly see in Fig. 6.5 that for all q_{eff} simulated in the lattice, $E_K/E_{\text{Tot}} \approx 15\%$ and $(E_G + E_V)/E_{\text{Tot}} \approx E_G/E_{\text{Tot}} \approx 15\%$. Consequently,

$$\frac{E_{\text{Hig}}}{E_{\text{Tot}}} = 0.3 \,, \quad \frac{E_{\text{EM}}}{E_{\text{Tot}}} = 0.7 \,, \tag{6.47}$$

i.e. the Higgs field eventually transfers 70% of the energy to gauge bosons. We can also observe that for low resonance parameters $q_{\text{eff}} \lesssim 100$, the electromagnetic energy is not equally distributed between the Abelian sector and the three colors of the non-Abelian sector. For example, for $q_{\text{eff}} = 5$, we have $E_{E,1}/E_{\text{Tot}} \approx E_{M,1}/E_{\text{Tot}} \approx 0.05$, while for each of the three
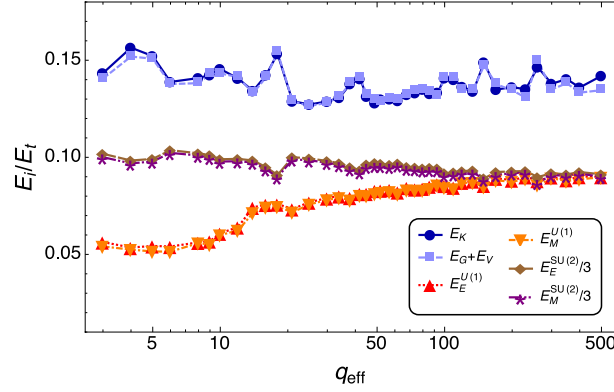
Figure 6.5.: We show the energy fractions $E_i/E_{\rm Tot}$ as a function of $q_{\rm eff}$, in the stationary regime $z \to \infty$. Note that the electromagnetic energies of the SU(2) sector have been divided by 3, to account for the three different colors.

colors of the SU(2) sector, $(E_{E,2} + E_{M,2})/(3E_{\rm Tot}) \approx 0.1$. However, as $q_{\rm eff}$ grows, the distribution becomes more democratic, and for $q_{\rm eff} \gtrsim 100$ the equipartiton between the U(1) and SU(2) components of the electromagnetic energy is quite good, with

$$E_{E,1} \approx E_{M,1} \approx \frac{E_{E,2}}{3} \approx \frac{E_{M,2}}{3} \ . \tag{6.48}$$

6.3.1. Comparison with Abelian-Higgs simulations

In this section, we simulate the post-inflationary dynamics of the SM Higgs with an analogue Abelian-Higgs set-up, neglecting this way the non-Abelian interactions in the field EOM. We will afterwards compare our results with the ones presented above for the full SU(2)×U(1) gauge system. Note that similar Abelian-Higgs simulations have been presented in Section 4.5; however, we have found convenient to repeat these with a larger set of resonance parameters. Following the discussion in Section 6.2, we couple a single Abelian gauge boson A_μ to a complex scalar Higgs doublet $\varphi \equiv \varphi_0 + i\varphi_1$ with gauge coupling $g_{\rm eff} = \sqrt{g_1^2 + g_2^2}$, and hence with resonance parameter $q_{\rm eff} \equiv q_1 + q_2 = g_1^2/(4\lambda) + g_2^2/(4\lambda) \equiv g_{\rm eff}^2/(2\lambda)$ [see Eq. (6.18)]. The EOM of this system are displayed in Eqs. (6.21)-(6.23). The energy of the Higgs+gauge system can be written in the Abelian-Higgs model as

$$\rho = \frac{\lambda \varphi_*^4}{4a^4} E_{\rm Tot} \equiv \frac{\lambda \varphi_*^4}{4a^4} (E_K + E_V + E_G + E_E + E_M) \, , \tag{6.49}$$

where E_K, E_G and E_V are the Higgs kinetic, gradient and potential energies respectively, defined in Eq. (6.37), and $E_E \equiv E_{E,1}$ and $E_M \equiv E_{M,1}$ are the Abelian electric and magnetic energies defined in Eqs. (6.38)-(6.39).
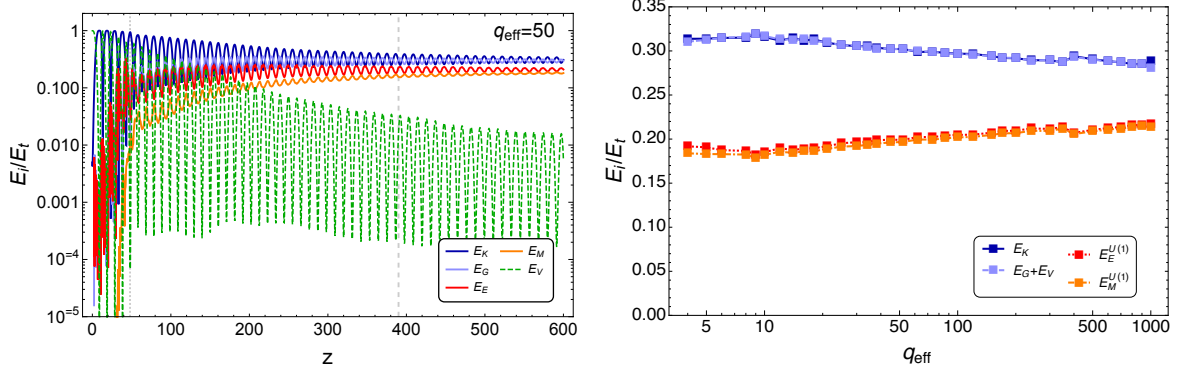
Figure 6.6.: Left: We show the time evolution of the different energy ratios [see Eq. (6.49)] as a function of time for the Abelian-Higgs simulations, with $q_{\rm eff} = 50$, $\beta = 0.1$, and a RD post-inflationary equation of state. Right: We show the final energy ratios $E_i/E_{\rm Tot}$ for the Abelian-Higgs simulations [see Eq. (6.49)] as a function of $q_{\rm eff}$ (i.e. the energy ratios well in the stationary regime $z \to \infty$)

We show in the left panel of Fig. 6.6 the different energy ratios $E_i/E_{\rm Tot}$ as a function of time, for an Abelian-Higgs simulation with $q_{\rm eff} = 50$. We can clearly see that, at late times, the following equipartition equalitites hold,

$$E_K \approx E_G + E_V , \quad E_E \approx E_M , \tag{6.50}$$

i.e. we find equipartition between the Higgs kinetic and gradient+potential energies, as well as between the electric and magnetic energies. These identities are equivalent to the ones found for the SU(2)×U(1) system in Eq. (6.40). In that case, there was equipartition at late times between the electric and magnetic energies of both the U(1) and SU(2) sectors. This shows that the way in which equipartition is attained at late times is independent on the non-Abelian nature of the gauge fields.

We show now how the time scales $z_{\rm br}$ and $z_{\rm dec}$ behave as a function of $q_{\rm eff}$ in the Abelian-Higgs modelling. Let us focus first on the backreaction time $z_{\rm br}$. We have plotted the values of $z_{\rm br}$ for different values of $q_{\rm eff}$ in Fig. 6.2, again for $\beta = 0.1$ and a RD post-inflationary equation of state. We see that the value of $z_{\rm br}$ also correlates with the structure of resonance bands of the Lamé equation in the linear regime, and shows a clear oscillatoary pattern. Like in the SU(2)×U(1) simulations, the minimum of these oscillations corresponds to $z_{\rm br} \approx 40$, and it is attained for values of $q_{\rm eff}$ in the intervals $q_{\rm eff} \in [1,3], [6,10] \dots$, where as expected, the resonance is stronger. The maximum of $z_{\rm br}$ is attained, on the other hand, for values of $q_{\rm eff}$ in the intervals $q_{\rm eff} \in (3,6), (10,15) \dots$, where the resonance is expected to weaker. However, in the second case, the agreement between U(1) and SU(2)×U(1) simulations is much worse. For example, for $q_{\rm eff} \approx 4$ the U(1) simulation gives $z_{\rm br} \approx 260$, while the SU(2)×U(1) one gives $z_{\rm br} \approx 50$. This is expected because when the resonance is stronger, the linear terms in the gauge EOM dominate over the non-linear ones, and hence the Abelian approximation holds better.

On the other hand, we plot in Fig. 6.3 the values of z_{dec} as a function of q_{eff} for the Abelian-Higgs simulations. Here, we have technically defined z_{dec} as the time when the Higgs kinetic and gradient+potential energies are equiparted at the 2% level, like we did in the SU(2)×U(1) simulations. We find that z_{dec} also follows a clear power-law dependence with q_{eff}, which we fit (for $\beta = 0.1$ and $w = 1/3$) as,

$$z_{\mathrm{dec}} = 440 \left(\frac{q_{\mathrm{eff}}}{100}\right)^{0.55} + z_{\mathrm{br}} \, , \quad (q_{\mathrm{eff}} > 20, \beta = 0.1, \mathrm{RD}) \, . \tag{6.51}$$

Using the rescalings of Eqs. (4.88) and (4.89), this fit can be generalized to arbitrary values of β and w as

$$z_{\mathrm{dec}} = 140 \left(\frac{q_{\mathrm{eff}}}{100}\right)^{0.55} \beta^{\frac{-(1+3w)}{3(1+w)}} + z_{\mathrm{br}} \, , \quad (q_{\mathrm{eff}} > 20) \, . \tag{6.52}$$

The exponent of the power-law obtained from the Abelian-Higgs simulations is quite similar to the $z_{\mathrm{dec}} \propto q^{0.53}$ found for the full SU(2)×U(1) simulations [Eq. (6.44)]. However, the estimated value of z_{dec} in the Abelian-Higgs simulation is a factor $4/3$ greater than in the SU(2)×U(1) case. In other words, in the presence of non-Abelian interactions, the field dynamics go faster to an equipartition regime than when such interactions are not present.

Finally, we show in the right panel of Fig. 6.6 how the energy is distributed between its different energy components at late times, as a function of q_{eff}, in the Abelian-Higgs model. We can clearly see that, independently of the value of q_{eff}, the energy at late times is distributed as $E_K \approx 30\%$, $E_G + E_V \approx E_G \approx 30\%$, $E_E \approx 20\%$ and $E_M \approx 20\%$, so

$$\frac{E_{\mathrm{Hig}}}{E_{\mathrm{Tot}}} \approx 0.6 \, , \quad \frac{E_{\mathrm{EM}}}{E_{\mathrm{Tot}}} \approx 0.4 \, . \tag{6.53}$$

In other words, in the U(1) simulations, the Higgs field only transfers 40% of its energy to gauge fields, as defined in Eqs. (6.45) and (6.46) This is in sharp contrast with the results from SU(2)× U(1) simulations, where the total energy transfer is approximately 70% [see Eq. (6.47)]. Therefore, we see here that an important effect of the non-Abelian interactions is to enhance significantly the energy transfer from the mother to the daughter fields (i.e. electric and magnetic energies).

6.4. Summary

In this chapter, we have studied the decay of the Standard Model Higgs condensate after inflation into the SU(2)×U(1) electroweak gauge fields. We have considered the same scenario as in Chapter 4. There, we simulated the dynamics with lattice simulations of global and Abelian-Higgs set-ups. As described in Section 4.5.2, this approach is justified at initial times,

where the system is in the linear regime. However, the non-Abelian interactions could have relevant effects in the field dynamics at late times, which can only be quantified with lattice simulations of the full SU(2)×U(1) gauge group. In this section, we have studied and quantified precisely these effects.

First we have described how parametric resonance works, when the parametrically excited species are a combination of several Abelian and non-Abelian gauge fields. We have found that a set of N Abelian gauge bosons, coupled to an oscillating complex scalar field, can be imitated exactly with a effective gauge coupling q_{eff}, which is a direct sum of the resonance parameters of all independent gauge bosons. This is valid at all times. Analogously, a similar construction can be done when the gauge sector is formed by several Abelian and non-Abelian gauge bosons. In the case of a SU(2)×U(1) gauge structure, dynamics can be described as a single Abelian gauge boson with effective resonance parameter, $q_{\text{eff}} = q_1 + q_2$, where q_1 and q_2 are the independent resonant parameters of the Abelian and non-Abelian sectors [defined in Eq. (6.34)]. However, in the case of the SU(2)×U(1) gauge group, the effective description is only valid in the linear regime, at early times.

We have then presented the results obtained from a set of lattice simulations of the Higgs decay process. As said, the main difference is that, unlike in Chapter 4, we have simulated explicitly the SU(2)×U(1) gauge structure in the lattice. We have parametrized the time scales and energy ratios, and we have compared with the results from the Abelian-Higgs system. As discussed, there are two important time scales in parametric resonance processes: the backreaction time z_{br} and the decay time z_{dec}. We have compared both times scales in both scenarios. In the case of z_{br}, we have seen that, for resonance parameters with larger average *Floquet index* (i.e. when the resonance is stronger), the Abelian approximation holds quite well, while it fails when the resonance is weaker, see Fig. 6.2. In the case of z_{dec}, we have found that in both U(1) and SU(2)×U(1) simulations, it grows as $z_{\text{dec}} \sim q^{0.5}$. However, we find that, in the presence of non-Abelian interactions, the equipartion regime is achieved a factor 4/3 faster than when such interactions are not present, see Fig. 6.3.

The presence of non-Abelian interaction do not change the equipartition identities at late times. In both the U(1) and SU(2)×U(1) simulations, we have found that at late times, there is equipartition betwen the Higgs kinetic and gradient+potential energies, as well as between electric and magnetic energies. However, the amount of energy that the Higgs transfers to the electric and magnetic fields is much larger in the presence of non-Abelian interactions. In the SU(2)×U(1) simulations, we have found that 70% of the total energy is accumulated by the gauge fields, while in the U(1) simulations, the energy transfer is only 40%.

Chapter 7.

Higgs-curvature coupling and post-inflationary vacuum instability

We study in this chapter the post-inflationary dynamics of the Standard Model (SM) Higgs in the presence of a non-minimal coupling $\xi|\Phi|^2 R$ to gravity, both with and without the electroweak gauge fields coupled to the Higgs. We assume a minimal scenario in which inflation and reheating are caused by chaotic inflation with quadratic potential, and no additional new physics is relevant below the Planck scale. By using classical real-time lattice simulations with a renormalisation group improved effective Higgs potential, and by demanding the stability of the Higgs vacuum after inflation, we obtain upper bounds for ξ, taking into account the experimental uncertainty of the top-Yukawa coupling. We compare the bounds in the absence and presence of the electroweak gauge bosons, and conclude that the addition of gauge interactions has a rather minimal impact. In the unstable cases, we parametrize the time when such instability develops. For a top quark mass $m_t \approx 173.3 \text{GeV}$, the Higgs vacuum instability is triggered for $\xi \gtrsim 4 - 5$, although a slightly lower mass $m_t \approx 172.1 \text{GeV}$ pushes up this limit to $\xi \gtrsim 11 - 12$. This, together with the estimation $\xi \gtrsim 0.06$ for stability during inflation, provides tight constraints to the Higgs-curvature coupling within the SM.

7.1. Introduction

As described in Section 4.2, the Standard Model (SM) potential may become negative at very high energies [131, 132]. This has prompted an important effort to determine whether the electroweak vacuum is, in the present, stable or unstable. Current measurements of the top quark and Higgs masses indicate that we live in a meta-stable Universe: the probability of the Higgs field to decay into a higher-scale negative-energy vacuum is non-zero, but the estimated decay time is much larger than the present age of the Universe [127].

However, the situation is quite different in the early Universe. In this case, high energies and high spacetime curvature can make the vacuum more unstable. In particular, this may happen during inflation [127, 143, 144, 145, 129, 146, 147, 148, 149, 150], or during the successive period of (p)reheating [151, 152, 153, 84, 154]. The dynamics of the Higgs field Φ during and after inflation, as well as the potential instability of the Higgs vacuum, depend very sensitively on the strength of its non-minimal coupling to the scalar curvature, defined as $\xi|\Phi|^2 R$, with R the Ricci scalar. This interaction is necessary to renormalise the theory in curved space [155, 156], and given that ξ runs with energy, it cannot be set to zero at all energy scales. Gravitation is very weak in comparison with the other interactions, so current particle-physics experiments provide only very weak constraints to this coupling, $|\xi| \lesssim 2.6 \times 10^{15}$ GeV [157]. The coupling ξ can be considered, therefore, as the last unknown parameter of the SM.

In chapters 4 to 6, we have considered the dynamics of the SM Higgs during and after inflation, when the Higgs is effectively light during inflation ($\xi \lesssim 0.1$), and behaves as a spectator field, forming a condensate with a large vacuum expectation value (VEV) [54, 127, 56, 55]. If it exceeds the position of the potential barrier, the Higgs reaches its true negative-energy vacuum and generates patches of anti-de Sitter space, resulting in a catastrophic outcome for our Universe [127, 143, 144, 145, 129, 146, 148, 149, 150]. As discussed in Section 4.2, one way to prevent this from happening is to consider values of the top quark mass 2-3 sigma below its central value, so that the instability scale is pushed to sufficiently high energies, or it is simply not present (see Fig. 4.1 of Section 4). Another way of ensuring vacuum stability is to consider a sufficiently low inflationary scale, so that even if the Higgs is excited during inflation, its amplitude never reaches the potential barrier. In any case, if the Higgs field remains stable during inflation, it starts oscillating around the minimum of its potential shortly after inflation ends, rapidly decaying into the SM gauge bosons and fermions via non-perturbative parametric effects. We have studied this process extensively in Chapters 4, 5, and 6.

On the other hand, if $\xi \gg 0.1$, the height of the potential barrier increases at tree level, and the Higgs is no longer a light degree of freedom during inflation [127, 129]. In this case, the Higgs field acquires an effective mass of the order $m_\Phi^2 \simeq \xi R \sim 12\xi H_i^2 \gtrsim H_i^2$ during inflation, with H_i the inflationary Hubble rate. This prevents the Higgs from developing large amplitude fluctuations during inflation. However, the situation is quite the opposite after inflation ends. The post-inflationary oscillations of the inflaton ϕ around the minimum of its potential induce rapid changes in the spacetime curvature R, which becomes negative during a significant fraction of time in each oscillation. The effective mass of the Higgs field becomes tachyonic during those moments, $m_\Phi^2 \propto R < 0$. If ξ is sufficiently large, the Higgs field may be significantly excited during the tachyonic periods, potentially triggering the vacuum instability [151]. This issue was studied previously in [151, 152, 153], using both analytical and numerical techniques, as well as classical real-time lattice simulations. The results of all of these works agreed qualitatively, finding $\xi \lesssim \mathcal{O}(1) - \mathcal{O}(10)$ as an upper bound for achieving

stability after inflation. A similar lattice analysis of the values of the Higgs-inflaton coupling inducing the instability of the Higgs vacuum was also carried out in [84], while an analysis of the combined effects of both Higgs-curvature and Higgs-inflaton couplings was done in [154].

In this chapter, we use classical field theory lattice simulations to constrain the range of allowed ξ values which ensure the stability of the Higgs vacuum after inflation. We do a systematic parameter analysis of the Higgs post-inflationary dynamics. We use in the simulations the renormalization group improved Higgs effective potential, Eq. (4.3), and study the impact of the initial conditions and number of Higgs components in the results. We include also an analysis of how the time scale at which the Higgs field develops the instability depends on ξ and the top-quark mass. Furthermore, we consider the more realistic situation where the Higgs field is coupled to the electroweak gauge bosons. We mimic the SM gauge interactions with an Abelian-Higgs analogue model, which captures well the gauge boson field effects onto the Higgs post-inflationary dynamics, as we expect the non-Abelian terms of the Lagrangian to be subdominant, especially at the earliest times (see Section 4.5.1 for an explanation in the context of parametric resonance). In this chapter we assess for the first time the implications for the ξ bounds due to the presence of the SM electroweak interactions. We have assumed throughout this chapter a chaotic inflation model with quadratic potential.

The structure of the chapter is as follows. In Section 7.2 we present a brief review of the inflaton and Higgs dynamics after inflation in the presence of a Higgs-curvature non-minimal coupling. We also present the equations of motion and the initial conditions of the different fields, as well as some qualitative aspects of our lattice simulations. The following three sections present the results from our lattice simulations, with increasing degree of complexity. In Section 7.3 we consider a free scalar field with no potential. This is useful to understand better the results in Section 7.4, where we introduce the renormalisation group improved Higgs potential. We determine the values of the coupling ξ that give rise to an unstable Universe, and parametrize the time scale at which the instability takes place, as a function of ξ and m_t. In Section 7.5 we repeat the same analysis, but including also the gauge bosons in the lattice. In Section 7.6 we discuss our results and conclude.

7.2. Higgs excitation due to inflaton oscillations

We consider throughout the chapter the inflationary chaotic model $V(\phi) = \frac{1}{2}m_\phi^2\phi^2$, where ϕ is the inflaton, and $m_\phi = 1.5 \times 10^{13}$GeV. If $\phi \gtrsim \mathcal{O}(10)m_p$, the field is in a slow-roll regime, causing the inflationary expansion of the Universe. However, when $H(t) \approx m_\phi$ with $H(t)$ the Hubble parameter, the inflaton field starts oscillating around the minimum of its potential, ending the inflationary stage. Details of the preheating process in this model have been studied in Section 2.4. There we defined t_i as the time when $H(t_i) = m_\phi$ holds exactly, and considered
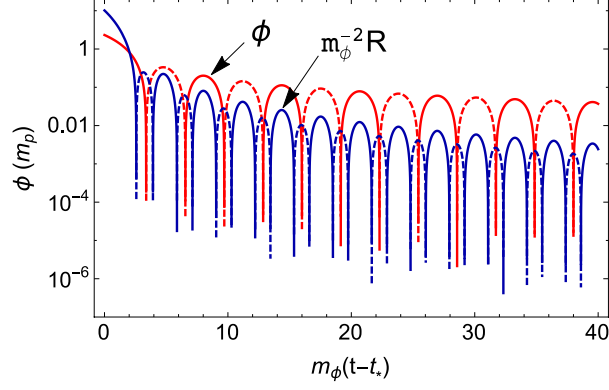
Figure 7.1.: The red line shows the oscillations of the inflaton field as a function of time in units of $m_p = (8\pi G)^{-1/2}$, and the blue line shows, for comparison, the corresponding (dimensionless) Ricci scalar $m_\phi^{-2}R$. A solid line indicates positive values, and a dashed line negative values.

this moment as the onset of the inflaton oscillations. The coupled equations of motion of the inflaton and scale factor are

$$\ddot{\phi} + 3H(t)\dot{\phi} + m_\phi^2\phi = 0 \,, \tag{7.1}$$

$$H^2(t) \equiv \left(\frac{\dot{a}}{a}\right)^2 = \frac{1}{6m_p^2}(\dot{\phi}^2 + m_\phi^2\phi^2) \,. \tag{7.2}$$

To obtain the initial conditions for the homogeneous inflaton, we have solved numerically the coupled inflaton and Friedmann equations, Eq. (7.1) and Eq. (7.2), imposing the slow-roll conditions $\dot{\phi} \simeq -m_\phi^2\phi^2/3H^2$, $\ddot{\phi} \ll m_\phi^2\phi^2$ well before the end of inflation. From the numerical solution, we obtain the time t_i when $H(t_i) = m_\phi$ holds exactly. At this moment we find $\phi(t_i) \simeq 2.32m_p$ and $\dot{\phi}(t_i) \simeq -0.78m_\phi m_p$. Using Eqs. (7.1) and (7.2), the Ricci scalar can be expressed in terms of ϕ and $\dot{\phi}$, as

$$R(t) \equiv 6\left[\left(\frac{\dot{a}}{a}\right)^2 + \frac{\ddot{a}}{a}\right] = \frac{1}{m_p^2}(2m_\phi^2\phi^2 - \dot{\phi}^2) \,. \tag{7.3}$$

The inflaton field after inflation behaves, approximately, as a damped oscillator with decaying amplitude [25]

$$\phi(t) \simeq \phi_a(t)\sin(m_\phi t) \,, \quad \phi_a(t) = \sqrt{\frac{8}{3}}\frac{m_p}{m_\phi t} \,. \tag{7.4}$$

Each time the inflaton field crosses around zero, $\phi \approx 0$, we have $R(t) < 0$ from Eq. (7.3). This can be clearly seen in Fig. 7.1, where we plot both the inflaton and the Ricci scalar as a function of time.

Let us focus now on the post-inflationary dynamics of the Higgs field. We wrote the relevant piece of the SM action in Eq. (4.1). Due to the coupling to the scalar curvature, the Higgs gets an effective mass $m_\Phi^2(t) = \xi R(t)$. Therefore, the Higgs becomes effectively tachyonic with $m_\Phi^2 < 0$, during the intervals when the Ricci scalar becomes negative. Due to this, there is a strong periodic excitation of the Higgs field, a phenomenon known as tachyonic resonance [81].

We can estimate both the period of time that the Ricci scalar becomes negative, as well as the maximum momenta excited by the resonance. The inflaton crosses zero periodically at $m_\phi t_n = (n - 1/2)\pi$, $n = 1, 2, 3, ...$ We can determine a typical envelope amplitude between the n-th and the $(n + 1)$-th crossings, as $\phi_n/m_p = \sqrt{8/3}/\pi n$, with $\phi_n = \phi(t_n)$. When the inflaton crosses around zero, the Ricci scalar becomes negative $R \simeq \phi_n^2(m_\phi/m_p)^2(3m_\phi^2\Delta t^2 - 1) < 0$ for a time $m_\phi\Delta t \lesssim 2/\sqrt{3} \approx 1.2$, while the inflaton amplitude is $|\phi| \lesssim \phi_n/\sqrt{3} \sim 0.3 m_p/n$. On the other hand, the greater the coupling ξ, the larger the range of Higgs tachyonic modes excited while the curvature is negative. We estimate this as an infrared (IR) band from $k = 0$ up to a cutoff Λ, $k \in [0, \Lambda]$, with

$$\Lambda \simeq \frac{2\sqrt{2}}{\sqrt{3}} \frac{a_n}{\pi n} \sqrt{\xi} \,, \tag{7.5}$$

where a_n is the scale factor at t_n (we take initially $a_1 = 1$). Let us consider the unitary gauge, so that the SM Higgs doublet can be written as a real degree of freedom, $\Phi = \varphi/\sqrt{2}$. Let us redefine the Higgs amplitude as $h \equiv \varphi/a^{3/2}$ so that in cosmic time, this re-scaling eliminates the friction term in the Higgs EOM. If we ignore the presence of the gauge bosons and of the Higgs self-interacting potential, the equation of motion of its Fourier modes is

$$\ddot{h}_k + \left[\frac{k^2}{a^2} + \xi R(t) + \Delta\right] h_k = 0 \,, \tag{7.6}$$

where $\Delta \equiv -\frac{3}{4}\frac{\dot{a}^2}{a^2} - \frac{3}{2}\frac{\ddot{a}}{a}$, so that $\Delta \ll k^2/a^2$ for sub-horizon scales, and we can ignore it. Using Eqs. (7.3)-(7.4), we can write the previous EOM as

$$\frac{d^2 h_k}{dz^2} + (A_k - 2q\cos(2z))h_k = 0 \,, \tag{7.7}$$

where $z \equiv m_\phi(t - t_i)$ and

$$A_k \equiv \frac{k^2}{a^2 m_\phi^2} + \frac{\phi_n^2(z)}{2m_p^2}\xi \,, \qquad q \equiv \frac{3\phi_n^2(z)}{4m_p^2}\left(\xi - \frac{1}{4}\right) \,. \tag{7.8}$$

This corresponds to a *Mathieu* equation, as the one shown in Eq. (2.45) in the context of parametric resonance with quadratic potential. Its properties have been studied in Section 2.4.1. The main difference with respect to standard parametric resonance is that we are not constrained now to the case $A_k > 2q$, and hence we have greater resonance bands which induce a stronger particle creation effect in the broad resonance regime $q \gg 1$. However, note that

due to the expansion of the Universe, $\phi_n(z)$ decreases, and hence this pushes the Higgs into a narrow resonance regime, where this effect is much weaker. The dynamics of this theory was studied in [129] with the properties of tachyonic resonance of [81], and after that numerically in [152] and in the lattice in [153, 84, 154].

Let us consider now the effect of plugging back the Higgs potential. In particular we consider the renormalisation group improved Higgs potential, written in Eq. (4.2). In that expression, $\lambda(\varphi)$ is the renormalised Higgs self-coupling at the renormalisation scale $\mu = \varphi$, whose running was computed up in [131, 132] to three loops in Minkowski spacetime[1]. As explained in Section 4.2, the running of $\lambda(\varphi)$ is very sensitive to the particular value of the top quark mass, and in fact, it may become negative at large energies for top quark masses $m_t > m_{t,c} \approx 171.1\text{GeV}$.

Let us now incorporate the potential into the Higgs mode equation,

$$\ddot{h}_k + \left[\frac{k^2}{a^2} + \xi R(t) + \frac{\lambda(\varphi)}{a^3}\langle h^2 \rangle \right] h_k = 0 \,. \tag{7.9}$$

If $\lambda > 0$, the Higgs tachyonic resonance effect weakens, as the Higgs self-interaction $\lambda(\varphi)\langle h^2 \rangle > 0$ compensates the negativeness of $\xi R < 0$. If $\lambda < 0$, the tachyonic effect, on the contrary, is enhanced. The presence of the Higgs potential represents a correction over the mode excitation described by Eqs. (7.6), (7.8). We need therefore to introduce the system into a lattice, where we can solve numerically the EOM of the Higgs including its own potential non-linearities, and taking into account both cases $\lambda < 0$ and $\lambda > 0$.

7.2.1. Higgs potential in the lattice

The equation of motion for the Higgs field (in the absence of electroweak gauge interactions) can be derived from the minimization of action (4.1). It is

$$\ddot{\Phi} - \frac{1}{a^2}\nabla^2\Phi + 3\frac{\dot{a}}{a}\dot{\Phi} + 2[\xi R + \lambda(|\varphi|)(\Phi^\dagger\Phi)]\Phi = -\frac{\partial\lambda}{\partial|\varphi|}(\Phi^\dagger\Phi)^2 \,, \tag{7.10}$$

where the Higgs field $\Phi \equiv \varphi/\sqrt{2}$ is a complex doublet with four real components

$$\varphi = \begin{pmatrix} \varphi_1 + i\varphi_2 \\ \varphi_3 + i\varphi_4 \end{pmatrix} \,, \quad \varphi_n \in \mathfrak{Re} \,. \tag{7.11}$$

The form of $a(t)$ in this equation, as well as the Ricci scalar $R(t) = R[a, \dot{a}, \ddot{a}]$, is obtained from the self-consistent solution of the inflaton and Friedmann equations (7.1) and (7.2). As we shall

---

[1]Let us note that the effective potential also depends on the spacetime curvature through loop corrections, but as seen in [158], these terms are only relevant for small couplings $\xi \lesssim 1$.
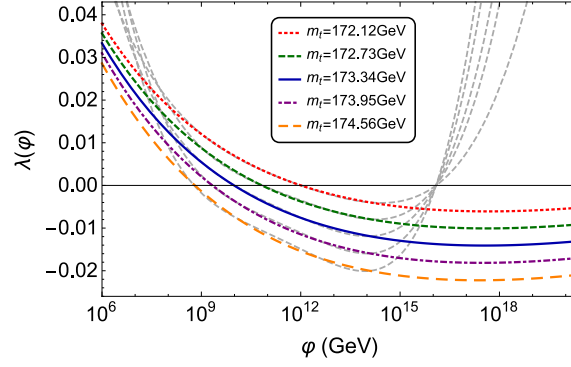
Figure 7.2.: Running of $\lambda(\varphi)$ as a function of the Higgs field φ for $\alpha_s = 0.1184$, $m_h = 125.5$GeV, for the different values of the top quark mass m_t considered in this chapter, obtained from the public package provided in Ref. [130]. The corresponding grey dashed lines indicate the interpolations $\lambda_{in}(|\varphi|)$ used in the lattice simulations.

see, for the values of ξ considered in this chapter, the energy of the Higgs field is always several orders of magnitude subdominant with respect the energy of the inflaton. Hence, we can just ignore the contribution of the Higgs field to the Friedmann equation. Note that the inflaton is taken as a homogeneous field, and we do not introduce it explicitly in the lattice, it simply dictates the form of $a(t)$ and $R(t)$ as a function of time.

We introduce in the lattice the renormalization group improved effective potential[2], Eq. (4.3), as

$$V(|\varphi|) = \frac{\lambda(|\varphi|)}{4}|\varphi|^4, \quad |\varphi| = \sqrt{\sum_{n=1}^{4} \varphi_n^2}, \tag{7.12}$$

where we assume $|\varphi| \gg v$. As seen before, the Higgs self-coupling $\lambda(\varphi)$ runs with the value of φ. We introduce the running in our simulations as a local function of the lattice point n, i.e. $\lambda(|\varphi(n)|)$: as the value of $|\varphi|$ changes from lattice point to lattice point, so does too the value of the Higgs self-interaction. More specifically, we introduce a quartic logarithmic polynomial $\lambda_{in}(|\varphi|) = \sum_{n=0}^{4} c_n (\log|\varphi|)^n$, interpolating the 3-loop calculation of the running obtained in [130] for the relevant range of Higgs amplitudes $|\varphi|$ (see Fig. 7.2). As we have mentioned, the running of the potential depends strongly on the value of the top quark mass, the current world average being $m_t = 172.44^{\pm 0.13(stat)}_{\pm 0.47(syst)}$ GeV [133]. We take this uncertainty into account by providing different sets of $\{c_n\}$ constants, corresponding to different interpolations of the running for each value of m_t. Note also that in Section 4.2 we characterized, for each different running, two scales: $\varphi = \varphi_+$, which indicates the position of the barrier in the effective potential; and $\varphi = \varphi_0$, which indicates when the Higgs potential becomes negative. We indicated the values of these scales for different top quark masses in Table 4.1.

---

[2]As argued in Ref. [129], the scale choice should also involve the Ricci scalar R, but in the current time-dependent case it could lead to unphysical effects.

Our interpolation can only describe appropriately the running of λ for certain values of $|\varphi|$, failing at low and large field amplitudes. This is however not a problem, because those field values are never reached anywhere in the lattice, before the instability of the Higgs field is developed. On the other hand, when the Higgs has become unstable and decays towards the negative-energy vacuum, the amplitude of the Higgs field starts increasing very fast, reaching the region where the interpolation fails. However, our aim in this chapter is to determine the specific time when the instability is developed, not to characterize the dynamics of the Higgs field once the instability has commenced. In fact, in order to ensure numerical stability during the Higgs field transition from positive to negative λ, it is convenient to modify the high-energy running of the latter, so that it generates a second vacuum at an energy lower than that dictated by the real running predicted in the Standard Model. This is achieved for $c_4 > 0$. In particular, we have chosen the constants so that the negative-energy vacuum is generated at approximately $\varphi = \varphi_v \approx 10^{16}$GeV. If the Higgs amplitude goes to this vacuum with negative potential energy, we say that the Higgs has become unstable. We have explicitly checked that our characterization of the times of instability is independent on the particular choice of constants c_n (for a given m_t value), as long as they fit the Higgs effective potential within the range $\sim 10^9 - 10^{14}$ GeV.

In Section 7.3 we study tachyonic resonance in the lattice, taking the Higgs as a free field without self-interaction. The Higgs will then be excited only due to the rapidly changing spacetime background. In Section 7.4 we re-introduce back the Higgs potential, but ignore yet its interaction with the gauge bosons. We determine under those circumstances, what values of ξ lead the Higgs field to become unstable, so that it rolls rapidly into the true vacuum. In Section 7.5 we finally incorporate a gauge structure into the simulations, and study their effect on the post-inflationary Higgs dynamics, re-evaluating again the critical values of ξ.

7.2.2. Initial conditions

We start the lattice simulations at time $t = t_i$, where we impose for all four components of the Higgs that their initial homogeneous amplitude vanishes, $\varphi_n(t_i) = 0$, $n = 1, 2, 3, 4$. We then add on top a spectrum of fluctuations[3], which mimic the spectra of quantum vacuum

---

[3]Our initial conditions are set at a time when the slow-roll conditions are not yet totally broken. Therefore, we can introduce instead quantum vacuum fluctuations in *de Sitter*,

$$\langle |\varphi_k|^2 \rangle = \frac{\pi e^{-\pi \mathfrak{Im}[\nu]}}{4 H_i a_i^3} \left| H_\nu^{(1)} \left(\frac{k}{a_i H_i} \right) \right|^2 \tag{7.13}$$

with $\nu = \sqrt{9/4 - (\xi R_i / H_i)^2}$. However, for the couplings $\xi > 4$ we are considering, this spectra is almost identical to the FLRW case described by Eq. (7.14).

fluctuations,

$$\langle|\varphi_k|^2\rangle = \frac{1}{2a_{\mathrm{i}}^3\omega_k}\,, \qquad \omega_k = \sqrt{\frac{k^2}{a_{\mathrm{i}}^2} + \xi R_{\mathrm{i}}}\,, \tag{7.14}$$

where $a_{\mathrm{i}} = a(t_{\mathrm{i}}) \equiv 1$, and $R_{\mathrm{i}} \equiv R(t_{\mathrm{i}}) \approx 10 H_{\mathrm{i}}^2$ from Eq. (7.3).

The spectra of quantum fluctuations (7.14) is set in the lattice in a similar way as in *Latticeeasy* [47], imposing in momentum space the following spectra for the Higgs field amplitude and derivatives

$$\begin{aligned}
\varphi_n(k) &= \frac{|\varphi_n|}{\sqrt{2}}(e^{i\theta_{n1}} + e^{i\theta_{n2}})\,, \quad (k < k_c)\\
\varphi_n'(k) &= \frac{|\varphi_n|}{\sqrt{2}}i\omega_{k,n}(e^{i\theta_{n1}} - e^{i\theta_{n2}})\,, \quad (k < k_c)
\end{aligned} \tag{7.15}$$

where $\omega_{k,n} \equiv \sqrt{(k/a_{\mathrm{i}})^2 + \xi R_{\mathrm{i}}}$, θ_{n1} and θ_{n2} are real phases drawn from a uniform random distribution in the interval $\theta_{n1}, \theta_{n2} \in [0, 2\pi)$, whereas $|\varphi_n|$ varies according to the probability distribution

$$P(|\varphi_n|)d|\varphi_n| = \frac{2|\varphi_n|}{\omega_{k,n}^2}e^{-\frac{|\varphi_n|^2}{\omega_{k,n}^2}}d|\varphi_n|\,. \tag{7.16}$$

The ultraviolet cutoff k_c is introduced in order to prevent the excitation of UV modes which are not expected to be excited by the tachyonic resonance, i.e. $k_c \approx \Lambda$ with Λ given by Eq. (7.5).

Hence, the variance of (a component of) the Higgs field initially is

$$\langle\varphi_{\mathrm{i}}^2\rangle = \frac{1}{4\pi^2a_{\mathrm{i}}^3}\int_0^{k_c}dk\frac{k^2}{\omega_k} = \frac{1}{8\pi^2}\left(k_c\omega_{k_c} + \xi R_{\mathrm{i}}\log\left[\frac{\xi R_{\mathrm{i}}}{k_c + \omega_{k_c}}\right]\right)\,, \tag{7.17}$$

where we have taken $a_{\mathrm{i}} = 1$ in the second equality. Typical numbers chosen in our simulations are $\xi \sim 10$ and $k_c \sim 10 H_{\mathrm{i}}$, which gives an initial Higgs amplitude

$$\sqrt{\langle\varphi_{\mathrm{i}}^2\rangle} \approx 0.82 H_{\mathrm{i}} \approx 1.2 \times 10^{13}\mathrm{GeV}\,. \tag{7.18}$$

Typically $\sqrt{\langle\varphi_{\mathrm{i}}^2\rangle} \gg \varphi_+$, and hence, in most of the physical space, the Higgs field is already in the right side of the barrier when initial conditions are set. This, however, does not mean that the Higgs field will immediately become unstable, as the mainly positive sign of R may impede it. We shall discuss this issue in more detail in Sections 7.4 and 7.5. Let us also remark that this way of fixing the initial conditions is only appropriate if the tachyonic resonance regime of the system enhances the Higgs amplitude significantly over the value given in Eq. (7.18). If it does not, we cannot trust the lattice approach. Finally, let us also note that there is a contribution to the Higgs effective mass from its self-interactions, i.e. the effective Higgs mass should be
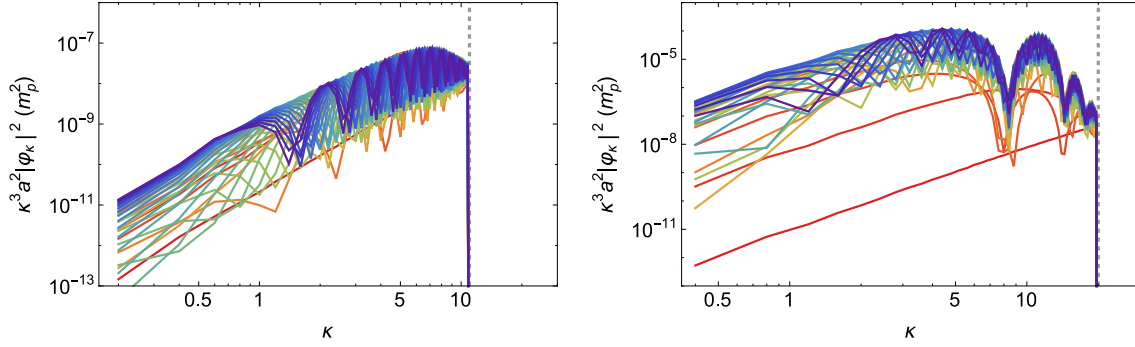
Figure 7.3.: The time-evolution of the Higgs field spectra $\kappa^3 a^2 |\varphi_\kappa|^2$ as a function of $\kappa \equiv k/m_\phi$, for the non-interacting case (Section 7.3) with the Higgs-curvature couplings $\xi = 5$ (left panel) and 30 (right panel). The different coloured lines show the spectra at different times, going from early times (red) to late times (purple). The time interval between lines is $m_\phi \Delta t = 2$, so $m_\phi(t - t_\mathrm{i}) = 0, 2, 4, \ldots 100$.

rather $m_\mathrm{eff}^2 \approx \xi R_\mathrm{i} + \lambda \langle \varphi_\mathrm{i} \rangle^2$. Taking $\lambda \approx -0.01$, $\xi \approx 10$, and $H_\mathrm{i} = m_\phi \approx 6 \times 10^{-6} m_p$, we see that the second term (Higgs self-interaction) is negligible with respect to the first one (Higgs non-minimal coupling).

7.3. Simulations with a free scalar field

We study first the case of a non-interacting scalar field, i.e. we solve only Eq. (7.10), setting $\lambda = 0$. Although this is obviously not a physical case, it will be helpful to understand our later results better when we include the Higgs self-interactive potential. Thus we consider now a 4-component Higgs field, coupled to the spacetime curvature through the term $\xi R \Phi^\dagger \Phi$, with $R[\phi, \dot\phi]$ evolving due to the oscillating inflaton. We have done several lattice simulations of this system, varying the coupling ξ within the range $\xi \in [4, 70]$.

We show in Fig. 7.3 the spectra of the Higgs field for the particular cases $\xi = 5$ and $\xi = 30$. In both panels, the red color corresponds to early times, while dark blue/purple corresponds to late times. In these spectra, a cutoff has been put in the distribution of initial fluctuations at the scale k_c, as indicated in Eq. (7.15). The value of k_c has been estimated from a previous set of lattice simulations without cutoff, in which we see that for $k > k_c$, the Higgs excitation due to the tachyonic resonance is negligible. Both spectra grow very fast, saturating eventually at a time $t \approx t_\mathrm{res}$, defined below. Naturally, the spectra grows several orders of magnitude more in the $\xi \approx 30$ case (right panel in Fig. 7.3) than in the $\xi \approx 5$ case (left panel in Fig. 7.3), as the tachyonic effect is stronger in the first case.

In Fig. 7.4 we show the conformal and physical amplitudes of the Higgs field as a function of time, averaged over the whole volume of the lattice, for the couplings $\xi = 3, 6, 10, 15, 30$. We
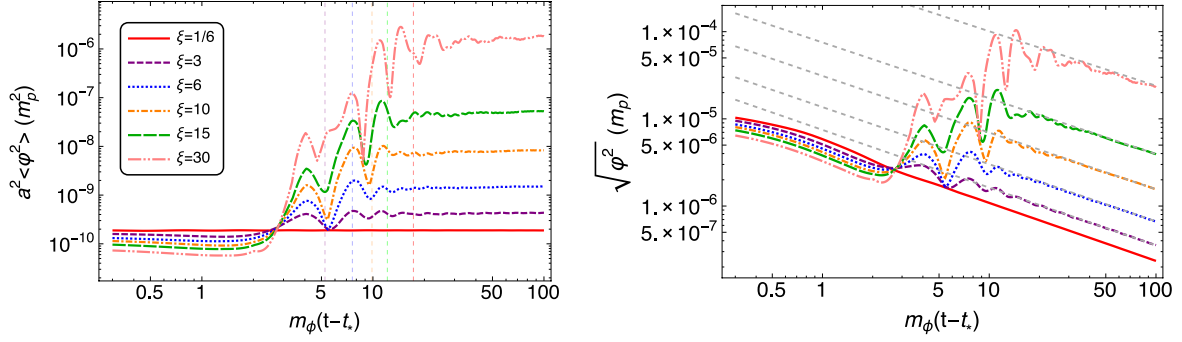
Figure 7.4.: Left: The Higgs conformal amplitude $a^2\langle\varphi^2\rangle$ obtained from lattice simulations, for the non-interacting case (Section 7.3) with the Higgs-curvature couplings $\xi = 1/6, 3, 6, 10, 15, 30$. The dashed, vertical lines indicate the estimated time t_{res}. Right: The root mean square of the Higgs physical amplitude $\langle\varphi^2\rangle$ for the same couplings. We indicate in dashed lines the corresponding fit (7.20) for the late-time dynamics.

remind that this plot is for a four-component Higgs field, while for a single component we have $\langle\varphi_n^2\rangle \approx \langle\varphi^2\rangle/4$ for each $n = 1, 2, 3, 4$.

We expect the Higgs excitation to end when $q \lesssim 1$, see Eq. (7.8). Taking $q = 0.2$ as the condition signalling the end of the tachyonic resonance regime, we find, using Eq. (7.4), that the time t_{res} it takes to switch off the resonance, is

$$m_\phi(t_{\text{res}} - t_{\text{i}}) \approx 1.58\sqrt{4\xi - 1}\,. \tag{7.19}$$

In the figure we indicate this time with vertical dashed lines. We see that for $t \lesssim t_{\text{res}}$ particle creation is exponential, and the greater the ξ, the stronger the growth of the conformal Higgs amplitude $h = a\varphi$. However, as we approach $t \approx t_{\text{res}}$, the Higgs excitation stops. From then on, the dynamics of the Higgs field is dominated by the expansion of the universe. More specifically, we have found that the late-time behaviour of the Higgs amplitude is

$$\langle|\varphi(t)|\rangle \sim (m_\phi t)^{-(0.64\pm0.03)}\,, \quad m_\phi t \to \infty\,, \tag{7.20}$$

where the particular numerical value of the exponent depends on the value of ξ considered. We indicate this in the left panel of Fig. 7.4 with dashed lines. As expected, Eq. (7.20) indicates that $\langle\varphi\rangle \propto a^{-1}(t)$. We have found that a rough estimate for the Higgs amplitude for late times is

$$
\begin{aligned}
\langle|\varphi(t)|\rangle &\approx e^{s(\xi)}(m_\phi t)^{-p(\xi)}m_p\,, \\
s(\xi) &\equiv -12.1 + 0.17\xi + 0.00046\xi^2\,, \\
p(\xi) &\equiv 0.67 - 0.0048\log\xi - 0.0017(\log\xi)^2\,,
\end{aligned}
\tag{7.21}
$$

where the first factor accounts for the initial excitation of the Higgs modes, and the second accounts for the later energy dilution.

Before we move on, it is important to note that, as we decrease ξ, the amplitude of the excited IR modes decreases significantly, being comparable to the amplitude of the (non-excited) UV modes for very low couplings. This signals that the lattice simulations cannot be trusted for these low couplings, because there is no significant excitation of the Higgs field over the initial vacuum fluctuations. Correspondingly, for these low couplings, the contribution of the UV modes to the Higgs amplitude becomes increasingly important, and hence its value can depend strongly on where we put the cutoff k_c of the initial fluctuations. Therefore, there is a minimum value ξ for which we can trust the lattice simulations. In this chapter we have determined this condition as $\frac{\langle \varphi(t_{\text{res}}) \rangle}{\langle \varphi_{\text{i}} \rangle} \frac{a(t_{\text{res}})}{a_{\text{i}}} > 2$, which means basically that the contribution to the Higgs amplitude from the Higgs excitation, is greater than the one from the Higgs initial vacuum fluctuations. With this, we find that we cannot trust simulations with $\xi \lesssim 4$.

7.4. Simulations with unstable potential

Let us now move to simulations with the full Higgs potential (7.12), including the four components of the Higgs field but yet without including gauge interactions. All the results of this Section have been obtained with lattice cubes of $N^3 = 256^3$ points, and minimum momentum $p_{\text{min}} = 0.18 m_\phi$.

To get a qualitative understanding of the dynamics, let us recall the linearised equation of motion (7.6) for the Higgs field modes $h_k \equiv \varphi_k a^{3/2}$. For high Higgs field values, $\varphi > \varphi_0$, the self-coupling is negative $\lambda(\varphi) < 0$, and therefore the interaction term tends to increase the Higgs field value, and induce a transition to the negative-energy vacuum. The more the Higgs field has been amplified by the tachyonic resonance, the faster the instability is. On the other hand, because the Ricci scalar remains larger time positive than negative during each inflaton oscillaton, the non-minimal coupling term $\xi R(t)$ effectively creates a potential barrier that resists this increase. The amplitude of the curvature term decays as $\xi R(t) \propto a^{-3}(t) \propto t^{-2}$, so it becomes however gradually less important. If it counteracts the instability until the Higgs field amplitude has decreased below the barrier scale $\varphi < \varphi_0$, then the Higgs field remains stable throughout the entire evolution. Because the amplification by the tachyonic resonance depends exponentially on the non-minimal coupling ξ [see Eq. (7.21)], whereas the effective barrier due to ξ depends on it only linearly, one expects that for high ξ, the instability takes place faster, and for low enough ξ it is prevented completely.

Fig. 7.5 shows the volume-averaged amplitude of the Higgs field $\langle |\varphi| \rangle$ as a function of time, for different choices of the Higgs-curvature coupling ξ, obtained directly from lattice simulations. In this Figure, we have used the running of the potential corresponding to the top
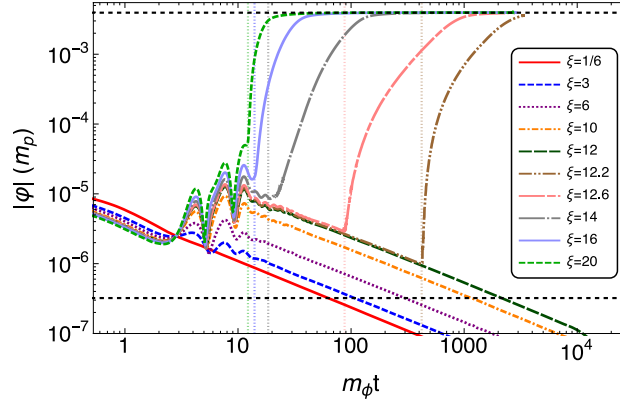
Figure 7.5.: The volume-average value of the Higgs field $|\varphi| = \sqrt{\sum_n \varphi_n^2}$ obtained from lattice simulations with unstable potential (Section 7.4), for the top quark mass $m_t = 172.12$GeV. Each line represents simulations with a different value of ξ. For the cases in which the Higgs field develops an instability, the vertical dashed lines indicate the instability time $m_\phi t_i$. The two dashed horizontal lines indicate the position of the barrier φ_+ estimated for this potential, and the (modified) high-amplitude, negative-energy vacuum φ_v.

quark mass $m_t = 172.12$ GeV, see Fig. 4.1. This potential has the barrier at $\varphi_+ \approx 7.8 \times 10^{11}$GeV. We can see that, for initial times $m_\phi(t - t_i) \lesssim 10$, the amplitude grows (in an oscillating way) due to the Higgs tachyonic resonance regime, as described in Section 4.2.

In Fig. 7.5 we see that for high values of the non-minimal coupling, $\xi \geq 16$, the Higgs field becomes unstable during the tachyonic resonance, triggering a transition to the high-energy vacuum $\varphi = \varphi_v$. For lower values of the non-minimal coupling, the tachyonic resonance ends before the Higgs has become unstable. After this the behaviour is initially similar to the free field case discussed in Section 7.3: the system settles in a quasi-stationary state in which the field amplitude gradually decreases due to the expansion of space. In the intermediate range of couplings, $12.2 \leq \xi \leq 14$, the instability eventually takes place, at a time that we denote by t_i. We indicate this with a vertical dashed line in Fig. 7.5.

For $\xi \leq 12$, the field amplitude eventually decreases below the potential barrier, $\varphi < \varphi_+$. By this time, the barrier stabilises the field, and therefore the instability does not take place at all. This demonstrates that physically the instability is due to the tachyonic resonance. Even though the amplitude of the initial vacuum fluctuations is higher than the barrier scale, it is not high enough to lead to an instability before it is damped to safe values by the expansion of the universe. From the spectra shown in Fig. 7.6 we can see that the infrared modes have to be amplified by roughly three orders of magnitude by the tachyonic resonance in order for the instability to take place. In particular, this means that the use of classical field theory simulations is well justified in this case.
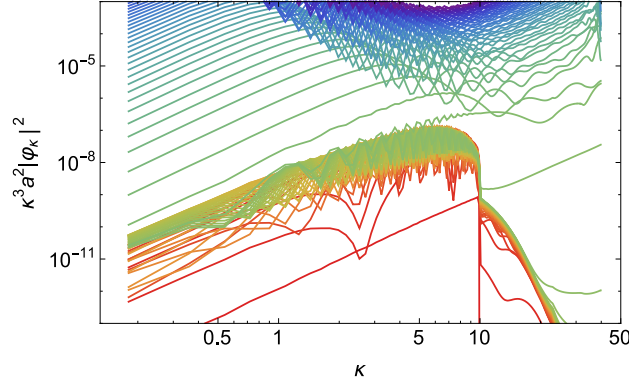
Figure 7.6.: Higgs field spectra $\kappa^3 a^2 |\varphi_k|^2$ as a function of $\kappa = k/m_\phi$ in the presence of a unstable potential (Section 7.4), for $\xi = 12.2$ and $m_t = 172.12\,\text{GeV}$. The spectra is depicted at times $m_\phi(t - t_i) = 0, 10, 20...$, going from early times (red) to late times (dark blue).

We can explain the triggering of the Higgs instability in terms of the balance between the terms ξR and $-\lambda(\varphi)\langle\varphi^2\rangle$ that appear in the EOM of the field modes, Eq. (7.9). We have plotted in Fig. 7.7 the time-evolution of these two terms for $m_t = 172.12\,\text{GeV}$ and different values of ξ. Although ξR is periodically oscillating between positive and negative values, the resulting oscillation average is always positive. We observe that initially, the first term dominates over the second, but as commented, when (if) the absolute value of the second term becomes of the same order of magnitude that the first one, the Higgs field becomes unstable. This can happen during the initial regime of tachyonic resonance, or later on due when the resonance is already switched off, as $R \propto 1/a^3$ whereas $\langle\varphi^2\rangle \propto 1/a^2$.

In conclusion, as expected, we can define a critical coupling, $\xi_c \approx 12$ for $m_t = 172.12$ GeV, so that for $\xi \lesssim \xi_c$ the Higgs field is always stable, while for $\xi \gtrsim \xi_c$ the field becomes unstable at a certain time $m_\phi t_i$, whose numerical value decreases as ξ gets greater. This general picture also applies for other values of the top mass. If we take the top quark mass a bit higher, φ_+ is lower, and hence the Higgs field takes a much longer time to settle on the safe side of the potential barrier. Due to this, the larger the mass m_t the lower the value of the critical coupling ξ_c.

The order of magnitude fit of the time-dependence of the amplitude obtained for the free case in Eq. (7.21) also holds quite well in the self-interacting scenario, before the instability takes place. This indicates that the effect on the Higgs dynamics of λ is not very important before the transition to the high-energy vacuum takes place. Inverting this fit, we can find an order-of-magnitude estimate of the time t_0 at which we recover $\lambda(\varphi) > 0$,

$$m_\phi t_0 \approx \left(\varphi_0 m_p^{-1} e^{-s(\xi)}\right)^{-\frac{1}{p(\xi)}}, \tag{7.22}$$
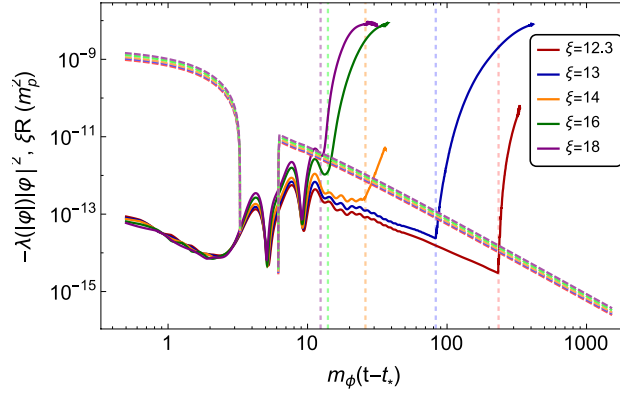
Figure 7.7.: We show, for $m_t = 172.12\,\text{GeV}$ and different values of ξ (Section 7.3), the time-evolution of the terms ξR (dashed lines) and $-\lambda(|\varphi|)\varphi^2$ (continuous lines). For ξR, we plot an oscillation-average to compare both terms more easily. These are the terms that appear in the Eq. (7.9) for the field modes. We also plot, with vertical lines, the corresponding time $m_\phi t_i$ at which the Higgs becomes unstable.

where φ_0 is given in Table 4.1. For $\xi \approx 5$, this gives $m_\phi t_0 \approx \mathcal{O}(10^{2,4,5,6,7})$ for top quark masses $m_t = 172.12, 172.73, 173.34, 173.95, 174.56\ \text{GeV}$ respectively.

We show in Fig. 7.8 the instability time as a function of ξ obtained from our lattice simulations. We have observed that the specific value of $m_\phi t_i$ depends on the particular random realization of the Higgs field initial conditions in Eq. (7.15), so for each point, we have done several simulations for different realizations of the initial conditions (this is discussed in more detail in Section 7.4.1). Points indicate the average value of $m_\phi t_i$, while the shadow region surrounding each of the curves indicate the standard deviation.

The behaviour of the five curves with ξ is quite similar. In all curves we can identify two critical values, $\xi_c^{(1)} \equiv \xi_c$ and $\xi_c^{(2)}$, which are identified in the Figure with dotted and dotted-dashed vertical lines, and indicated in Table 7.1. The meaning of these values is as follows:

- $\xi > \xi_c^{(2)}$: For these values, we observe that the Higgs field always develops an instability, at a time $m_\phi t_i \lesssim \mathcal{O}(10)$, quite independently on the value ξ (at least for the cases we have simulated). This is seen as a plateau in the right part of the numerical curves shown in Fig. 7.8. Qualitatively, for this range of values, the Higgs field becomes unstable when it is still in the tachyonic resonance regime. One can see an example of this in Fig. 7.5 for $m_t = 172.12\ \text{GeV}$: for the cases $\xi = 16, 18, 20$, which verify $\xi > \xi_c^{(2)} \approx 14$, the Higgs becomes unstable in the oscillatory regime, while for $\xi = 12, 14$, with $\xi \lesssim \xi_c^{(2)}$, the instability is developed when the resonance has already finished.

- $\xi_c^{(1)} < \xi < \xi_c^{(2)}$: For these values, the Higgs field also develops an instability, but this happens only after the tachyonic resonance has ended. For these values, the instability
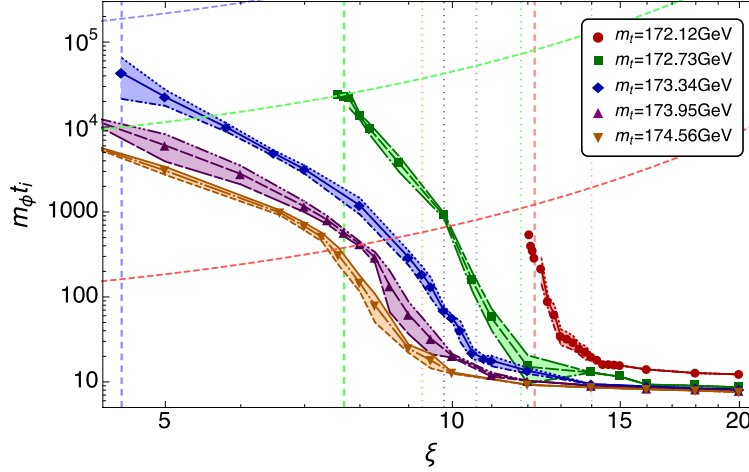
Figure 7.8.: The instability time $m_\phi t_i$ at which the Higgs field develops an instability and decays to the true negative-energy vacuum, as a function of the Higgs-curvature coupling ξ (Section 7.4). These results are obtained directly from lattice simulations. Each of the five lines correspond to the five different interpolating potentials, corresponding to the top quark masses $m_t = 172.12\text{GeV}$ (red), $m_t = 172.73\text{GeV}$ (green), $m_t = 173.34\text{GeV}$ (blue), $m_t = 173.95\text{GeV}$ (purple), and $m_t = 174.56\text{GeV}$ (brown). The dashed vertical lines indicate the position of the critical couplings $\xi_c^{(1)}$, while the dotted lines indicate the position of the couplings $\xi_c^{(2)}$, see Table 7.1. For each data point we have done several lattice simulations corresponding to different realizations of the initial Higgs field conditions, see bulk text. The points indicate the average value $m_\phi t_i$, while the envelope of each of the lines indicate the standard deviation $\sigma \equiv N^{-1/2}\sqrt{\sum_i (x_i - \bar{x}_i)^2}$. For data points with $\xi \approx \xi_c$, only some of the ten simulations do not become unstable, and hence we do not show the deviation in these cases. For $\xi \lesssim \xi_c^{(1)}$ all simulations are always stable (i.e. $m_\phi t_i = \infty$), and hence data points are not drawn.

time $m_\phi t_i$ depends very strongly on the value ξ. A change of few units in ξ changes $m_\phi t_i$ in several orders of magnitude.

- $\xi < \xi_c^{(1)}$: Finally, for these values, we observe that the Higgs field is always stable, coming back to the safe side of the potential without having become unstable.

We indicate the values of both $\xi_c^{(1)}$ and $\xi_c^{(2)}$ for the cases $m_t = 173.34$ GeV, $m_t = 172.73$ GeV, and $m_t = 172.12$ GeV (blue, green, and red curves) in Table 7.1. Note that, as expected, as we increase the value of the top quark mass, the position of the barrier in the Higgs potential moves to smaller field values, and hence the initial distribution of the Higgs field is much deeper in the negative-energy region. Due to this, $\xi_c^{(1),(2)}$ are lower, and the Higgs field takes much longer to enter into the safe side of the potential. Let us note that the identification of these critical values is not unambiguous, and in particular, for couplings near the critical one $\xi \approx \xi_c^{(1)}$, we observe that depending on the specific realization of the initial conditions, the Higgs may or may not become unstable. This source of uncertainty is indicated with a $\pm$ sign

$m_t(\text{GeV})$	$\xi_c^{(1)}$	$\xi_c^{(2)}$
172.12	12.2 ± 0.2	14
172.73	7.7 ± 0.1	11.8
173.34	4.3 ± 0.2	10.6
173.95	< 4.0	9.8
174.56	< 4.0	9.3

Table 7.1.: Higgs-curvature critical couplings $\xi_c^{(1)}$ and $\xi_c^{(2)}$, obtained from lattice simulations, for different values of the top quark mass. The error in ξ_c signals the uncertainty with respect initial conditions. The meaning of this parameters is explained in the bulk text.

in Table 7.1. Finally, let us note that our technical definition of the second critical coupling is such that for $\xi > \xi_c^{(2)}$, we have $m_\phi t_i < 20$.

The curved, dashed lines in Figure 7.8 indicate the approximated time at which the Higgs enters into the safe side of the potential, using Eq. (7.22). The idea is that at the critical coupling $\xi = \xi_c^{(1)}$, the curve for $m_\phi t_i$ obtained from the numerical simulations (bands in colors in Fig. 7.8) will meet approximately the corresponding dashed ones. We can see in Fig. 7.8 that this works relatively well, taking into account that Eq. (7.22) is only a rough estimation.

In Fig. 7.8 it can also be seen that for $m_t = 173.95$ GeV and $m_t = 174.56$ GeV, the instability curves do not meet their corresponding curved-dashed lines for $\xi \gtrsim 4$, which are the cases that we cannot study in the lattice as discussed at the end of Section 7.3. Hence, for these masses we can only provide the upper bound $\xi_c \lesssim 4$.

Let us remark that in all our simulations we made the inflaton to oscillate indefinitely, even though this is clearly not realistic. The inflaton is expected to be coupled to other species, which will eventually induce its decay due to parametric resonance effects at a certain time. In Chapter 2, we denoted this time scale as t_{br}, where the label $_{\text{br}}$ stands for the *back-reaction* from the decay products of the inflaton. After this time, the energy density is no longer dominated by a coherently oscillating scalar field, and therefore Eq. (7.3) is no longer valid. This puts an end to the tachyonic resonance regime of the Higgs field. Therefore, the estimates for ξ_c provided here will not be valid if $t_{\text{br}} \lesssim t_{\text{res}}$. For example, if the inflaton is coupled to a single scalar field χ with coupling $g^2 \phi^2 \chi^2$, we find, using Eq. (2.50), $m_\phi t_{\text{br}} \gtrsim 40$ for $g^2 \lesssim 6.9 \cdot 10^{-3}$. As $t_{\text{br}} \gtrsim t_{\text{res}}$ for the values of ξ considered here, our bounds can be applied.

7.4.1. Dependence of lattice simulations on the Higgs number of components and initial conditions

We address now how our results depend on the position of the momenta cutoff in the spectra of initial conditions, as well as on the number of Higgs components we put in our simulations.

Dependence on Higgs initial conditions

We have explained previously how the initial conditions of the Higgs field are set throughout the lattice. Basically, we impose at initial time $t = t_i$ vanishing homogeneous modes $\varphi_n = 0$ ($n = 1, 2, 3, 4$), and then we add quantum fluctuations to each of the components. These fluctuations are imposed only up to a certain cutoff momentum k_c, so that for $k > k_c$ the fluctuations are set to zero. Also, the random nature of the initial conditions is implemented in the code through a pseudo-random number generator, so that different seeds produce different realizations for the initial conditions.

It is essential to fix the initial cutoff appropriately, so that the non-excited UV quantum modes, which cannot be treated in the lattice, are not excited as classical modes. In the results presented in Fig. 7.8, we have done several simulations with different initializations for each point. More specifically, for values $\xi < 5$, we have done ten simulations, five of them with $\kappa_c = 10$ ($\kappa_c \equiv k_c / m_\phi$), and the other five with $\kappa_c = 12$. We have also varied the seed in each of the ten simulations. This matches quite well the analytical estimation for the classical estimation of modes during tachyonic resonance given in Eq. (7.5). For values $5 < \xi < \xi_c^{(2)}$, the second set of five simulations has been done instead with cutoff $\kappa_c = 15$. Finally, for points $\xi > \xi_c^{(2)}$, we have only done four simulations (two with $\kappa_c = 10$ and two with $\kappa_c = 15$), because for these points the dependence of our results on the initial conditions is negligible.

The left panel of Fig. 7.9 shows how the instability curves change for different choices of the initial cutoff κ_c for the particular case $m_t = 173.34$ GeV. The inclusion of UV modes in the lattice beyond the physical cut-off, makes larger the Higgs amplitude $\langle h^2 \rangle$, so that the negative $\lambda \langle h^2 \rangle / a^3$ term in Eq. (7.9) is enhanced, and hence reduces the instability time $m_\phi t_i$. For $\xi \gtrsim 10$, this effect is negligible, because as we saw in Section 7.3, the amplitude of the excited IR modes dominates over the UV ones, but it becomes increasingly important as ξ diminishes. As we decrease the coupling, the UV modes become more relevant, and if they are not appropriately eliminated, their contribution can make the instability time wrongly smaller. At very low couplings, this is related to the invalidity of the lattice approach, as explained in the last paragraph of Section 7.3.

Finally, let us note that, although the vacuum always becomes unstable for values $\xi > \xi_c^{(1)}$, the opposite condition $\xi < \xi_c^{(1)}$ does not guarantee stability. To show that, we would need to do
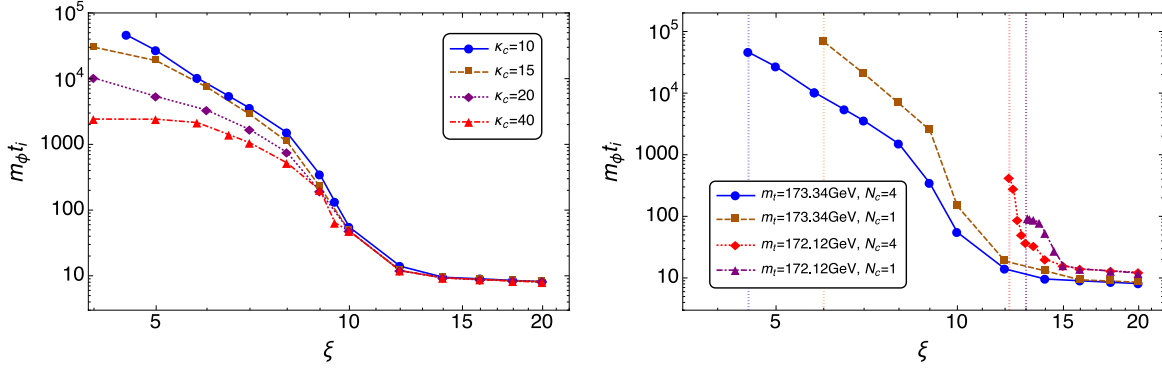
Figure 7.9.: Left: The instability time $m_\phi t_i$ for the top quark mass $m_t = 173.34$ GeV. Each curve corresponds to a different value of the cutoff of the initial fluctuations $\kappa_c \equiv k_c/m_\phi$, and each point corresponds to a particular lattice simulation. We depict here the interval $4 < \xi < 20$. Right: The instability curves for $m_t = 173.34$ GeV and $m_t = 172.12$ GeV when we introduce a 4-component or a 1-component Higgs field. Each point corresponds to a single lattice simulation.

e^{150} runs to account for the number of different causally disconnected patches of the Universe, and check that none of them leads to vacuum decay. This is not feasible, so we simply exclude parameters where vacuum decay happens in a typical run. Note also that the uncertainty in m_t propagates as a much larger change in ξ_c.

Dependence on Higgs number of components

We now compare our results, in which we have taken the Higgs as a 4-component field ($N_c = 4$), with a similar set of lattice simulations with a 1-component field ($N_c = 1$).

We expect differences between the two scenarios for several reasons. The first one is that, if we include a 4-component field, the tachyonic mass is exciting 4 scalar fields instead of one. If we neglect at first the Higgs self-interaction term, this means $\langle \varphi_n^2 \rangle \approx \langle \varphi^2 \rangle / 4$ ($n = 1, 2, 3, 4$). Due to this, if we consider only a 1-component Higgs, the magnitude of the negative self-interaction term is being underestimated, and increases artificially the instability time $m_\phi t_i$ for a given coupling ξ, as well as the critical value ξ_c.

To check this, we show in the right panel of Fig. 7.9 the dependence of the instability curve on the number of components, for the top quark masses $m_t = 172.12$ GeV and $m_t = 173.34$ GeV. We compare the cases $N_c = 4$ (i.e. the case we have presented above), and $N_c = 1$. As expected, for the 1-component case the critical coupling ξ_c increases slightly. For the $m_t = 173.34$ GeV case, we have $\xi_c \approx 6$ instead of $\xi_c \approx 4$, while for the $m_t = 172.12$ GeV we have $\xi_c \approx 13$ instead of $\xi_c \approx 12$. Apart from that, we see that the particular shape of the instability curve is significantly changed, meaning that the effect of the interaction between the different Higgs components is relevant for the dynamics of the system.

7.5. Simulations with gauge fields

Until now, we have ignored the coupling of the Higgs field to the gauge bosons of the Standard Model. We now evaluate if the effects of this interaction modify significantly the results presented in the last section. For this, let us approximate the SU(2)xU(1) gauge structure of the SM with the following U(1) action,

$$\mathcal{L} = -\int d^4x \sqrt{-g} \left(\frac{1}{4e^2} F_{\mu\nu} F^{\mu\nu} + |D_\mu \Phi|^2 + \xi R |\Phi|^2 + V(|\Phi|) \right) , \tag{7.23}$$

with the usual definitions $F_{\mu\nu} = \partial_\mu A_\nu - \partial_\nu A_\mu$ and $D_\mu = \partial_\mu - iA_\mu$, where Φ is complex doublet with four real components [see Eq. (7.11)], and $V(|\Phi|)$ the Higgs potential energy given in Eq. (7.12). This action describes correctly the Higgs-gauge fields interactions of the SM, as long as the non-linear interactions of the gauge fields among themselves (due to the truly non-Abelian nature of the SM symmetries) can be ignored. This is typically a good approximation as long as the gauge fields are not largely excited, as described in Section 4.5.1 in the context of parametric resonance. We also fix the coupling strength as $e^2 = (g_Z^2 + 2g_W^2)/4$, with g_Z and g_W the gauge couplings of the Higgs to the $W\pm$ and Z bosons respectively. As explained in Section 4.5.2, this way the Abelian gauge boson A_μ effectively describes the simultaneous interaction of the Higgs to the three massive electroweak gauge bosons. We take $g_Z^2 = 0.6$ and $g_Y^2 = 0.3$, corresponding to their value at very high energies, according to the SM renormalization group. The equations of motion, in the temporal gauge $A_0 = 0$, are

$$\ddot{\Phi} - \frac{1}{a^2} D_i D_i \Phi + 3\frac{\dot{a}}{a}\dot{\Phi} + 2[\xi R + \lambda(|\varphi|)(\Phi^\dagger \Phi)]\Phi = -\frac{\partial \lambda}{\partial |\varphi|}(\Phi^\dagger \Phi)^2 , \tag{7.24}$$

$$\ddot{A}_j - \frac{1}{a^2}(\partial_i \partial_i A_j - \partial_i \partial_j A_i) + \frac{\dot{a}}{a}\dot{A}_j = 2e^2 \mathfrak{Im}[\Phi^\dagger(D_j \Phi)] , \tag{7.25}$$

as well as the following Gauss constraint, which is a relation that must be obeyed at all times,

$$\partial_i \dot{A}_i = 2e^2 a^2 \mathfrak{Im}[\Phi^\dagger \dot{\Phi}] . \tag{7.26}$$

Note also that this is not, strictly speaking, the standard Abelian-Higgs model, as we are introducing two Higgs complex fields [via Eq. (7.11)] instead of just one.

Naturally, what our lattice simulations do is to solve a discrete version of Eqs. (7.25), which we provide in Appendix A of this thesis. Details of how we derive this equations and the assumptions we made are provided in more detail there. The results we present in this section are based on lattice simulations with $N^3 = 128^3$ points, with a minimum infrared momenta $k_{\min} = 0.5 m_\phi$. This captures quite well the relevant range of momenta excited during the tachyonic resonance regime, for both the Higgs and the gauge fields.
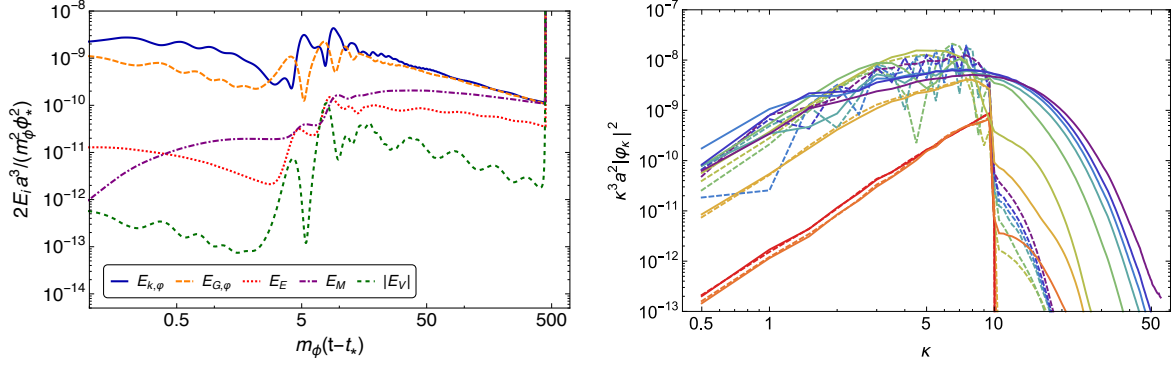
Figure 7.10.: Left: We plot, for $\xi = 8$ and $m_t = 173.34\,\text{GeV}$, the different contributions to the energy density (7.27) as a function of time (Section 7.5). The Higgs field becomes unstable around $m_\phi t_i \approx 500$. Right: We plot the spectra of the conformal Higgs field for different times (Section 7.5). Continuous lines correspond to a Higgs coupled to gauge bosons, while the dashed lines indicate the equivalent when such coupling is set to zero. Here, we have chosen $m_t = 173.34\,\text{GeV}$ and $\xi = 8$. From early (red) to late times (purple), we have $m_\phi(t - t_i) = 0, 2, 4, 8, 18, 59, 100, 161, 403$.

Let us try to quantify the energy transferred from the Higgs into the electroweak gauge bosons. Action (7.23) can be written as $S = S_m + S_R$, with $S_R \equiv \int d^4x \sqrt{-g}\,\xi R |\Phi|^2$ containing the Ricci-Higgs interaction term, and S_m containing the other terms. We define the matter stress-energy tensor as $T_{\mu\nu}^{(m)} = \frac{2}{\sqrt{-g}} \frac{\delta S_m}{\delta g^{\mu\nu}}$. The energy density can then be written as

$$
\begin{aligned}
T_{00}^{(m)} &= \frac{1}{2}|\dot{\varphi}|^2 + \frac{1}{2a^2}\sum_i |D_i\varphi|^2 + \frac{1}{2e^2a^2}\sum_i F_{0i}^2 + \frac{1}{2e^2a^4}\sum_{i,j<i} F_{ij}^2 + V(|\varphi|) \\
&\equiv E_K^\varphi + E_G^\varphi + E_E + E_M + E_V \, .
\end{aligned}
\tag{7.27}
$$

We show in the left panel of Fig. 7.10 the evolution of the different contributions to the energy density (7.27) as a function of time, for the case $\xi = 8$. These energies have been divided by the inflaton energy $\sim \frac{m_\phi^2 \phi_i^2}{2a^3}$. We see that the Higgs and gauge fields energy is several orders of magnitude lower than the inflaton energy, which justifies neglecting their contribution to the Friedmann equation. At late times, the Higgs kinetic and gradient energies evolve as $E_K^\varphi, E_G^\varphi \sim a^{-4}$, and thus eventually become sub-dominant with respect the magnetic energy.

We show in the right panel of Fig. 7.10 the time-evolution of the Higgs spectra in the presence of a gauge interaction, and compare it when such interaction is not present. We clearly see that the gauge bosons have a very important backreaction effect on the Higgs field, propagating its spectra to the UV.

Finally, Fig. 7.11 shows the instability time $m_\phi t_i$ as a function of ξ obtained from lattice simulations, when we do include the coupling of the Higgs with the gauge bosons. We have simulated the cases $m_t = 172.12, 172.73, 173, 34\,\text{GeV}$, and compared with the results obtained
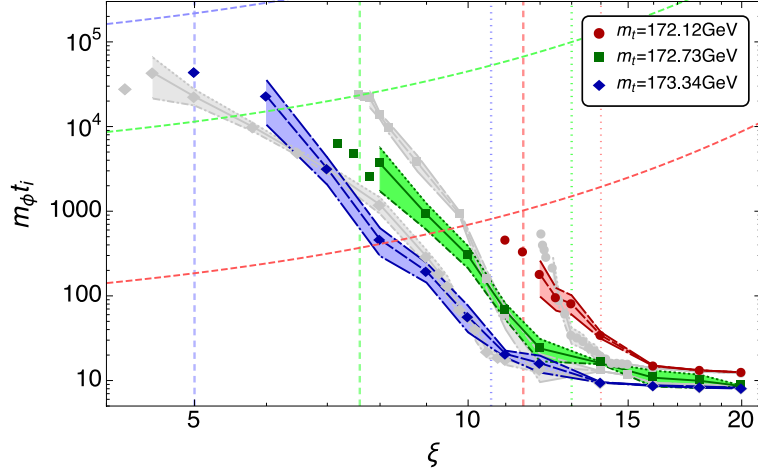
Figure 7.11.: The instability time $m_\phi t_i$ as a function of ξ, obtained from the lattice simulations with both Higgs and gauge bosons (Section 7.5). We have depicted the cases for the top-quark mass $m_t = 172.12\text{GeV}$ (red), $m_t = 172.73\text{GeV}$ (green), and $m_t = 173.34\text{GeV}$ (blue). The three grey curves show the results, for these same three masses, of the lattice simulations with no gauge bosons incorporated (i.e. the curves of Fig. 7.8). As before, the dashed, and dotted-dashed vertical lines indicate the estimations $\xi_c^{(1)}$ and $\xi_c^{(2)}$ respectively, whose meaning is described in the bulk text of Section 7.4, and the curved dashed lines show the estimation of Eq. (7.22) for the three different top-quark masses.

in Section 7.4, when we ignored such coupling. Although the instability curves are slightly different with respect the case without gauge bosons, the values for the critical coupling $\xi_c^{(1)}$ and $\xi_c^{(2)}$ do not change significantly. We show these values in Table 7.2.

In conclusion, our simulations demonstrate that the addition of gauge fields does not impact significantly in the post-inflationary dynamics of the system. The interaction of the Higgs with the electroweak gauge fields only changes marginally the results on the critical couplings $\xi_c^{(1),(2)}$. Besides, as we used an Abelian set-up, this also indicates that the addition of the truly non-Abelian gauge bosons will not change the above conclusion, as the non-linear nature of the non-Abelian gauge field interactions cannot stimulate further the gauge bosons. Quite on the contrary, the non-linear structure of non-Abelian interactions typically prevents the stimulation of the gauge fields up to the level of excitation that (linear) Abelian interactions allow for.

7.6. Summary

In this chapter, we have studied the post-inflationary dynamics of the Standard Model Higgs with lattice simulations, in the case where it possesses a non-minimal coupling ξ to gravity.

$m_t(\text{GeV})$	$\xi_c^{(1)}$	$\xi_c^{(2)}$
172.12	11.3 ± 0.4	15
172.73	7.4 ± 0.3	13
173.34	5 ± 0.5	11

Table 7.2.: Higgs-curvature critical couplings $\xi_c^{(1)}$ and $\xi_c^{(2)}$, obtained from lattice simulations for different values of the top quark mass, in the presence of a coupling of the Higgs field to the gauge bosons. The meaning of this parameters is explained in the bulk text.

This term is necessary for the renormalization of the theory in curved spacetime. We have assumed a chaotic inflation model with $m_\phi^2 \phi^2$ potential. We include the running of $\lambda(\varphi)$ in our simulations as a function of the value of the Higgs field at the lattice point. We have considered different runnings, corresponding to different experimental values of the top-quark mass. The running is such that it generates two vacua to the Higgs potential: one at $\varphi \approx 0$, and one at high-energies. With our lattice simulations, we have been able to obtain the critical coupling ξ_c such that for $\xi \gtrsim \xi_c$ the Higgs field becomes unstable and decays into the negative-energy Planck-scale vacuum. Our lattice simulations also take into account the 4 components of the Higgs field and the cutoff of the spectra of initial fluctuations, which are necessary to correctly quantify the value of ξ_c. We have done two sets of lattice simulations; one with only the Higgs field, including the effective expansion caused by the post-inflationary dynamics of the inflaton; and another in which we also include the coupling of the Higgs to gauge bosons (modelled with an Abelian-Higgs-like approach). We have observed that the effect of the gauge bosons is not relevant for the Higgs post-inflationary dynamics.

The upper bounds in Tables 7.1 and 7.2, together with the estimation $\xi \gtrsim 0.06$ from the stability of the Higgs field during inflation [129], provide tight constraints to the values of this coupling compatible with observations. However, we have assumed a chaotic inflationary model with potential $m_\phi^2 \phi^2$. It is expected that inflationary models with lower inflaton amplitudes during preheating will widen this range of values, as the value of the Ricci scalar $|R(t)|$ decreases, and hence the excitation of the Higgs field due to the tachyonic resonance is less strong. If the Standard Model potential does not have a second negative-energy vacuum at high energies, we cannot find upper bounds for ξ_c in this way.

In this chapter, we have neglected the terms coming purely from the non-Abelian structure of the SM Lagrangian, considering instead that the $\{W^\pm, Z\}$ bosons can be regarded as Abelian gauge fields. We have argued that considering linear Abelian interactions leads to a larger excitation of the gauge fields, so that the non-Abelian terms can be safely ignored. We reach the important conclusion that the inclusion of gauge bosons in the system (even in the Abelian approach) does not change significantly the upper bound for ξ. The critical values $\xi_c^{(1),(2)}$ only change marginally when comparing both the absence and presence of gauge fields.

Discussion

Chapter 8.

Summary and outlook

In this thesis we have studied several aspects of the out-of-equilibrium dynamics of the Universe after inflation, as well as their implications for Higgs cosmology and gravitational wave production. The thesis is divided in two parts. Part I is focused on preheating: an explosive production of particles due to non-perturbative effects. Part II is focused on the dynamics and phenomenology of the Standard Model Higgs after inflation. We now proceed to summarize our main findings and results.

In Part I of the thesis (Chapters 2 and 3), we have studied different scenarios of preheating after inflation. We have focused on inflationary potentials with monomial shapes. This gives rise to parametric resonance, which consists in an exponential growth of field occupation numbers due to the inflaton post-inflationary oscillations. In these scenarios, dynamics can be described in terms of the *resonance parameter q*, which is a dimensionless number that depends on the different particle couplings, initial conditions, as well as on the form of the inflationary potential.

In Chapter 2 we have presented a full parametrization of parametric resonance in terms of q, for chaotic models of inflation with quartic and quadratic potentials, as well as for energetically subdominant fields with quadratic potentials. The analysis is based on classical lattice simulations. We have identified and quantified two relevant time scales. The first one is the *backreaction time $z_{\rm br}$*, which indicates when backreaction effects from the decay products start affecting the oscillating condensate. The second time scale is the *decay time $z_{\rm dec}$*, which signals the moment when the system achieves a stationary regime. We find that $z_{\rm dec} \propto q^{\alpha}$, with α a real coefficient, that depends on the shape of the potential. The decay time grows with the coupling between the mother and daughter fields, which is counterintuitive. This is due to the non-linear physics of the system. We have also quantified how the energy is distributed between its different contributions at each time scale. Although we have focused on chaotic inflationary models, other inflationary potentials present monomial shapes after inflation. Results could be potentially generalized to these scenarios.

In Chapter 3 we have studied gravitational wave production from preheating, for models of chaotic inflation with quartic and quadratic potentials. Preheating is a powerful source of primordial gravitational waves in the early Universe. With lattice simulations, we have parametrized the frequency and amplitude of the peaks in the GW spectra as a function of q. For preheating with quartic potential, the GW spectra has several infrared peaks located at fixed scales, as well as a more ultraviolet peak with a characteristic *hunchback* shape, whose frequency grows as $\propto q^{1/2}$. The amplitude of these peaks follows a characteristic oscillatory pattern with q, which is correlated with the structure of resonance bands in the linear regime. For preheating with quadratic potential, only one peak is observed, whose frequency scales as $\propto q^{2/3}$, and its amplitude as $\propto q^{-2/5}$. With these results, we have provided predictions for the GW signal today, coming from preheating in the early Universe. The GW background in all cases is peaked at high frequencies, $f_p \gtrsim 10^7 \text{Hz}$, but its amplitude can be quite large, of the order of $h^2 \Omega_{\text{GW}}^{(\text{o})}(f_p) \lesssim 10^{-11}$.

In Part II (Chapters 4 to 7) of the thesis, we have studied the nonperturbative dynamics of the Standard Model (SM) after inflation. We have assumed an scenario where the Higgs is not the inflaton, and it is is decoupled from (or weakly coupled to) the inflationary sector. Depending on the circumstances, the Higgs forms a condensate at the end of inflation. When inflation ends, the Higgs starts oscillating around the minimum of its potential, and decays to the SM electroweak gauge bosons, through a process of parametric resonance (there is also an energy transfer from the Higgs to fermions, but it is subdominant). As in the models of parametric resonance studied in Part I, we can identify in this process a *backreaction time* and a *decay time*. Initially, the occupation number of the gauge bosons grows exponentially, due to the Higgs oscillations. When backreaction effects from the gauge bosons onto the Higgs condensate become important, the system evolves in a coupled way towards a stationary regime, when the energy ratios of the different fields remain constant, and follow specific equipartition identities.

In Chapter 4 we have studied the post-inflationary decay of the Higgs, capturing the non-linearities of the system with classical lattice simulations in an expanding box. We have modelled the Higgs-gauge interactions with two different set-ups: a global model, where the gauge fields are taken as scalars; and an Abelian-Higgs model, which includes a gauge structure in the simulations, but ignores the effects of the non-Abelian interaction terms. The dynamics of the system depend basically on three quantities: the initial amplitude of the Higgs field, the value of the Higgs self-coupling at inflationary energies, and the post-inflationary equation of state. We have parametrized the dynamics of the Higgs and its dominant decay products, from the end of inflation, until a stationary regime is achieved, in terms of these unknowns. We have found an extremely useful rescaling law between simulations with different parameters, from which we have been able to obtain a generic equation for the decay time of the Higgs condensate.

In Chapter 5 we have studied the gravitational waves produced during the decay of the SM Higgs. The out-of-equilibrium dynamics converts a fraction of the available energy into GW. We have characterized the GW spectra as a function of the running couplings, post-inflationary expansion rate, and initial Higgs amplitude. We have also obtained predictions for the GW signal today. The amplitude and frequency of the GW background depend on the post-inflationary expansion rate of the Universe after inflation: for a standard radiation-dominated stage, the amplitude goes as $h^2\Omega_{\rm GW}^{\rm (o)} \lesssim 10^{-29}$, while for a kination-dominated regime, the amplitude is enhanced to $h^2\Omega_{\rm GW}^{\rm (o)} \lesssim 10^{-16}$, although the GW spectra is peaked in this second case at very high frequencies, $f_p \lesssim 10^{11}{\rm Hz}$. The reason for this low amplitude is that the Higgs field is energetically subdominant with respect the total energy of the Universe, which is dominated by the inflationary sector. This suppresses the signal several orders of magnitude with respect preheating scenarios.

In Chapter 6 we have extended the lattice simulations of Chapter 4, but incorporating in this case the electroweak SU(2)×U(1) gauge sector into the lattice simulations. We have provided an analytical derivation of the structure of resonance bands in parametric resonance, when the decay products are a combination of Abelian and non-Abelian gauge bosons. We have also parametrized the dynamics of the Higgs and its energetically dominant decay products. This way, we have quantified the effects that the non-Abelian interaction terms have of the Higgs and gauge dynamics, in comparison with the simulations of the Abelian-Higgs set-up of Chapter 4. The estimation of $z_{\rm br}$ in this case coincides quite well with the results predicted within the Abelian-Higgs modelling, especially when the resonance is stronger (i.e. when the Floquet index is larger). However, the late-time dynamics of the system change. In particular, the energy transfer from the Higgs to the gauge species is found to be 70%, while in the Abelian-Higgs modelling, the energy transfer is only 40%.

In Chapter 7 of the thesis, we have incorporated a non-minimal Higgs-curvature coupling $\propto \xi R|\Phi|^2$ to the study of the SM post-inflationary dynamics. This term is required to renormalize the theory in a curved spacetime, and it can have important implications for vacuum stability during and after inflation. We have assumed for the inflationary sector a chaotic inflation model with quadratic potential. The oscillations of the inflaton during preheating induce similar oscillations in the Ricci scalar, which excite the Higgs field due to tachyonic effects. The potential can develop a negative-energy vacuum at very large energies, and the Higgs could decay into it, with catastrophic consequences for the Universe. Vacuum stability is very sensible to the numerical value of the coupling constant. By doing classical lattice simulations of the system, and by requiring compatibility with vacuum stability during preheating, we have obtained upper bounds for ξ. For a top-quark mass $m_t \approx 173.3{\rm GeV}$, we found that the Higgs vacuum becomes unstable during preheating for $\xi \gtrsim 4-5$, while for a smaller mass $m_t \approx 172.1{\rm GeV}$, this constraint becomes $\xi \gtrsim 11-12$. We have also incorporated into the analysis the coupling of the Higgs to the electroweak gauge fields. The existence of gauge

interactions in the lattice simulations does not significantly change the boundaries for ξ, but does modify the shape of the matter field spectra.

We would like now to present a couple of other directions in which the work carried out in this thesis could be extended. In particular, we have studied in this thesis several aspects of the post-inflationary dynamics of the Standard Model (SM). We have focused in scenarios where the Higgs field 1) is not the inflaton, and 2) is weakly coupled to the inflationary sector. A natural extension of our work would be to study the post-inflationary dynamics of the Standard Model, when any of these two conditions is lifted.

One possibility would be to study (p)reheating in *Higgs-inflation* scenarios, where the Higgs is the field responsible for the inflation of the Universe [19]. This is possible if the Higgs has a non-minimal coupling to the Ricci scalar, which must be appropriately fixed to fit the amplitude of the anisotropies in the Cosmic Microwave Background. (P)reheating in these models has been studied previously in [64, 65], but using only analytical and numerical methods in the linear regime. By doing classical lattice simulations, we could capture the full non-linear dynamics of the system, from the initial resonant stage, until the later stationary regime. Like in the simulations of Chapters 4 and 6, the Higgs decays into all gauge bosons and fermions of the SM, but in this case both the Higgs and its decay products are the energetically dominant fields in the Universe. Hence, in the lattice simulations we would need to solve self-consistently the field and Friedmann equations, which makes their resolution more complex. Lattice simulations could be done in both Jordan and Einstein frames, and check that the classical dynamics of the system are the same. Moreover, we have seen in Chapter 3 that preheating constitutes a strong source of primordial gravitational waves. Analogously, we could compute GW production during preheating in Higgs-inflation, and predict the typical frequency and amplitude for a GW signal today. The GW amplitude will be enhanced with respect the Higgs-spectator scenario studied in Chapter 5, because now the Higgs would dominate the energy budget of the Universe. If detected, this GW background could be a direct evidence of the validity of the Standard Model at high-energies.

On the other hand, even if the Higgs is not the inflaton, the presence of a Higgs-inflaton coupling could affect significantly the dynamics of the Higgs and its decay products after inflation. In particular, a coupling of the Higgs to the inflaton of the type $g^2\phi^2\varphi^2$ could prompt vacuum instability after inflation, in the same fashion as in Chapter 7, as long as the coupling constant is large enough. The post-inflationary oscillations of the inflaton induce a periodically negative effective mass to the Higgs field, which gets excited due to tachyonic effects, and can decay into the negative-energy vacuum of the SM potential. In Chapter 7 we studied this process with lattice simulations, and by requiring vacuum stability after inflation, we obtained upper bounds for the Higgs-curvature coupling within the Standard Model. This analysis could be extended to include the Higgs-inflaton coupling, as in Ref. [84, 154]. On the other hand, we have also assumed a chaotic inflationary model with quadratic potential. Although this is a

natural first step, the bounds obtained this way are obviously quite restrictive, because they only apply for this particular scenario. We could generalize our analysis to other potentials, such as quadratic shapes of the type $V(\phi) \propto m_\phi^2 \phi_i^2$, with m_ϕ a free parameter. Also, let us note that in Chapter 7, the electroweak gauge bosons were introduced in the lattice with an Abelian-Higgs-like modelling. This was done for simplicity, but we could extend the analysis to include explicitly the SU(2)×U(1) gauge-invariant structure in the lattice, using the lattice formulation of Appendix A.

8.1. Resumen y perspectivas

En esta tesis hemos estudiado diversos aspectos de la dinámica fuera del equilibrio del Universo después de inflación, así como sus implicaciones en *Higgs Cosmology* y producción de ondas gravitacionales. Esta tesis se ha dividido en dos partes. En la Parte I hemos estudiado el precalentamiento: una producción explosiva de partículas debida a efectos no perturbativos. En la Parte II nos hemos centrado en la dinámica y fenomenología del Higgs del Modelo Estándar después de inflación. A continuación, haremos un resumen de los resultados de nuestra investigación.

En la Parte I de la tesis (Capítulos 2 y 3), hemos estudiado distintos escenarios de precalentamiento después de inflación. Nos hemos centrado en potenciales inflacionarios de tipo monomial. Estos potenciales dan lugar a un proceso de resonancia paramétrica, consistente en un crecimiento exponencial de los números de ocupación de los distintos campos debido a las oscilaciones post-inflacionarias del inflatón. En estos casos, la dinámica puede describirse exclusivamente en términos del *parámetro de resonancia q*, que es un número adimensional que depende de las diferentes constantes de acoplamiento y condiciones iniciales, así como de la forma del potencial.

En el Capítulo 2 hemos realizado una parametrización completa del proceso de resonancia paramétrica después de inflación en función de q, en modelos caóticos de inflación con potenciales cuadrático y cuártico, así como para campos energéticamente subdominantes con potencial cuadrático. El análisis se ha basado en simulaciones lattice del proceso. Hemos identificado y cuantificado dos escalas temporales. La primera es el *tiempo de backreaction z_{br}*, que indica cuándo los efectos de *backreaction* provenientes de los productos de desintegración comienzan a afectar al condensado oscilante. La segunda es el *tiempo de desintegración z_{dec}*, que señala el momento en que el sistema alcanza un régimen estacionario. Hemos encontrado que $z_{dec} \propto q^\alpha$, con α un coeficiente numérico fijado por la forma del potencial. El tiempo de desintegración crece con la constante de acoplamiento entre los campos, lo que es contraintuitivo, y está relacionado con las no-linealidades del sistema. También hemos cuantificado cómo se distribuye la energía entre sus distintas componentes en cada escala temporal. Aunque nos hemos

centrado en modelos caóticos de inflación, otros potenciales inflacionarios presentan formas monomiales después de inflación. Nuestros resultados podrían en principio generalizarse a estos casos.

En el Capítulo 3 hemos estudiado la producción de ondas gravitacionales (OG) en escenarios de precalentamiento, también para modelos caóticos de inflación con potencial cuártico y cuadrático. El precalentamiento es una poderosa fuente de ondas gravitacionales primordiales en el Universo temprano. Con simulaciones lattice, hemos parametrizado la frecuencia y la amplitud de los picos en los espectros de OG en función de q. Para un potencial cuártico, hemos encontrado varios picos infrarrojos ubicados a escalas fijas independientes de q, y un pico más ultravioleta, cuya posición crece como $\propto q^{1/2}$. La amplitud de estos picos describe un patrón oscilatorio característico como función de q, que se correlaciona con la estructura de bandas de resonancia en el régimen lineal. Para un potencial cuadrático, solo se observa un pico, cuya frecuencia crece como $\propto q^{2/3}$, y su amplitud decrece como $\propto q^{-2/5}$. Con estos resultados, hemos obtenido predicciones para la señal de ondas gravitacionales provenientes del precalentamiento en el Universo temprano. El fondo de ondas gravitacionales alcanza su máximo en todos los casos a frecuencias muy elevadas, $f_p \gtrsim 10^7 \text{Hz}$, pero su amplitud puede ser bastante grande, del orden de $h^2 \Omega_{\text{GW}}^{(\text{o})}(f_p) \lesssim 10^{-11}$.

En la Parte II de la tesis (Capítulos 4 a 7), hemos estudiado la dinámica no perturbativa del Modelo Estándar (ME) después de inflación. Hemos asumido un escenario en el que el Higgs no es el inflatón, ni tampoco está acoplado al sector inflacionario. En este caso, el Higgs puede acabar formando un condensado al final de inflación. Cuando inflación termina, el Higgs empieza a oscilar alrededor del mínimo de su potencial, y se desintegra en los bosones gauge electrodébiles a través de un proceso de resonancia paramétrica (también hay una transferencia de energía del Higgs a fermiones, pero es subdominante). Como en los modelos de precalentamiento estudiados en la Parte I, también podemos identificar en este proceso un *tiempo de backreaction* y un *tiempo de desintegración*. Inicialmente, debido a las oscilaciones del Higgs, los números de ocupación de los bosones gauge crecen exponencialmente. No obstante, cuando los efectos de *backreaction* provenientes de los bosones gauge se vuelven importantes, el sistema evoluciona hacia un régimen estacionario, en el que los ratios de energía de los distintos campos permanecen constantes y siguen un régimen de equipartición.

En el Capítulo 4 hemos estudiado la desintegración postinflacionaria del Higgs con simulaciones lattice. Hemos modelado las interacciones Higgs-gauge de dos maneras diferentes: con un modelo global, donde los campos gauge se aproximan con campos escalares; y un modelo *Abelian-Higgs*, que incluye una estructura gauge en las simulaciones, pero ignora los efectos generados por lo términos de interacción no Abelianos. La dinámica del sistema depende básicamente de tres cantidades: la amplitud inicial del campo de Higgs, el valor de las constantes de acoplamiento a grandes energías, y el ritmo de expansión post-inflacionario del Universo. Hemos parametrizado la dinámica del Higgs y los bosones gauge, desde el final de inflación,

hasta que el sistema alcanza un régimen estacionario. En particular, hemos encontrado una ecuación de reescaleo extremedamente útil entre simulaciones con distintos parámetros, a partir de la cuál hemos obtenido una ecuación general para el tiempo de desintegración del Higgs.

En el Capítulo 5 hemos estudiado las ondas gravitacionales producidas durante la desintegración del Higgs después de inflación. La dinámica fuera del equilibrio convierte una fracción de la energía disponible en ondas gravitacionales. Hemos parametrizado los espectros de OG en función de las constantes de acoplamiento, el ritmo de expansión postinflacionario, y la amplitud inicial de Higgs. También hemos obtenido predicciones para la señal de OG que se mediría hoy. La amplitud y frecuencia del fondo dependen significativamente del ritmo de expansión después de inflación: en el caso de un universo dominado por radiación, la amplitud es del orden $h^2\Omega_{\rm GW}^{\rm (o)} \lesssim 10^{-29}$, mientras que en un universo dominado por grados de libertad cinéticos, la amplitud es aproximadamente $h^2\Omega_{\rm GW}^{\rm (o)} \lesssim 10^{-16}$. No obstante, en este segundo caso, la amplitud alcanza su máximo a frecuencias muy altas, del orden de $f_p \lesssim 10^{11}{\rm Hz}$. En este escenario, la amplitud es tan pequeña porque el campo de Higgs es energéticamente subdominante con respecto a la energía total (dominado por el sector inflacionario), lo que suprime la señal en varios órdenes de magnitud.

En el Capítulo 6 hemos extendido las simulaciones del Capítulo 4, incorporando completamente en este caso el sector electrodébil SU(2)$\times$ U(1) en la lattice. Hemos obtenido una derivación analítica del *parametro de resonancia efectivo*, en el caso en el que los campos excitados por la resonancia parmétrica son una combinación de bosones gauge abelianos y no abelianos. También hemos parametrizado la dinámica del Higgs y los bosones gauge. De esta manera, hemos cuantificado el impacto que los términos de interacción no Abelianos tienen en la dinámica de los campos, en comparación con las simulaciones puramente abelianas del Capítulo 4. La estimación de $z_{\rm br}$ en éste caso coincide bastante bien con los resultados predichos por el modelo Abelian-Higgs, especialmente cuando la resonancia es más fuerte (es decir, cuando el *índice de Floquet* es más grande). Sin embargo, la dinámica del sistema a tiempos tardíos es distinta. En particular, la transferencia de energía del Higgs a los bosones gauge es del 70%, mientras que en el modelo Abelian-Higgs es solo del 40%.

En el Capítulo 7 de la tesis, hemos seguido estudiando la dinámica post-inflacionaria del Modelo Estándar, pero incluyendo en el análisis un acoplamiento $\propto \xi R|\Phi|^2$ entre el Higgs y la curvatura espaciotemporal. Este término es necesario para renormalizar la teoría en un espacio-tiempo curvo, y podría tener importantes implicaciones en la estabilidad del vacío durante y después de inflación. En particular, hemos asumido para el sector inflacionario un modelo caótico con potencial cuadrático. Las oscilaciones del inflatón durante el precalentamiento inducen oscilaciones similares en el escalar de Ricci, que excitan el campo de Higgs debido a efectos taquiónicos. Sabemos que el potencial del Higgs podría desarrollar un vacío de energía negativa a amplitudes muy grandes. Por lo tanto, si el Higgs se excita lo suficiente, podría

caer en este vacío, con consecuencias catastróficas para el Universo. La estabilidad del vacío es muy sensible al valor numérico de la constante de acoplamiento. Con simulaciones lattice del sistema, y exigiendo que el vacío permanezca estable durante el precalentamiento, hemos encontrado límites superiores para el valor de ξ. Si la masa del top quark es $m_t \approx 173.3\text{GeV}$, encontramos que el vacío de Higgs se vuelve inestable durante el precalentamiento para $\xi \gtrsim 4 - 5$, mientras que para una masa menor $m_t \approx 172.1\text{GeV}$, encontramos que el límite es $\xi \gtrsim 11 - 12$. También hemos incorporado al análisis el acoplamiento del Higgs con los campos gauge electrodébiles, imitando la interacción entre el Higgs y los campos gauge con un modelo Abelian-Higgs. Estas interacciones no cambian significativamente los límites para ξ, pero modifican la forma de los espectros de materia.

A continuación, me gustaría presentar otras direcciones en las que se podría extender el trabajo realizado en esta tesis. Como hemos visto, hemos estudiado varios aspectos de la dinámica post-inflacionaria del Modelo Estándar (ME). Nos hemos enfocado en escenarios donde el campo de Higgs 1) no es el inflatón, y 2) está desacoplado del (o está débilmente acoplado al) sector inflacionario. Una extensión natural de nuestro trabajo sería estudiar la dinámica post-inflacionaria del ME, en el caso de que se cambie cualquiera de estas dos condiciones.

Una posibilidad sería estudiar el (p)recalentamiento en un modelo de *Higgs-inflation*, donde el Higgs es el campo responsable de la inflación del universo [19]. Ésto es posible si el Higgs posee un acoplo no mínimo a la curvatura, fijado de tal manera que explique la amplitud de las anisotropías del Fondo Cósmico de Microondas. El (p)recalentamiento en estos modelos se ha estudiado previamente en [64, 65], pero utilizando sólo métodos analíticos y numéricos en el régimen lineal. Al hacer simulaciones lattice, podríamos capturar completamente la dinámica no lineal del sistema, desde la etapa resonante inicial hasta el régimen estacionario final. Como en las simulaciones de los capítulos 4 y 6, el Higgs se desintegra en todos los bosones gauge y fermiones del ME. Sin embargo, en este caso tanto el Higgs como sus productos de desintegración dominan la energía del Universo. Por lo tanto, las simulaciones lattice serían más complejas, porque tendríamos que resolver auto-consistentemente las ecuaciones de campo y las de Friedmann. Las simulaciones lattice podrían realizarse tanto en el frame de Jordan como en el de Einstein, y verificar así que la dinámica clásica del sistema es la misma. Además, hemos visto en el Capítulo 3 que el precalentamiento constituye una fuente importante de ondas gravitacionales primordiales. De la misma manera, podríamos calcular la producción de OG durante el precalentamiento en Higgs-inflation, y predecir la frecuencia y amplitud típicas para una señal de OG en la actualidad. La amplitud de OG sería mayor que en el escenario estudiado en el Capítulo 5, porque ahora el Higgs-inflatón dominaría el contenido de energía del Universo. Si este fondo de ondas gravitacionales se detectara, constituiría una evidencia directa de la validez del Modelo Estándar a altas energías.

Por otro lado, incluso si el Higgs no es el inflatón, la presencia de un acoplamiento Higgs-inflaton puede afectar significativamente la dinámica del Higgs y sus productos de desintegración después de inflación. En particular, si el acoplamiento Higgs-inflaton es lo suficientemente grande, puede inducir la inestabilidad del vacío, de la misma manera que en el Capítulo 7. Las oscilaciones post-inflacionarias del inflatón inducen periódicamente una masa efectiva negativa al campo de Higgs, que se excita debido a efectos taquiónicos, y por lo tanto, podría acabar cayendo en el vacío de energía negativa del potencial del Modelo Estándar. En el Capítulo 7 hemos estudiado este proceso con simulaciones lattice, y requiriendo la estabilidad de vacío después de inflación, hemos acotado los valor numéricos que el acoplo Higgs-curvatura puede tener dentro del Modelo Estándar. Este análisis podría extenderse para incluir un acoplamiento Higgs-inflaton, como en Ref. [84, 154]. Por otro lado, también hemos asumido un modelo caótico de inflación con potencial cuadrático. Aunque este es un primer paso natural, los límites obtenidos de esta manera son obviamente bastante restrictivos, ya que solo se aplican a este escenario en particular. Podríamos generalizar nuestro análisis a otros potenciales, como formas cuadráticas del tipo $V(\phi) \propto m_\phi^2 \phi_i^2$, con m_ϕ un parámetro libre. Además, en el Capítulo 7, los bosones electrodébiles se introdujeron en la lattice con un modelo Abelian-Higgs. Esto se ha hecho por simplicidad, pero podríamos extender el análisis para incluir explícitamente la estructura gauge SU(2)×U(1) en la lattice, usando el formalismo descrito en el Apéndice A.

Appendices

Appendix A.

Lattice formulation of scalar and gauge theories in expanding backgrounds

In this Appendix, we provide a lattice formulation to simulate the dynamics of scalar and gauge fields in an expanding Universe. We will start by presenting the field and metric equations of motion in a continuum spacetime. We will then derive equivalent equations in the discrete. The lattice formulation is based on a discretized version of the theory action, which recovers the continuum action up to second order terms in time step and lattice spacing. From the minimization of this action we obtain the discrete equations, which can be solved self-consistently with an appropriate iterative scheme. A discretization of the Friedmann equations is also presented.

A.1. Theory in the continuum

A.1.1. Field equations

Let us start by showing the field equations of motion in a continuum spacetime. We will assume that spacetime can be described by a homogeneous and isotropic FLRW metric. In this Appendix, we write it for convenience as follows,

$$ds^2 \equiv g_{\mu\nu}dx^\mu dx^\nu = -a^{2\alpha}dt^2 + a^2 d\vec{x}^2 \, , \quad \begin{cases} \text{cosmic time,} & \text{if } \alpha = 0 \, , \\ \text{conformal time,} & \text{if } \alpha = 1 \, , \end{cases} \tag{A.1}$$

where α is a free parameter that fixes the definition of time t. Depending on the choice of α, t may represent either cosmic or conformal time, as well as any other convenient time defined adhoc.

Let us consider a matter action containing a real scalar field χ, a complex scalar field φ (which we call the *Higgs* field for convenience), an Abelian gauge boson A_μ, and three non-Abelian gauge bosons B_μ^a ($a = 1, 2, 3$). We take the gauge structure as invariant under local transformations of the SU(2)$\times$U(1) group. In curved spacetime, the matter action takes the form

$$S = \int d^4x \sqrt{-g} \mathcal{L}_m \,, \tag{A.2}$$

where g is the determinant of the metric $g_{\mu\nu}$, and $\mathcal{L}_m$ is the matter Lagrangian. For metric (A.1), we have $g = -a^{6+2\alpha}$, so we will consider

$$S = -\int d^4x a^{3+\alpha} \left\{ \frac{1}{4} F_{\mu\nu} F^{\mu\nu} + \frac{1}{4} G_{\mu\nu}^a G^{\mu\nu} + \frac{1}{2}(D_\mu \varphi)^\dagger (D^\mu \varphi) + \frac{1}{2}\partial_\mu \chi \partial^\mu \chi + V(|\varphi|, \chi) \right\} \,, \tag{A.3}$$

where $F_{\mu\nu}$ and $G_{\mu\nu}^a$ are the U(1) and SU(2) field strengths respectively, and we have introduced an arbitrary potential $V = V(\chi, |\varphi|)$, containing all interactions and self-interactions between the real and complex scalar fields. The Higgs covariant derivative is defined as

$$(D_\mu)_{ij} \equiv \delta_{ij} \left(\partial_\mu - i(g_1/2)A_\mu \right) - i(g_2/2)B_\mu^a (\sigma_a)_{ij} \,, \tag{A.4}$$

where g_1 and g_2 are the Abelian and non-Abelian gauge couplings respectively, and σ_a ($a = 1, 2, 3$) are the Pauli matrices with $[\sigma_a, \sigma_b] = i f_{abc}\sigma_c$ and $f_{abc} = 2\epsilon_{abc}$. The covariant derivative contains the interaction between the Higgs and gauge fields. The quantities φ, $F_{\mu\nu}$, and $G_{\mu\nu}^a$ are written in terms of components as

$$\varphi = \begin{pmatrix} \varphi_0 + i\varphi_1 \\ \varphi_2 + i\varphi_3 \end{pmatrix} \,, \quad \varphi_n \in \mathfrak{Re} \,, \quad (n = 0, 1, 2, 3) \,, \tag{A.5}$$

$$F_{\mu\nu} \equiv \partial_\mu A_\nu - \partial_\nu A_\mu \,, \tag{A.6}$$

$$G_{\mu\nu} \equiv G_{\mu\nu}^a T_a \,, \quad G_{\mu\nu}^a \equiv \partial_\mu B_\nu^a - \partial_\nu B_\mu^a + \frac{g_2}{2} f^{abc} B_\mu^b B_\nu^c \,. \tag{A.7}$$

Finally, the gauge-invariant electric and magnetic fields for the U(1) and SU(2) sectors are defined respectively, in terms of the field strengths, as

$$E_0^i \equiv F^{0i} \,, \quad M_0^i \equiv \frac{1}{2}\epsilon_{ijk} F^{jk} \,, \tag{A.8}$$

$$E_a^i \equiv G_a^{0i} \,, \quad M_a^i \equiv \frac{1}{2}\epsilon_{ijk} G_a^{jk} \,. \tag{A.9}$$

Minimization of action (A.3) with respect the field variables give the matter equations of motion. In the case of a Minkowski spacetime ($a = 1$), these are

$$\partial_\mu \partial^\mu \chi = \frac{\partial V}{\partial \chi} \,, \tag{A.10}$$

$$D_\mu D^\mu \varphi = \frac{\partial V}{\partial \varphi^\dagger}, \tag{A.11}$$

$$\partial_\mu F^{\mu\nu} = -\frac{g_1}{2} \mathfrak{Im}[\varphi^\dagger (D^\nu \varphi)], \tag{A.12}$$

$$(\mathcal{D}_\mu)_{ab} G_b^{\mu\nu} = -\frac{g_2}{2} \mathfrak{Im}[\varphi^\dagger \sigma_a (D^\nu \varphi)], \tag{A.13}$$

where we define $(\mathcal{D}_\nu)_{ab} O_b \equiv (\delta_{ab}\partial_\nu + f_{abc}B_\nu^c) O_b$. In order to obtain the EOM in a FLRW spacetime, we can either minimize directly action (A.3) for an arbitrary scale factor, or simply promote the partial derivatives to covariant ones in Eqs. (A.10)-(A.13), i.e. $\partial_\mu \to \nabla_\mu$. We follow the second approach. For this, we use the following identities for the divergences of a vector V^σ and an antisymmetric (2,0)-tensor $A^{\sigma\lambda}$,

$$\nabla_\sigma V^\sigma \equiv \frac{1}{\sqrt{-g}} \frac{\partial(V^\sigma \sqrt{-g})}{\partial x^\sigma} = \frac{1}{a^{3+\alpha}} \frac{\partial(V^\sigma a^{3+\alpha}(t))}{\partial x^\sigma} = \partial_\sigma V^\sigma + (3+\alpha)\frac{\dot{a}}{a}V^0, \tag{A.14}$$

$$\nabla_\sigma A^{\sigma\lambda} \equiv \frac{1}{\sqrt{-g}} \frac{\partial(A^{\sigma\lambda}\sqrt{-g})}{\partial x^\sigma} = \frac{1}{a^{3+\alpha}} \frac{\partial(A^{\sigma\lambda}a^{3+\alpha}(t))}{\partial x^\sigma} = \partial_\sigma A^{\sigma\lambda} + (3+\alpha)\frac{\dot{a}}{a}A^{0\lambda}, \tag{A.15}$$

with $\dot{} \equiv d/dt$. From this, the dynamical field equations of motion in a FLRW metric become

$$\ddot{\chi} - \frac{1}{a^{2(1-\alpha)}}\partial_i\partial_i\chi + (3-\alpha)\frac{\dot{a}}{a}\dot{\chi} = -a^{2\alpha}\frac{\partial V}{\partial\chi}, \tag{A.16}$$

$$\ddot{\varphi} - \frac{1}{a^{2(1-\alpha)}}D_iD_i\varphi + (3-\alpha)\frac{\dot{a}}{a}\dot{\varphi} = -a^{2\alpha}\frac{\partial V}{\partial\varphi^\dagger}, \tag{A.17}$$

$$\partial_0 F_{0j} - \frac{1}{a^{2(1-\alpha)}}\partial_i F_{ij} + (1-\alpha)\frac{\dot{a}}{a}F_{0j} = \frac{g_1}{2}a^{2\alpha}\mathfrak{Im}[\varphi^\dagger(D_j\varphi)], \tag{A.18}$$

$$(\mathcal{D}_0)_{ab}(G_{0j})^b - \frac{1}{a^{2(1-\alpha)}}(\mathcal{D}_i)_{ab}(G_{ij})^b + (1-\alpha)\frac{\dot{a}}{a}(G_{0j})^b = \frac{g_2}{2}a^{2\alpha}\mathfrak{Im}[\varphi^\dagger\sigma_a(D_j\varphi)], \tag{A.19}$$

where we have fixed the gauge condition $A_0 = B_0^a = 0$ for simplicity. In particular, gauge equations (A.18) and (A.19) have obtained from Eqs. (A.12) and (A.13) respectively, with the index choice $\nu = j$. The choice $\nu = 0$ yields, instead, the Gauss constraints,

$$\partial_i F_{0i} = \frac{g_1}{2}a^2\mathfrak{Im}[\varphi^\dagger(D_0\varphi)], \tag{A.20}$$

$$(\mathcal{D}_i)_{ab}(G_{0i})^b = \frac{g_2}{2}a^2\mathfrak{Im}[\varphi^\dagger\sigma_a(D_0\varphi)]. \tag{A.21}$$

These are not dynamical equations, but simply constraints of the system that are obeyed at all times.

A.1.2. Friedmann equations

The stress-energy tensor sourcing the expansion of the Universe, requires a perfect-fluid form in order to be compatible with the FLRW metric. It can be written as

$$T^{\mu\nu} \equiv (\rho + p)u^\mu u^\nu + p g^{\mu\nu} , \tag{A.22}$$

where ρ is the energy density, p is the pressure, and u_μ is the 4-velocity, with normalization condition $u^\mu u^\nu = -1$. For a particle at rest, $u_\mu = (a^\alpha, 0, 0, 0)$, and hence $u^\mu = -(a^{-\alpha}, 0, 0, 0)$. In this case, we have

$$\rho = a^{2\alpha} T^{00} = \frac{1}{a^{2\alpha}} T_{00} , \tag{A.23}$$

$$p = \frac{a^2}{3} \sum_j T^{jj} = \frac{1}{3a^2} \sum_j T_{jj} . \tag{A.24}$$

The expression for the stress-energy tensor $T_{\mu\nu}$ in terms of the Lagrangian was written in Eq. (1.12). In our case, it is given by

$$
\begin{aligned}
T^{\mu\nu} &\equiv \frac{2}{\sqrt{-g}} \frac{\delta(\sqrt{-g}\mathcal{L}_m)}{\delta g_{\mu\nu}} = g^{\mu\nu}\mathcal{L}_m + 2\frac{\delta\mathcal{L}}{\delta g_{\mu\nu}} \\
&= -g^{\mu\nu} \left[\frac{1}{4}(G^a_{\alpha\beta}G^{\alpha\beta}_a + F_{\alpha\beta}F^{\alpha\beta}) + \frac{1}{2}(D_\alpha\varphi)^\dagger(D^\alpha\varphi) + \frac{1}{2}(\partial^\alpha\chi)(\partial_\alpha\chi) + V(|\varphi|,\chi) \right] \\
&\quad + g^{\alpha\mu}g^{\beta\nu}[(D_\alpha\varphi)^\dagger(D_\beta\varphi) + (D_\alpha\chi)^\dagger(D_\beta\chi)] + g^{\alpha\beta}(G^{\mu a}_\alpha G^\nu_{a\beta} + F^\mu_\alpha F^\nu_\beta) ,
\end{aligned} \tag{A.25}
$$

where in the first equality we have used $\delta\sqrt{-g} = \frac{1}{2}g^{\mu\nu}\sqrt{-g}\delta g_{\mu\nu}$, and in the second we have used $\delta g^{\alpha\beta} = -g^{\alpha\mu}g^{\beta\nu}\delta g_{\mu\nu}$. From Eqs. (A.23) and (A.24), we obtain for the energy density and pressure,

$$\rho = E^\chi_K + E^\varphi_K + E^\chi_G + E^\varphi_G + E^{U(1)}_E + E^{U(1)}_M + E^{SU(2)}_E + E^{SU(2)}_M + E_V , \tag{A.26}$$

$$p = E^\chi_K + E^\varphi_K - \frac{1}{3}(E^\chi_G + E^\varphi_G) + \frac{1}{3}(E^{U(1)}_E + E^{SU(2)}_E) + \frac{1}{3}(E^{U(1)}_M + E^{SU(2)}_M) - E_V , \tag{A.27}$$

where E^χ_K and E^χ_G are the kinetic and gradient energies of the scalar field,

$$E^\chi_K = \frac{1}{2a^{2\alpha}}\dot{\chi}^2 , \quad E^\chi_G = \frac{1}{2a^2}\sum_i |\partial_i\chi|^2 , \tag{A.28}$$

E^φ_K and E^φ_G are the kinetic and gradient energies of the Higgs field,

$$E^\varphi_K = \frac{1}{2a^{2\alpha}}|D_0\varphi|^2 , \quad E^\varphi_G = \frac{1}{2a^2}\sum_i |D_i\varphi|^2 , \tag{A.29}$$

$E_E^{U(1)}$ and $E_M^{U(1)}$ are the electric and magnetic energies of the U(1) sector,

$$E_E^{U(1)} = \frac{1}{2a^{2+2\alpha}} \sum_i F_{0i}^2 , \quad E_M^{U(1)} = \frac{1}{2a^4} \sum_{i,j<i} F_{ij}^2 , \tag{A.30}$$

$E_E^{SU(2)}$ and $E_M^{SU(2)}$ are the electric and magnetic energies of the SU(2) sector,

$$E_E^{SU(2)} = \frac{1}{2a^{2+2\alpha}} \sum_{a,i} (G_{0i}^a)^2 , \quad E_M^{SU(2)} = \frac{1}{2a^4} \sum_{a,i,j<i} (G_{ij}^a)^2 , \tag{A.31}$$

and E_V is the potential energy, $E_V = V(|\varphi|, \chi)$.

The Friedmann equations were written in Eq. (1.4)-(1.5) in cosmic time ($\alpha = 0$). For arbitrary parameter α, they are

$$\dot{a}^2 = a^{2\alpha+2} \frac{\langle \rho \rangle}{3m_p^2} , \tag{A.32}$$

$$\ddot{a} = \frac{a^{2\alpha+1}}{6m_p^2} [(2\alpha - 1)\langle \rho \rangle - 3\langle p \rangle] , \tag{A.33}$$

where $\langle \dots \rangle$ is a volume-average. If the energy budget of the Universe is dominated by the different fields of action (A.3), then the expansion of the Universe is sourced by its stress-energy tensor. Substituting Eqs. (A.26)-(A.27) into the second Friedmann equation (A.33), we find

$$\ddot{a} = \frac{a^{2\alpha+1}}{3m_p^2} \left[(\alpha - 2)\langle E_K^\chi + E_K^\varphi \rangle + (\alpha - 1)\langle E_G^\chi + E_G^\varphi \rangle + \alpha \langle E_E^{U(1)} + E_E^{SU(2)} \rangle \right.$$
$$\left. - (\alpha - 1)\langle E_M^{U(1)} + E_M^{SU(2)} \rangle + (\alpha + 1)\langle E_V \rangle \right] . \tag{A.34}$$

This expression will be extremely useful when we discrete the theory in the next section.

On the other hand, there are situations where the expansion is sourced by a fluid with fixed equation of state $p/\rho = w$, which is not modelled explicitly, and which is energetically dominant with respect the fields of action (A.3). In this case, we can get, by combining the two Friedmann equations (A.32) and (A.33),

$$2\ddot{a} + (1 + 3\omega - 2\alpha)\frac{\dot{a}^2}{a} = 0 . \tag{A.35}$$

The solution for this differential equation is

$$a(t) = a_i \left(1 + \frac{H_i}{p} t \right)^p , \quad p \equiv \frac{2}{3(1 + \omega) - 2\alpha} , \tag{A.36}$$

where we have set the initial conditions $a(t_i) \equiv a_i$ and $H(t_i) \equiv H_i$ at time $t = t_i$, with $H(t) \equiv \dot{a}/a(t)$ the Hubble parameter. In cosmic time ($\alpha = 0$), Eq. (A.36) recovers $a \sim t^{1/2}$ for

radiation domination ($w = 1/3$), and $a \sim t^{2/3}$ for matter domination ($w = 0$), as stated in Eq. (1.7).

A.2. Lattice formulation

A.2.1. The Lattice: definitions and conventions

Let us now provide the details of our lattice formulation. We shall present the discrete field differential equations below, as well as an iterative scheme to solve them self-consistently. For this, it is convenient to define new gauge fields as

$$\mathcal{A}_\mu \equiv \frac{g_1}{2} A_\mu \, , \quad \mathcal{B}_\mu^a \equiv \frac{g_2}{2} B_\mu^a \, . \tag{A.37}$$

Let us also define new field strengths as

$$\mathcal{F}_{\mu\nu} \equiv \frac{g_1}{2} F_{\mu\nu} = \partial_\mu \mathcal{A}_\nu - \partial_\nu \mathcal{A}_\mu \, , \tag{A.38}$$

$$\mathcal{G}_{\mu\nu}^a \equiv \frac{g_2}{2} G_{\mu\nu}^a = \partial_\mu \mathcal{B}_\nu^a - \partial_\nu \mathcal{B}_\mu^a + f^{abc} \mathcal{B}_\mu^b \mathcal{B}_\nu^c \, . \tag{A.39}$$

Continuous action (A.3) can be then written as

$$S = - \int \mathrm{d}x^4 a^{3+\alpha} \left\{ \frac{1}{g_1^2} \mathcal{F}_{\mu\nu} \mathcal{F}^{\mu\nu} + \frac{1}{g_2^2} \mathcal{G}_{\mu\nu}^a \mathcal{G}_a^{\mu\nu} + \frac{1}{2} (D_\mu \varphi)^\dagger (D^\mu \varphi) + \frac{1}{2} \partial_\mu \chi \partial^\mu \chi + V(|\varphi|, \chi) \right\} . \tag{A.40}$$

We now proceed to discretize this action in a lattice in 3+1 dimensions. Let us define a lattice cube of $N^3 = N \times N \times N$ points and lattice spacing dx, so that the length of the cube is $L \equiv \mathrm{d}x N$. Let us also define the time-step of the iterative scheme as dt. In such lattice, the minimum and maximum momenta covered are

$$p_\mathrm{min} = \frac{2\pi}{L} \, , \quad p_\mathrm{max} = \frac{\sqrt{3}N}{2} p_\mathrm{min} \, . \tag{A.41}$$

It is convenient to define a 4-component vector as $\mathrm{d}x^\mu \equiv (\mathrm{d}t, \vec{\mathrm{d}x})$. A position $\vec{x}$ in the lattice can be then specified as

$$\vec{x} \equiv n_\mu \mathrm{d}x^\mu = n_0 \mathrm{d}t \hat{n}^0 + \sum_i n_i \mathrm{d}x \hat{n}^i \, , \tag{A.42}$$

with $\mathrm{d}t \equiv \mathrm{d}x^0$ the time step, $\mathrm{d}x \equiv \mathrm{d}x^i$ ($i = 1, 2, 3$) the lattice spacing, $\hat{n}^\mu$ a set of orthonormal vectors, and (n_0, n_i) the coordinates specifying the lattice point.

Let us consider from now on that fields live in the nodes of the lattice, so that $f \equiv f(\vec{x})$, where $f = \chi, \varphi, A_\mu, B_\mu^a$ is an arbitrary field variable, and $\vec{x}$ is given by vector (A.42). Let us also introduce the notation $f_\mu \equiv f(\vec{x} + dx^\mu \hat{n}^\mu)$ and $f_{-\mu} \equiv f(\vec{x} - dx^\mu \hat{n}^\mu)$. For the U(1) and SU(2) gauge fields, we also define the following link variables (not sum on μ implied),

$$V_\mu \equiv V_\mu(\vec{x}) = e^{-i dx^\mu \mathcal{A}_\mu(\vec{x})}, \tag{A.43}$$

$$U_\mu \equiv U_\mu(\vec{x}) = e^{-i dx^\mu \mathcal{B}_\mu^a(\vec{x})\sigma_a}, \tag{A.44}$$

as well as introduce the notation $V_{\mu,\nu} \equiv V_\mu(\vec{x} + dx^\nu \hat{n}^\mu)$ and $U_{\mu,\nu} \equiv U_\mu(\vec{x} + dx^\nu \hat{n}^\mu)$, as well as $V_{\mu,-\nu} \equiv V_\mu(\vec{x} - dx^\nu \hat{n}^\mu)$ and $U_{\mu,-\nu} \equiv U_\mu(\vec{x} - dx^\nu \hat{n}^\mu)$. Note that in the temporal gauge $\mathcal{B}_0^a = 0$, we have $U_0 = \mathcal{I}$, with $\mathcal{I}$ the identify matrix.

Let us define the following ordinary discrete derivatives,

$$\Delta_\mu^+ f \equiv \frac{1}{dx_\mu}(f_\mu - f), \quad \Delta_\mu^- \varphi \equiv \frac{1}{dx_\mu}(f - f_{-\mu}), \tag{A.45}$$

which recover the continuous ones in the continuum limit up to second-order terms in dx^μ. Let us also define the following discrete covariant derivatives for the Higgs field,

$$D_\mu^+ \varphi \equiv \frac{1}{dx_\mu}(U_\mu V_\mu \varphi_\mu - \varphi), \quad D_\mu^- f \equiv \frac{1}{dx_\mu}(\varphi - V_{-\mu}^* U_{-\mu}^\dagger \varphi_{-\mu}), \tag{A.46}$$

which also recover the continuum ones up to second order terms. The SU(2) plaquettes are defined as the following product of four links,

$$P_{\mu\nu} \equiv U_\mu U_{\nu,+\mu} U_{\mu,+\nu}^\dagger U_\nu^\dagger. \tag{A.47}$$

We can check that, in the continuum limit,

$$P_{\mu\nu} = e^{-i dx_\mu dx_\nu \mathcal{G}_{\mu\nu}^a \sigma_a + \dots} \tag{A.48}$$

where we have ignored higher-order terms in dx^μ. Expression (A.48) can be proven using repeatedly the Baker-Campbell-Hausdorff formula,

$$\exp(X)\exp(Y) = \left(X + Y + \frac{1}{2}[X, Y]\right), \tag{A.49}$$

which is valid for two central commutators X and Y, obeying $[X, [X, Y]] = [Y, [X, Y]] = 0$.

Any matrix M of SU(2) can be written as $[\bar{\sigma}_a \equiv (1, i\vec{\sigma})]$

$$M = \sum_{a=0}^3 m^{(a)} \bar{\sigma}_a = \begin{pmatrix} m^{(0)} + im^{(3)} & m^{(2)} + im^{(1)} \\ -m^{(2)} + im^{(1)} & m^{(0)} - im^{(3)} \end{pmatrix}, \tag{A.50}$$

where $m_\mu^{(a)} \in \mathfrak{Re}$ and $\sum_{a=0}^{3}(m_\mu^{(a)})^2 = 1$. Let us define $u_\mu^{(a)}$ and $p_{\mu\nu}^{(a)}$ as the components of U_μ and $P_{\mu\nu}$ respectively. From Eq. (A.48), we can check that

$$\mathcal{G}_{\mu\nu}^a = -\frac{p_{\mu\nu}^{(a)}}{dx_\mu dx_\nu} \ . \tag{A.51}$$

With this, we can write expressions for the non-Abelian electric and magnetic fields, Eqs. (A.8) and (A.9), in terms of the plaquette matrix elements as,

$$
\begin{aligned}
\mathcal{E}_i^a &\equiv \mathcal{G}_{0i}^a = -\frac{p_{0i}^{(a)}}{dtdx} \ , \\
\mathcal{M}_i^a &\equiv \frac{1}{2}\epsilon_{ijk}\mathcal{G}_{jk}^a \approx \frac{-\epsilon_{ijk}}{2dx^2}p_{jk}^{(a)} \ .
\end{aligned}
\tag{A.52}
$$

We can also prove that in the continuum limit,

$$\sum_a (\mathcal{G}_{\mu\nu}^a)^2 = \frac{1}{dx_\mu^2 dx_\nu^2}\mathrm{Tr}[\mathcal{I}_{2\times 2} - P_{\mu\nu}] \ . \tag{A.53}$$

Finally, let us consider the scale factor. We proceed to discretize it such that it is only defined in semi-integer time steps. It is convenient then to define $a_{+0/2} \equiv a(t + dt/2)$ and $a_{-0/2} \equiv a(t - dt/2)$, as well as

$$a \equiv \frac{a_{+0/2} + a_{-0/2}}{2} \ . \tag{A.54}$$

A.2.2. Field equations

Having defined all necessary variables and functions in the previous section, we present now the discrete action in which our lattice formulation is based. It is written as

$$S = -\sum_{\hat{n}} dtdx^3(\mathcal{L}_\mathrm{I} + \mathcal{L}_\mathrm{II} + \mathcal{L}_\mathrm{III} + \mathcal{L}_\mathrm{IV} + \mathcal{L}_\mathrm{V} + \mathcal{L}_\mathrm{VI} + \mathcal{L}_\mathrm{VII} + \mathcal{L}_\mathrm{VIII} + \mathcal{L}_\mathrm{IX}) \ , \tag{A.55}$$

where the different pieces of the action are defined as

$$
\begin{aligned}
\mathcal{L}_\mathrm{I} &= \frac{-2a_{+0/2}^{1-\alpha}}{g_1^2}\sum_i(\Delta_0^+ A_i - \Delta_i^+ A_0)^2 \ , \tag{A.56} \\[4pt]
\mathcal{L}_\mathrm{II} &= \frac{a^{-1+\alpha}}{g_1^2}\sum_{i,j}(\Delta_i^+ A_j - \Delta_j^+ A_i)^2 \ , \tag{A.57} \\[4pt]
\mathcal{L}_\mathrm{III} &= \frac{-2a_{+0/2}^{1-\alpha}}{g_2^2 dx^2 dt^2}\sum_i \mathrm{Tr}(P_{0i}) \ , \tag{A.58} \\[4pt]
\mathcal{L}_\mathrm{IV} &= \frac{a^{-1+\alpha}}{g_2^2 dx^4}\sum_{i,j}\mathrm{Tr}(P_{ij}) \ , \tag{A.59}
\end{aligned}
$$

$$\mathcal{L}_V \;=\; -\frac{1}{2}a_{+0/2}^{3-\alpha}|D_0^+\varphi|^2\,, \tag{A.60}$$

$$\mathcal{L}_{VI} \;=\; \frac{1}{2}a^{1+\alpha}\sum_i|D_i^+\varphi|^2\,, \tag{A.61}$$

$$\mathcal{L}_{VII} \;=\; -\frac{1}{2}a_{+0/2}^{3-\alpha}(\Delta_0^+\chi)^2\,, \tag{A.62}$$

$$\mathcal{L}_{VIII} \;=\; \frac{1}{2}a^{1+\alpha}\sum_i(\Delta_i^+\varphi)^2\,, \tag{A.63}$$

$$\mathcal{L}_{IX} \;=\; a^{3+\alpha}V(\chi,|\varphi|)\,. \tag{A.64}$$

The discrete action presented here recovers in the continuum limit the action (A.40), up to second order terms in time step and lattice spacing. Here, the expressions (A.56)-(A.63) correspond respectively to the kinetic and gradient terms of the Abelian gauge fields, non-Abelian gauge fields, complex fields, and scalar fields, while Eq. (A.64) is the potential energy.

The discrete field equations of motion are obtained from the minimization of this lattice action. We will show, as an example, the derivation of the discrete EOM of a single scalar field χ. Let us define $\delta_\chi f \equiv \frac{\partial \sum_{\hat{n}} f}{\partial \chi}\delta\chi$. We have, for the different Lagrangian pieces involving χ,

$$\delta_\chi\mathcal{L}_{VII} \;=\; \frac{-1}{2dt^2}\delta_\chi\left[a_{+0/2}^{3-\alpha}(\chi_{+0}-\chi)^2\right]$$

$$\;=\; \frac{-1}{dt^2}\left[a_{-0/2}^{3-\alpha}(\chi-\chi_{-0})-a_{+0/2}(\chi_{+0}-\chi)\right]\delta\chi = \Delta_0^-[a_{+0/2}^{3-\alpha}(\Delta_0^+\chi)]\delta\chi\,,$$

$$\delta_\chi[a^{1+\alpha}(\Delta_i^+\chi)^2] \;=\; \frac{1}{2dx^2}\delta_\chi[a^{1+\alpha}(\chi_{+i}-\chi)^2] = \frac{1}{dx^2}a^{1+\alpha}\left[(\chi-\chi_{-i})-(\chi_{+i}-\chi)\right] =$$

$$-a^{1+\alpha}(\Delta_i^-\Delta_i^+\chi)\delta\chi\,,$$

$$\delta_\chi\mathcal{L}_{IX} \;=\; a^{3+\alpha}\frac{\partial V}{\partial\chi}\delta\chi\,. \tag{A.65}$$

Hence, the scalar discrete EOM is obtained from the condition $\delta_\chi\mathcal{L}=0$. It is

$$\Delta_0^-[a_{+0/2}^{3-\alpha}\Delta_0^+\chi] - a^{1+\alpha}\sum_i\Delta_i^-\Delta_i^+\chi + a^{3+\alpha}\frac{\partial V}{\partial\chi} = 0\,. \tag{A.66}$$

Note that the kinetic and gradient term of this equation behave, in the continuum limit, as

$$\Delta_0^-[a_{+0/2}^{3-\alpha}\Delta_0^+\chi] \;=\; a^{3-\alpha}\left(\chi'' + (3-\alpha)\frac{a'}{a}\chi'\right) + \mathcal{O}(dt^2)\,,$$

$$a^{1+\alpha}\sum_i\Delta_i^-\Delta_i^+\chi \;=\; a^{1+\alpha}\nabla^2\chi + \mathcal{O}(dx^2)\,. \tag{A.67}$$

From this, we can easily check that the discrete equation (A.66) recovers the continuum one (A.16) up to second order terms in dx^μ, as expected.

The other dynamical equations of motion are obtained in a similar way, from the conditions $\delta_\varphi \mathcal{L} = 0$, $\delta_{A_i} \mathcal{L} = 0$, and $\delta_{B_i^a} \mathcal{L} = 0$. The full system of equations is then

$$\Delta_0^- [a_{+0/2}^{3-\alpha} \Delta_0^+ \chi] - a^{1+\alpha} \sum_i \Delta_i^- \Delta_i^+ \chi = -a^{3+\alpha} \frac{\partial V}{\partial \chi} , \tag{A.68}$$

$$\Delta_0^- \left[a_{+0/2}^{3-\alpha} \Delta_0^+ \varphi \right] - a^{1+\alpha} \sum_i D_i^- D_i^+ \varphi = -a^{3+\alpha} \frac{\varphi}{|\varphi|} \frac{\partial V}{\partial |\varphi|} , \tag{A.69}$$

$$\Delta_0^- [a_{+0/2}^{1-\alpha} \Delta_0^+ A_i] - a^{-1+\alpha} \left(\sum_j \Delta_j^- \Delta_j^+ A_i - \sum_j \Delta_j^- \Delta_i^+ A_j \right) = \frac{-g_1^2 a^{1+\alpha}}{4 dx} \mathfrak{Im}[\varphi_{+i}^\dagger V_i^* U_i^\dagger \varphi] , \tag{A.70}$$

$$\mathrm{Tr}[(iT_a)(a_{+0/2}^{1-\alpha} P_{0i} - a_{-0/2}^{1-\alpha} P_{0i,-0})] = \frac{g_2^2}{2} dt^2 a^{1+\alpha} \mathfrak{Re}[\varphi_{+i}^\dagger V_i^* U_i^\dagger (iT_a) \varphi] \tag{A.71}$$

$$- \frac{dt^2}{dx^2} a^{-1+\alpha} \sum_{j \neq i} \mathfrak{Re}\{\mathrm{Tr}[(iT_a)(P_{ij} - U_{j,-j}^\dagger P_{ij,-j} U_{j,-j})]\} ,$$

where we have fixed the temporal gauge $A_0 = B_0^a = 0$. This constitutes a set of 17 different equations of motion: 1 for the scalar field χ, 4 for the components of the Higgs field φ, 3 for the Abelian gauge field components A_i, and 9 for the non-Abelian gauge components, which are represented in the lattice by the components $u_i^{(a)}$ of the link U_i.

The system of Eqs. (A.68)-(A.71) can be solved iteratively with a Hamiltonian scheme. For this, let us define the following conjugate momenta for each of the fields,

$$\pi_{\chi, +0/2} \equiv \Delta_0^+ \chi , \tag{A.72}$$

$$\pi_{\varphi, +0/2} \equiv \Delta_0^+ \varphi , \tag{A.73}$$

$$\pi_{A_i, +0/2} \equiv \Delta_0^+ A_i , \tag{A.74}$$

$$\pi_{u_i^{(a)}, +0/2} \equiv p_{0i}^{(a)} , \tag{A.75}$$

where we have defined the momenta living naturally at semiinteger time steps, like the scale factor. We can then rewrite Eqs. (A.68)-(A.71) as

$$\pi_{\chi, +0/2} = \frac{dt}{a_{+0/2}^{3-\alpha}} \left(a^{1+\alpha} \Delta_i^- \Delta_i^+ \chi - a^{3+\alpha} \frac{\partial V}{\partial \chi} \right) + \left(\frac{a_{-0/2}}{a_{+0/2}} \right)^{3-\alpha} \pi_{\chi, -0/2}, \tag{A.76}$$

$$\pi_{\varphi, +0/2} = \frac{dt}{a_{+0/2}^{3-\alpha}} \left(a^{1+\alpha} D_i^- D_i^+ \varphi - dt a^{3+\alpha} \frac{\partial V}{\partial |\varphi|} \frac{\varphi}{|\varphi|} \right) + \left(\frac{a_{-0/2}}{a_{+0/2}} \right)^{3-\alpha} \pi_{\varphi, -0/2}, \tag{A.77}$$

$$\pi_{A_i, +0/2} = dt \frac{a^{-1+\alpha}}{a_{+0/2}^{1-\alpha}} \left(\sum_j \Delta_j^- \Delta_j^+ A_i - \sum_j \Delta_j^- \Delta_i^+ A_j \right)$$

$$- \frac{dt}{dx} \frac{g_1^2 a^{1+\alpha}}{4 a_{+0/2}^{1-\alpha}} \mathfrak{Im}[\varphi_{+i}^\dagger V_i^* U_i^\dagger \varphi] + \left(\frac{a_{-0/2}}{a_{+0/2}} \right)^{1-\alpha} \pi_{A_i, -0/2} , \tag{A.78}$$

$$\pi_{u_i^{(a)},+0/2} = \frac{dt^2}{2dx^2} \frac{a^{-1+\alpha}}{a_{-0/2}^{1-\alpha}} \sum_{j\neq i} \Re\{\text{Tr}[(i\sigma_a)(P_{ij} - U_{j,-j}^\dagger P_{ij,-j} U_{j,-j})]\} \tag{A.79}$$

$$-dt^2 \frac{g_2^2}{4} \frac{a^{1+\alpha}}{a_{+0/2}^{1-\alpha}} \Re[\varphi_{+i}^\dagger V_i^* U_i^\dagger (i\sigma_a)\varphi] + \left(\frac{a_{-0/2}}{a_{+0/2}}\right)^{1-\alpha} \pi_{u_i^{(a)},-0/2}.$$

These expressions give the momenta at the time $t + dt/2$ as a function of the momenta at the previous time $t - dt/2$, as well as the fields at time t. On the other hand, by inverting Eqs. (A.72)-(A.75), we find

$$\chi_{+0} = \pi_{\chi,+0/2} dt + \chi, \tag{A.80}$$

$$\varphi_{+0} = \pi_{\varphi,+0/2} dt + \varphi, \tag{A.81}$$

$$A_{i,+0} = \pi_{A_i,+0/2} dt + A_i, \tag{A.82}$$

$$u_{i,+0}^{(1)} = \pi_{u_i^{(1)},+0/2} u_i^{(0)} + \pi_{u_i^{(0)},+0/2} u_i^{(1)} + \pi_{u_i^{(3)},+0/2} u_i^{(2)} - \pi_{u_i^{(2)},+0/2} u_i^{(3)}, \tag{A.83}$$

$$u_{i,+0}^{(2)} = \pi_{u_i^{(2)},+0/2} u_i^{(0)} + \pi_{u_i^{(0)},+0/2} u_i^{(2)} + \pi_{u_i^{(1)},+0/2} u_i^{(3)} - \pi_{u_i^{(3)},+0/2} u_i^{(1)}, \tag{A.84}$$

$$u_{i,+0}^{(3)} = \pi_{u_i^{(3)},+0/2} u_i^{(0)} + \pi_{u_i^{(2)},+0/2} u_i^{(1)} + \pi_{u_i^{(0)},+0/2} u_i^{(3)} - \pi_{u_i^{(1)},+0/2} u_i^{(2)}. \tag{A.85}$$

[Note that Eqs. (A.83)-(A.85) come from Eq. (A.75), each equation evaluated for each of the three colors $a = 1, 2, 3$]. These expressions give the values for the different fields at the time step $t + dt$, as a function of the fields at the previous time t, and the momenta at the time $t + dt/2$.

Let us assume that we know the time-evolution of the scale factor at all times. For example, this could be when the expansion is caused by a fluid with equation of state w. In this case, the scale factor is given by Eq. (A.36). In this scenario, the first-order field and momentum equations can be solved iteratively. For example, if initial conditions for $\{\chi, \varphi_n, A_i, u_i^{(a)}\}$ are set at time $t = 0$, and for $\{\pi_\chi, \pi_\varphi, \pi_{A_i}, \pi_{u_i^{(a)}}\}$ are set at time $t = dt/2$, we must simply solve first Eqs. (A.80)-(A.85) to obtain the fields at time $t = dt$, and then Eqs. (A.76)-(A.79) to obtain the momenta at time $t = 3dt/2$. These steps can be then repeated for the whole temporal evolution of the system.

A.2.3. Friedmann equations

Let us consider now the case when the evolution of the scale factor is not previously known, but it is sourced by the different fields. This situation is more complicated, because we must solve the scale factor equations self-consistently with the discrete field equations. In our approach, we do not derive the scale factor equations from a discrete action, but simply discretize directly the continuum Friedmann equations (A.32)-(A.33). For this, let us define the operator

$$b \equiv \Delta_0^- (a_{+0/2}), \tag{A.86}$$

such that, in the continuum limit,

$$a' \rightarrow b , \quad a'' \rightarrow \Delta_0^+ b . \tag{A.87}$$

A discretized version of the second Friedmann equation (A.33) can be written as

$$
\begin{aligned}
b_{+0} \;=\; & b + \frac{\mathrm{dt}}{6m_p^2} \Big[(\alpha - 2) a_{+0/2} \langle \pi_{\chi,+0/2}^2 + \pi_{\varphi,+0/2}^2 \rangle \\
& + \frac{\alpha}{2} a_{+0/2}^{2\alpha-1} \langle \mathcal{G}[\chi] + \mathcal{G}[\chi_{+0}] + \mathcal{G}[\varphi] + \mathcal{G}[\varphi_{+0}] \rangle + (\alpha + 1) a_{+0/2}^{2\alpha+1} \langle V + V_{+0} \rangle \\
& + (\alpha - 1) a_{+0/2}^{-1} \sum_{i,a} \langle \mathcal{E}_{i,+0/2}^{(a)2} \rangle - \frac{(\alpha - 1)}{2} a_{+0/2}^{2\alpha-3} \sum_{i,a} \left(\langle \mathcal{M}_i^{(a)2} \rangle + \langle \mathcal{M}_{i,+0}^{(a)2} \rangle \right) \Big] ,
\end{aligned}
\tag{A.88}
$$

where we have defined the discrete gradient energy as $\mathcal{G}[f] \equiv \sum_i (\Delta_i^+ f)^2$. On the other hand, we find, from the definition of b,

$$a_{+0/2} = a_{-0/2} + b\mathrm{dt} . \tag{A.89}$$

This way, we have obtained a Hamiltonian evolution scheme for the scale factor, where b (defined at integer times) is the conjugate momenta of a (defined at semi-integer times). We can solve these equations iteratively, in a similar fashion as the field equations.

A.2.4. Gauss constraints and initial conditions

We now explain how to set the initial conditions for the Higgs and gauge fields, so that the Gauss constraints (A.20)-(A.21) are obeyed initially. We will do it first in the continuum. Let us set the initial conditions at the time $t = t_i$, and denote the initial amplitude and velocity of the Higgs field as φ_i and $\dot{\varphi}_i$ respectively. For the Higgs components, we impose the initial homogeneous modes as,

$$\varphi_n(t_i) \equiv \frac{1}{2}\varphi_i , \quad \dot{\varphi}_n(t_i) \equiv \frac{1}{2}\dot{\varphi}_i , \tag{A.90}$$

for each of the four Higgs components $n = 0, 1, 2, 3$. This way, the initial amplitude and velocity of the Higgs field is distributed equally between all its components. On top of these, we put the following spectra of initial fluctuations,

$$
\varphi_n(\vec{k}) \;=\; \frac{|a_n(\vec{k})|}{\sqrt{2}} \left(e^{\theta_{n0}} + e^{\theta_{n1}} \right) , \tag{A.91}
$$

$$
\dot{\varphi}_n(\vec{k}) \;=\; \frac{|a_n(\vec{k})|}{\sqrt{2}} i\omega_{k,n} \left(e^{\theta_{n0}} - e^{\theta_{n1}} \right) - H\varphi_n(\vec{k}) . \tag{A.92}
$$

These spectra represent a sum of left-moving and right-moving waves. Here, $\omega_k = \sqrt{k^2 + a^2 m_{\text{eff,n}}^2}$ is the frequency of the field modes with $m_{\text{eff,n}}^2 = (\partial^2 V / \partial \varphi_n^2)$, θ_{n0} and θ_{n1} are random phases, and $a_n(\vec{k})$ follow the Rayleigh distribution,

$$P(|a_n(\vec{k})|) = \frac{2|a_n|}{\langle |a_n|^2 \rangle} e^{-\frac{|a_n|^2}{\langle |a_n|^2 \rangle}}, \quad \langle |a_n|^2 \rangle = \frac{1}{2a^2 \omega_k}. \tag{A.93}$$

The Gauss constraints (A.20) and (A.21) can be written in terms of components, in the temporal gauge $A_0 = B_0^a = 0$, as

$$\partial_i \dot{A}_i = j_0(x), \quad j_0(x) \equiv \frac{g_1}{2} a^2(t) \mathfrak{Im}[\varphi^\dagger \dot{\varphi}], \tag{A.94}$$

$$\partial_i \dot{B}_i^a - \epsilon_{abc} B_i^c \dot{B}_i^b = j_0^a(x), \quad j_0^a(x) \equiv \frac{g_2}{2} a^2(t) \mathfrak{Im}[\varphi^\dagger \sigma_a \dot{\varphi}]. \tag{A.95}$$

There are four different constraints: one for the U(1) sector [Eq. (A.94)], and one for each of the three components of the SU(2) sector [Eq. (A.95)]. At initial time $t = t_i$, we impose exactly $A_i(\vec{x}, t_i) = B_i^a(\vec{x}, t_i) = 0$ at all volume space. This is equivalent to imposing the magnetic fields to zero at all points. We also set the homogeneous components of the time-derivatives of the gauge fields (electric fields) to zero, $\dot{A}_i = 0$ and $\dot{B}_i^a = 0$, but we shall put fluctuations on top of them, so that the Gauss constraints are preserved initially. The Gauss laws (A.94) and (A.95) are written in momentum space as

$$k_i \dot{A}^i(\vec{k}) = j^0(\vec{k}), \quad k_i \dot{B}_a^i(\vec{k}) = j^a(\vec{k}). \tag{A.96}$$

Hence, we impose in momentum space

$$\dot{A}_i(\vec{k}) = i \frac{k_i}{k^2} j^0(\vec{k}), \quad \dot{B}_i^a(\vec{k}) = i \frac{k_i}{k^2} j^a(\vec{k}), \tag{A.97}$$

where the fluctuations of $j^0(\vec{k})$ and $j^a(\vec{k})$ are given by the ones of the Higgs field, through Eqs. (A.94) and (A.95). For consistency with (A.96), these fluctuations must also obey $j(\vec{0}) = j^a(\vec{0}) = 0$ for the zero mode $\vec{k} = 0$. If this condition is not fullfilled, then Eq. (A.97) cannot be derived from Eq. (A.96). These conditions can be written as $[\varphi_n \equiv \varphi_n(\vec{k})]$

$$j^0(\vec{k} = \vec{0}) = \int d^3\vec{k} \, \mathfrak{Re}[\varphi_0 \dot{\varphi}_1 - \dot{\varphi}_0 \varphi_1 + \varphi_2 \dot{\varphi}_3 - \dot{\varphi}_2 \varphi_3] = 0,$$

$$j^1(\vec{k} = \vec{0}) = \int d^3\vec{k} \, \mathfrak{Re}[\varphi_3 \dot{\varphi}_0 - \dot{\varphi}_3 \varphi_0 + \varphi_1 \dot{\varphi}_2 - \dot{\varphi}_1 \varphi_2] = 0,$$

$$j^2(\vec{k} = \vec{0}) = \int d^3\vec{k} \, \mathfrak{Re}[\varphi_0 \dot{\varphi}_2 - \dot{\varphi}_0 \varphi_2 + \varphi_1 \dot{\varphi}_3 - \dot{\varphi}_1 \varphi_3] = 0,$$

$$j^3(\vec{k} = \vec{0}) = \int d^3\vec{k} \, \mathfrak{Re}[\varphi_1 \dot{\varphi}_0 - \dot{\varphi}_1 \varphi_0 + \varphi_2 \dot{\varphi}_3 - \dot{\varphi}_2 \varphi_3] = 0. \tag{A.98}$$

This is a system of four equations with four unknowns. Its solution is

$$\dot\varphi_n(\vec{k})\varphi_0(\vec{k}) = \dot\varphi_0(\vec{k})\varphi_n(\vec{k}) , \quad (n = 1, 2, 3) \tag{A.99}$$

Using Eqs. (A.91) and (A.92), we can write solution (A.99) as

$$e^{\frac{i}{2}(\theta_{00}+\theta_{01}+\theta_{n0}+\theta_{n1})}a_{k,0}a_{k,n} \times \left[(\omega_{k,0} - \omega_{k,n})\sin\left(\frac{1}{2}(\theta_{00} - \theta_{01} + \theta_{n0} - \theta_{n1})\right) + \right. \tag{A.100}$$

$$\left. (\omega_{k,0} + \omega_{k,n})\sin\left(\frac{1}{2}(\theta_{00} - \theta_{01} - \theta_{n0} + \theta_{n1})\right)\right] = 0 ,$$

for each $n = 1, 2, 3$. The initialization of the homogeneous mode of the Higgs field, given in Eq. (A.90), guarantees that $m^2_{\text{eff,n}} = m^2_{\text{eff,0}}$ for $n = 1, 2, 3$, and hence $\omega_0 = \omega_n$. This way, the first term in Eq. (A.100) goes away. Then, Eq. (A.100) is simply reduced to

$$\theta_{n1} = \theta_{n0} + \theta_{01} - \theta_{00} , \quad (n = 1, 2, 3) . \tag{A.101}$$

If the initialization preserves this relation between the random phases, the Gauss constraints are initially preserved. This condition can be imposed by letting only five of the phases be generated randomly, and fixing the other three phases via Eq. (A.101).

Let us move to the discrete. The discrete gauge dynamical equations written above were obtained by minimizing the discrete action (A.55) with respect the spatial gauge components, A_i and B_i^a. On the other hand, by minimizing the action with respect the temporal components, $\delta_{A_0}\mathcal{L} = 0$ and $\delta_{B_0^a}\mathcal{L} = 0$, we obtain the discrete Gauss constraints,

$$\sum_i \Delta_i^- \Delta_0^+ A_i = \frac{g_1^2 a_{+0/2}^2}{4\text{dt}}\mathfrak{Im}[\varphi^\dagger \Delta_0^+ \varphi] , \tag{A.102}$$

$$\sum_i \text{Tr}[(i\sigma_a)(P_{0i} - U_{i,-i}^\dagger P_{0i,-i} U_{i,-i})] = g_2^2 \text{dx}^2 a_{+0/2}^2 \mathfrak{Re}[\varphi^\dagger \sigma_a \Delta_0^+ \varphi] . \tag{A.103}$$

The initial conditions for the different fields must be imposed, so that these constraints are preserved at machine precision. If this is the case, the temporal resolution of Eqs. (A.76)-(A.79) is guaranteed to obey constraints (A.102)-(A.103) at all times, except a small accumulated error due to machine precision. In the lattice, this can be achieved by a analogous procedure to the one in the continuum. In particular, we let $|a_n(\vec{k})|$ vary from point to point in momentum space, according to probability distribution (A.93). On the other hand, we let five of the eight phases $\theta_{n0}(\vec{k})$ and $\theta_{n1}(\vec{k})$ ($n = 0, 1, 2, 3$) vary randomly within the interval $[0, 2\pi)$, and fix the other three phases via condition (A.101).

Appendix B.

Adiabatic regularization for fermionic species

When a quantum field is coupled to a classical, non-adiabatic time-dependent background field, it gets excited, and undergoes a non-perturbative regime of particle creation. The background may be a classical homogeneous scalar field, such as in preheating, or spacetime itself, such as in inflation. In this thesis, we have mainly considered scenarios in which the created particles are bosonic species (either scalar and gauge fields), and the background fields are scalars, such as the inflaton (Part I) or the Higgs field (Part II).

In this Appendix, we consider instead the case of fermions. In particular, we will consider a situation in which a fermionic species is coupled to a homogeneous, time-dependent scalar field via a Yukawa coupling. This kind of system appears for example in fermionic preheating, where the inflaton acts as a background scalar field oscillating around the minimum of its potential, and decays nonperturbatively into fermions due to its Yukawa interactions [29, 30, 159, 138, 31, 32, 33]. Another example is the decay of the Standard Model (SM) Higgs after inflation, in which the Higgs condensate oscillates around the minimum of its potential, and transfers part of its energy into all the massive fermions of the SM, coupled to the Higgs with the usual SM Yukawa couplings [122, 55] (another part of the energy is transferred to gauge bosons, as analyzed in Chapters 4 and 6).

In this Appendix we present a formalism to study non-perturbative excitation of fermionic fields due to a time-dependent background field. Fermions are much more complicated than bosons in this context. There are two important differences. First, bosonic production can be studied with classical, real-time lattice simulations, as the ones we have presented throughout this thesis. In regimes of strong particle creation (i.e. when the mean particle number is much greater than $n_k \gg 1$), the quantum nature of the fields can be typically ignored, and we can simply solve the (3+1)-dimensional classical equations of motion in the lattice. In this approach, expectation values are simply volume averages over the lattice. On the contrary,

the fermion particle number is constrained to be $n_k < 1$ due to Pauli blocking, and hence, the lattice approach is not valid. Second, due to the the non-adiabatic time dependence of the background field, new ultraviolet (UV) divergent terms appear in the vacuum expectation values of the fermionic quadratic products (such as the stress-energy tensor), which must appropriately be removed to obtain a physical, finite quantity. UV divergences also appear in the case of bosonic species, but in this case, there is usually a clear hierarchy between infrared and ultraviolet modes, see for example the left panels of Fig. 3.4. Hence, for boson fields, a cutoff is simply introduced to get rid of the divergent modes (in the lattice approach, the cutoff coincides with the maximum momentum captured by the lattice). On the contrary, in the case of fermions the hierarchy is not so clear, due again to Pauli blocking, so a more refined regularization/renormalized scheme is necessary in this case.

The results presented here are a summary of our work in Ref. [4]. There we derived a generalization of the adiabatic regularization method (originally developed in [160, 161] for scalar fields) for the case of fermionic species coupled, via Yukawa interactions, to a time-dependent background scalar field. This method is based on an adiabatic expansion of the field modes, which allows to identify the covariant UV-divergent terms of the corresponding UV-divergent bilinear, and subtract them directly to obtain a finite quantity. The renormalized expectation value is hence expressed as a finite integral in momentum space, depending exclusively on the mode functions defining the quantum state. We will not focus here on a particular scenario, but simply consider arbitrary time-dependent background fields. The application of this formalism to particular situations (like fermionic preheating) will be done somewhere else.

In this Appendix, for coherence with notation of Ref. [4], we temporally switch the signature of the FLRW metric from $(-,+,+,+)$ to $(+,-,-,-)$.

B.1. Adiabatic regularization with Yukawa interaction

Let us consider here a theory defined by the action functional $S = S[g_{\mu\nu}, \Phi, \psi, \nabla\psi]$, where ψ represents a Dirac field, Φ is a scalar field, and $g_{\mu\nu}$ stands for the spacetime metric. We decompose the action as $S = S_g + S_m$, where S_m is the matter sector containing all terms dependent on the Dirac field,

$$S_m = \int d^4x \sqrt{-g} \left\{ \frac{i}{2}[\bar{\psi}\underline{\gamma}^\mu \nabla_\mu \psi - (\nabla_\mu \bar{\psi})\underline{\gamma}^\mu \psi)] - m\bar{\psi}\psi - g_Y \Phi \bar{\psi}\psi \right\}, \qquad (B.1)$$

and S_g is the gravity-scalar sector, presented later in Eq. (B.30). Here, $\underline{\gamma}^\mu(x)$ are the spacetime-dependent Dirac matrices satisfying the anticommutation relations $\{\underline{\gamma}^\mu, \underline{\gamma}^\nu\} = 2g^{\mu\nu}$, $\nabla_\mu \equiv \partial_\mu - \Gamma_\mu$ is the covariant derivative associated to the spin connection Γ_μ; m is the mass of the

Dirac field; and g_Y is the dimensionless coupling constant of the Yukawa interaction. In (B.1), both the metric $g_{\mu\nu}(x)$ and the scalar field $\Phi(x)$ are regarded as classical external fields. The Dirac spinor $\psi(x)$ will be our quantized field, living in a curved spacetime and possessing a Yukawa coupling to the classical field Φ. The Dirac equation is obtained from the minimization of action (B.1), with respect ψ. It is

$$(i\underline{\gamma}^{\mu}\nabla_{\mu} - m - g_Y\Phi)\psi = 0 . \tag{B.2}$$

On the other hand, the fermionic stress-energy tensor is [156]

$$T^m_{\mu\nu} = \frac{2}{\sqrt{-g}}\frac{\delta S_m}{\delta g^{\mu\nu}} = \frac{i}{2}\left[\bar{\psi}\underline{\gamma}_{(\mu}\nabla_{\nu)}\psi - (\nabla_{(\mu}\bar{\psi})\underline{\gamma}_{\nu)}\psi\right] . \tag{B.3}$$

In this Appendix, we take the FLRW metric as $ds^2 = dt^2 - a^2(t)d\vec{x}^2$, and use the Dirac-Pauli representation for the Dirac gamma matrices,

$$\gamma^0 = \begin{pmatrix} I & 0 \\ 0 & -I \end{pmatrix} , \quad \vec{\gamma} = \begin{pmatrix} 0 & \vec{\sigma} \\ -\vec{\sigma} & 0 \end{pmatrix} , \tag{B.4}$$

with $\vec{\sigma}$ the usual Pauli matrices. The time-dependent gamma matrices are related with the Minkowskian ones by $\underline{\gamma}^0(t) = \gamma^0$ and $\underline{\gamma}^i(t) = \gamma^i/a(t)$, and the components of the spin-connections are $\Gamma_0 = 0$ and $\Gamma_i = (\dot{a}/2)\gamma_0\gamma_i$. For the case of a homogeneous time-dependent scalar field $\Phi = \Phi(t)$, Eq. (B.2) takes the form

$$\left(\partial_0 + \frac{3}{2}\frac{\dot{a}}{a} + \frac{1}{a}\gamma^0\vec{\gamma}\vec{\nabla} + i(m + s(t))\gamma^0\right)\psi = 0 , \tag{B.5}$$

where we have defined $s(t) \equiv g_Y\Phi(t)$ for convenience. The solution for this equation can be written as the following Fourier expansion of the Dirac field operator (see for instance [162, 163])

$$\psi(x) = \frac{1}{\sqrt{(2\pi)^3 a^3(t)}}\int d^3\vec{k}\sum_{\lambda=-1,+1}\left[B_{\vec{k}\lambda}e^{i\vec{k}\vec{x}}u_{\vec{k}\lambda}(x) + D^{\dagger}_{\vec{k}\lambda}e^{-i\vec{k}\vec{x}}v_{\vec{k}\lambda}(x)\right] , \tag{B.6}$$

where here, $B_{\vec{k},\lambda}$ and $D_{\vec{k},\lambda}$ are the creation and annihilation operators that follow the standard anticommutaiton relations $\{B_{\vec{k},\lambda}, B^{\dagger}_{\vec{k}',\lambda'}\} = \delta^3(\vec{k} - \vec{k}')\delta_{\lambda\lambda'}$, $\{B_{\vec{k},\lambda}, B_{\vec{k}',\lambda'}\} = 0$ (and similarly for $D_{\vec{k},\lambda}$), and the field modes $u_{\vec{k},\lambda}$ and $v_{\vec{k},\lambda}$ can be written as

$$u_{\vec{k},\lambda}(t) = \begin{pmatrix} h^I_k(t)\xi_\lambda(\vec{k}) \\ h^{II}_k(t)\frac{\vec{\sigma}\vec{k}}{k}\xi_\lambda(\vec{k}) \end{pmatrix} , \quad v_{\vec{k},\lambda}(t) = \begin{pmatrix} h^{II*}_k(t)\xi_{-\lambda}(\vec{k}) \\ h^{I*}_k(t)\frac{\vec{\sigma}\vec{k}}{k}\xi_{-\lambda}(\vec{k}) \end{pmatrix} , \tag{B.7}$$

with ξ_λ two constant orthonormal two-spinors ($\xi_\lambda^\dagger \xi_{\lambda'} = \delta_{\lambda,\lambda'}$), eigenvectors of the helicity operator $\frac{\vec{\sigma}\vec{k}}{2k}\xi_\lambda = \frac{\lambda}{2}\xi_\lambda$, and h_k^I and h_k^{II} two time-dependent functions. The functions h_k^I and h_k^{II} satisfy the following equations,

$$h_k^{II} = \frac{ia}{k}\left(\frac{\partial h_k^I}{\partial t} + i(m+s(t))h_k^I\right), \tag{B.8}$$

$$h_k^I = \frac{ia}{k}\left(\frac{\partial h_k^{II}}{\partial t} - i(m+s(t))h_k^{II}\right), \tag{B.9}$$

$$1 = |h_k^I|^2 + |h_k^{II}|^2. \tag{B.10}$$

The first two expressions are the fermionic first-order coupled equations of motion, which can be obtained by substituting Eq. (B.6) into (B.5). The third one is the normalization condition, which is preserved by the cosmological evolution at all times.

We now present the adiabatic expansion of a Dirac field living in a FLRW spacetime, and having a Yukawa interaction term with a classical background field. The particular form of the adiabatic expansion depends on the spin of the quantized field. For scalar fields, a WKB expansion provides an adequate solution (see, for instance, [155, 156, 164, 165]). For fermions fields, however, we showed in Refs. [163, 166] that the adiabatic expansion takes a different form. The adiabatic expansion is based on the following ansatz for the fermion field modes h_k^I and h_k^{II},

$$h_k^I(t) = \sqrt{\frac{\omega(t)+m}{2\omega(t)}}e^{-i\int^t \Omega(t')dt'}F(t), \qquad h_k^{II}(t) = \sqrt{\frac{\omega(t)-m}{2\omega(t)}}e^{-i\int^t \Omega(t')dt'}G(t), \tag{B.11}$$

where $\Omega(t)$, $F(t)$ and $G(t)$ are time-dependent functions, which are expanded adiabatically as

$$\begin{aligned}
\Omega &= \omega + \omega^{(1)} + \omega^{(2)} + \omega^{(3)} + \omega^{(4)} + \dots, \\
F &= 1 + F^{(1)} + F^{(2)} + F^{(3)} + F^{(4)} + \dots, \\
G &= 1 + G^{(1)} + G^{(2)} + G^{(3)} + G^{(4)} + \dots.
\end{aligned} \tag{B.12}$$

Here, $\omega(t) = \sqrt{(k/a)^2 + m^2}$ is the frequency of the field mode, and $F^{(n)}$, $G^{(n)}$ and $\omega^{(n)}$ are terms of nth adiabatic order (we explain what we mean by that below). The zeroth-order term of the field mode expansion recovers, in the adiabatic limit, the usual solution for a free fermion field in Minkowski spacetime. By substituting (B.11) into the equations of motion and normalization conditions Eqs. (B.8)-(B.10), we obtain the following system of three equations,

$$\begin{aligned}
(\omega - m)G &= \Omega F + i\dot{F} + \frac{iF}{2}\frac{d\omega}{dt}\left(\frac{1}{\omega+m} - \frac{1}{\omega}\right) - (m+s)F, \\
(\omega + m)F &= \Omega G + i\dot{G} + \frac{iG}{2}\frac{d\omega}{dt}\left(\frac{1}{\omega-m} - \frac{1}{\omega}\right) + (m+s)G, \\
(\omega + m)FF^* &+ (\omega - m)GG^* = 2\omega.
\end{aligned} \tag{B.13}$$

To obtain the expressions for $\Omega^{(n)}$, $F^{(n)}$, and $G^{(n)}$, we introduce the adiabatic expansions (B.12) into (B.13), and solve order by order. As usual in the adiabatic regularization method [155], we consider $\dot{a}$ of adiabatic order 1, $\ddot{a}$ of adiabatic order 2, and so on. On the other hand, we consider the interaction term $s(t)$ of adiabatic order 1, so that the zeroth order term in (B.11) recovers the free field solution in the adiabatic limit. Similarly, time-derivatives of the interaction increase the adiabatic order, so that $\dot{s}$ is of order 2, $\ddot{s}$ of order 3, and so on. With this, a generic expression $f^{(n)}$ of adiabatic order n (e.g. $f = F, G, \Omega$) can be written as a sum of all possible products of nth adiabatic order formed by s, a, and their time-derivatives. For example, generic functions of adiabatic orders 1 and 2 are written respectively as

$$
\begin{aligned}
f^{(1)} &= \alpha_1 s + \alpha_2 \dot{a} , \\
f^{(2)} &= \beta_1 s^2 + \beta_2 \dot{s} + \beta_3 \ddot{a} + \beta_4 \dot{a}^2 + \beta_5 \dot{a} s ,
\end{aligned}
\tag{B.14}
$$

with $\alpha_n \equiv \alpha_n(m, k, a)$ and $\beta_n \equiv \beta_n(m, k, a)$. The assignment of s as adiabatic order 1 is consistent with the scaling dimension of the scalar field, as it possesses the same dimensions as $\dot{a}$. By keeping only terms of first adiabatic order in (B.13), we get

$$
\begin{aligned}
(\omega - m)G^{(1)} &= (\omega - m)F^{(1)} + \omega^{(1)} - s + \frac{i}{2}\frac{d\omega}{dt}\left(\frac{1}{\omega + m} - \frac{1}{\omega}\right) , \\
(\omega + m)F^{(1)} &= (\omega + m)G^{(1)} + \omega^{(1)} + s + \frac{i}{2}\frac{d\omega}{dt}\left(\frac{1}{\omega - m} - \frac{1}{\omega}\right) , \\
(\omega + m)(F^{(1)} + F^{(1)*}) &+ (\omega - m)(G^{(1)} + G^{(1)*}) = 0 .
\end{aligned}
\tag{B.15}
$$

It is convenient to treat independently the real and imaginary parts of $F^{(1)}$ and $G^{(1)}$ as $F^{(1)} = f_x^{(1)} + i f_y^{(1)}$ and $G^{(1)} = g_x^{(1)} + i g_y^{(1)}$ ($w^{(n)}$ is always real). By solving (B.15), we find for the real part,

$$
f_x^{(1)} = \frac{s}{2\omega} - \frac{ms}{2\omega^2} , \qquad g_x^{(1)} = -\frac{s}{2\omega} - \frac{ms}{2\omega^2} , \qquad \omega^{(1)} = \frac{ms}{\omega} ,
\tag{B.16}
$$

and, for the imaginary part,

$$
f_y^{(1)} = -\frac{m\dot{a}}{4\omega^2 a} , \qquad g_y^{(1)} = \frac{m\dot{a}}{4\omega^2 a} .
\tag{B.17}
$$

The solution for the imaginary part has an ambiguity, which we have solved by imposing the additional condition $F^{(1)}(m, s) = G^{(1)}(-m, -s)$. This way, the adiabatic expansion also preserves the symmetries of the equations (B.9) with respect to the change $(m, s) \to (-m, -s)$. We have checked that physical expectation values are independent of this ambiguity.

Similarly, by keeping only the second-order terms in Eq. (B.13), we get

$$(\omega - m)G^{(2)} = (\omega - m)F^{(2)} + (\omega^{(1)} - s)F^{(1)} + \omega^{(2)} + i\dot{F}^{(1)} + i\frac{F^{(1)}}{2}\frac{d\omega}{dt}\left(\frac{1}{\omega + m} - \frac{1}{\omega}\right),$$

$$(\omega + m)F^{(2)} = (\omega + m)G^{(2)} + (\omega^{(1)} + s)G^{(1)} + \omega^{(2)} + i\dot{G}^{(1)} + i\frac{G^{(1)}}{2}\frac{d\omega}{dt}\left(\frac{1}{\omega - m} - \frac{1}{\omega}\right),$$

$$(\omega + m)(F^{(2)} + F^{(1)}F^{(1)*} + F^{(2)*}) + (\omega - m)(G^{(2)} + G^{(1)}G^{(1)*} + G^{(2)*}) = 0, \quad \text{(B.18)}$$

where the first-order terms have already been obtained above. The solutions for the real and imaginary part of these equations are

$$f_x^{(2)} = \frac{m^2\ddot{a}}{8a\omega^4} - \frac{m\ddot{a}}{8a\omega^3} - \frac{5m^4\dot{a}^2}{16a^2\omega^6} + \frac{5m^3\dot{a}^2}{16a^2\omega^5} + \frac{3m^2\dot{a}^2}{32a^2\omega^4} - \frac{m\dot{a}^2}{8a^2\omega^3} + \frac{5m^2s^2}{8\omega^4} - \frac{ms^2}{2\omega^3} - \frac{s^2}{8\omega^2},$$

$$\omega^{(2)} = \frac{-m^2s^2}{2\omega^3} + \frac{s^2}{2\omega} + \frac{5m^4\dot{a}^2}{8a^2\omega^5} - \frac{3m^2\dot{a}^2}{8a^2\omega^3} - \frac{m^2\ddot{a}}{4a\omega^3}, \quad \text{(B.19)}$$

$$f_y^{(2)} = \frac{5m^2s\dot{a}}{8a\omega^4} - \frac{s\dot{a}}{4a\omega^2} - \frac{\dot{s}}{4\omega^2}.$$

Again, there is an ambiguity in the solution of the imaginary part, which we have solved by imposing $F^{(2)}(m,s) = G^{(2)}(-m,-s)$. The same procedure can be repeated for all orders. The real part of the expansion is totally determined by the system of equations (B.13), while every imaginary part contains an ambiguity that can be solved by fixing the condition $F^{(n)}(m,s) = G^{(n)}(-m,-s)$. The third and fourth order terms of the expansion are explicitly written in [4].

Let us define a vacuum state $|0\rangle$ as $B_{\vec{k},\lambda}|0\rangle \equiv D_{\vec{k},\lambda}|0\rangle \equiv 0$, and denote any expectation value on this vacuum as e.g. $\langle T_{\mu\nu}\rangle \equiv \langle 0|T_{\mu\nu}|0\rangle$. In the quantum theory, the temporal and spatial components of the expectation value of the fermionic stress-energy tensor, Eq. (B.3), take the form, in the FLRW metric, (see for example [166])

$$\langle T_{00}\rangle = \frac{1}{2\pi^2a^3}\int_0^\infty dk k^2 \rho_k(t), \quad \rho_k(t) \equiv 2i\left(h_k^I\frac{\partial h_k^{I*}}{\partial t} + h_k^{II}\frac{\partial h_k^{II*}}{\partial t}\right), \quad \text{(B.20)}$$

and

$$\langle T_{ii}\rangle = \frac{1}{2\pi^2a}\int_0^\infty dk k^2 p_k(t), \quad p_k(t) \equiv -\frac{2k}{3a}(h_k^I h_k^{II*} + h_k^{I*}h_k^{II}). \quad \text{(B.21)}$$

The above formal expressions contain quartic, quadratic, and logarithmic UV divergences, which turn out to be independent of the particular quantum state. To characterize them, one plugs in (B.20)-(B.21) the adiabatic expansions of h_k^I and h_k^{II}, which are given in equation (B.11). We shall see that, in the presence of a Yukawa interaction, all adiabatic orders up to the fourth one generate UV divergences. In general, adiabatic regularization proceeds by subtracting those adiabatic terms from the integrand of the expectation values, producing a formal finite quantity.

We now proceed to calculate the renormalized expressions for the energy density and pressure. We start by performing the adiabatic expansion of the energy density in momentum space (B.21),

$$\rho_k = \rho_k^{(0)} + \rho_k^{(1)} + \rho_k^{(2)} + \rho_k^{(3)} + \rho_k^{(4)} + \dots , \qquad (B.22)$$

where $\rho_k^{(n)}$ is of nth adiabatic order. The adiabatic terms producing UV divergences (after integration in momenta) are

$$\rho_k^{(0)} = -2\omega , \qquad (B.23)$$

$$\rho_k^{(1)} = -\frac{2ms}{\omega} , \qquad (B.24)$$

$$\rho_k^{(2)} = -\frac{\dot{a}^2 m^4}{4a^2\omega^5} + \frac{\dot{a}^2 m^2}{4a^2\omega^3} + \frac{m^2 s^2}{\omega^3} - \frac{s^2}{\omega} , \qquad (B.25)$$

$$\rho_k^{(3)} = \frac{5\dot{a}^2 m^5 s}{4a^2\omega^7} - \frac{7\dot{a}^2 m^3 s}{4a^2\omega^5} + \frac{\dot{a}^2 ms}{2a^2\omega^3} - \frac{\dot{a} m^3 \dot{s}}{2a\omega^5} + \frac{\dot{a} m \dot{s}}{2a\omega^3} - \frac{m^3 s^3}{\omega^5} + \frac{ms^3}{\omega^3} , \qquad (B.26)$$

and,

$$\begin{aligned}
\rho_k^{(4)} = {} & \frac{105\dot{a}^4 m^8}{64a^4\omega^{11}} - \frac{91\dot{a}^4 m^6}{32a^4\omega^9} + \frac{81\dot{a}^4 m^4}{64a^4\omega^7} - \frac{\dot{a}^4 m^2}{16a^4\omega^5} - \frac{7\dot{a}^2 m^6 \ddot{a}}{8a^3\omega^9} + \frac{5\dot{a}^2 m^4 \ddot{a}}{4a^3\omega^7} - \frac{3\dot{a}^2 m^2 \ddot{a}}{8a^3\omega^5} \\
& - \frac{35\dot{a}^2 m^6 s^2}{8a^2\omega^9} + \frac{15\dot{a}^2 m^4 s^2}{2a^2\omega^7} - \frac{m^4 \ddot{a}^2}{16a^2\omega^7} - \frac{27\dot{a}^2 m^2 s^2}{8a^2\omega^5} + \frac{m^2 \ddot{a}^2}{16a^2\omega^5} + \frac{\dot{a}^2 s^2}{4a^2\omega^3} + \frac{\dot{a} m^4 a^{(3)}}{8a^2\omega^7} \\
& - \frac{\dot{a} m^2 a^{(3)}}{8a^2\omega^5} + \frac{5\dot{a} m^4 s\dot{s}}{2a\omega^7} - \frac{3\dot{a} m^2 s\dot{s}}{a\omega^5} + \frac{\dot{a} s\dot{s}}{2a\omega^3} + \frac{5m^4 s^4}{4\omega^7} - \frac{3m^2 s^4}{2\omega^5} - \frac{m^2 \dot{s}^2}{4\omega^5} + \frac{s^4}{4\omega^3} + \frac{\dot{s}^2}{4\omega^3} ,
\end{aligned} \qquad (B.27)$$

where we have used the notation $a^{(3)} \equiv d^3a/dt^3$, $a^{(4)} \equiv d^4a/dt^4$, etc. Note here that in the UV limit, $\rho_k^{(0)} \sim k$, $(\rho_k^{(1)} + \rho_k^{(2)}) \sim k^{-1}$, and $(\rho_k^{(3)} + \rho_k^{(4)}) \sim k^{-3}$. This indicates that subtracting the zeroth-order term cancels the natural quartic divergence of the stress-energy tensor, subtracting up to second order cancels also the quadratic divergence, and subtracting up to fourth order cancels the logarithmic divergence. Therefore, defining the adiabatic subtraction terms as

$$\langle T_{00}\rangle_{Ad} \equiv \frac{1}{2\pi^2 a^3} \int_0^\infty dk k^2 (\rho_k^{(0)} + \rho_k^{(1)} + \rho_k^{(2)} + \rho_k^{(3)} + \rho_k^{(4)}) \equiv \frac{1}{2\pi^2 a^3} \int_0^\infty dk k^2 \rho_k^{(0-4)} , \quad (B.28)$$

the renormalized 00-component of the stress-energy tensor is

$$\langle T_{00}\rangle_{ren} \equiv \langle T_{00}\rangle - \langle T_{00}\rangle_{Ad} = \frac{1}{2\pi^2 a^3} \int_0^\infty dk k^2 (\rho_k - \rho_k^{(0-4)}) . \qquad (B.29)$$

This integral is, by construction, finite. A similar construction can be applied for the ii components of the stress-energy tensor, which we show in Ref. [166]. Similarly, we can also obtain a renormalized expression for the two-point function $\langle \bar{\psi}\psi\rangle_{ren}$, which in this case requires subtraction up to third order. Note also that the ultraviolet divergent terms of the adiabatic subtractions can be univocally related to particular counterterms in a Lagrangian density including the background gravity-scalar sector [166].

Finally, the complete theory, including the gravity-scalar sector in the action, is

$$S = S_g + S_m = \frac{1}{16\pi G} \int d^4x \sqrt{-g} R + \int d^4x \sqrt{-g} \left\{ \frac{1}{2} g^{\mu\nu} \nabla_\mu \Phi \nabla_\nu \Phi - V(\Phi) \right\} + S_m , \quad \text{(B.30)}$$

where S_m is the action for the matter sector given in (B.1). The semiclassical equations are obtained by minimizing action (B.30) with respect Φ, $g^{\mu\nu}$ and ψ, and replacing $T_m^{\mu\nu}$ and $\bar{\psi}\psi$ by the corresponding (renormalized) vacuum expectation values $\langle T_m^{\mu\nu} \rangle_{ren}$ and $\langle \bar{\psi}\psi \rangle_{ren}$. These are

$$G^{\mu\nu} + 8\pi G (\nabla^\mu \Phi \nabla^\nu \Phi - \frac{1}{2} g^{\mu\nu} \nabla^\rho \Phi \nabla_\rho \Phi + g^{\mu\nu} V(\Phi)) \;\; = \;\; -8\pi G \langle T_m^{\mu\nu} \rangle_{ren} , \quad \text{(B.31)}$$

$$\Box \Phi + \frac{\partial V}{\partial \Phi} \;\; = \;\; -g_Y \langle \bar{\psi}\psi \rangle_{ren} . \quad \text{(B.32)}$$

When the spacetime is an expanding universe and Φ is an homogeneous scalar field $\Phi = \Phi(t)$ (e.g. an inflaton), Eqs. (B.31), (B.32), and the Dirac equation (B.2), describe the backreaction on the metric-inflaton system due to matter particle production and vacuum polarization, codified in the renormalized vacuum expectation values $\langle T_m^{\mu\nu} \rangle_{ren}$ and $\langle \bar{\psi}\psi \rangle_{ren}$.

Bibliography

[1] D. G. Figueroa, J. Garcia-Bellido and F. Torrenti, Phys. Rev. **D92**, 083511 (2015), [1504.04600], 10.1103/PhysRevD.92.083511.

[2] D. G. Figueroa, J. Garcia-Bellido and F. Torrenti, Phys. Rev. **D93**, 103521 (2016), [1602.03085], 10.1103/PhysRevD.93.103521.

[3] D. G. Figueroa and F. Torrenti, JCAP **1702**, 001 (2017), [1609.05197], 10.1088/1475-7516/2017/02/001.

[4] A. Del Rio, A. Ferreiro, J. Navarro-Salas and F. Torrenti, Phys. Rev. **D95**, 105003 (2017), [1703.00908].

[5] D. G. Figueroa and F. Torrenti, JCAP **1710**, 057 (2017), [1707.04533], 10.1088/1475-7516/2017/10/057.

[6] D. G. Figueroa, A. Rajantie and F. Torrenti, Phys. Rev. **D98**, 023532 (2017), [1709.00398], 10.1103/PhysRevD.98.023532.

[7] D. G. Figueroa, J. Garcia-Bellido and F. Torrenti, unpublished .

[8] Planck, P. A. R. Ade *et al.*, Astron. Astrophys. **594**, A13 (2016), [1502.01589], 10.1051/0004-6361/201525830.

[9] S. Weinberg, *Cosmology* (Oxford University Press, Oxford, 2008).

[10] M. E. Peskin and D. V. Schroeder, *An Introduction to quantum field theory* (Addison-Wesley, Reading, USA, 1995).

[11] D. J. Fixsen, Astrophys. J. **707**, 916 (2009), [0911.1955], 10.1088/0004-637X/707/2/916.

[12] A. H. Guth, Phys. Rev. **D23**, 347 (1981), 10.1103/PhysRevD.23.347.

[13] A. A. Starobinsky, Phys. Lett. **B91**, 99 (1980), 10.1016/0370-2693(80)90670-X.

[14] A. D. Linde, Phys. Lett. **B108**, 389 (1982), 10.1016/0370-2693(82)91219-9.

[15] A. Albrecht and P. J. Steinhardt, Phys. Rev. Lett. **48**, 1220 (1982), 10.1103/PhysRevLett.48.1220.

[16] Planck, P. A. R. Ade *et al.*, Astron. Astrophys. **594**, A20 (2016), [1502.02114], 10.1051/0004-6361/201525898.

[17] D. H. Lyth and A. Riotto, Phys. Rept. **314**, 1 (1999), [hep-ph/9807278], 10.1016/S0370-1573(98)00128-8.

[18] S. Tsujikawa, J. Ohashi, S. Kuroyanagi and A. De Felice, Phys. Rev. **D88**, 023529 (2013), [1305.3044], 10.1103/PhysRevD.88.023529.

[19] F. L. Bezrukov and M. Shaposhnikov, Phys.Lett. **B659**, 703 (2008), [0710.3755], 10.1016/j.physletb.2007.11.072.

[20] F. Bezrukov, A. Magnin, M. Shaposhnikov and S. Sibiryakov, JHEP **1101**, 016 (2011), [1008.5157], 10.1007/JHEP01(2011)016.

[21] J. H. Traschen and R. H. Brandenberger, Phys.Rev. **D42**, 2491 (1990), 10.1103/PhysRevD.42.2491.

[22] L. Kofman, A. D. Linde and A. A. Starobinsky, Phys.Rev.Lett. **73**, 3195 (1994), [hep-th/9405187], 10.1103/PhysRevLett.73.3195.

[23] Y. Shtanov, J. H. Traschen and R. H. Brandenberger, Phys. Rev. **D51**, 5438 (1995), [hep-ph/9407247], 10.1103/PhysRevD.51.5438.

[24] D. I. Kaiser, Phys. Rev. **D53**, 1776 (1996), [astro-ph/9507108], 10.1103/PhysRevD.53.1776.

[25] L. Kofman, A. D. Linde and A. A. Starobinsky, Phys.Rev. **D56**, 3258 (1997), [hep-ph/9704452], 10.1103/PhysRevD.56.3258.

[26] P. B. Greene, L. Kofman, A. D. Linde and A. A. Starobinsky, Phys.Rev. **D56**, 6175 (1997), [hep-ph/9705347], 10.1103/PhysRevD.56.6175.

[27] D. I. Kaiser, Phys. Rev. **D56**, 706 (1997), [hep-ph/9702244], 10.1103/PhysRevD.56.706.

[28] D. I. Kaiser, Phys. Rev. **D57**, 702 (1998), [hep-ph/9707516], 10.1103/PhysRevD.57.702.

[29] P. B. Greene and L. Kofman, Phys.Lett. **B448**, 6 (1999), [hep-ph/9807339], 10.1016/S0370-2693(99)00020-9.

[30] P. B. Greene and L. Kofman, Phys.Rev. **D62**, 123516 (2000), [hep-ph/0003018], 10.1103/PhysRevD.62.123516.

[31] M. Peloso and L. Sorbo, JHEP **0005**, 016 (2000), [hep-ph/0003045], 10.1088/1126-6708/2000/05/016.

[32] J. Garcia-Bellido, S. Mollerach and E. Roulet, JHEP **0002**, 034 (2000), [hep-ph/0002076], 10.1088/1126-6708/2000/02/034.

[33] J. Garcia-Bellido and E. Ruiz Morales, Phys.Lett. **B536**, 193 (2002), [hep-ph/0109230], 10.1016/S0370-2693(02)01820-8.

[34] J. Berges, D. Gelfand and J. Pruschke, Phys.Rev.Lett. **107**, 061301 (2011), [1012.4632], 10.1103/PhysRevLett.107.061301.

[35] R. Allahverdi, R. Brandenberger, F.-Y. Cyr-Racine and A. Mazumdar, Ann. Rev. Nucl. Part. Sci. **60**, 27 (2010), [1001.2600], 10.1146/annurev.nucl.012809.104511.

[36] M. A. Amin, M. P. Hertzberg, D. I. Kaiser and J. Karouby, Int. J. Mod. Phys. **D24**, 1530003 (2014), [1410.3808], 10.1142/S0218271815300037.

[37] K. Enqvist and M. S. Sloth, Nucl.Phys. **B626**, 395 (2002), [hep-ph/0109214], 10.1016/S0550-3213(02)00043-3.

[38] D. H. Lyth and D. Wands, Phys.Lett. **B524**, 5 (2002), [hep-ph/0110002], 10.1016/S0370-2693(01)01366-1.

[39] T. Moroi and T. Takahashi, Phys.Lett. **B522**, 215 (2001), [hep-ph/0110096], 10.1016/S0370-2693(01)01295-3.

[40] A. Mazumdar and J. Rocher, Phys. Rept. **497**, 85 (2011), [1001.0993], 10.1016/j.physrep.2010.08.001.

[41] K. Enqvist, S. Nurmi and G. Rigopoulos, JCAP **0810**, 013 (2008), [0807.0382], 10.1088/1475-7516/2008/10/013.

[42] K. Enqvist, D. G. Figueroa and R. N. Lerner, JCAP **1301**, 040 (2013), [1211.5028], 10.1088/1475-7516/2013/01/040.

[43] K. Enqvist, R. N. Lerner and S. Rusak, JCAP **1311**, 034 (2013), [1308.3321], 10.1088/1475-7516/2013/11/034.

[44] K. Enqvist, R. N. Lerner and T. Takahashi, JCAP **1401**, 006 (2014), [1310.1374], 10.1088/1475-7516/2014/01/006.

[45] S. Yu. Khlebnikov and I. I. Tkachev, Phys. Rev. Lett. **77**, 219 (1996), [hep-ph/9603378], 10.1103/PhysRevLett.77.219.

[46] T. Prokopec and T. G. Roos, Phys. Rev. **D55**, 3768 (1997), [hep-ph/9610400], 10.1103/PhysRevD.55.3768.

[47] G. N. Felder and I. Tkachev, Comput. Phys. Commun. **178**, 929 (2008), [hep-ph/0011159], 10.1016/j.cpc.2008.02.009.

[48] A. V. Frolov, JCAP **0811**, 009 (2008), [0809.4904], 10.1088/1475-7516/2008/11/009.

[49] R. Easther, H. Finkel and N. Roth, JCAP **1010**, 025 (2010), [1005.1921], 10.1088/1475-7516/2010/10/025.

[50] Z. Huang, Phys. Rev. **D83**, 123509 (2011), [1102.0227], 10.1103/PhysRevD.83.123509.

[51] http://cosmo.kenyon.edu/gabe.html.

[52] M. S. Turner, Phys.Rev. **D28**, 1243 (1983), 10.1103/PhysRevD.28.1243.

[53] Q.-G. Huang, JCAP **0811**, 005 (2008), [0808.1793], 10.1088/1475-7516/2008/11/005.

[54] A. A. Starobinsky and J. Yokoyama, Phys.Rev. **D50**, 6357 (1994), [astro-ph/9407016], 10.1103/PhysRevD.50.6357.

[55] K. Enqvist, T. Meriniemi and S. Nurmi, JCAP **1310**, 057 (2013), [1306.4511], 10.1088/1475-7516/2013/10/057.

[56] A. De Simone and A. Riotto, JCAP **1302**, 014 (2013), [1208.1344], 10.1088/1475-7516/2013/02/014.

[57] R. Micha and I. I. Tkachev, Phys.Rev.Lett. **90**, 121301 (2003), [hep-ph/0210202], 10.1103/PhysRevLett.90.121301.

[58] R. Micha and I. I. Tkachev, Phys.Rev. **D70**, 043538 (2004), [hep-ph/0403101], 10.1103/PhysRevD.70.043538.

[59] D. I. Podolsky, G. N. Felder, L. Kofman and M. Peloso, Phys. Rev. **D73**, 023501 (2006), [hep-ph/0507096], 10.1103/PhysRevD.73.023501.

[60] K. D. Lozanov and M. A. Amin, Phys. Rev. Lett. **119**, 061301 (2017), [1608.01213], 10.1103/PhysRevLett.119.061301.

[61] J. Garcia-Bellido, D. Yu. Grigoriev, A. Kusenko and M. E. Shaposhnikov, Phys. Rev. **D60**, 123504 (1999), [hep-ph/9902449], 10.1103/PhysRevD.60.123504.

[62] A. Rajantie, P. M. Saffin and E. J. Copeland, Phys. Rev. **D63**, 123512 (2001), [hep-ph/0012097], 10.1103/PhysRevD.63.123512.

[63] J. Garcia-Bellido, M. Garcia-Perez and A. Gonzalez-Arroyo, Phys.Rev. **D69**, 023504 (2004), [hep-ph/0304285], 10.1103/PhysRevD.69.023504.

[64] F. Bezrukov, D. Gorbunov and M. Shaposhnikov, JCAP **0906**, 029 (2009), [0812.3622], 10.1088/1475-7516/2009/06/029.

[65] J. Garcia-Bellido, D. G. Figueroa and J. Rubio, Phys.Rev. **D79**, 063531 (2009), [0812.4624], 10.1103/PhysRevD.79.063531.

[66] F. Bezrukov, J. Rubio and M. Shaposhnikov, Phys. Rev. **D92**, 083512 (2015), [1412.3811], 10.1103/PhysRevD.92.083512.

[67] J.-F. Dufaux, D. G. Figueroa and J. Garcia-Bellido, Phys.Rev. **D82**, 083518 (2010), [1006.0217], 10.1103/PhysRevD.82.083518.

[68] J. T. Deskins, J. T. Giblin and R. R. Caldwell, Phys. Rev. **D88**, 063530 (2013), [1305.7226], 10.1103/PhysRevD.88.063530.

[69] P. Adshead, J. T. Giblin, T. R. Scully and E. I. Sfakianakis, JCAP **1512**, 034 (2015), [1502.06506], 10.1088/1475-7516/2015/12/034.

[70] K. Enqvist, S. Nurmi, S. Rusak and D. Weir, JCAP **1602**, 057 (2016), [1506.06895], 10.1088/1475-7516/2016/02/057.

[71] K. D. Lozanov and M. A. Amin, JCAP **1606**, 032 (2016), [1603.05663], 10.1088/1475-7516/2016/06/032.

[72] D. G. Figueroa and C. T. Byrnes, Phys. Lett. **B767**, 272 (2017), [1604.03905], 10.1016/j.physletb.2017.01.059.

[73] J. Garcia-Bellido and A. D. Linde, Phys. Rev. **D57**, 6075 (1998), [hep-ph/9711360], 10.1103/PhysRevD.57.6075.

[74] G. N. Felder *et al.*, Phys. Rev. Lett. **87**, 011601 (2001), [hep-ph/0012142], 10.1103/Phys-

RevLett.87.011601.

[75] G. N. Felder, L. Kofman and A. D. Linde, Phys. Rev. **D64**, 123517 (2001), [hep-th/0106179], 10.1103/PhysRevD.64.123517.

[76] E. J. Copeland, S. Pascoli and A. Rajantie, Phys. Rev. **D65**, 103517 (2002), [hep-ph/0202031], 10.1103/PhysRevD.65.103517.

[77] J. Garcia-Bellido, M. Garcia Perez and A. Gonzalez-Arroyo, Phys. Rev. **D67**, 103501 (2003), [hep-ph/0208228], 10.1103/PhysRevD.67.103501.

[78] J. Garcia-Bellido and D. G. Figueroa, Phys. Rev. Lett. **98**, 061302 (2007), [astro-ph/0701014], 10.1103/PhysRevLett.98.061302.

[79] J. Garcia-Bellido, D. G. Figueroa and A. Sastre, Phys. Rev. **D77**, 043517 (2008), [0707.0839], 10.1103/PhysRevD.77.043517.

[80] J.-F. Dufaux, G. Felder, L. Kofman and O. Navros, JCAP **0903**, 001 (2009), [0812.2917], 10.1088/1475-7516/2009/03/001.

[81] J. F. Dufaux, G. N. Felder, L. Kofman, M. Peloso and D. Podolsky, JCAP **0607**, 006 (2006), [hep-ph/0602144], 10.1088/1475-7516/2006/07/006.

[82] D. Croon, V. Sanz and E. R. M. Tarrant, Phys. Rev. **D94**, 045010 (2016), [1507.04653], 10.1103/PhysRevD.94.045010.

[83] S. Antusch, F. Cefala, D. Nolde and S. Orani, JCAP **1602**, 044 (2016), [1510.04856], 10.1088/1475-7516/2016/02/044.

[84] K. Enqvist, M. Karciauskas, O. Lebedev, S. Rusak and M. Zatta, JCAP **1611**, 025 (2016), [1608.08848], 10.1088/1475-7516/2016/11/025.

[85] I. Tkachev, S. Khlebnikov, L. Kofman and A. D. Linde, Phys. Lett. **B440**, 262 (1998), [hep-ph/9805209], 10.1016/S0370-2693(98)01094-6.

[86] K. A. Olive and M. Peloso, Phys. Rev. **D74**, 103514 (2006), [hep-ph/0608096], 10.1103/PhysRevD.74.103514.

[87] A. E. Gumrukcuoglu, K. A. Olive, M. Peloso and M. Sexton, Phys. Rev. **D78**, 063512 (2008), [0805.0273], 10.1103/PhysRevD.78.063512.

[88] M. P. DeCross, D. I. Kaiser, A. Prabhu, C. Prescod-Weinstein and E. I. Sfakianakis, Phys. Rev. **D97**, 023526 (2018), [1510.08553], 10.1103/PhysRevD.97.023526.

[89] G. Ballesteros, J. Redondo, A. Ringwald and C. Tamarit, Phys. Rev. Lett. **118**, 071802 (2017), [1608.05414], 10.1103/PhysRevLett.118.071802.

[90] B. A. et al. [LIGO Scientific and V. Collaboration], Phys. Rev.Lett. **116**, 061102 (2016), [1602.03837], 10.1103/PhysRevLett.116.061102.

[91] A. A. Starobinsky, JETP Lett. **30**, 682 (1979).

[92] S. Y. Khlebnikov and I. I. Tkachev, Phys. Rev. **D56**, 653 (1997), [hep-ph/9701423], 10.1103/PhysRevD.56.653.

[93] J. Garcia-Bellido, Preheating the universe in hybrid inflation, in *Proceedings, 33rd Rencontres de Moriond fundamental parameters in cosmology*, pp. 29–34, 1998, [hep-ph/9804205].

[94] R. Easther and E. A. Lim, JCAP **0604**, 010 (2006), [astro-ph/0601617], 10.1088/1475-7516/2006/04/010.

[95] J. F. Dufaux, A. Bergman, G. N. Felder, L. Kofman and J.-P. Uzan, Phys. Rev. **D76**, 123517 (2007), [0707.0875], 10.1103/PhysRevD.76.123517.

[96] M. Kamionkowski, A. Kosowsky and M. S. Turner, Phys.Rev. **D49**, 2837 (1994), [astro-ph/9310044], 10.1103/PhysRevD.49.2837.

[97] C. Caprini, R. Durrer and G. Servant, Phys.Rev. **D77**, 124015 (2008), [0711.2593], 10.1103/PhysRevD.77.124015.

[98] S. J. Huber and T. Konstandin, JCAP **0809**, 022 (2008), [0806.1828], 10.1088/1475-7516/2008/09/022.

[99] M. Hindmarsh, S. J. Huber, K. Rummukainen and D. J. Weir, Phys. Rev. Lett. **112**, 041301 (2014), [1304.2433], 10.1103/PhysRevLett.112.041301.

[100] M. Hindmarsh, S. J. Huber, K. Rummukainen and D. J. Weir, Phys. Rev. **D92**, 123009 (2015), [1504.03291], 10.1103/PhysRevD.92.123009.

[101] T. Damour and A. Vilenkin, Phys.Rev. **D71**, 063510 (2005), [hep-th/0410222], 10.1103/PhysRevD.71.063510.

[102] T. Vachaspati and A. Vilenkin, Phys.Rev. **D31**, 3052 (1985), 10.1103/PhysRevD.31.3052.

[103] K. Jones-Smith, L. M. Krauss and H. Mathur, Phys.Rev.Lett. **100**, 131302 (2008), [0712.0778], 10.1103/PhysRevLett.100.131302.

[104] E. Fenu, D. G. Figueroa, R. Durrer and J. Garcia-Bellido, JCAP **0910**, 005 (2009), [0908.0425], 10.1088/1475-7516/2009/10/005.

[105] D. G. Figueroa, M. Hindmarsh and J. Urrestilla, Phys.Rev.Lett. **110**, 101302 (2013), [1212.5458], 10.1103/PhysRevLett.110.101302.

[106] C. Caprini and D. G. Figueroa, Class. Quant. Grav. **35**, 163001 (2018), [1801.04268], 10.1088/1361-6382/aac608.

[107] R. Easther, J. T. Giblin, Jr. and E. A. Lim, Phys. Rev. Lett. **99**, 221301 (2007), [astro-ph/0612294], 10.1103/PhysRevLett.99.221301.

[108] D. G. Figueroa, J. Garcia-Bellido and A. Rajantie, JCAP **1111**, 015 (2011), [1110.0337], 10.1088/1475-7516/2011/11/015.

[109] L. Bethke, D. G. Figueroa and A. Rajantie, Phys.Rev.Lett. **111**, 011301 (2013), [1304.2657], 10.1103/PhysRevLett.111.011301.

[110] L. Bethke, D. G. Figueroa and A. Rajantie, JCAP **1406**, 047 (2014), [1309.1148], 10.1088/1475-7516/2014/06/047.

[111] E. J. Copeland, M. Gleiser and H. R. Muller, Phys. Rev. **D52**, 1920 (1995), [hep-ph/9503217], 10.1103/PhysRevD.52.1920.

[112] M. A. Amin, R. Easther, H. Finkel, R. Flauger and M. P. Hertzberg, Phys. Rev. Lett. **108**, 241302 (2012), [1106.3335], 10.1103/PhysRevLett.108.241302.

[113] S.-Y. Zhou *et al.*, JHEP **10**, 026 (2013), [1304.6094], 10.1007/JHEP10(2013)026.

[114] S. Antusch, F. Cefala and S. Orani, Phys. Rev. Lett. **118**, 011303 (2017), [1607.01314], 10.1103/PhysRevLett.120.219901, 10.1103/PhysRevLett.118.011303.

[115] S. Antusch, F. Cefala and S. Orani, JCAP **1803**, 032 (2018), [1712.03231], 10.1088/1475-7516/2018/03/032.

[116] M. A. Amin *et al.*, 1803.08047.

[117] R. Easther, J. T. Giblin and E. A. Lim, Phys. Rev. **D77**, 103519 (2008), [0712.2991], 10.1103/PhysRevD.77.103519.

[118] L. R. Price and X. Siemens, Phys. Rev. **D78**, 063541 (2008), [0805.3570], 10.1103/PhysRevD.78.063541.

[119] A. D. Linde, Contemp.Concepts Phys. **5**, 1 (1990), [hep-th/0503203].

[120] K. Enqvist, D. G. Figueroa and T. Meriniemi, Phys.Rev. **D86**, 061301 (2012), [1203.4943], 10.1103/PhysRevD.86.061301.

[121] D. G. Figueroa and T. Meriniemi, JHEP **10**, 101 (2013), [1306.6911], 10.1007/JHEP10(2013)101.

[122] D. G. Figueroa, JHEP **1411**, 145 (2014), [1402.1345], 10.1007/JHEP11(2014)145.

[123] G. Ballesteros, J. Redondo, A. Ringwald and C. Tamarit, JCAP **1708**, 001 (2017), [1610.01639], 10.1088/1475-7516/2017/08/001.

[124] A. Tranberg, S. Tahtinen and D. J. Weir, JCAP **1804**, 012 (2018), [1706.02365], 10.1088/1475-7516/2018/04/012.

[125] ATLAS Collaboration, G. Aad *et al.*, Phys.Lett. **B716**, 1 (2012), [1207.7214], 10.1016/j.physletb.2012.08.020.

[126] CMS Collaboration, S. Chatrchyan *et al.*, Phys.Lett. **B716**, 30 (2012), [1207.7235], 10.1016/j.physletb.2012.08.021.

[127] J. Espinosa, G. Giudice and A. Riotto, JCAP **0805**, 002 (2008), [0710.2484], 10.1088/1475-7516/2008/05/002.

[128] K. Enqvist, S. Nurmi and S. Rusak, JCAP **1410**, 064 (2014), [1404.3631], 10.1088/1475-7516/2014/10/064.

[129] M. Herranen, T. Markkanen, S. Nurmi and A. Rajantie, Phys.Rev.Lett. **113**, 211102 (2014),

[1407.3141], 10.1103/PhysRevLett.113.211102.

[130] F. Bezrukov, http://www.inr.ac.ru/˜fedor/SM/.

[131] F. Bezrukov, M. Y. Kalmykov, B. A. Kniehl and M. Shaposhnikov, JHEP **1210**, 140 (2012), [1205.2893], 10.1007/JHEP10(2012)140.

[132] G. Degrassi *et al.*, JHEP **1208**, 098 (2012), [1205.6497], 10.1007/JHEP08(2012)098.

[133] C. Collaboration, Phys. Rev. **D93**, 072004 (2016), [1509.04044], 10.1103/PhysRevD.93.072004.

[134] A. A. Starobinsky, Lect.Notes Phys. **246**, 107 (1986).

[135] B. Spokoiny, Phys.Lett. **B315**, 40 (1993), [gr-qc/9306008], 10.1016/0370-2693(93)90155-B.

[136] M. Joyce, Phys.Rev. **D55**, 1875 (1997), [hep-ph/9606223], 10.1103/PhysRevD.55.1875.

[137] R. Casadio, P. Iafelice and G. Vacca, Nucl.Phys. **B783**, 1 (2007), [hep-th/0702175], 10.1016/j.nuclphysb.2007.05.015.

[138] G. Giudice, M. Peloso, A. Riotto and I. Tkachev, JHEP **9908**, 014 (1999), [hep-ph/9905242], 10.1088/1126-6708/1999/08/014.

[139] A. Kusenko, L. Pearce and L. Yang, Phys.Rev.Lett. **114**, 061302 (2015), [1410.0722], 10.1103/PhysRevLett.114.061302.

[140] L. Pearce, L. Yang, A. Kusenko and M. Peloso, Phys. Rev. **D92**, 023509 (2015), [1505.02461], 10.1103/PhysRevD.92.023509.

[141] K. Enqvist, S. Nurmi, T. Tenkanen and K. Tuominen, JCAP **1408**, 035 (2014), [1407.0659], 10.1088/1475-7516/2014/08/035.

[142] D. G. Figueroa, *Aspects of Reheating*, PhD thesis, 2010.

[143] A. Kobakhidze and A. Spencer-Smith, Phys.Lett. **B722**, 130 (2013), [1301.2846], 10.1016/j.physletb.2013.04.013.

[144] M. Fairbairn and R. Hogan, Phys. Rev. Lett. **112**, 201801 (2014), [1403.6786], 10.1103/PhysRevLett.112.201801.

[145] K. Enqvist, T. Meriniemi and S. Nurmi, JCAP **1407**, 025 (2014), [1404.3699], 10.1088/1475-7516/2014/07/025.

[146] J. Kearney, H. Yoo and K. M. Zurek, Phys. Rev. **D91**, 123537 (2015), [1503.05193], 10.1103/PhysRevD.91.123537.

[147] K. Kamada, Phys.Lett. **B742**, 126 (2015), [1409.5078], 10.1016/j.physletb.2015.01.024.

[148] J. R. Espinosa *et al.*, JHEP **09**, 174 (2015), [1505.04825], 10.1007/JHEP09(2015)174.

[149] A. Joti *et al.*, JHEP **07**, 058 (2017), [1706.00792], 10.1007/JHEP07(2017)058.

[150] A. Rajantie and S. Stopyra, Phys. Rev. **D97**, 025012 (2018), [1707.09175], 10.1103/PhysRevD.97.025012.

[151] M. Herranen, T. Markkanen, S. Nurmi and A. Rajantie, Phys. Rev. Lett. **115**, 241301 (2015), [1506.04065], 10.1103/PhysRevLett.115.241301.

[152] K. Kohri and H. Matsui, Phys. Rev. **D94**, 103509 (2016), [1602.02100], 10.1103/PhysRevD.94.103509.

[153] Y. Ema, K. Mukaida and K. Nakayama, JCAP **1610**, 043 (2016), [1602.00483], 10.1088/1475-7516/2016/10/043.

[154] Y. Ema, M. Karciauskas, O. Lebedev and M. Zatta, JCAP **1706**, 054 (2017), [1703.04681], 10.1088/1475-7516/2017/06/054.

[155] L. Parker and D. Toms, *Quantum Field Theory in Curved Spacetime: Quantized Fields and Gravity* (Cambridge Monographs on Mathematical Physics, 2009).

[156] N. Birrell and P. Davies, *Quantum Fields in Curved Space* (Cambridge Monographs on Mathematical Physics, 1984).

[157] M. Atkins and X. Calmet, Phys. Rev. Lett. **110**, 051301 (2013), [1211.0281], 10.1103/PhysRevLett.110.051301.

[158] T. Markkanen, S. Nurmi, A. Rajantie and S. Stopyra, JHEP **06**, 040 (2018), [1804.02020], 10.1007/JHEP06(2018)040.

[159] J. Baacke, K. Heitmann and C. Patzold, Phys. Rev. **D58**, 125013 (1998), [hep-ph/9806205], 10.1103/PhysRevD.58.125013.

[160] L. Parker, Phys. Rev. Lett. **21**, 562 (1968), 10.1103/PhysRevLett.21.562.

[161] L. Parker and S. A. Fulling, Phys. Rev. **D9**, 341 (1974), 10.1103/PhysRevD.9.341.

[162] A. Landete, J. Navarro-Salas and F. Torrenti, Phys. Rev. **D88**, 061501 (2013), [1305.7374], 10.1103/PhysRevD.88.061501.

[163] A. Landete, J. Navarro-Salas and F. Torrenti, Phys. Rev. **D89**, 044030 (2014), [1311.4958], 10.1103/PhysRevD.89.044030.

[164] P. R. Anderson, C. Molina-Paris, D. Evanich and G. B. Cook, Phys. Rev. **D78**, 083514 (2008), [0801.0730], 10.1103/PhysRevD.78.083514.

[165] C. Molina-Paris, P. R. Anderson and S. A. Ramsey, Phys. Rev. **D61**, 127501 (2000), 10.1103/PhysRevD.61.127501.

[166] A. del Rio, J. Navarro-Salas and F. Torrenti, Phys. Rev. **D90**, 084017 (2014), [1407.5058], 10.1103/PhysRevD.90.084017.